Modular Connected Machines System for Electrified Vehicles

Système de Machines Connectées Modulaires pour Véhicules Électriques

Thèse de doctorat en cotutelle de

l'Université Lille, France et

Harbin Institute of Technology, Chine

Spécialité : **Génie électrique**

par

Kaibo LI

Soutenue le 19 mars 2020 devant le jury composé de :

M. Alain Bouscayrol	Directeur de thèse	Professeur à l'Université de Lille, laboratoire L2EP, France
Ms. Shumei Cui	Codirecteur de thèse	Professeur à Harbin Institute of Technology, Chine
M. Daniel Hissel	Rapporteur	Professeur à l'Université de Bourgogne, France
M. Yongdong Li	Président	Professeur à Tsinghua University, Chine
M. Jianxin Shen	Examinateur	Professeur à Zhejiang University, Chine
M. Rochdi Trigui	Rapporteur	Directeur de recherche à IFSTTAR, France

Acknowledgement

I sincerely thank my supervisor Professor **Alain Bouscayrol** and Professor **Cui Shumei** for their meticulous guidance. Both supervisors gave me the full guidance and help throughout my PhD career. Each part of the work and achievement of this thesis embodies their wisdom. On the occasion of the completion of this thesis, I would like to express my respect and sincere gratitude to my supervisors. They are knowledgeable and their words and deeds will benefit me for the rest of my life.

During my studies, Professor **Zhang Qianfan** gave a lot of support and help for my international cooperation and academic research. I would like to express my heartfelt thanks. I also thank Professor **Michel Hecquet**, Dr. **Walter Lhomme**, Dr. **Ronan Germam** and Dr. **Yuan Cheng** for their kind help.

I am grateful to **Florian Tournez** for his strong technique support of my experiment. I would also acknowledge **Bao-Huy Nguyen**, **Pam Abdoulaye**, **Shouliang Han**, **Zhi Kuang**, **Bochao Du**, **Zetao Ma**, **Zhenyuan Zhang**, **Ling Ding** and **Chenchen Tian** for the help in my research.

The support and encouragement of my family is a strong backing on the road of my study. I would like to thank my family and friends for their encouragement and care.

Finally, I am grateful to National Natural Science Foundation (NNSF) of Chine for funding this subject. I would also like to thank China Scholarship Council (CSC) and University of Lille for supporting my wonderful and unforgettable stay in France.

Abstract

Modular Connected Machines (MCM) system is one kind of multi-machine system, where several machines are integrated into a module. It has wider high-efficiency area, better fault tolerance ability and numerous operation modes, and is perspective in the fields of electrified vehicles. The objective of this PhD subject is to develop different MCM systems for electrified vehicles.

For this, this PhD thesis firstly organizes the model and control of a MCM-based vehicle by Energetic Macroscopic Representation (EMR). The use of EMR emphasizes the important couplings, which distribute energy. Through inversion rules, EMR highlights the necessity for introducing energy distribution criteria in the control structure. Then a fast efficiency map estimation method for different EMs are proposed. The elimination of Electrical Machine (EM) pre-design saves a lot of time, which lays a foundation for MCM sizing. Next, a multi-objective-based sizing method for a MCM is proposed, which can ensure lager high-efficiency area, larger torque density and less usage amount of Permanent Magnet (PM). The interest of different MCM systems for different vehicles are compared and analysed. Finally, two kinds of power split strategies of a MCM system are developed. They are compared in terms of efficiency and EM operating property. A reduced-scale Hardware-In-the-Loop (HIL) setup is established and the strategies are validated in real-time.

Key words : electrified vehicle, multi-machine, sizing, efficiency map estimation, modelling and control, energy management

Résumé

Le système de Machines Connectées Modulaires (MCM) est un type même système multi-machine, dans lequel plusieurs machines électriques sont intégrées dans un module. Il possède une zone à haute efficacité plus large, une meilleure capacité de tolérance aux pannes et de nombreux modes de fonctionnement. Il a des perspectives possibles dans le domaine des véhicules électrifiés. L'objectif de cette thèse est de développer différents systèmes MCM pour véhicules électrifiés.

Pour cela, cette thèse organise tout d'abord le modèle et la commande d'un véhicule à base de MCM via la Représentation Energétique Macroscopique (REM). L'utilisation de la REM met l'accent sur les couplages importants, qui distribuent de l'énergie. Par le biais de règles d'inversion, la REM souligne la nécessité d'introduire des critères de répartition de l'énergie dans la structure de commande. Ensuite, une méthode de calcul rapide de la cartographie de rendement pour différentes machines électriques est proposée. L'élimination de la préconception de machine électrique permet de gagner beaucoup de temps, ce qui jette les bases du dimensionnement de MCM. En suite, une méthode de dimensionnement basée sur plusieurs objectifs est proposée, pour assurer une zone à haute efficacité plus large, une densité de couple plus grande et un volume d'aimant permanent moins important. Les intérêts de différents MCM pour différents véhicules sont comparés et analysés. Enfin, deux stratégies de répartition de la puissance au sein du MCM sont développées sur la base de la stratégie d'efficacité optimale. Elles sont comparées en termes d'efficacité et de condition de fonctionnement. Une configuration Hardware-In-the-Loop (HIL) à échelle réduite est établie et les stratégies sont validées en temps réel.

Mots clés : véhicule électrifié, multi-machine, dimensionnement, calcul de cartographie de rendement, modélisation et commande, gestion de l'énergie

Contents

Introduction **1**

1 Context and Objective **5**
1.1 Development of traction machines 6
1.1.1 Common types 6
1.1.2 Modular machine 7
1.2 Topologies of multi-machine system 9
1.2.1 Multi-machine system for EV 10
1.2.2 Multi-machine system for HEV 13
1.3 Challenges of a multi-machine system 15
1.3.1 System sizing 15
1.3.2 Power split strategy 17
1.4 Methods related to the study of MCM 18
1.4.1 Graphical description tools 18
1.4.2 Efficiency map calculation method of an EM 19
1.5 Objective of the subject 20
1.5.1 Positioning 20
1.5.2 Objective 21
1.5.3 Organization 22
1.6 Conclusion 23

2 Modelling and control of a MCM-based vehicle **24**
2.1 Introduction 25
2.2 Topologies and properties of a MCM 25
2.3 Modelling of an electric drive using EMR 27
2.3.1 Model of an inverter 27
2.3.2 Model of an EM 29

2.4 Inversion-based control of an electric drive . . . 34
2.4.1 Control an electric drive . . . 34
2.4.2 Validation of the control . . . 36
2.5 Modelling of a MCM-based vehicle using EMR . . . 39
2.5.1 Model of a MCM-based EV . . . 39
2.5.2 Model of a MCM-based HEV . . . 42
2.6 Inversion-based control of a MCM-based vehicle . . . 46
2.6.1 Control of a MCM-based EV . . . 46
2.6.2 Control of a MCM-based HEV . . . 47
2.7 Conclusion . . . 48

3 Fast efficiency map estimation method for different EMs 50
3.1 Introduction . . . 51
3.2 Description of efficiency map estimation . . . 51
3.3 IM efficiency map estimation . . . 53
3.3.1 Current angle and slip ratio calculation . . . 54
3.3.2 Rated losses calculation . . . 58
3.3.3 Loss map calculation for IMs . . . 60
3.4 PM-SM efficiency map estimation . . . 61
3.4.1 Current angle calculation . . . 62
3.4.2 Rated losses calculation . . . 64
3.4.3 Loss map calculation for PM-SMs . . . 66
3.5 Validation of the efficiency map estimation methods . . . 68
3.5.1 Experimental test of EM efficiency maps . . . 68
3.5.2 Errors of the estimated efficiency maps . . . 69
3.5.3 Errors of vehicle energy consumption with the estimated efficiency maps . . . 72
3.6 Conclusion . . . 75

4 MCM sizing based on multi-objective optimization 76
4.1 Introduction . . . 77
4.2 Descriptions of the sizing problem . . . 77
4.2.1 Flowchart of sizing . . . 77
4.2.2 Initial requirements of sizing . . . 78
4.3 MCM sizing method . . . 79
4.3.1 Objective function . . . 80
4.3.2 Constraints . . . 85
4.4 Results of sizing . . . 86
4.4.1 Sizing results of series MCM . . . 86
4.4.2 Sizing results of parallel MCM . . . 88
4.4.3 Extension of MCM sizing . . . 91
4.5 Impact of different sizings on vehicle energy consumption . . . 94
4.5.1 MCM for pure EV . . . 94

4.5.2 MCM for HEV . . . 97
4.6 Conclusion . . . 100

5 Power split strategy of a MCM system 101
5.1 Introduction . . . 102
5.2 MCM design based on the sizing results . . . 102
5.3 Description of MCM power split . . . 103
5.4 Design of MCM power split strategies . . . 105
5.4.1 ANFIS-based strategy . . . 105
5.4.2 Predictive-based strategy . . . 108
5.4.3 Comparisons of MCM power split strategies . . . 111
5.5 MCM power split strategy validation . . . 114
5.5.1 Methodology of the reduce-scale HIL . . . 114
5.5.2 Real-time implementation . . . 117
5.5.3 Experimental results . . . 118
5.6 Conclusion . . . 122

Conclusion 124

A Appendix 127
A.1 Energetic Macroscopic Representation . . . 128
A.2 Planetary gear-train . . . 130
A.3 Optimal strategy of a MCM-based vehicle . . . 131
A.4 Optimal-efficiency strategy of a MCM system . . . 134
A.5 Properties of different wavelet mother functions . . . 135

B Publications 136

List of figures 141

List of tables 143

References 155

Introduction

Electric Vehicles (EVs) mostly represent the future of sustainable mobility [Ehsani.M 2018]. It was a technological reality at the beginning of the 20th century, in conjunction with Internal Combustion Engines (ICE) [Chan.C.C 2013]. After 30 years of development of EVs, the competition between electric and ICE vehicles was lost from 1920s by the Battery powered Electric Vehicle (BEV) due to its lower performances, as well as the low cost of petroleum and quick development in ICE. Faced with the crisis of environment and petroleum availability today, EVs come back to stay after a century of hiccups, thanks to the development of energy storage systems, new Electrical Machines (EM), power electronics and microprocessor devices [Lequesne.B 2015].

Electric drive is one of the 3 cores for electrified vehicles [Ehsani.M 2007; Emadi.A 2008]. The basic requirements for traction EMs include [Chau.K 2008; Zhu.Z 2008]: (1) high torque and power density; (2) high torque at low speed and high power at high speed; (3) high efficiency over a wide torque and speed range; (4) good frequent instantaneous overload ability; (5) high reliability and robustness for vehicular environments; (6) acceptable cost and friendly maintenance ability. Nevertheless, some conventional EMs, such as Permanent Magnet Synchronous Machines (PMSMs) and Induction Machines (IMs), are inefficient in some cases, lacking the ability of fault tolerance [Diallo.D 2013; Zhu.Z 2007; Zhang.L 2017]. Therefore, some researches move to multi-machine [Bouscayrol.A 2000; Martinez.J.S 2011; Dizqah.A.M 2016], special structure machine [Hoeijmakers.M.J 2006; Raisemche.A 2014; Ghayebloo.A 2016] and multi-phase machine systems [Nguyen.N.K 2015; Patel.V.I 2016; dos Santos Moraes.T.J 2017]. These systems can realize a variety of operation modes and can optimize power systems to obtain better traction performances.

Modular Connected Machines (MCM) system is one kind of multi-machine system

that was proposed based on this background [Han.S 2013; Cui.S 2014; Han.S 2015; Li.K 2016]. A MCM system integrates several EMs into one module, where all the machines are independent and have the same philosophies as the conventional EMs, but with standard mechanical interfaces, which enables different connection architectures. The torque-speed plane of a MCM is the superposition of the outer characteristics of all the EMs, which can have the same or different specifications. In that way, it contributes to special system output properties. Besides, different types of EMs are possible to be integrated. For example, a PMSM being connected with an IM, which can fully take the advantages of each kind of EM. For MCM systems, different power demands can be satisfied by tuning the number of EMs in service. It can achieve better characteristics of low speed with high torque and high speed with high power. What is more, MCM system high efficiency area can be expanded via an appropriate control strategy. When a certain EM breaks down, others can still work. Thus more flexible and reliable performances can be realized by managing each EM in an efficient way. It has possible perspectives in the field of electrified vehicles and other applications, specially in the case where wide speed range, complex operating properties and high reliability are required.

Currently, some relevant researches on MCM system have been carried out [Han.S 2015], but there are many techniques still remained to be further studied. For example: How to develop the control of a complex MCM-based vehicle? How to size an efficient and compact system? How to develop an efficient and reliable power split strategy? This PhD thesis is carried out focusing on the above problems.

The objective of this PhD subject is to develop different kinds of MCM systems for electrified vehicles. Some key techniques from system sizing to power spilt strategies are thus investigated. This goal is achieved within the collaboration between Harbin Institute of Technology (HIT, China) and Laboratory of Electrical Engineering and Power Electronics (L2EP, France). HIT is specialist in EMs design and MCM system control, which mainly focuses on vehicle components. Some basic researches on MCM system have been done [Han.S 2015]. L2EP is dominant in the theory of Energetic Macroscopic Representation (EMR) [Bouscayrol.A 2000, 2012] and energy management in EVs [Allègre.A.L 2013] and HEVs [Boulon.L 2013], which more focuses on global control and management. This research collaboration is expected to well develop a MCM system in interaction between component level and system level. The achievements could provide some practical instructions for the application of a MCM to electrified vehicles. This thesis is composed of 5 chapters.

Chapter 1 introduces the contents and objective of the subject. The development, topologies and key challenges of traction systems are presented. Then the positioning of the work is summarised and the objective is introduced.

Chapter 2 focuses on the modelling and control of a MCM-based vehicle. A MCM-based vehicle is modeled and described with Energetic Macroscopic Representation (EMR). The control of the MCM-based vehicle is deduced according to inversion rules.

Chapter 3 studies the efficiency map calculation method of different EMs, which is the means for MCM sizing. The efficiency map calculation method for IM and PM-SM are proposed. The method is validated by comparisons with the experimental efficiency maps.

Chapter 4 deals with MCM sizing. A multi-objective-based MCM sizing method is proposed, which aims to improve system efficiency, torque density and reduce the usage amount of PM. The interest of different MCMs for different vehicles are compared and analysed.

Chapter 5 aims at developing the power split strategies for a MCM system. Two kinds of power split strategies are developed and compared in terms of efficiency and EM operating property. A reduced-scale Hardware-In-the-Loop (HIL) setup is established and the strategies are validated in real time.

1

Context and Objective

This chapter defines the objective of the thesis. For this, the state-of-art of traction systems is firstly overviewed, which reveals its topology and development tendencies. Then the key challenges for multi-machine systems are discussed. Finally the scientific positioning is summarised and the objective of this thesis is introduced.

Contents

1.1 Development of traction machines 6
1.2 Topologies of multi-machine system 9
1.3 Challenges of a multi-machine system 15
1.4 Methods related to the study of MCM 18
1.5 Objective of the subject 20
1.6 Conclusion 23

1.1 Development of traction machines

1.1.1 Common types

Since the invention of world's first Electric Vehicle (EV) in 1834 [Chan.C.C 2013], there are mainly 4 kinds of Electrical Machines (EMs) for EVs and Hybrid Electric Vehicles (HEVs), i.e. Direct Current Machines (DCMs), Induction Machines (IMs), Synchronous Machines (SMs) and Switched Reluctance Machines (SRMs) [Zhu.Z 2007; Chau.K 2008, 2014, 2016].

DCM, with simple principle and good controllability, was firstly used in EVs. However, it has gradually lost competitiveness due to its low efficiency and poor maintainability [Chau.K 2008, 2014]. With the development of semiconductor devices and microprocessors, as well as the emergence of new control theories, the advantages of Alternative Current (AC) EMs are gradually emerging. SRMs are once regarded as one kind of the most promising EMs for automotive drive thanks to its simple structure and low processing cost. Nevertheless, noise and vibrations are the key challenges [Ahn.J.W 2004; Li.J 2008; Yang.H 2013].

Since Nikola Tesla developed the theory of rotating magnetic field in 1882, IMs were once the most popular EMs in the next century. Then the advantages of IMs were quickly replaced by Permanent Magnet Machines (PMMs). In recent years, due to the success of Tesla EVs, the research upsurge of IMs has again been ignited [Lyons.D 2013; Zhang.X 2013; Sharifan.S 2015; Su.J 2018]. IMs do not use PMs, which reduces the cost. The use of squirrel cage rotor makes the EM flux-weakening easily and have a wider speed range. However, IMs are electrically excited, thus the power/torque density and efficiency are low.

PMMs currently occupies a high market share due to its high power/torque density, small size, high efficiency and good low-speed characteristics. Moreover, Tesla company abandons its IMs and uses Permanent Magnet SMs (PM-SMs) since Model 3. However, PM-SMs use PM for excitation, the flux weakening capability is limited. If the EM needs to be accelerated by weakening the flux when the supply voltage saturates, the speed increasing is often poor. There is even a risk of permanently demagnetization for PM. In addition, when it operates above the base speed, its efficiency decreases rapidly, which results in weak high-speed performance. Most importantly, PM resources are limited and expensive, which is the main bottleneck that limits the application of PMMs [Chau.K 2016]. Table 1.1 provides a comprehensive evaluation of several commonly used EMs [Chau.K 2014]. A point grading system (from 1 to 5) is used, where 1 is the worst and 5 is the best.

Making full use of the efficiency distributions of EMs based on actual applications is a recent trend of design and use of the traction EMs [Lukic.S 2003; Chu.W 2015; Mahmoudi.A 2015, 2017]. Fig. 1.1 shows the efficiency distribution of different EMs. PM-Ms mainly have 2 configurations: Interior PM-SM (I-PM-SM) and Surface PM-

Table. 1.1. Evaluations of different EMs for electrified vehicles

	DCM	IM	PM-SM	SRM
Power density	2	3	4.5	3.5
Efficiency	2	3	4.5	3.5
Controllability	5	4	4	3
Reliability	3	5	4	5
Cost	4	5	3	4
Noise level	3	5	5	2
Maintainability	1	5	5	5
Total	20	30	30	25

SM (S-PM-SM). Compared with an I-PM-SM, the copper losses of a S-PM-SM increase faster when the speed increases, while the iron losses are inverse. So an I-PM-SM has a high-efficiency area near its rated point. While a S-PM-SM has a high-efficiency area near the point with peak power and rated torque. For an IM, it has large rotor copper losses and low efficiencies below the base speed. As the speed increases, the rotor copper losses decrease rapidly, so that the high-efficiency area of an IM is located above the base speed, and near the rated torque point. In summary, PM-SMs are more efficient with low speed, while the IMs are more proletariate in high speed applications. The combination of PM-SMs and IMs could have efficient performances in a wide operation area.

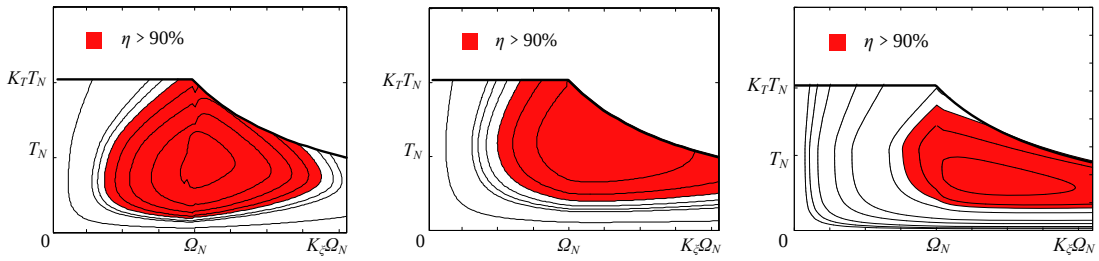

(a) I-PM-SM (b) S-PM-SM (c) IM

Figure. 1.1. Efficiency distributions of different EMs

In a word, PM-SMs are more used for EVs and HEVs currently due to its high efficiency and high power/torque density. The PM-free property of IM makes it more competitive than PM-SMs in terms of cost and speed extension capability. Even though SRMs are the most promising thanks to its simple structure and high reliability, while the noise and vibrations are the key challenges.

1.1.2 Modular machine

In 1999, E. Cengelci from U.S. proposed the concept of modular EM and modular inverters [Cengelci.E 1999]. The modularization is reflected in the independence, standardization and interchangeability of the unit module, which can reduce cost

and improve fault tolerance capability. From recent literatures, the study of modular EM can be classified into 2 categories: internal modular EM and integral modular EM. An internal modular EM modularizes its stator/rotor segments, which are then assembled into an entire EM. While for an integral modular EM, the entire EM is modularly designed in mechanic, which makes it possible to form a multi-machine system by connecting several EMs.

1.1.2.1 Internal modular machine

The research on internal modular EMs starts from modular SRMs. In 2005, a C-core modular SRM was firstly proposed [Mao.S.H 2005]. Its stator is assembled from several C-core segments. Its stator winding is wounded around a yoke. The outstanding feature of the C-core SRM is that it has a larger slot area for higher torque density and power density. However, its fault tolerance performance is limited and its long magnetic circuit increases the core losses. In 2009, a 2-phase E-core structured SRM was proposed after C-core SRMs [Lee.C 2009]. The stator consists of 2 E-shaped modules with one big tooth and 2 small teeth. Its windings are wounded around the 2 small teeth (Fig. 1.2(b)). This structure electromagnetically isolates the 2 E-shaped modules, and its shorter magnetic circuit can greatly reduce the core losses. It has been shown that the E-core SRM using common stator pole has 50% less iron in the magnetic path compared to a conventional two-phase SRM. However, the number of rotor teeth makes the EM not suitable for high-speed operation. Subsequently, other modular EMs are derived in succession. For example, modular FSM [Hua.W 2008; Taras.P 2015] and modular PMM [Jack.A.G 1996; Li.G 2016].

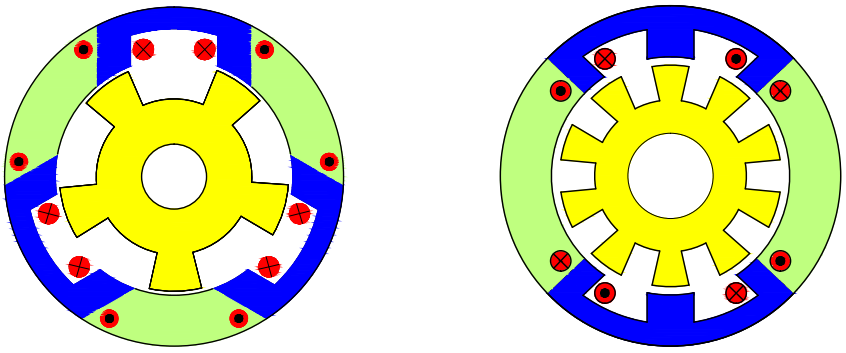

(a) C-core stator (b) E-core stator

Figure. 1.2. Modular switching reluctance machine

1.1.2.2 Integral modular machine

Integral modular EM treats the entire EM as a module. The aim of integral modular EM is to form a multi-machine system, where all the machines are replaceable and

portable. It is essentially different from the internal modular EM. The modularity use and design of the integral EM can shorten the development time for a new traction system, since different power level can be satisfied by tuning the number of EMs. The research of integral modular EMs stars from 2013 [Han.S 2013], which is called Modular Connected Machines (MCM) system. The EMs in MCM system are integral modular EMs [Cui.S 2014; Han.S 2015; Li.K 2016]. Its electromagnetic principle is identical to that of the traditional EMs. The standard interfaces, the same mechanical structures and positioning components are designed to facilitate the connection of different modular EMs (Fig. 1.3).

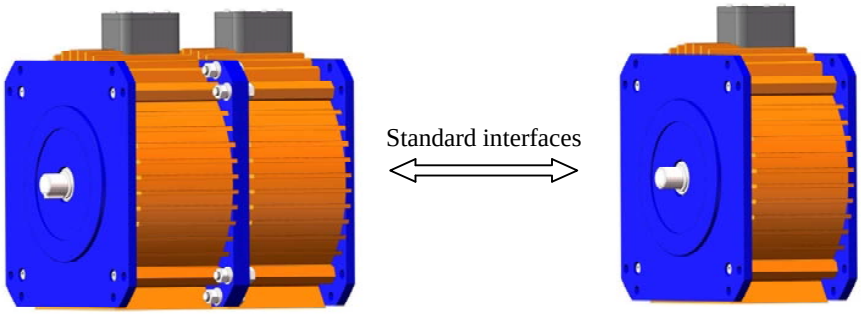

Figure. 1.3. Integral modular EM

In a word, the design of modular EM could focus on the rotor/stator segments of a EM or the entire EM, which refers to the internal modular EM or integral modular EM. Each segment of a internal modular EM cannot work individually, they must be assembled to form a functional EM. While the integral modular EM itself is a functional individual, and more properties could be realised when several EMs are connected to form a multi-machine system.

1.2 Topologies of multi-machine system

Traction system is the power source of the vehicle. Since the invention of vehicle, many traction system topologies are explored, which various from mono-machine system to multi-machine system [Chan.C.C 2010]. Mono-machine system uses only one energy conversion equipment, which could be an EM or an Internal Combustion Engine (ICE). In 1834, the world's first EV was invented, which was driven by a DCM. This is the first application of mono-electric drive system in automobiles (Fig. 1.4(a)). The appearance of EV was about 50 years earlier than the ICE drive system [Chan.C.C 2013]. A mono-electric drive is simple, and the EM is directly connected to the mechanical transmission system. Therefore, the operating points of the EM cannot be optimized. Mono-electric drive once ushered in its peak development from the end of the 19th century to the early of the 20th century.

Regarding to the increasingly demand for driving range and the decline in oil prices

from the 20th century, mono-electric drive systems were quickly replaced by the ICE drive systems (Fig. 1.4(b)). Compared with a mono-electric drive system, an ICE drive vehicle must have a gear-train to shift the ICE to a better operation area. The ICE drive system still occupies the most market share since the beginning of the 20th century, even a lots of EVs and HEVs are produced in recent years [Mock.P 2017].

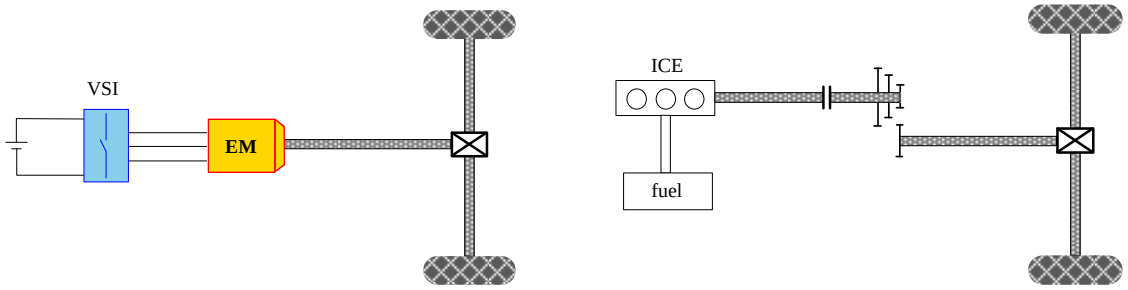

(a) Mono-electric drive (b) Mono-ICE drive

Figure. 1.4. Mono-machine system

Nevertheless, with the increase in the requirements of the drive system, mono-machine systems have been unable to meet the demands, then the multi-machine systems have emerged, which are commonly used in pure EVs and Hybrid Electric Vehicles (HEV).

1.2.1 Multi-machine system for EV

For pure EVs, multi-machine systems are mainly divided into 2 categories: centralized system and distributed system. The centralized multi-machine system has only one mechanical port. The output shafts of the machines are coupled through a power coupling device, such as a gear-train or a belt, and then they concentratedly output power to the mechanical system (Fig. 1.5(a)). In this structure, the control is complex and there is a speed coupling between each EM. Fortunately, when the power-train needs to be updated, less changes are needed for reconfiguring the whole vehicle. The distributed multi-machine system has at least 2 mechanical ports, and all the EMs synchronously output power to the mechanical power-train through the respective mechanical ports (Fig. 1.5(b)). The control of distributed systems is more flexible than centralized systems. If the EMs are assembled in the front and in the rear, it can recover more energy during braking.

In addition, another common distributed multi-machine system is wheel drive system, i.e. in-wheel drive system and wheel-side drive system (Fig. 1.6). An in-wheel drive system generally adopts a low-speed EM that buried in the wheel. The EM directly drives the wheel, and the differential is omitted. Hence the transmission efficiency is improved, and the vehicle space is saved. However, the in-wheel drive

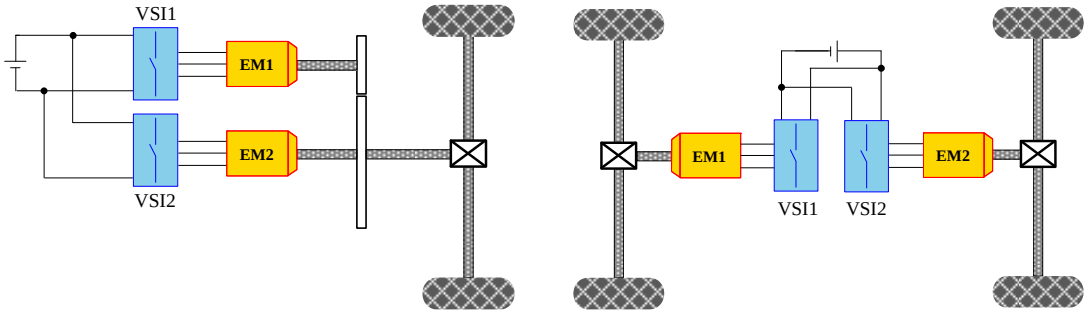

(a) Centralized multi-machine system (b) Distributed multi-machine system

Figure. 1.5. Multi-machine systems for EVs

integrates the function of driving, braking, and loading, which increases the difficulty of system optimization. And the power/torque of the EM is directly limited by the size of the wheel. In addition, the integration of EM and wheel results in a large unsprung mass and high anti-vibration requirements [Kostic Perovic.D 2012]. Therefore, the existing in-wheel system is mainly used in large coaches [Labak.A 2012], such as BYD-K9 and electric mining vehicles. A wheel-side drive system generally adopts a high-speed EM, and a transmission is inserted between the EM and the wheel. The final reducer and the differential are eliminated, and the overall transmission efficiency is relatively high. Regardless of a in-wheel or a wheel-side drive, the coordinated control of the EMs is demanding and difficult.

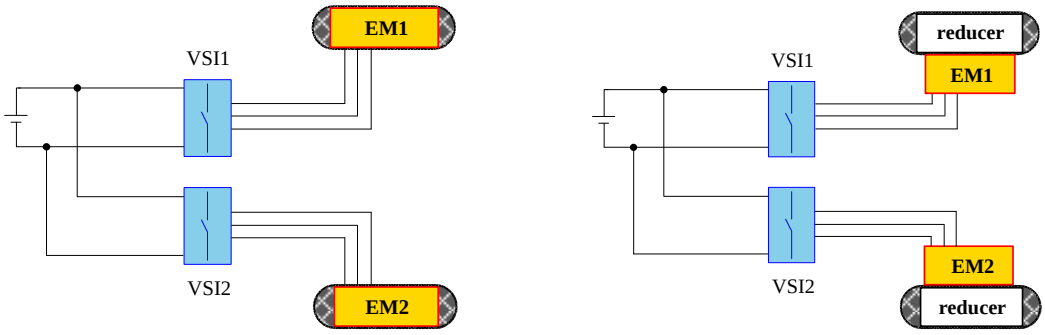

(a) In-wheel machine system (b) Wheel-side machine system

Figure. 1.6. Other distributed multi-machine systems for EVs

MCM system is one kind of centralized multi-machine system which could be applied to electrical vehicles [Han.S 2013; Cui.S 2014; Han.S 2015; Li.K 2016]. It has only one electric port and one mechanical port, which makes it possible to replace the mono-machine system. To have independent control, each EM is controlled by its own inverter. Regarding to the electrical connection of the inverters and the mechanical connections of the EMs, there are basically 4 topologies (Fig. 1.7). All the inverters can be fed by the same DC bus, which will impose a big battery current. Or the inverters can be connected in series, thus it will require a higher battery voltage. Once a inverter is broken, all the system will fall in fault. Similarly, the EMs have

basically 2 mechanical connection possibilities, such as sharing the same shaft or coupled by a mechanical device. Different mechanical architecture makes it possible to optimize the operation of each EM. [Han.S 2015] studied the system performance of category 2 in Fig. 1.7, and other categories still need to be further studied.

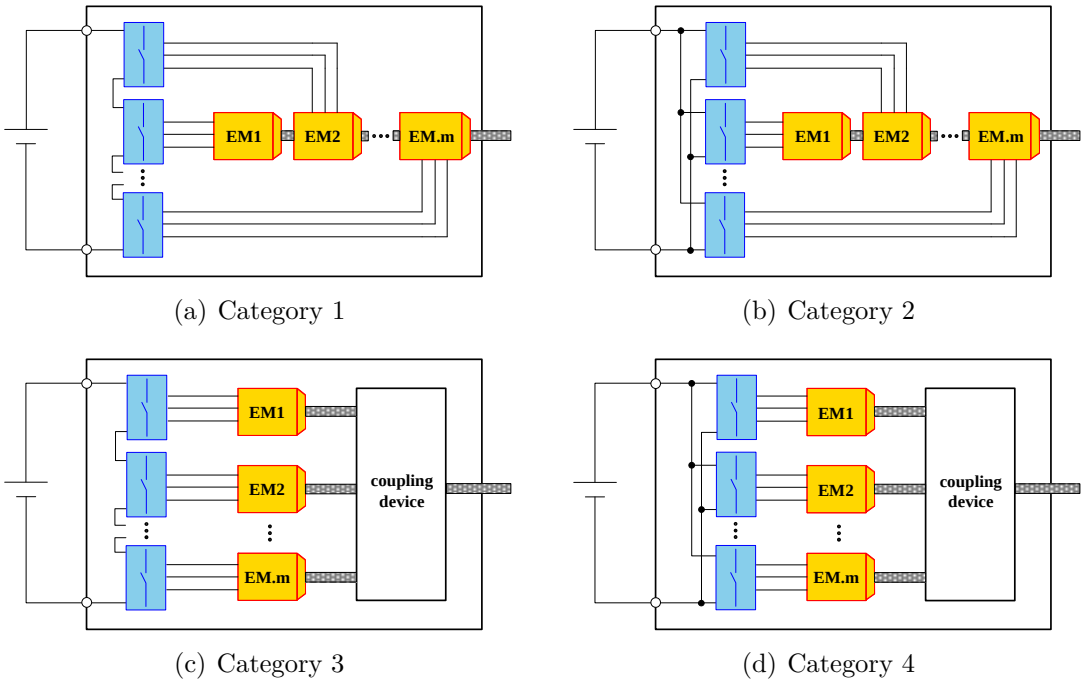

(a) Category 1 (b) Category 2

(c) Category 3 (d) Category 4

Figure. 1.7. Categories of MCM system

In this always-connected machines system, one EM can rise is the mechanical losses of the system even if no torque is needed. For example, if the speed ranges of the machines in a MCM are different, when the demand speed is higher than the maximal speed the one machines, then this machine would be a mechanical load to the other machines, which reduces the system efficiency. We can install a mechanical overrunning clutch between the rotor and shaft of a machine. The rotor and the shaft is separated when the speed of the shaft is higher than that of the rotor, which can reduce the mechanical losses. Nevertheless, this clutch can only carry a small torque.

The pros and cons of the MCM system could be concluded. First, the MCM system can fully utilize the high-efficiency area of both machines, which reduces the global energy consumption. Besides, the MCM system is more reliable when one machine breaks down since another one can still work. Moreover, different operation modes are also available by switching on/off the different machines. However, the MCM system will require higher mass, volume, materials and resources than a single drive solution. Its cost will probably be higher than the classical solution. Therefore, the MCM system is more suitable for applications where it is more tolerable for mass, volume and cost, such as military applications, limousines, buses and trucks. What is more, the MCM system needs two controllers that increases complexity for the

control and implementation.

Currently, a MCM with 2 EMs has been applied to an electrical bus (ZK6115) by YUTONG company. According to the test in Jiuzhaigou tourist area in China, this MCM-based bus can save about 10% of energy comparing the bus with a single EM. Moreover, the maximal grade ability is improve from 16% to 20%.

1.2.2 Multi-machine system for HEV

Generally, power demand of a vehicle is stochastic and the high-efficiency area of an ICE is narrow. To have more efficient operation of an ICE, EMs are used to work with ICE to optimize the ICE operation. By using EMs, the high-efficiency area of the EM and the ICE can be complementarily utilised. The operating points of the ICE can be maintained as close as possible to the highest efficiency area. Currently, the most well-known multi-machine systems in HEVs include: Toyota Hybrid System (THS), Voltec hybrid system, Honda hybrid system and Corun hybrid system.

THS uses a planetary gear-train as the power splitting device [Xu.Q 1998; Muta.K 2004]. The ICE is connected to the carrier, EM1 is connected to the ring gear, and EM2 is connected to the sun gear. This configuration enriches the system operation modes, which is beneficial to optimize the system efficiency and improve the fuel economy. A THS mainly drive the vehicle by the ICE, the optimization of ICE speed is limited. So it is difficult to further improve the thermal efficiency. In addition, EM2 and the wheels are directly coupled so that EM2 cannot operate in its high efficiency area at low speeds.

Similar to THS, Voltec hybrid system by General Motor, also uses the planetary gear-train to achieve a comprehensive distribution of power [Grebe.U.D 2011; Matthe.R 2014]. However, in Voltec system, the sun gear is connected to EM2, the carrier is connected to the reducer, and the ring gear is connected to the fixed shell or to EM1 and the ICE according to actual situations (Fig. 1.8).

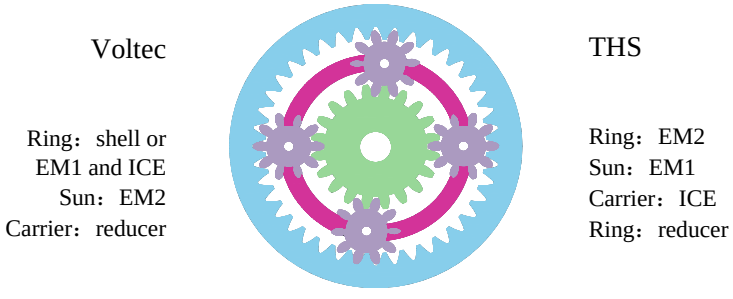

Figure. 1.8. Comparisons of THS and Voltec

In 2012, Honda proposed 3 hybrid systems. (1) Mono-machine system with dual-clutch: intelligent Dual Clutch Drive (i-DCD). (2) Dual-EM system: intelligent Multi Mode Drive (i-MMD) [Higuchi.N 2013; Ide.H 2014]. (3) Treble-EM system:

Sports Hybrid-Super Handling-All Wheel Drive (Sports Hybrid SH-AWD) [Ono.K 2014; Honda.T 2015]. An i-MMD system (Fig. 1.9(a)) mainly drives the vehicle by EM, while the ICE is mainly used for power generation and cruising. Thus, the ICE can work in its high-efficiency area. However, the ICE is used for frequent power generation, and more energy conversions will result in more energy losses. A Sports Hybrid SH-AWD adopts a two-EM unit in the rear axle and an EM-assisted ICE in the front axle (Fig. 1.9(b)). Thanks to Honda's steering vector control technology of the two-EM unit, the cornering control can be further enhanced. And by applying regenerative braking torque to the inward rear wheel, it is possible to recover some energy during cornering.

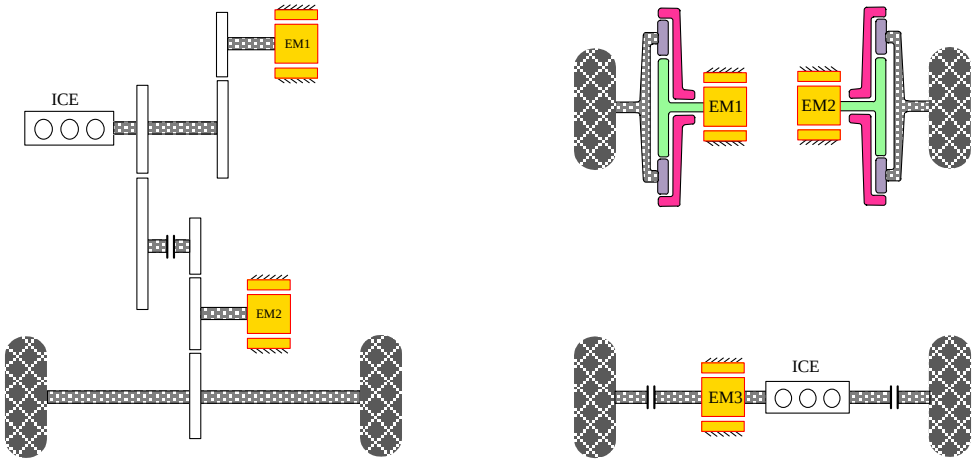

(a) i-MMD (b) Sports Hybrid SH-AWD

Figure. 1.9. Honda hybrid system

In 2016, Corun introduced the Corun Hybrid System (CHS) [Yu.H 2011; Li.S 2012a,b, 2013] based on Ravigneaux planetary gear-train (Fig. 1.10) [Le.T.G 2007; Lhomme.W 2017]. Compared with THS, its double sun gear sets decouple the 2 EMs and enrich the system operation mode. However, CHS has complicated mechanical structure, its control is difficult, and the cost is high. Besides, it has a great challenge for system reliability.

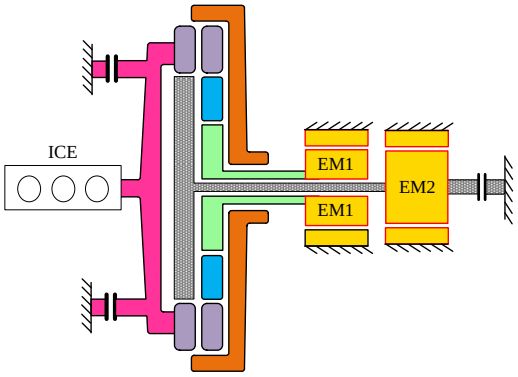

Figure. 1.10. Topology of CHS

In 2016, Jingjin Electric (JJE), China, has developed the integrated two-EM system for HEV. It is divided into 3 categories according to the power level: large hybrid, medium hybrid, and small hybrid [Yu.P 2015]. The system is equipped with 2 compact high-torque EMs in axial direction, and an Electromagnetic Maintenance-free Disc Clutch (EMDC) is installed between the 2 EMs. Its application to hybrid trucks proves that with this two-EM system, the vehicle has excellent climbing performance, outstanding fuel-saving and emission reduction effects.

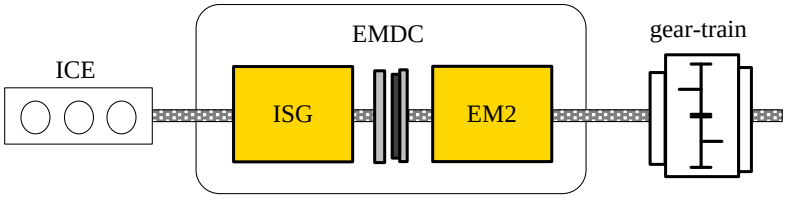

Figure. 1.11. Topology of JJE dual-machine system

In summary, multi-machine systems are more and more developed in the direction of introducing more degree of freedom in sizing, control and energy management, which is expected to increase the global efficiency and fault tolerance ability.

1.3 Challenges of a multi-machine system

Traction system is the power source of the vehicle, which has direct influences on the performances of the vehicle, such as efficiency, reliability and driving comfort. Besides, traction systems has developed a lot of topologies and multi-machine systems are gradually becoming more competitive than mono-machine systems. Generally, a multi-machine system has special requirements for EM specifications and system power split according to its application. The key challenges of a multi-machine traction system includes system sizing and power split strategy.

1.3.1 System sizing

Sizing is a process of selecting key components and determine their specifications according to the vehicle parameters and its dynamical requirements. For example, selecting the appropriate power-train topology and define the specifications of the ICE, EMs, gear ratio, etc. The specifications of each component will be further used for component design and manufacturing. System sizing is closely related to the vehicle performance, it is an important part of vehicle design and development. Currently, there are mainly 2 kinds of sizing methods: basic sizing, optimization-based sizing.

Basic sizing is the simplest sizing method, which is similar to the engine sizing method of the traditional thermal vehicle. The torque-speed plane of the traction

system is deduced according to the power demand of the vehicle [Gao.Y 2006; Xu.Q 2017]. The peak speed of the traction system is determined by the maximal speed of the vehicle. The peak power depends on the acceleration performance of the vehicle. The rated power is calculated from the maximal speed of the vehicle. When the traction system has multiple power sources, the power of each subsystem is generally sized by experience. This method is easy to deal with and implement, thus can shorten the development period. Nevertheless, this sizing only meets the basic dynamical requirements of the vehicle, does not consider the cycles and the component couplings. The sizing result is often with poor economical performances, which has a lot of room for improvement. Hence this sizing method is gradually being replaced by other sizing methods.

Optimization-based sizing refers to an optimization process to optimize the specification of a certain component, with the basic dynamical requirements of the vehicle as constraints [Fish.S 2001a,b; Mineeshma.G 2016; Lee.H 2017a,b; Ramakrishnan.K 2018]. [Hall.E 2001] sized the speed expansion ratio of an IM with the goal of reducing its weight and volume by taking the power demands as the constraints. It takes into account the influence of speed expansion ratio on EM volume/weight, peak power, peak current, and average efficiency under different cycles. This sizing method can provide ideas and theoretical basis for the sizing of other traction system. [Ramamurthy.S.S 2001] proposed a sizing method for a SRM by considering its efficiency at a single operation point. This sizing is based on the SRM losses model, where the relationship of copper losses and iron losses versus vehicle velocity and EM power is investigated. However, for the traction EM of electrified vehicles, it is necessary to consider its efficiency in the entire working area, i.e. the efficiency in the whole torque-speed plane. Thus this sizing method has limitations for improving the system efficiency.

Meanwhile, it could be of interest to optimize the overall parameters of battery, electric drive, engine, gear ratio, etc, with the goal of increasing driving range and reducing fuel or energy consumption by a systemic optimization. [Vandana.R 2010] explored the method to size the in-wheel EM, the inverter and the battery, with the aim of reducing the volume and weight of the EM. This method is realised under the premise of meeting the power requirements of the vehicle and the mutual couplings between each component are considered. [Wu.X 2013] optimized the parameters of the battery, EM and transmission system of a vehicle by Particle Swarm Optimization (PSO). Systemic optimization builds the vehicle model and optimize each component from vehicle level. However, in order to shorten the optimization time, the component model is often too simple to accurately reflect the real situation [Fish.S 2001b; Wang.Z 2018].

For MCM system, we can make full use of the efficiency distribution of each EM, it is one of effective ways to improve system efficiency. In order to highlight this advantage, [Han.S 2015] investigated the I-PM-SM based MCM sizing method to enlarge the system high-efficiency area. In that way, the high-efficiency area of the system could be expanded. Nevertheless, this method only takes I-PM-SM as research objectives, system properties with other kinds of EM, such as IM and S-

PM-SM are have not been studied yet.

1.3.2 Power split strategy

Power split of the vehicle aims to coordinate the energy distribution between each power component according to certain algorithms and rules, by collecting different signals from the sensors. It is important to achieve energy saving, emission reduction and improve driving comfort [Mayet.C 2014b]. Some subsystems, such as multi-machine system, hybrid systems with ICE and EM, hybrid energy sources with batteries and supercapacitors, all require a reasonable power split strategy for better performances. Power split strategy has become one of the key challenges for electrified vehicles. Regarding to the power split strategies that proposed in recent years, they can be divided into 2 categories: optimization-based strategy and rule-based strategies [Chau.K 2002; Salmasi.F.R 2007].

Optimization-based strategy can be regarded as an optimization problem with constraints. Its final output is optimized by the core algorithm, which can achieve global or real-time optimal solution [Silvas.E 2017]. Dynamic Programming (DP) is one of the most commonly used global optimal algorithm, and DP strategy is often chosen as the benchmark for evaluating other strategies. However, a DP strategy requires accurate vehicle velocity and road information, and its calculation time is long. Thus, it cannot be applied to real-time system. Nevertheless, the result of the DP strategy can provide guidance for the formulation of the rule-based strategy. Regarding to these problems, there are mainly 2 kinds of improvement solutions. (1) To establish the cycle as a stochastic Markov process by stochastic DP algorithm, thus overcoming the dependence of the deterministic DP algorithm on cycle [Johannesson.L 2007; Vagg.C 2016; Zou.Y 2017; Liu.B 2018]. It can provide the possibility to implement an online EMS for unknown driving conditions. (2) Reduce the DP calculation time and computer memory requirements. By using algorithms such as Convex Optimization (CP) can not only effectively reduce the calculation time, but also can deal with the optimization of discrete variables [Hedlund.S 2002; Pourabdollah.M 2018]. In addition, there are also other artificial intelligence algorithms being applied for global optimization, such as Genetic Algorithm (GA)[Samanta.C 2014], Particle Swarm Optimization (PSO), etc, [Wu.J 2010; Samanta.C 2013].

Rule-based strategies are the strategies that firstly being applied to electrified vehicles. It does not require complicated algorithms and it is easy to be implemented to real-time systems [Wirasingha.S.G 2011]. However, the formulation of rules often relies on expert experience or a large amount of experimental data, without a priori knowledge of pre-defined cycle. Hence it is difficult to adapt to the real-time dynamical changes of the cycle. What is more, the optimal control cannot be achieved. Rule-based strategy can be classified into deterministic and fuzzy rule-based methods. Compared with deterministic rule-based strategies, the fuzzy rule-based strategies are more robust and adaptable, and have gained considerable popularity in recent years.

[Han.S 2015] studied the optimal-efficiency strategy and the deterministic rule-based strategy for MCM power split. The optimal-efficiency strategy uses the off-line iterative method to calculate the optimal torque distribution according to the efficiency maps. It is applied through look-up tables in real time. Due to the nonlinear distribution of the efficiency maps, the EM sometimes starts/stops frequently in order to pursue the best efficiency, which leads to noise and vibrations. The deterministic rule-based strategy divides the MCM 'torque-speed' plane into several areas, and specifies the corresponding rules in each area. This strategy reduces the mutation of EM torque to a certain extent, while it results in higher energy consumption. Additionally, the torque mutation still exists when switching between different areas.

1.4 Methods related to the study of MCM

1.4.1 Graphical description tools

A lot of functional modelings are available for describing a complex systems, from the physical relationships to state space models, the classical transfer function schemes [Routex.J.Y 2002]. Especially, some graphical description tools have been used to suggest other views of these systems, such as Bond Graphs (BG) [Karnopp.D 1990], Causal Ordering Graph (COG) [Hautier.J.P 2004], Power Flow Diagram (PFD) [Schönfeld.R 2004] and Energetic Macroscopic Representation (EMR) [Bouscayrol.A 2012].

BG is a modelling tool based on energy flow. It describes the system with the exact number of subsystems. The power is changed between connected elements by a combination of 'effort' and 'flow', whose product is the instantaneous power. A derivative causality is assigned to connect the subsystems when the physical casuality exists, i.e., the output is a derivative function of input. BG is a unified formalisation to describe a multi-physical system, and it highlights the transferred energy between system components.

COG is a graphical description tool, with integral causality as the only allowable physical causality, i.e., the output is an integral function of input. It uses causal processor and bi-directional arrow to organise the model. Thanks to the integral causality, a systematic control scheme can be deduced from the model description. Therefore, COG is dedicated to develop the control of a system. As COG is focused on inputs, outputs and internal causality of processors, other properties as dissipative components are not pointed out.

PFD was developed to study the flow of power and the energy efficiency. It organises signal flows between connected subsystems with implicit power flow. In comparison with COG, it points out dissipative elements, which are energy consumers. PFD can provide a detailed graphical description of the energy distribution associated with classical visible representation of the sum of power signals as well as use of block

symbols. This property can be useful in reverse operation.

EMR is a graphical description tool which is based on 'action and reaction' principle. Integral causality is the only allowable physical causality in EMR. EMR has 4 basic elements to describe a system, source element, conversion element, accumulation element and coupling element. EMR emphasises the modelling on coupling device, which distribute energy. According to inversion rules, one can systematically deduce the control of the system. Hence, EMR is appropriate for control purpose.

Taking a simple electrical parallel node as an example, Fig. 1.12 indicated the formalization of different description tools. They are all based on energetic considerations in a systemic philosophy while suggest different graphical descriptions of the same modelling relationships, in order to graphically point out one or several characteristics of the system [Bouscayrol.A 2005]. For these reasons, they give another global view of system in comparison with classical tools as transfer function or state space models. In contrast, EMR describes the system based on integral causality, it can systematically derive the control scheme of the system. It has been successfully used in the related fields of electric vehicles [Lhomme.W 2007; Chen.Y 2010; Sayed.S 2012; Letrouvé.T 2013]

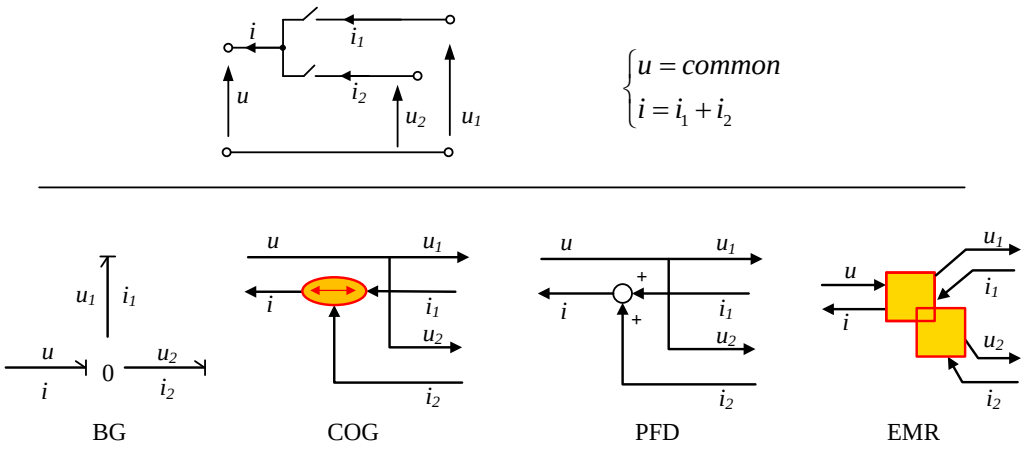

Figure. 1.12. Example of the above graphical description tools

1.4.2 Efficiency map calculation method of an EM

MCM sizing is a problem of optimization with a lot of iterations, and each iteration needs the efficiency map of each EM. If they are calculated through EM design in each iteration, it would take numerous time. One of the possible solutions is linear-scale method, which re-scales the torque and speed ranges by using an existing map, and it is used in the software of ADVISOR 2002 [Wipke.K.B 1999]. Another solution is by using empirical equations to calculate all the losses [Levi.E 1984]. The above 2 solutions are feasible, but with poor portability or considerable errors.

Some literatures explored the efficiency map calculation methods. [Heins.G 2016]

models the machine losses in the form of $I^m\omega^n$, where m and n are integers, I and ω are the current and speed. But the discussion didn't examine the accuracy of efficiency map, but just the error of different losses. Moreover, it has to use experiment to fit the value of m and n. Then [Mahmoudi.A 2017, 2015] improved this method by replacing the current by torque, as the metric of the machine load. The losses are expressed in the form of $k_{m,n}T^m\omega^n$, saturation and flux weakening operations are also considered, and different types of machines are analyzed. The model is proved to have good accuracy. However, the same as the method by [Heins.G 2016], there are too many coefficients to be determined. And the coefficients $k_{m,n}$ must be obtained by nonlinear fitting with the help the FE or experimental results. [Williamson.S.S 2007] models the inverter and IM losses/efficiencies over typical driving schedules. The IM losses, mainly the stator copper loss, the rotor copper loss, and the iron loss are considered. Losses of the machine are derived according to the per-phase equivalent circuit. But no overload fact is considered and it still needs some rated parameters, such as inductance and resistances. Besides, it is not accurate to calculate the copper loss by thinking the torque is proportional to the current. Instead, the one part of the current is used to modulate the flux, thus the torque is proportional to $I_s^2 \sin\gamma \cos\gamma$ in Rotor Flux Oriented Control (RFOC), where I_s is the stator current, and γ is the current angle. Moreover, there is no validation on the accuracy of the model. [Stanislav.F 2013] proposed a way to roughly analyze an IM efficiency based on the state description by T-circuit model of the IM. The method can calculate IM efficiency map fast, and it can be used further for the optimization of the IM control algorithm. However, the method is not validated by FEM or experiment. Moreover, it is only feasible when the machine is pre-designed to provide some mandatory parameters. Thus, it is not applicable to the sizing applications. [Chedot.L 2007] uses a classic uncoupled dq reluctant circuit model (with saturation taken into account) to obtain the efficiency map of an EM. However, its geometry must be optimal designed. Moreover, FE method is needed to have a more accurate model to compute optimal currents for the control on the whole torque-speed plane. Finally, we conclude some limitations for the current fast efficiency calculation methods: (1) pre-design of the EM is needed; (2) parameters (inductance or resistance) dependent; (3) too many coefficients are needed to fit by the data from FE or experiment; (4) weak consideration on flux weakening and overload fact.

1.5 Objective of the subject

1.5.1 Positioning

Traction systems are developed in the direction of introducing more degree of freedom for optimization. As a centralized multi-machine system, MCM is promising in electrified vehicles. A MCM system can enrich system operation modes, optimize system power, and improve system fault tolerance ability. Nevertheless, it also leads

to some complex problems, such as how to sizing the system, how to manage the power or energy in the system in a efficient way. Thereby, sizing and power split are the 2 key technologies of the MCM system. From the above sections, the current research on MCM could be summarized as:

For MCM sizing, it has single optimization objective, i.e., only optimizes the MCM high-efficiency area. Hence it could also be of interest to introduce other optimization objectives, such as torque density and the usage amount of PM. Besides, it has single optimization subject, i.e., only considers I-PM-SM, lacking the research on other EMs (such as IMs) and different EM combinations. In addition, sizing and performance of other MCM topologies are still remain to be studied.

For MCM power split, the optimal-efficiency strategy optimize the system efficiency, and only pays attention to the current power demand. It does not consider historical and future power distribution, thus torque mutation, noise and vibration occurred. The rule-based strategy can improve the EM operating property to a certain extent, but the deterministic rules are sensitive to parameters and poor in robustness. Therefore, more advanced MCM power split strategies are expected to be developed.

Modelling is the first step for the control design in model-based design processes. A lot a modelling tools are available for complex system, such as BG, COG, PFD and EMR. They can provide a global view of system in comparison with classical tools. In contrast, EMR describes the system based on integral causality, it can systematically derive the control scheme of the system. It has been successfully used in the related fields of electric vehicles.

The evaluation of EM efficiency map is a key step in MCM sizing. Fast, acceptable accuracy and without EM design are the basic requirements of EM efficiency map evaluation for MCM sizing. Currently, some efficiency map calculation methods can not satisfy the above requirements,Therefore, it is necessary to study the efficiency map calculation method, which is dedicated for MCM sizing.

1.5.2 Objective

The objective of this PhD thesis is to develop different MCM systems for electrified vehicles. This research mainly focuses the 2 key technologies, i.e., MCM sizing and power split strategy. The thesis will consist of following works.

(1) **Modelling and control of a MCM-based vehicle.** Analyze the efficiency characteristics of MCM with different topologies. EMR is used to organise the model. The control scheme is deduced according to the inversion rules. The model and control will be verified in simulation and experiment.

(2) **A fast efficiency map evaluation method for different EMs.** Analyze the key points for efficiency map fast evaluation. Study the fast efficiency map evaluation method for IM and PM-SM. The experimental efficiency maps are then

used for comparisons.

(3) **MCM sizing method based on multi-objective optimization.** A multi-objective-based sizing method of MCM system is studied and different sizing results are analyzed. The characteristics of different MCMs in different vehicles are compared andsummarised.

(4) **Power split strategy of a MCM system.** Two MCM power split strategies based on ANFIS (Adaptive Network based Fuzzy Interface System) and model prediction are developed. They are compared in terms of system efficiency and EM operating property. Finally, they are validated and compared in real time.

Fig. 1.13 shows the research plan of this thesis. Chapter 2 and 3 are the methods that related to the study of MCM. The model and control that established in chapter 2 are the inputs of other chapters. The EM efficiency map estimation method in chapter 3 helps to establish the objective function of MCM sizing in chapter 4. Finally, according to the sizing results in chapter 4, a MCM system is selected for the study of its power split strategy in chapter 5.

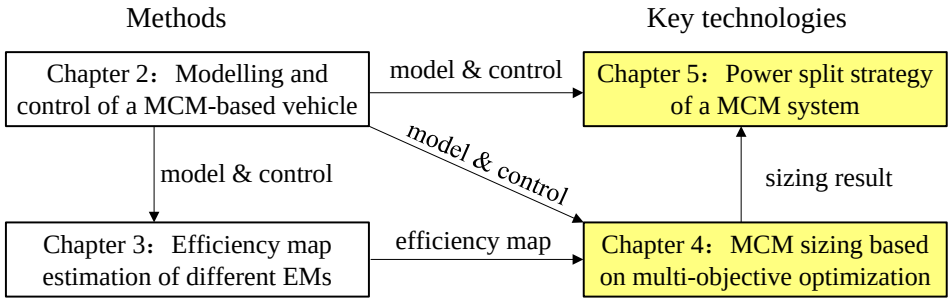

Figure. 1.13. Research plan of the thesis

1.5.3 Organization

This PhD subject is realized in co-supervision between HIT, China and L2EP, France. HIT has the earliest laboratory for EMs in China. In the recent years, some work in HIT is focusing on green mobility, such as EVs/HEVs, airplanes. It includes high-speed EMs [Wan.Y 2016], dynamic wireless charging [Cui.S 2018], fault tolerance [Du.B 2016a,b], modular compulsator [Wu.S 2013], compound-structure EMs [Cheng.Y 2011]. HIT is specialist in EMs design and control, which mainly focus on the vehicle components. The concept of MCM is firstly proposed from HIT. Up to now, 2 set of MCM prototypes have been manufactured. A Chinese automobile manufacturing (Yutong) has adopted the MCM for a bus (Yutong-ZK6115). Besides, the idea of MCM system are extended to the other applications, such as pulse-generator [Cui.S 2017]. L2EP is dominant in EMR theory and electrical sustainable development, which mainly concentrates on global control and management of vehicle, especially in system modelling, energy management in EVs and HEVs. EMR, devel-

oped in L2EP, has already been used and validated on a wide variety of systems all over the world. For example, there are works on alternator-generators [Bruyère.A 2009], electric and hybrid vehicles [Lhomme.W 2007; Chen.Y 2010; Sayed.S 2012; Letrouvé.T 2013], thermal domains [Horrein.L 2015] or fluidic domains [Boulon.L 2009]. It is adopted by the French national research group of MEGEVH (Modélisation Énergétique et Gestion d'Énergie des Véhicules Hybrides et électriques), who is dedicated to the energy management of HEVs.

For this PhD subject, the work in HIT deals with MCM sizing and the design of EM. The task in L2EP focuses on system modelling and control, as well as energy management for MCM-based vehicle. The achievements could provide some practical instructions for the application of a MCM to electrified vehicles.

1.6 Conclusion

This chapter overviews the research background of this PhD subject. The main works are the following.

(1) The state-of-art of the traction systems are analysed.

(2) The key challenges of a multi-machine system are compared.

(3) The methods that related to the study of MCM is summarized.

(4) The objective and the organization of this PhD subject is introduced.

The main conclusions are summarized.

(1) Multi-machine systems are more and more popular in electrified vehicles, which increase the degree of freedom for better optimization and fault tolerance.

(2) MCM system is one kind of multi-machine system that is promising to improve system efficiency and enhance reliability.

(3) Sizing and power split strategy are 2 key technologies for a MCM system. Nevertheless, the current sizing of MCM only is only dedicated to one topology, one kind of EM and one optimization objective, which limits the comprehensive MCM properties. Moreover, the proposed power split strategies are either inefficient in energy reduction or unsatisfactory regarding to noise and vibrations.

The objective of this PhD thesis is to develop different MCM systems for several vehicles. For this, the 2 key technologies, i.e., sizing and power split strategy will be studied in the following chapters.

2

Modelling and control of a MCM-based vehicle

This chapter studies the modelling and control of a MCM-based vehicle. Firstly, the concept of MCM and its properties are introduced and analysed. Then the model of a MCM-based vehicle is developed and organised by Energetic Macroscopic Representation (EMR). Its control scheme is deduced step-by-step according to the inversion rules. The EMR-based control of the electric drive is validated by experiment.

Contents

2.1 Introduction 25
2.2 Topologies and properties of a MCM 25
2.3 Modelling of an electric drive using EMR 27
2.4 Inversion-based control of an electric drive 34
2.5 Modelling of a MCM-based vehicle using EMR 39
2.6 Inversion-based control of a MCM-based vehicle 46
2.7 Conclusion 48

2.1 Introduction

Modelling is the first step for the control design in a model-based design process. In order to integrate a MCM into a vehicle and investigate the internal relationships between each Electrical Machine (EM), it is necessary to develop a global model and control of the vehicle. This global view will enable to better catalogue the request at the component level. MCM system is a multi-machine system, its control is more complex than a classical single drive, since there exists more operation possibilities. This chapter is dedicated to develop a model and control for a MCM-based vehicle, which will be used to analyse the MCM energy consumption behavior and develop power split strategies.

In this chapter, the concept of MCM, its topologies and efficiency properties are firstly introduced. Then a MCM and different vehicles are represented by Energetic Macroscopic Representation (EMR). Finally the control is deduced step-by-step according to inversion rules of EMR.

2.2 Topologies and properties of a MCM

The main philosophy of a MCM system is to integrate several EMs into a module in order to meet specific requirements. Inspired by the usage of battery, a MCM system has 2 basic topologies (Fig. 2.1).

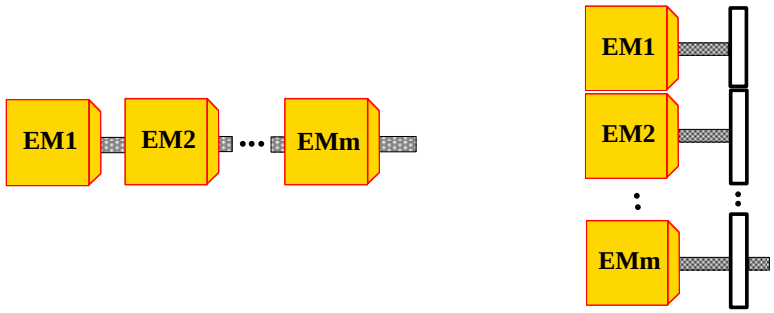

(a) Series MCM (b) Parallel MCM

Figure. 2.1. Basic topologies of a MCM

A series MCM has all the EMs coaxially connected, and intensively output power through the shaft of the final EM. In order to reduce the axial length, the EMs in series MCM are mostly flatly designed. Their shafts, end covers and houses are designed with standard interfaces to facilitate the connections. All EMs in series MCM share the same speed, while the torques and powers are superimposed. Suppose T_{mcm} and Ω_{mcm} are the torque and speed of a series MCM, T_m and Ω_m are

the torque and speed of the m^{th} EM, respectively. We have the following relationship:

$$\begin{cases} \Omega_{mcm} = \Omega_1 = \Omega_2 = \cdots = \Omega_m \\ T_{mcm} = \sum_{i=1}^{m} T_i \end{cases} \tag{2.1}$$

In a parallel MCM, all the EMs are placed with their shafts in parallel, and their output shafts are coupled via a mechanical coupling device such as a gear-train or a belt. Different from a series MCM, all the EMs in a parallel MCM are elongated to reduce the radial size of the system. Assuming that k_i is the gear ratio between the i^{th} and $(i-1)^{th}$ EM, the torque and speed relationship within this system is:

$$\begin{cases} \Omega_{mcm} = \Omega_m = \Omega_{m-1}(k_m)^{-1} = \cdots = \Omega_1 \left(\prod_{i=2}^{m} k_i \right)^{-1} \\ T_{mcm} = T_m + k_m T_{m-1} + \cdots + \prod_{i=2}^{m} k_i T_1 = \sum_{i=1}^{m} T_i \prod_{j=i+1}^{m} k_j \end{cases} \tag{2.2}$$

The typical feature of a MCM system is that its high-efficiency area can be expanded with appropriate control strategies. In fact, MCM efficiency depends not only on the efficiency of each single EM, but also on the power split of the EMs. The efficiency of a MCM η_{mcm} can be expressed as:

$$\eta_{mcm} = \left(\frac{P_m}{P_e} \right)^{\varsigma} = \left(\frac{\sum_{i=1}^{m} T_i \Omega_i}{\sum_{i=1}^{m} \left(\frac{T_i \Omega_i}{\eta_i^{\varsigma}} \right)} \right)^{\varsigma} \tag{2.3}$$

where η_i is the efficiency of the i^{th} EM, P_m and P_e are the mechanical and electromagnetic powers. ς is used to distinguish the EM working mode, i.e., the motor mode or the generator mode:

$$\varsigma = \begin{cases} 1 & P_m \geq 0 \\ -1 & P_m < 0 \end{cases} \tag{2.4}$$

The system efficiency can be optimized by rational allocation of EM powers. Suppose $P_{\Omega i} = T_i \Omega_i$ is the mechanical power of the i^{th} EM, P_{mcm} is the total mechanical power of the MCM system, then Eq. (2.3) can be rewritten as:

$$\eta_{mcm} = \left(\frac{P_{mcm}}{\sum_{i=1}^{m} \frac{P_{\Omega i}}{\eta_i^{\varsigma}}} \right)^{\varsigma} = \left(\frac{P_{mcm} \prod_{i=1}^{m} \eta_i^{\varsigma}}{\sum_{i=1}^{m} \left(P_{\Omega i} \prod_{j=1, j \neq i}^{m} \eta_j^{\varsigma} \right)} \right)^{\varsigma} = \eta_k \left(\frac{P_{mcm}}{\sum_{i=1}^{m} P_{\Omega i} \left(\frac{\eta_k}{\eta_i} \right)^{\varsigma}} \right)^{\varsigma} \tag{2.5}$$

Suppose the k^{th} EM has the highest efficiency for a certain power demand, i.e., $\eta_k \geq \eta_i$, $i = 1, 2, ...m, i \neq k$, then:

$$\left(\frac{P_{mcm}}{\sum_{i=1}^{m} P_{\Omega i} \left(\frac{\eta_k}{\eta_i} \right)^{\varsigma}} \right)^{\varsigma} \leq 1 \tag{2.6}$$

Therefore:

$$\eta_k \geq \eta_{mcm} \geq \eta_i \tag{2.7}$$

It can be seen that the MCM efficiency is only lower than that of the k^{th} EM, but still higher than the others in the system. Eq. (2.1) and Eq. (2.2) indicate that in a series and parallel MCM, the torques of the EMs are independent, but their speeds are coupled. The potential of EM operating point optimization is limited.

2.3 Modelling of an electric drive using EMR

Modelling is essential for developing the control and power split strategies. There are 2 kinds of description formalizations for a model: structural description and functional description. Structural description, such as Finite Element (FE), analyzes a component based on its real structures and real physical interactions, thus it is mostly used for component design. On the contrary, functional description analyses the component function only by 'virtual' physical relationships, without considering its geometry. Generally, it is used for developing the control of a component. This thesis focuses on the control of a MCM-based vehicle, hence functional description is more appropriate.

EMR is a graphical description tool based on action-reaction principles [Bouscayrol.A 2012]. It is dedicated to develop the control of a system. Power is transmitted between the connected elements by a combination of 'action' and 'reactions', which has the relationship of $action \times reaction = power$. In EMR, integral causality is the only allowable physical causality for all the functional descriptions (Fig.2.2). More details about EMR could found in Appendix A.1.

Figure. 2.2. Principles of EMR

The use of EMR can highlight the power flow of the system and it clearly points out the important couplings that exist in the system. Through inversion rules, the control scheme can be deduced systematically. This thesis uses EMR to organize the model.

2.3.1 Model of an inverter

A MCM consists of m independent electric drives, and each drive has one EM and one inverter. A conventional inverter for a 3-phase AC machine has 3 legs, and each

leg has 2 power switches with a transistor and a diode. The total losses (switching and conduction losses) depend mainly on the AC Root-Mean-Square (RMS) current, power factor, switching frequency and modulation function. It is assumed that the ratio between the EM frequency and the switching frequency is high enough to consider the voltage and the current as sinusoidal. Therefore, the losses in a transistor module is expressed as [Werner.Q 2017]:

$$p_{cD} = U_{ce0} I_o \left(\frac{1}{2\pi} + \frac{m_s \cos\varphi}{3\pi}\right) + r_T I_o \left(\frac{1}{8} + \frac{m_s \cos\varphi}{3\pi}\right) \tag{2.8}$$

$$p_{cD} = U_{D0} I_o \left(\frac{1}{2\pi} - \frac{m_s \cos\varphi}{3\pi}\right) + r_D I_o \left(\frac{1}{8} - \frac{m_s \cos\varphi}{3\pi}\right) \tag{2.9}$$

$$p_{sw} = \frac{1}{\pi} \frac{U_{DC}}{U_{nom}} \frac{I_{ACrms}}{I_n om} \left(E_{on} + E_{off} + E_{rec}\right) f_{sw} \tag{2.10}$$

with

$$I_o = \sqrt{2} I_{ACrms} \tag{2.11}$$

where U_{ce0} and r_T are the transistor parameters, U_{D0} and r_D the diode parameters, m_s is the modulation function, $\cos\varphi$ is the power factor, U_{DC} is the input voltage, I_{ACrms} is the RMS value of the output current, E_{on}, E_{off} and E_{rec} are the switching energies for the on-switching of the transistor, the off switching of the transistor and the recovery of the diode, f_{sw} is the switching frequency. Parameters of the transistor module could be found in the corresponding data sheet [Graovac.D 2009].

Thus the total losses of the inverter p_{inv_losses} is:

$$p_{inv\_losses} = 3\left(p_{cT} + p_{cD} + p_{sw}\right) \tag{2.12}$$

In order to reduce the simulation time, an average inverter model can be used [Delarue.P 2003]. The relationship between the DC bus voltage u_{dc} and AC voltages $\underline{u_s}$ can be expressed as:

$$\underline{u_s} = \underline{m_s} u_{dc} \tag{2.13}$$

where $\underline{m}$ is the modulation vector.

The average model can be built based on the power conservation principle. The instantaneous power P_{dc} on the DC side must be the same as that of P_s on the AC side, by adding the inverter losses.

$$P_{dc} = P_s + \varsigma p_{inv\_losses} \tag{2.14}$$

$$P_{dc} = u_{dc}\, i_{bat} \tag{2.15}$$

$$P_s = \underline{m_s}^T u_{dc}\, \underline{i_s} \tag{2.16}$$

where ς is used for distinguish the direction of the power flow. It definition could be found in Eq. (2.5).

Then the DC current i_{bat} is:

$$i_{bat} = \frac{P_s + p_{inv\_losses}}{u_{bat}} \tag{2.17}$$

$$i_{bat} = \underline{m}_s^T \underline{i}_s + \frac{p_{inv\_losses}}{u_{bat}} \tag{2.18}$$

$$i_{bat} = i_{inv} + i_{inv\_losses} \tag{2.19}$$

We introduce a fictive current i_{inv_losses} that represents the inverter losses:

$$i_{inv\_losses} = \frac{p_{inv\_losses}}{u_{bat}} \tag{2.20}$$

The machine supply voltage and inverter current are deduced from the average model. The right side of inverter model will impose an AC voltage $\underline{u}_s$ to the model of EM, and receive an AC current $\underline{i}_s$ as a reaction. Then the inverter losses are calculated according to switching frequency, inverter output current and power factor. The fictive current that deduced from inverter losses and DC bus voltage is used to represent the inverter losses. The topology of the average model considering losses is indicated in Fig.2.3.

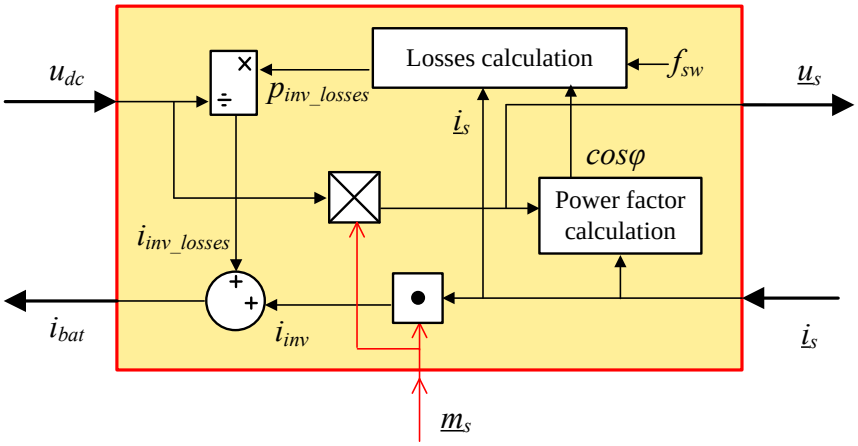

Figure. 2.3. Topology of the inverter model considering losses

2.3.2 Model of an EM

A $dq0$ system is widely used to analyze AC machines for their steady and transient performances. For a 3-phase EM, there are 2 independent phase-to-phase voltages and currents. The transformation between a static natural abc frame and a rotational dq frame is realised by a transformation matrix:

$$\begin{cases} \underline{u}_{sdq} = [P(\theta)]\,\underline{u}_{abc} = [P(\theta)]\,H_{us}\underline{u}_s \\ \underline{i}_s = H_{is}\underline{i}_{abc} = H_{is}\,[P(\theta)]^{-1}\,\underline{i}_{sdq} \end{cases} \tag{2.21}$$

where $\underline{u}_{sdq} = [u_{sd}, u_{sq}]^T$ and $\underline{i}_{sdq} = [i_{sd}, i_{sq}]^T$ are the stator voltages and currents vectors in dq frame, $\underline{u}_s = [u_{sac}, u_{sbc}]^T$ and $\underline{i}_s = [i_{sac}, i_{sbc}]^T$ are the stator phase-to-phase voltages and currents vectors in abc frame, $\underline{u}_{abc} = [u_a, u_b, u_c]^T$ and $\underline{i}_{abc} = [i_a, i_b, i_c]^T$ are the stator phase voltages and currents vectors in abc frame, θ is the

d axis position with respect to the stator stationary frame, $[H_{us}]$ and $[H_{is}]$ are the conversion matrixes.

The park transformation with power conservation is given by:

$$[P(\theta)] = \sqrt{\frac{2}{3}} \begin{bmatrix} \cos\theta & \cos\left(\theta - \frac{2\pi}{3}\right) & \cos\left(\theta + \frac{2\pi}{3}\right) \\ -\sin\theta & -\sin\left(\theta - \frac{2\pi}{3}\right) & -\sin\left(\theta + \frac{2\pi}{3}\right) \end{bmatrix} \tag{2.22}$$

The voltage transformation matrix $[H_{us}]$ is used to convert the phase-to-phase voltage $\underline{u}_s$ to the phase-to-neutral voltages $\underline{u}_{abc}$. Similarly, a matrix $[H_{is}]$ can convert the phase-to-neutral currents to line currents. Matrixes $[H_{us}]$ and $[H_{is}]$ varies with regard to different winding connections.

For Y connection:

$$H_{us} = \frac{1}{3} \begin{bmatrix} 2 & -1 \\ -1 & 2 \\ 1 & -1 \end{bmatrix} \qquad H_{is} = \begin{bmatrix} 1 & 0 & 0 \\ 0 & 1 & 0 \end{bmatrix} \tag{2.23}$$

For Δ connection:

$$H_{us} = \begin{bmatrix} 1 & 0 \\ -1 & 1 \\ 0 & -1 \end{bmatrix} \qquad H_{is} = \begin{bmatrix} -1 & 1 & 0 \\ 0 & -1 & 1 \end{bmatrix} \tag{2.24}$$

2.3.2.1 Model of an IM

For an IM, there are 3 kinds of dq models regarding to different vector control methods, such as Rotor Flux Oriented Control (RFOC), Stator Flux Oriented Control (SFOC), Air-gap Flux Oriented Control (AFOC). With RFOC, the stator and rotor voltage equations are given by:

$$\begin{bmatrix} u_{sd} \\ u_{sq} \\ 0 \\ 0 \end{bmatrix} = \begin{bmatrix} R_s + L_s p & -\omega_s L_s & L_m p & -\omega_s L_m \\ \omega_s L_s & R_s + L_s p & \omega_s L_m & L_m p \\ L_m p & 0 & R_r + L_r p & 0 \\ \omega_f L_m & 0 & \omega_f L_r & R_r \end{bmatrix} \begin{bmatrix} i_{sd} \\ i_{sq} \\ i_{rd} \\ i_{rq} \end{bmatrix} \tag{2.25}$$

where $\underline{u}_{sdq}$, $\underline{i}_{sdq}$ and $\underline{i}_{rdq}$ are the stator voltages, stator current and rotor current, R_s and R_r are the stator and rotor resistances per phase, L_s, L_r are the inductances, L_m is the mutual inductance, ω_s and ω_f are the synchronous and slip speeds, p is the differential operator.

With RFOC, $\psi_{rq} = L_m i_{sq} + L_r i_{rq} = 0$. Choosing stator currents $\underline{i}_{sdq}$ as state variables, then the stator voltage equation could be rewrite as:

$$\sigma L_s \frac{d\underline{i}_{sdq}}{dt} = \underline{u}_{sdq} - \underline{e}_{sdq} - R_{se}\underline{i}_{sdq} \tag{2.26}$$

$$R_{se} = R_s + \left(\frac{L_m}{L_r}\right)^2 R_r \tag{2.27}$$

$$\sigma = 1 - \frac{L_m^2}{L_s L_r} \tag{2.28}$$

where σ is the flux linkage coefficient.

In the frame of RFOC, the stator current is decomposed into a flux component and a torque component, $\psi_{rq} = 0$ and ψ_{rd} only corresponds to i_{sd}. Choosing ψ_{rd} as a state variable, the flux is generated by the following equation, with respecting the physical causality principle:

$$T_r \frac{d\psi_{rd}}{dt} = L_m i_{sd} - \psi_{rd} \tag{2.29}$$

with:

$$T_r = \frac{L_r}{R_r} \tag{2.30}$$

where T_r is the rotor time constant.

The electro-mechanical energy conversion is realised by:

$$T_e = n_p \frac{L_m}{L_r} \psi_{rd} i_{sq} \tag{2.31}$$

$$\begin{cases} e_{sd} = -\dfrac{L_m}{L_r T_r} \psi_{rd} - \sigma L_s i_{sq} \omega_s \\ e_{sq} = \sigma L_s i_{sd} \omega_s + \dfrac{L_m}{L_r} \psi_{rd} \omega_e \end{cases} \tag{2.32}$$

with

$$\begin{cases} \omega_f = \dfrac{L_m}{\psi_{rd} T_r} i_{sq} \\ \omega_s = \omega_f + \omega_e \\ \omega_e = n_p \Omega \end{cases} \tag{2.33}$$

where T_e is the torque, n_p is the number of poles, $\underline{e}_{sdq}$ is the equivalent back EMF, ω_e and Ω are the rotor electrical and mechanical speeds.

In reality, an EM cannot output all the torque as indicated in Eq. (2.31), due to some losses. In that case, the loss torque should be extracted. To well take the efficiency of an IM in to account, an efficiency map η_{em} is used, which considers the copper and iron losses by FEM. Nevertheless, the copper losses of the rotor and stator have already been involved in Eq. (2.26). Therefore, we only need to extract the loss torque which corresponds to iron loss. With the help of efficiency map, the iron loss p_{iron} is given by:

$$p_{iron} = \frac{T_e \Omega}{\eta_{em}^s} \left(1 - \eta_{em}^s\right) - 3 I_s^2 R_s - 3 I_r^2 R_r \tag{2.34}$$

with

$$\eta_{em} = \eta_{em}\left(T, \Omega\right) \tag{2.35}$$

$$\begin{cases} I_s^2 = \left(\sqrt{\frac{1}{2}}\sqrt{\frac{2}{3}}\right)^2 \left(i_{sd}^2 + i_{sq}^2\right) \\ I_r^2 = \left(\sqrt{\frac{1}{2}}\sqrt{\frac{2}{3}}\right)^2 \left(i_{rd}^2 + i_{rq}^2\right) \end{cases} \tag{2.36}$$

$$\begin{cases} i_{rd} = \dfrac{\psi_{rd} - L_m i_{sd}}{Lr} \\ i_{rq} = -\dfrac{L_m}{L_r} i_{sq} \end{cases} \tag{2.37}$$

where I_s and I_r are the phase currents of the stator and rotor, P_{em} is the power of the IM. In Eq. (2.21), a coordinate transformation with power conservation is used, thus the coefficient $\sqrt{\frac{2}{3}}$ is for estimating the maximum value of the real currents. The coefficient $\sqrt{\frac{1}{2}}$ is used for transforming the maximum value into RMS values.

The loss torque caused by iron loss is obtained:

$$T_{iron} = \frac{p_{iron}}{\Omega} = \frac{T_e\left(1 - \eta_{em}^{\varsigma}\right)}{\eta_{em}^{\varsigma}} - 3\left(I_s^2 R_s + I_r^2 R_r\right)\frac{1}{\Omega} \tag{2.38}$$

The effective output torque is derived by extracting the iron loss torque:

$$T = T_e - \varsigma T_{iron} \tag{2.39}$$

With the relationships above, the EMR of an IM drive could be obtained (Fig.2.4), with modelling relationship numbers in brackets. The inverter is depicted by a conversion element (circle is used since it is a mono domain conversion), the winding and excitation are expressed by accumulation elements due to the integration relationship. The electromagnetic energy conversion is realised by a coupling element, which reveals coupling relationships between the stator current and rotor flux. Since it is a multi-domain conversion, thus circle is used.

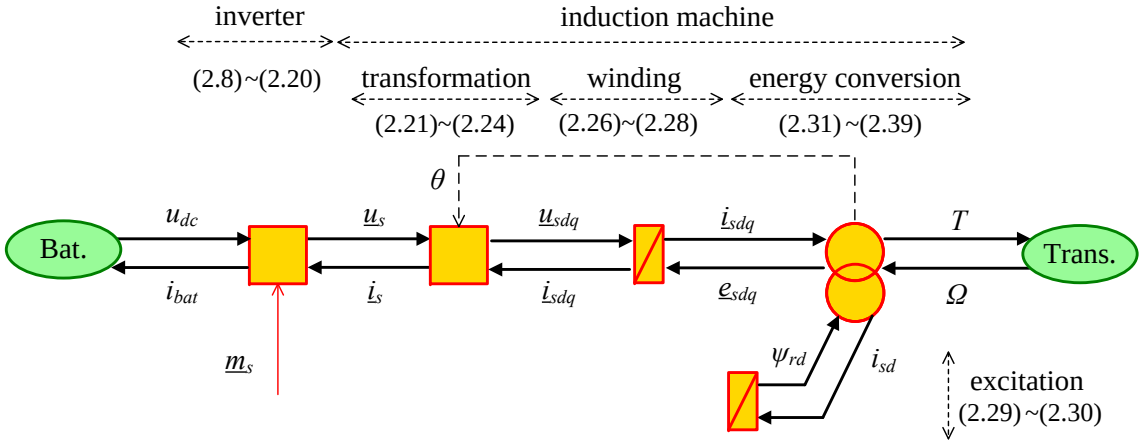

Figure. 2.4. EMR of an IM drive

2.3.2.2 Model of a PM-SM

As for PM-SM, its stator voltage equation in dq frame is given by:

$$\begin{bmatrix} u_{sd} \\ u_{sq} \end{bmatrix} = \begin{bmatrix} R_s + L_d p & -\omega_e L_q \\ \omega_e L_d & R_s + L_q p \end{bmatrix} \begin{bmatrix} i_{sd} \\ i_{sq} \end{bmatrix} + \begin{bmatrix} 0 \\ \psi_f \end{bmatrix} \omega_e \tag{2.40}$$

where L_d and L_q are the inductances in dq frame, ψ_f is the PM flux.

The coordinate transformation has been indicated in Eq. (2.21). Choosing $\underline{i}_{sdq}$ as state variables, the stator voltage equation is given by:

$$\underline{L}_{dq} \frac{d\underline{i}_{sdq}}{dt} = \underline{u}_{sdq} - \underline{e}_{sdq} - R_s \underline{i}_{sdq} \tag{2.41}$$

The electro-mechanical conversion can be described as:

$$T_e = n_p \psi_f i_{sq} + n_p i_{sd} i_{sq} \left(L_d - L_q\right) \tag{2.42}$$

$$\begin{cases} e_{sd} = -L_q i_{sq} \omega_e \\ e_{sd} = \left(L_d i_{sd} + \psi_f\right) \omega_e \end{cases} \tag{2.43}$$

Similar to an IM, the loss torque should be extracted from Eq. (2.42), in order to take the efficiency into account. The iron loss is derived by using an efficiency map:

$$p_{iron} = \frac{T_e \Omega}{\eta_{em}^{\varsigma}} \left(1 - \eta_{em}^{\varsigma}\right) - 3 I_s^2 R_s \tag{2.44}$$

The effective output torque is obtained by extracting the iron loss torque:

$$T_{iron} = \frac{p_{iron}}{\Omega} = \frac{T_e \left(1 - \eta_{em}^{\varsigma}\right)}{\eta_{em}^{\varsigma}} - 3 I_s^2 R_s \frac{1}{\Omega} \tag{2.45}$$

$$T = T_e - \varsigma T_{iron} \tag{2.46}$$

Finally, we have the EMR of a PM-SM drive (Fig.2.5), with corresponding modelling relationship numbers in brackets.

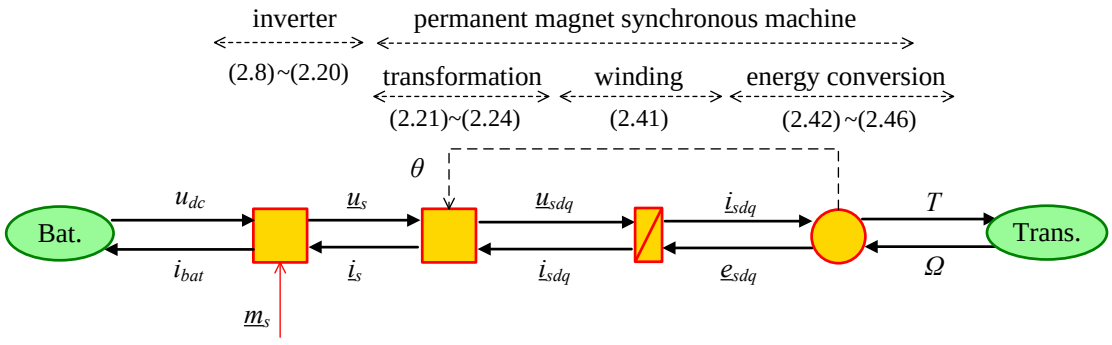

Figure. 2.5. EMR of an PM-SM drive

2.4 Inversion-based control of an electric drive

The aim of EMR is to systematically deduce the control structure of a system, which is achieved by inversion rules (Fig.2.6). Control blocks are depicted by blue parallelograms because all of them only handle information. More details about inversion-based control can be found in Appendix A.1.

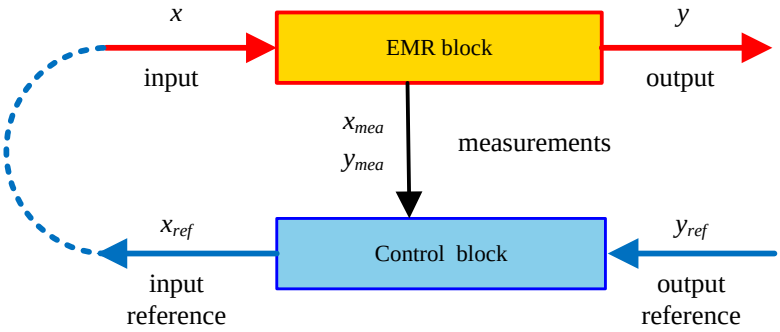

Figure. 2.6. Methodology of inversion-based control

2.4.1 Control an electric drive

2.4.1.1 Control an IM drive

For an IM, the inversion of Eq. (2.29) requires a flux controller C_{flux} to provide the reference current i_{sd_ref} from the reference flux ψ_{rd_ref} and the estimated flux ψ_{rd_est}:

$$i_{sd\_ref} = C_{flux}\left[\psi_{rd\_ref} - \psi_{rd\_est}\right] \tag{2.47}$$

The inversion of Eq. (2.31) leads to the reference current i_{sq_ref} from the reference torque T_{ref} and ψ_{rd_ref}:

$$i_{sq\_ref} = \frac{L_r}{L_m}\frac{1}{\psi_{rd\_ref} n_p} T_{ref} \tag{2.48}$$

The inversion of Eq. (2.26) generates the reference voltages $\underline{u}_{sdq\_ref}$ in the dq frame using 2 current controllers and back EMF compensations:

$$\begin{cases} u_{sd\_ref} = C_{i_{sd}}\left[i_{sd\_ref} - i_{sd\_est}\right] + e_{sd\_est} \\ u_{sq\_ref} = C_{i_{sq}}\left[i_{sq\_ref} - i_{sq\_est}\right] + e_{sq\_est} \end{cases} \tag{2.49}$$

Reference voltage vector $\underline{u}_{s\_ref}$ in a static natural coordinate is deduced by the inversion of Eq.(2.21):

$$\underline{u}_{s\_ref} = \left[H_{su}\right]\left[P\left(\theta\right)\right]^{-1}\underline{u}_{sdq\_ref} \tag{2.50}$$

with

$$\left[P\left(\theta\right)\right]^{-1} = \left[P\left(\theta\right)\right]^{T} \tag{2.51}$$

$$H_{su} = \begin{bmatrix} 1 & 0 & -1 \\ 0 & 1 & -1 \end{bmatrix} \qquad (Y\ connection) \tag{2.52}$$

$$H_{su} = \begin{bmatrix} 1 & 0 & 0 \\ 0 & 0 & -1 \end{bmatrix} \qquad (\Delta\ connection) \tag{2.53}$$

where $[H(su)]$ and $[P(\theta)]^{-1}$ are the inversions of $[H(us)]$ and $[P(\theta)]$.

Finally, the modulation functions are defined, which will be used to define the switch orders in reality. It provides the modulation functions $\underline{m}_{s\_ref}$ from $\underline{u}_{s\_ref}$ and the DC voltage measurement u_{dc_mea}:

$$\underline{m}_{s\_ref} = \frac{\underline{u}_{s\_ref}}{u_{dc\_mea}} \tag{2.54}$$

This control is a simple and graphical way of defining the control of an electrical drive assuming that all the variables are measurable. Nevertheless, as some variables are not measurable, so that estimations are required. They are generally estimated using the relationships obtained via the model. For example, the estimated flux ψ_{rd_est} is obtained from the d axle current i_{sd_est} using Eq. (2.29) with an integration method:

$$T_r \frac{d\psi_{rd\_est}}{dt} = L_m i_{sd\_est} - \psi_{rd\_est} \tag{2.55}$$

Some model elements are thus copied to calculate the estimations. This is a graphical way of describing classical estimations for electric drives. In this way, the estimation of the equivalent currents, the back EMF, and the flux in the dq frame are obtained from the measurement of the actual currents and speed. According to the equations above, we can deduce the control scheme of an IM drive (Fig.2.7). The estimated elements are represented in purple pictographs (see the middle part).

2.4.1.2 Control of a PM-SM drive

The PM-SM drive can also be inverted step-by-step according to the inversion rules. The electromechanical conversion (Eq. 2.42) of a PM-SM is directly inverted to deduce the machine reference currents $\underline{i}_{sdq\_ref}$ from the torque reference T_{ref}:

$$\begin{cases} i_{sd\_ref} = \dfrac{\psi_{d\_ref} - \psi_f}{L_d} \\ i_{sq\_ref} = \dfrac{1}{n_p \left[i_{sd\_ref} (L_d - L_q) + \psi_f \right]} T_{ref} \end{cases} \tag{2.56}$$

where ψ_{d_ref} is the flux reference, which is defined by the flux control strategy.

The inversions of other parts of a PM-SM drive just have the same mathematical relationships as those of the IM drive. For instance, the equivalent stator windings Eq. (2.41) also requires 2 currents controllers and compensations of EMFs to obtain the voltage references in the dq frame (see Eq. 2.49). The coordinate transformation is inverted by using an estimated angle θ_{est} (see Eq. 2.50). The inverter is inverted to obtain the modulation functions (see Eq. 2.54). The control scheme of a PM-SM is then deduced with variable estimation in the middle (Fig.2.8).

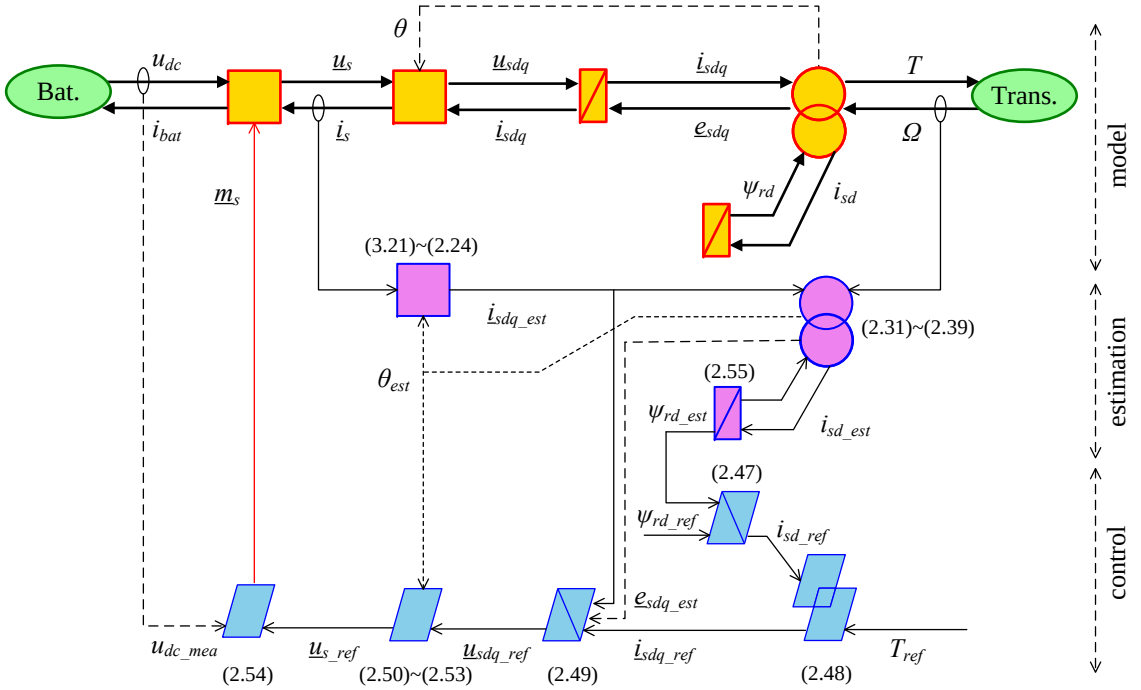

Figure. 2.7. EMR and control scheme of an IM drive

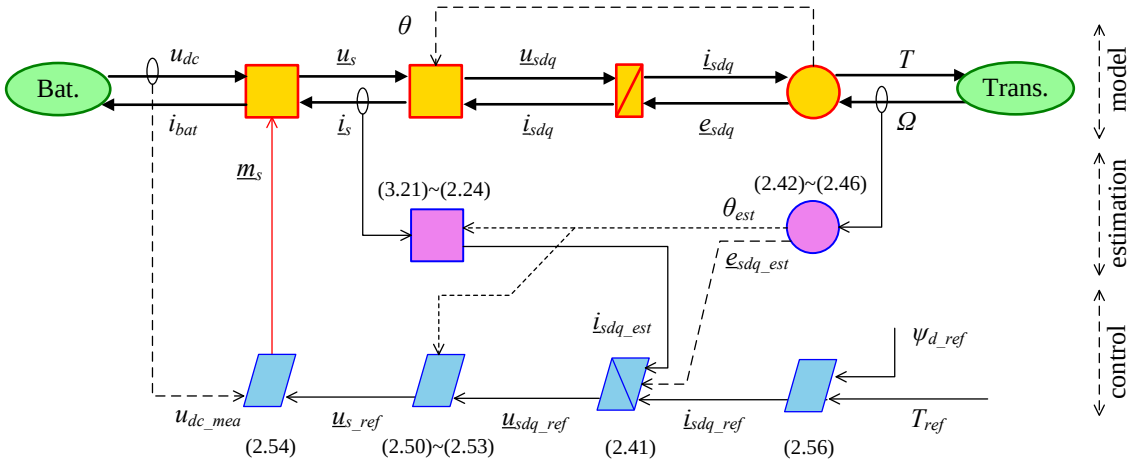

Figure. 2.8. EMR and control scheme of a PM-SM drive

2.4.2 Validation of the control

The control of the IM drive and the PM-SM drive are deduced with the help of inversion-based control in the above sections. This section will carry out the experimental validation using the eV (electricity and Vehicle) platform in University of Lille (France). Fig. 2.9 indicates the validation structure, which includes 2 batteries, 2 electrical drives and 1 speed controller. Among the 2 electrical drives, one is for test, which could be an IM drive or a PM-SM drive, another one is the load drive (DCM in this case). Torque controls are imposed to both electrical drives. According to the physical causality, the torque difference leads to the rotation speed. Thus

the torque reference of the load EM comes from the output of the speed controller. The experimental setup that used for this experiment is composed of one IM, one SM (Table. 2.1) and one DCM as load machine. There are 2 set of converters with 6 IGBT legs that can be used for the control of these EMs (Fig. 2.10). In this experiment, a salient-pole Synchronous Machine (SM) is used to replace the PM-SM by imposing a 1.9 A DC current in the rotor.

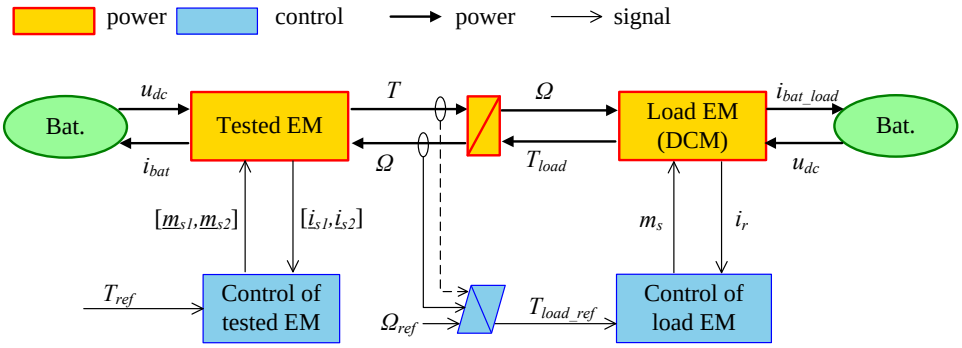

Figure. 2.9. Structure of control validation

Table. 2.1. Parameters of the experimental prototypes

Parameters	IM	SM	Parameters	IM	SM
Rated power P_N (kW)	1.5	1.5	Stator inductance L_s (H)	0.709	–
Rated speed Ω_N (rad/s)	1500	1500	Rotor inductance L_r (H)	0.019	–
Number of pole pairs n_p	2	2	Mutual inductance L_m (H)	0.106	–
Stator resistance R_s (Ω)	7.7	4.46	Stator inductance L_d (H)	–	0.36
Rotor resistance R_r (Ω)	0.264	–	Stator inductance L_q (H)	–	0.22

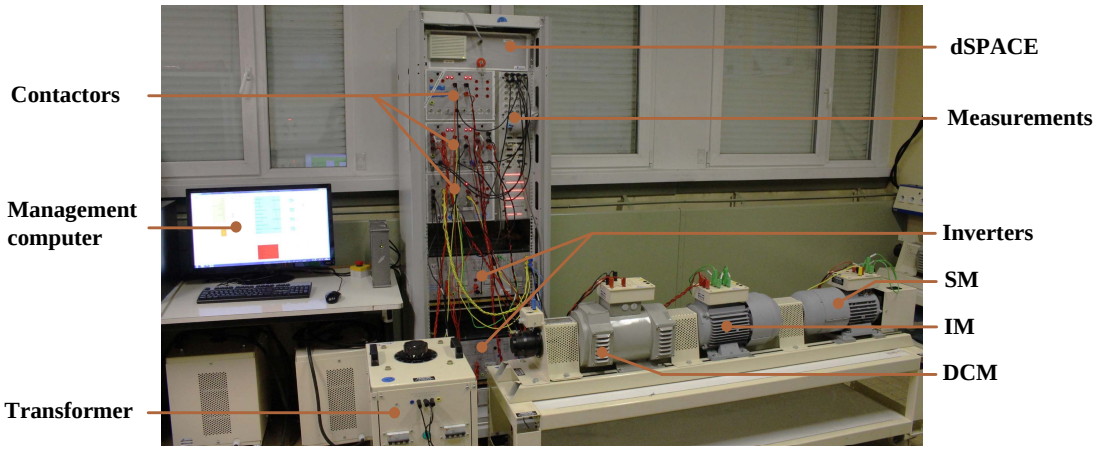

Figure. 2.10. Experimental platform

In this experiment, the stator of the IM is fed by a 3-leg IGBT inverter. A DC bus with 300 V supplies this inverter. The stator of the SM is fed by another 3-leg

IGBT inverter. The 2 tested EMs have the same shaft and the DCM simulates a mechanical 'load'. The tested EM is controlled in order to impose different load torques on the tested drive. The control scheme is directly transferred from Matlab-Simulink^{TM} to the dSPACE controller board. The results of control validation are shown in Fig. 2.11 and Fig. 2.12.

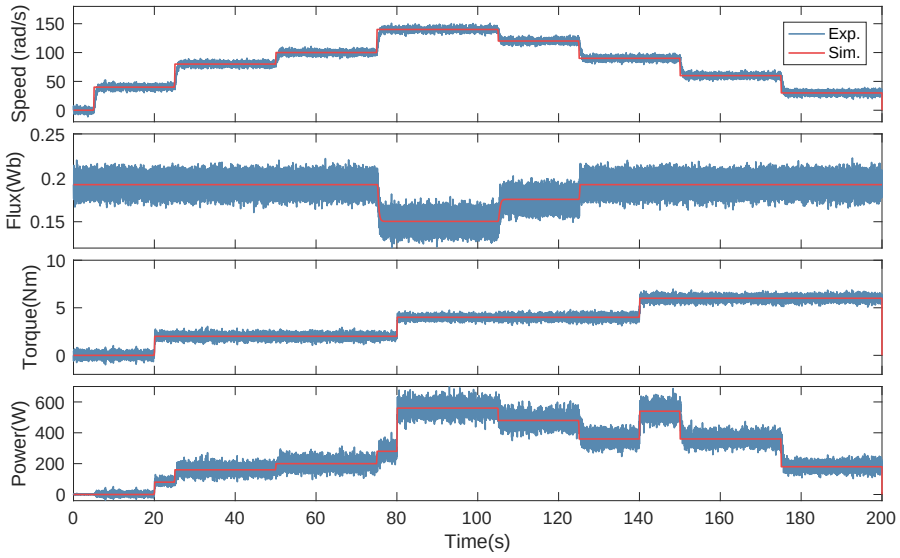

Figure. 2.11. Experimental results of IM control validation

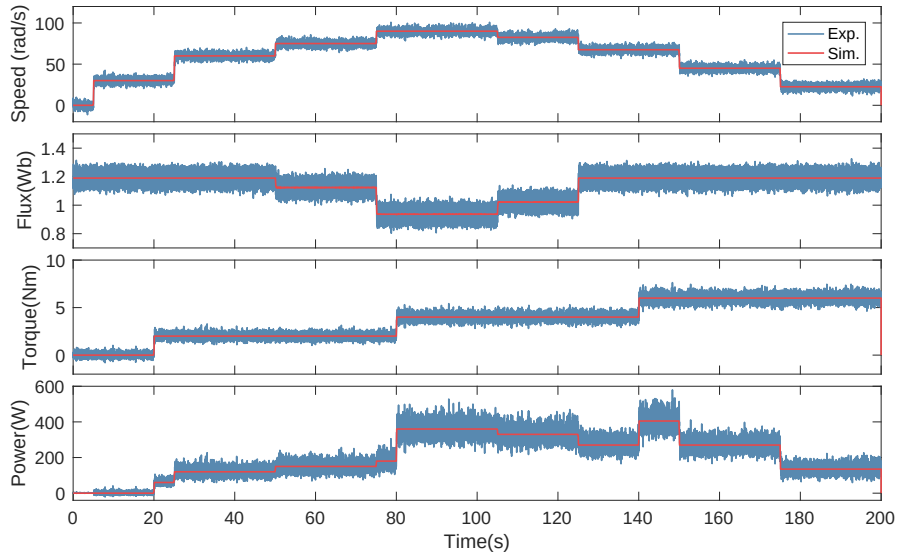

Figure. 2.12. Experimental results of SM control validation

For the IM, the rotor flux ψ_{rd} is set to its rated value (0.18 Wb) unto and including speed 100 rad/s, and is weakened beyond 100 rad/s. ψ_{rq} is set to zero. The flux is estimated by using the current in dq frame. Reference steps of speed and torque are imposed to the IM to make the it work with different powers. The experimental

results indicate that the experiment well comply with the simulation. When the speed is lower than 100 rad/s, the rotor flux stays at its rated value, and it is weakened if the speed is higher. What is more, the IM is controlled to work with different powers.

For the SM, its rotor is excited using a DC current (1.9 A) to replace the PM. Thus the flux ψ_{sd} is set to its rated value (1.8 Wb) below 70 rad/s with $i_{sd} = 0$, then the flux is weakened by changing i_{sd} beyond 70 rad/s. Similarly, stepped speed and torque references are imposed to the SM to make it work with different powers. The experimental carves respect the results of simulation. Flux weakening is realised beyond the 70 rad/s.

The above experimental results prove the validity and feasibility of the EMR-based control scheme. The EMR simulation model is directly downloaded to the dSPACE control board, which simplifies the experimental process.

2.5 Modelling of a MCM-based vehicle using EMR

The objective of this chapter is to develop the model and control for a MCM-based vehicle. This section will start with a pure EV and elaborate on the process of modelling. Then, the model will be extended to other kinds of vehicles, such as series HEV and parallel HEV. This model will lay the foundation for MCM sizing and the development of power split strategies in the following chapters.

2.5.1 Model of a MCM-based EV

The configuration of the studied pure EV is shown in Fig. 2.13 (only taking series MCM as an example). In this configuration, MCM is the only power source of the vehicle, it consists of m EMs. In the following part, these components will be modelled one-by-one.

MCM — Each EM in a MCM has its own inverter. And as described in section 1.1, there are 2 kinds of connections between inverters and the battery (Fig.1.7). Considering the independence and reliability, the topology where all the electric drives share the same DC bus is selected. Hence the current i_{batd} that imposed from MCM drive to battery is the superposition of the currents in each electric drive:

$$\begin{cases} u_{dc} = common \\ i_{batd} = \sum_{i=1}^{m} i_{bati} \end{cases} \tag{2.57}$$

Meanwhile, there are 2 basic mechanical connections for a MCM, i.e., series MCM where the EMs share the same shaft or parallel MCM where the shafts of the EMs

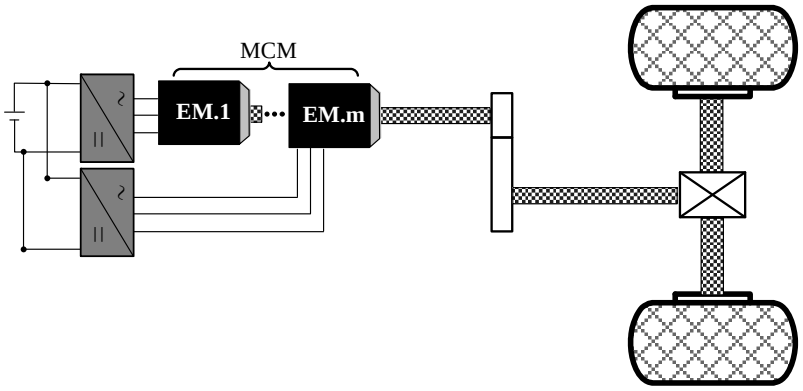

Figure. 2.13. The configuration of the studied vehicle

are aligned in parallel (Fig. 2.1). To describe these 2 mechanical connections in an unified form, a selection coefficients τ_{se} is used:

$$\begin{aligned}\begin{bmatrix} T_{mcm} \\ \Omega_1 \\ \vdots \\ \Omega_m \end{bmatrix} &= \tau_{se} \begin{bmatrix} 1 & \dots & 1 & 0 \\ 0 & \dots & 0 & 1 \\ \vdots & \vdots & \vdots & \vdots \\ 0 & \dots & 0 & 1 \end{bmatrix} \begin{bmatrix} T_1 \\ \vdots \\ T_m \\ \Omega_{mcm} \end{bmatrix} \\ &+ (1-\tau_{se}) \begin{bmatrix} \eta_{par}^{\varsigma} & k_m \eta_{par}^{\varsigma} & \dots & \eta_{par}^{\varsigma} \prod_{i=2}^{m} k_i & 0 \\ 0 & 0 & \dots & 0 & \prod_{i=2}^{m} \frac{1}{k_i} \\ 0 & \vdots & \vdots & \vdots & \vdots \\ 0 & 0 & \dots & 0 & 1 \end{bmatrix} \begin{bmatrix} T_1 \\ \vdots \\ T_m \\ \Omega_{mcm} \end{bmatrix}\end{aligned} \tag{2.58}$$

where the 2 items on the right of the equal sign corresponds to the series and parallel structure respectively, η_{par} is the efficiency of the gear-tain in the parallel MCM, which is used for connecting the shafts of the EMs, k_i is the gear ratio of the i^{th} EM to the $(i-1)^{th}$ EM. When $\tau_{se} = 1$, the MCM is in series structure. On the contrary, if $\tau_{se} = 0$, the MCM is in parallel structure. EMR of a MCM drive is shown in Fig.2.14. To simplify the representation, the circles in Fig.2.14 correspond to the dynamical models of the electric drives, including their controls. Thus there is a torque reference as the tuning input for each drive. The electric drive could be an IM drive or PM-SM drive, one can select according to the demand. Meanwhile, the number of EMs in a MCM could be easily adjusted since all the electric drives have the same formalization of inputs and outputs.

Gearbox — The gearbox is imposed by a fixed gear ratio k_{gear}. The mathematical model is given by the following formulation with a constant efficiency η_{gear}:

$$\begin{cases} T_{gear} = k_{gear} T_{trans} \eta_{gear}^{\varsigma} \\ \Omega_{trans} = k_{gear} \Omega_{gear} \end{cases} \tag{2.59}$$

where T_{gear} and Ω_{gear} are the torque and speed imposed by the gearbox.

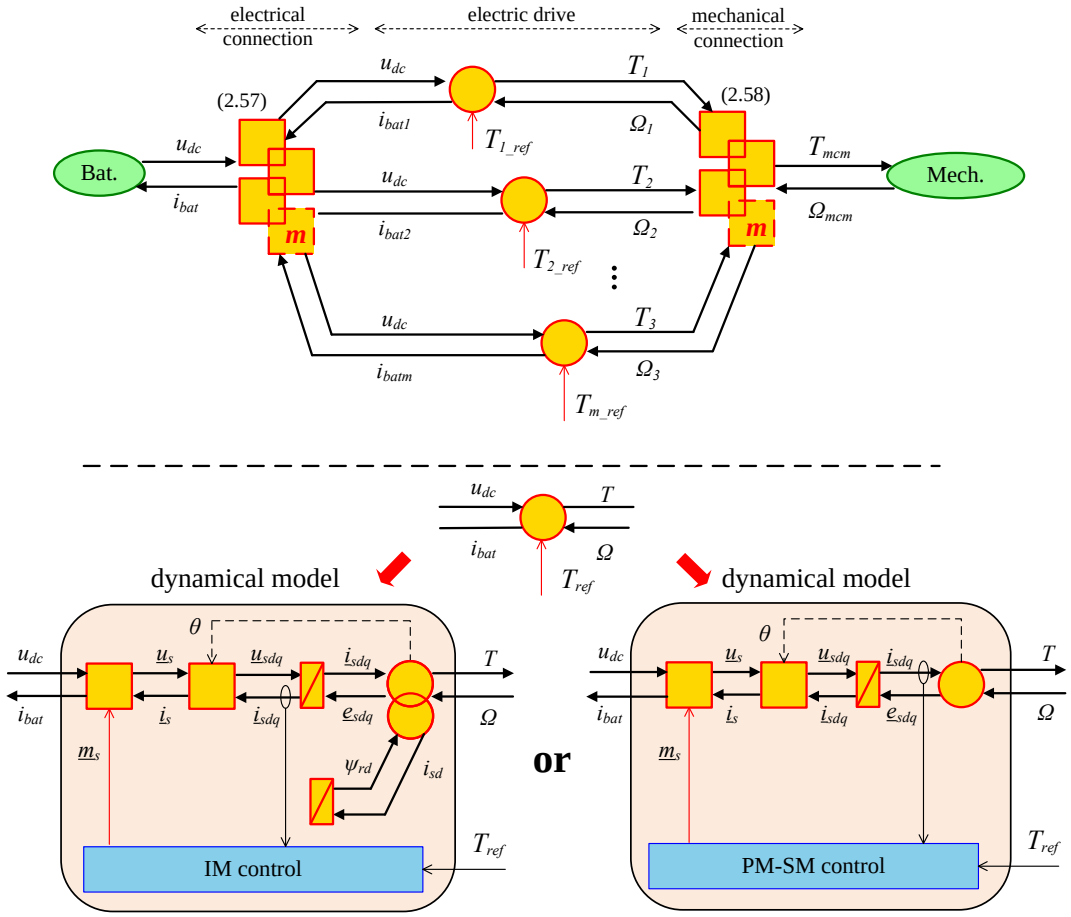

Figure. 2.14. EMR of the MCM drive

Equivalent wheel — If not considering the turning, the differential can be neglected and the equivalent wheel will be described by:

$$\begin{cases} F_{trans} = T_{gear} \dfrac{1}{R_{wh}} \\ \Omega_{gear} = v_{veh} \dfrac{1}{R_{wh}} \end{cases} \tag{2.60}$$

where F_{trans} and v_{veh} are the traction force and velocity of the vehicle, R_{wh} is the radius of the wheel.

Chassis — A chassis has 2 axles. Generally, the traction system is located in the front, thus the force in the front axle is a composition of electrical force and mechanical braking force. While for the rear axle, only mechanical braking force exists. Therefore, the force compositions in the chassis can be expressed as:

$$\begin{cases} F_{front} = F_{trans} + F_{bf} \\ v_{veh} = common \end{cases} \tag{2.61}$$

$$\begin{cases} F_{tot} = F_{front} + F_{br} \\ v_{veh} = common \end{cases} \tag{2.62}$$

where F_{front} is the total force in the front axle, F_{bf} is the front mechanical braking force, F_{tot} is the total force, F_{br} is the rear mechanical braking force.

The vehicle velocity v_{veh} is obtained with the classical dynamical relationship from the traction and resistive forces:

$$M_{veh\_eq}\frac{dv_{veh}}{dt} = F_{tot} - F_{res} \tag{2.63}$$

with

$$\begin{cases} M_{veh\_eq} = M_{veh} + \dfrac{J_{mcm}}{R_{wh}^2 k_{gear}^2} + \dfrac{J_{gear}}{R_{wh}^2} + \dfrac{J_{wh}}{R_{wh}^2} \\ M_{veh} = M_{cha} + M_{ed} + M_{bat} \end{cases} \tag{2.64}$$

where F_{res} is the resistive force, M_{veh_eq} is the equivalent mass of the vehicle, including the equivalent masses of the rotating parts, M_{veh} is the static mass of the vehicle, which consists of the mass of chassis M_{cha}, electric drive M_{ed} and battery M_{bat}. J_{mcm}, J_{gear} and J_{wh} are the initials of MCM, gear-box and wheels.

Road — The road provides a resistive force to the vehicle. The force is composed of rolling force, aerodynamic force and grade force:

$$F_{res} = M_{veh}gf + k_{areo}v_{veh}^2 + M_{veh}g\sin\alpha_{slop} \tag{2.65}$$

where g is the gravity, f is the rolling resistance coefficient, k_{areo} is the coefficient for air resistance, α_{slop} is the slop angle.

Battery — The battery is modeled as a voltage source in series with a resistance:

$$u_{dc} = u_{oc}\left(SoC\right) - R_{bat}\left(SoC\right)i_{bat} \tag{2.66}$$

where u_{dc} is the output voltage, u_{oc} and R_{bat} are the open circuit voltage the resistance, which are the function of battery State of Charge (SoC), i_{bat} is the battery current. SoC is the level of charge of an battery relative to its capacity, which is given by:

$$SoC = SoC_0 - \frac{1}{3600C_{bat}}\int_0^t i_{bat}dt \tag{2.67}$$

According to the equations above, the EMR of the studied MCM-based EV is given in the upper part of Fig. 2.15. In this EMR, there are 4 coupling elements, they are key elements for energy distributions. Besides, the battery, braking and road are the terminals of the system, thus are depicted by source elements (green ovals).

2.5.2 Model of a MCM-based HEV

HEVs are classified into parallel HEV, series HEV, and series-parallel HEV. The core idea of applying MCM to electrified vehicle is to replace the original traction EM

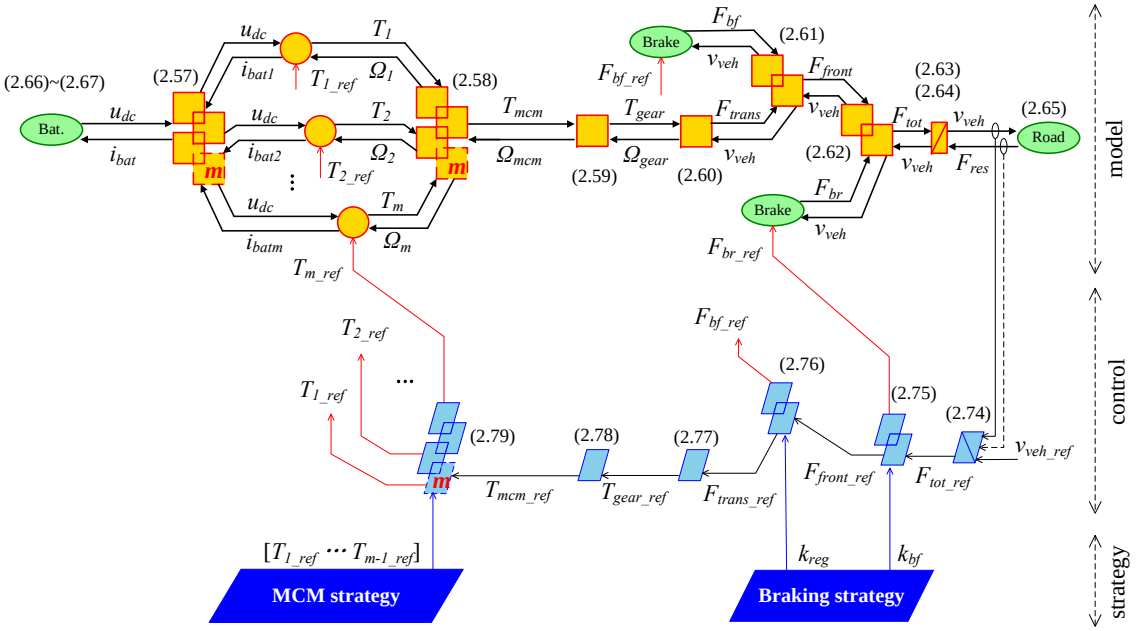

Figure. 2.15. EMR and control scheme of the MCM-based EV

by MCM in order to obtain better performances. Nevertheless, in a series-parallel HEV, both EMs can be used as traction EMs. Hence, if they are replaced by MCM, the system structure and control complexity will increase significantly. Therefore, this thesis only deals with the MCM-based parallel HEV and MCM-based series HEV (see their configuration in Fig. 2.16, only taking series MCM as an example).

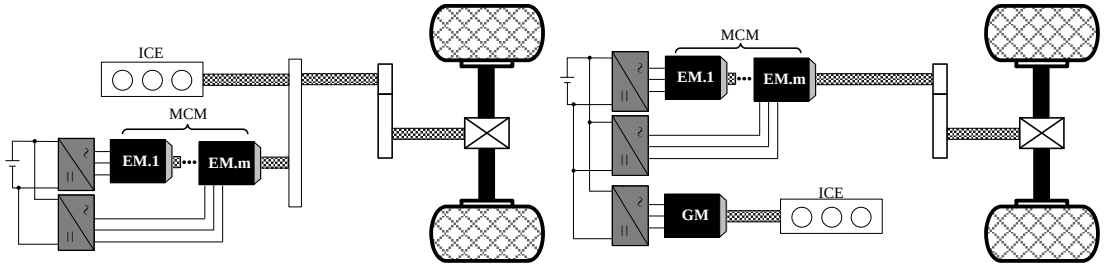

(a) Parallel HEV (b) Series HEV

Figure. 2.16. Configuration of MCM-based HEV

2.5.2.1 MCM-based parallel HEV

ICE — This can be considered as a controllable source which delivers torque T_{ice} and receives its speed Ω_{ice}. It's efficiency could be described by the means of the consumption map:

$$\dot{f}_{fuel} = \dot{f}_{fuel}\left(T_{ice}, \Omega_{ice}\right) \tag{2.68}$$

Belt — We assume that the ICE and MCM are coupled through a belt with a ratio k_{belt} and a constant efficiency η_{belt}, thus, the belt is expressed as:

$$\begin{cases} T_{trans} = T_{ice} + k_{belt}\eta_{belt}^{s} T_{mcm} \\ \Omega_{mcm} = k_{belt}\Omega_{trans} \\ \Omega_{ice} = \Omega_{trans} \end{cases} \tag{2.69}$$

In addition, for parallel HEV, Eq. (2.64) should be modified as follow.

$$\begin{cases} M_{veh\_eq} = M_{veh} + \dfrac{J_{mcm}}{R_{wh}^2 k_{gear}^2 k_{belt}^2} + \dfrac{J_{ice}}{R_{wh}^2 k_{gear}^2} + \dfrac{J_{gear}}{R_{wh}^2} + \dfrac{J_{wh}}{R_{wh}^2} \\ M_{veh} = M_{cha} + M_{ed} + M_{bat} + M_{ice} + M_{belt} \end{cases} \tag{2.70}$$

Based on Fig. 2.15 and according to Eq. (2.68) and (2.69), the MCM-based parallel HEV is represented in the upper part of Fig. 2.17. Compared to the model of the pure EV, there is only a belt being inserted between the MCM and gear-box. The belt is represented by a coupling element.

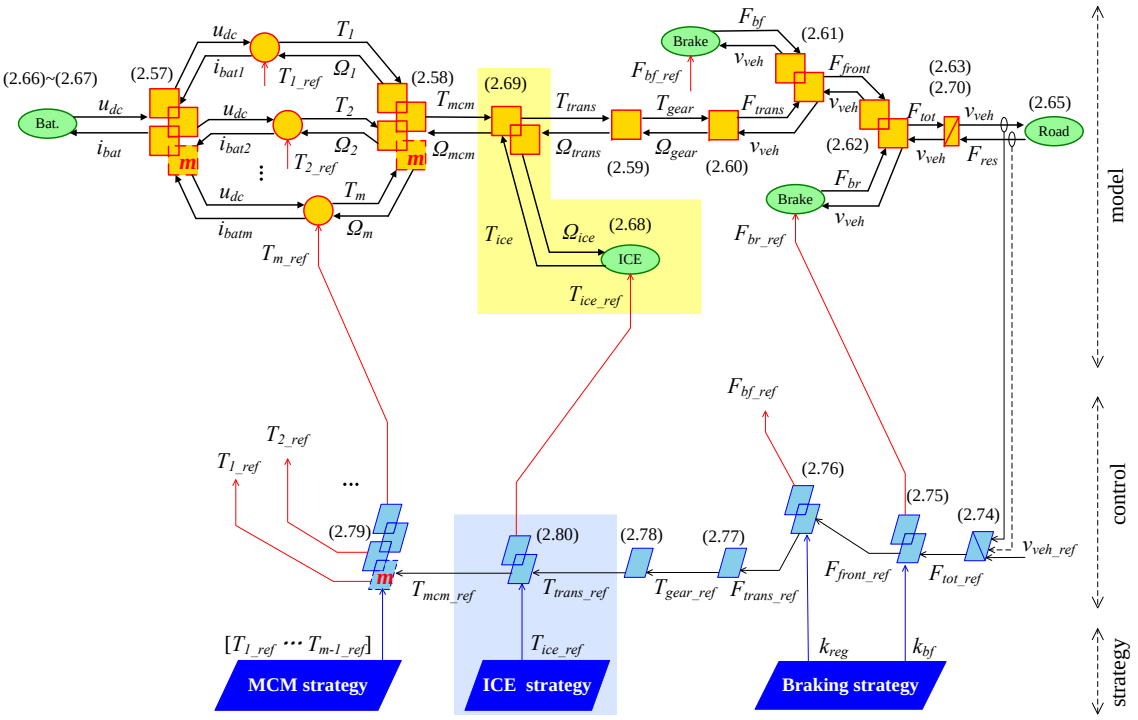

Figure. 2.17. EMR and control scheme of the MCM-based parallel HEV

2.5.2.2 MCM-based series HEV

Shaft of ICE — In a series HEV, the ICE and generator share the same shaft. The ICE speed Ω_{ice} is deduced by the following dynamical equation, according to

the physical causality:

$$J_{ice\_ge}\frac{d\Omega_{ice}}{dt} = T_{ice} - T_{ge} \tag{2.71}$$

where J_{ice_ge} is the total initial of ICE-generator, T_{ice} and T_{ge} are the torques of ICE and generator.

Electrical connection — For a series HEV, the generator drive and the MCM drive are connected to the same battery, thus the electrical connection is expressed by:

$$\begin{cases} u_{dc} = common \\ i_{bat} = i_{batd} + i_{batg} \end{cases} \tag{2.72}$$

where i_{batg} is the current imposed by the generator.

Meanwhile, for a series HEV, Eq. (2.64) should be modified as follow.

$$\begin{cases} M_{veh\_eq} = M_{veh} + \dfrac{J_{mcm}}{R_{wh}^2 k_{gear}^2} + \dfrac{J_{gear}}{R_{wh}^2} + \dfrac{J_{wh}}{R_{wh}^2} \\ M_{veh} = M_{cha} + M_{ed} + M_{bat} + M_{ice} + M_{ge} \end{cases} \tag{2.73}$$

where M_{ice} and M_{ge} are the mass of the ICE and the generator.

In the same way, based on Fig. 2.15, the MCM-based series HEV is represented in the upper part of Fig. 2.18. Compared to the model of pure EV, a ICE-generator system is inserted between the MCM and battery through a coupling element.

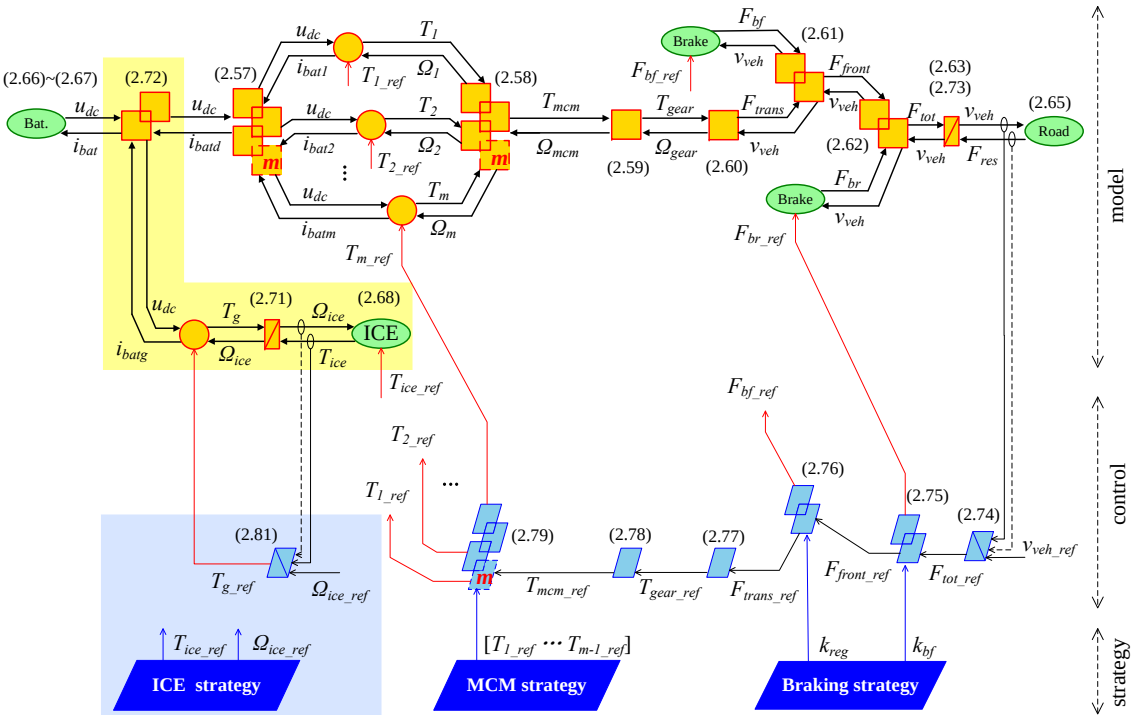

Figure. 2.18. EMR and control scheme of the MCM-based series HEV

2.6 Inversion-based control of a MCM-based vehicle

From the EMR of a system, one can deduce a control structure. Conversion elements can be inverted directly, while accumulation elements are inverted using controllers due to the physical causalities. Moreover, the inversions of coupling elements requires criterion inputs, which allocate the distribution of energy within the system.

2.6.1 Control of a MCM-based EV

The inversion of chassis dynamical process (Eq.2.63) requires a controller C_{veh} to provide the total force reference F_{tot_ref} from the velocity measurement v_{veh_mea} and reference v_{veh_ref} using a compensation of the resistive force F_{res_mea} (if it can be measured or estimated):

$$F_{tot\_ref} = C_{veh}\left[v_{veh\_ref} - v_{veh\_mea}\right] + F_{res\_mea} \tag{2.74}$$

The inversions of force compositions (Eq. 2.61 and Eq. 2.62) need distribution criterions:

$$\begin{cases} F_{br\_ref} = k_{br} F_{tot\_ref} \\ F_{front\_ref} = (1 - k_{bf})\, F_{tot\_ref} \end{cases} with \quad k_{bf} \in [0, 1] \tag{2.75}$$

$$\begin{cases} F_{trans\_ref} = k_{reg} F_{front\_ref} \\ F_{fb\_ref} = (1 - k_{reg})\, F_{front\_ref} \end{cases} with \quad k_{reg} \in [0, 1] \tag{2.76}$$

where F_{br_ref}, F_{front_ref}, F_{trans_ref} and F_{fb_ref} are the references forces, k_{br} and k_{reg} are the distribution criterions. They are crucial for energy recovery management. k_{br} determines the front and rear braking force distribution, while k_{reg} defines the proportion of regenerative force in the front axle when brake. During traction mode, $k_{br} = 0$ and $k_{reg} = 1$. In deceleration, if $k_{reg} = 1$, then all the braking force in the front axle is provided by the MCM. On the contrary, no regenerative braking force is used when $k_{reg} = 0$.

The equivalent wheel and the gearbox (Eq.2.60 and Eq.2.59) are directly inverted to provide the torque reference T_{trans_ref} of the traction system from the reference of the total traction force F_{trans_ref}:

$$T_{gear\_ref} = F_{trans\_ref} R_{wh} \tag{2.77}$$

$$T_{trans\_ref} = T_{gear\_ref} \frac{1}{k_{gear}} \tag{2.78}$$

The torque reference T_{m_ref} of the m^{th} EM in a MCM is obtained through inverting Eq.(2.58). Torque references of the $m-1$ EMs are used as energy distribution

criterions for MCM:

$$T_{m\_ref} = T_{mcm\_ref} - \left(\tau_{se} \sum_{i=1}^{m-1} T_{i\_ref} + (1 - \tau_{se}) \sum_{i=1}^{m-1} T_i \prod_{j=i+1}^{m} k_j \right) \tag{2.79}$$

Then the control scheme of the MCM-based EV is deduced step-by-step according to inversion rules, as shown the lower part of Fig. 2.15. Generally, for a certain system, its MCS is unique (blue parts), but some simplifications can be made to have more practical control. This control scheme consists of 2 levels, the local level (blue parts) that deals with the control of the subsystems, and the strategy level (dark blue parallelograms) which is responsible for the energy management of the whole system.

2.6.2 Control of a MCM-based HEV

In a parallel HEV, the ICE is directly coupled to the mechanical power-train, and its speed cannot be optimized. However, its coupling with MCM adds an optimizable degree of freedom, i.e., the ICE torque, which is given by the strategy. The inversion of the belt (Eq. 2.69) requires the ICE torque reference T_{ice_ref}:

$$T_{mcm\_ref} = \frac{T_{tans\_ref} - T_{ice\_ref}}{k_{belt}} \tag{2.80}$$

In a series HEVs, the engine is decoupled from the wheels, and its torque and speed are both optimizable. The inversion of Eq. (2.71) requires a speed controller C_{ice} to deduce the torque reference T_{ge_ref} of the generator:

$$T_{ge\_ref} = C_{ice} \left(\Omega_{ice\_ref} - \Omega_{ice\_mea} \right) + T_{ice\_mea} \tag{2.81}$$

where Ω_{ice_ref} and Ω_{ice_mea} are the speed reference and measurement of the ICE, T_{ice_mea} is the ICE torque measurement. The inversion control of the MCM-based parallel HEV and series HEV are shown in the lower part of Fig. 2.17 and Fig. 2.18 respectively. Similar to a pure EV, the control of a HEV is also divided into 2 levels: the local level and strategy level.

Once the control objectives have been determined, the tuning path can be defined. The tuning path refers to a set of oriented arrows starting from the tuning variables and acting to the control objective. Taking the pure EV in Fig. 2.15 as an example, the system has $2m + 2$ tuning variables, i.e., modulation vectors of m EM: $\underline{m}_{s1} = [m_{s1ac}, m_{s1bc}] \cdots \underline{m}_{sm} = [m_{smac}, m_{smbc}]$ and 2 mechanical braking forces: F_{bf_ref}, F_{br_ref}. These $2m + 2$ tuning variables are used to control the vehicle velocity v_{veh}, then the tuning path of pure EV is shown in Fig. 2.19.

The control path can be obtained by inverting the tuning path, i.e., from the velocity reference v_{veh_ref} to the reference of inverter modulations $[m_{s1\_ref}\ m_{s2\_ref} \cdots m_{sm\_ref}]$,

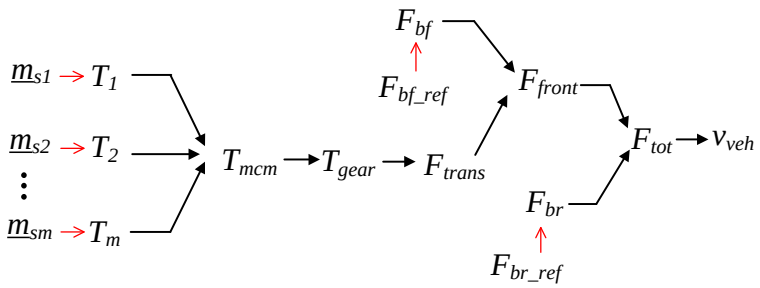

Figure. 2.19. Tuning path of the MCM-based EV

as shown in Fig. 2.20. In this control path, there are $m+1$ control variables are comes from the strategy, which are $m-1$ EM torque references $[T_{1\_ref} \ \cdots \ T_{m-1\_ref}]$ and 2 braking force references F_{br_ref} and F_{br_ref}.

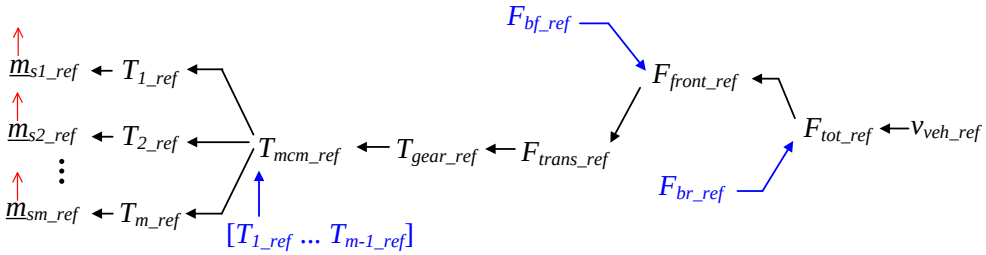

Figure. 2.20. Control path of the MCM-based EV

In the same way, the tuning path and control path of the parallel HEV and the serial HEV can be obtained. It indicates that using EMR to organize the model can clearly reflect the energy flow and important couplings within the system. By introducing the energy distribution criterions, a control path from the control objective to the tuning variables can be systematically established.

2.7 Conclusion

This chapter focuses on the modelling and control of a MCM-based vehicle, which is globally the foundation of the work in all the following chapters.

The main works in this chapter are the following.

(1) The different categories of MCM and their properties are analysed.

(2) The models of the IM and PM-SM drives are represented by EMR, their controls are established according to inversion rules and are validated by experiment.

(3) A MCM-based vehicle is modeled by EMR, its control is then deduced according to inversion rules.

The main conclusion and contributions are summarized.

(1) The use of EMR emphasizes the important couplings which exist between the different parts of the system. It focuses the modelling on the coupling devices that distribute energy and highlights the energy flow of the system.

(2) The inversion of the model leads to a general architecture of the control scheme. It defines the closed-loop control of every state variables. Through inversion rules, EMR highlights the necessity for introducing energy distribution criteria in the control structure.

The model and control in this chapter will be the input of the following chapters. For example, studying the influence of efficiency map on vehicle energy consumption in chapter 3, the comparisons of different MCM for different vehicles in chapter 4 and the development of MCM power split strategies in chapter 5.

3

Fast efficiency map estimation method for different EMs

This chapter deals with the fast efficiency map estimation method for different Electrical Machines (EMs). First, the keys of efficiency map fast estimation are described and analysed. Then the fast efficiency map estimation method for IM and PM-SM is studied. Finally, the efficiency map estimation method is verified by comparisons with the experimental efficiency maps.

Contents

3.1 Introduction 51
3.2 Description of efficiency map estimation 51
3.3 IM efficiency map estimation 53
3.4 PM-SM efficiency map estimation 61
3.5 Validation of the efficiency map estimation methods . . 68
3.6 Conclusion 75

3.1 Introduction

MCM is a multi-machine system, through a corresponding power split strategy, it can fully utilize the high-efficiency area of each Electrical Machine (EM). Therefore, having the ability of expanding the total high-efficiency area of the system is one of the typical advantages of a MCM. In order to give full play to this advantage, the efficiency distribution of each EM should be considered comprehensively, and the high-efficiency area of the MCM system should be taken as the objective function. As a result, the efficiency maps of the EMs are needed. MCM sizing is a problem of optimization with a lot of iterations, and each iteration needs to calculate the value of the objective function. If the efficiency map of each EM is calculated through EM design in each iteration, it would take a lot of time. Therefore, a fast EM efficiency map estimation is necessary for MCM sizing, and it is the core to construct the objective function.

This chapter aims to study the efficiency map estimation for different types of EMs, i.e., Induction Machine (EM), Permanent Magnet Synchronous Machine (PM-SM). Firstly, the core technology of the fast efficiency map estimation method is described. Then the efficiency map estimation method for IM and PM-SM is studied. Finally, the proposed method is validated by comparisons with the experimental efficiency maps. The studied efficiency map estimation method is dedicated for MCM sizing in chapter 4.

3.2 Description of efficiency map estimation

EMs for electric drive generally have wide speed and torque ranges, hence they have a certain degree of overload and flux weakening capability. Regarding to the speed regulation, the 'torque-speed' plane of an EM can be divided into 2 major regions: constant-torque region (region I) and constant-power region (region II), where the EM has different characteristics in these regions. In this chapter, the constant-torque region and the constant-power region are decomposed into 2 sub-regions. The rated-torque carve in constant-torque region and the maximum-torque carve with rated power in constant-power region are the boundaries. The 'torque-speed' plane of the EM is then divided into 4 different sub-regions, i.e., region I-1, I-2, II-1 and II-2. The EM efficiency is then calculated separately in each sub-regions.

The estimation of the EM efficiency map in this chapter is based on the following assumptions:

(1) The basic design specifications of an EM are known in advance, i.e., rated speed Ω_N, rated torque T_N, peak speed Ω_{max}, peak torque T_{max} and peak efficiency η_{max}. These parameters can be guaranteed by the EM design.

(2) The efficiency estimation only considers the iron loss, copper loss, mechanical

loss and stray loss. Additionally, the mechanical and stray losses only depend on the rotational speed and the mechanical power respectively.

(3) The EM has the same hysteresis and eddy-current losses at the rated operating point.

(4) The coefficients for hysteresis and eddy-current losses of the magnetic steel are constants.

(5) The variable and invariable losses are the same at the peak-efficiency point, i.e., the sum of mechanical loss and iron loss equals the copper loss.

(6) The EM is controlled by Rotor Flux Oriented Control (RFOC).

The efficiency of an EM $\eta_{(i,j)}$ at any operating point (T_i, Ω_j) can be calculated by the following formula:

$$\eta_{(i,j)} = \frac{P_{\Omega(i,j)}}{P_{\Omega(i,j)} + p_{copper(i,j)} + p_{iron(i,j)} + p_{stray(i,j)} + p_{mec(i,j)}} \tag{3.1}$$

where i and j are the torque and speed subscripts, P_Ω, p_{copper}, p_{iron}, p_{mec} and p_{Stray} are the mechanical power, copper loss, iron loss, mechanical loss and stray loss.

The mechanical power, mechanical loss, and stray loss can be approximated described by the empirical formula [Levi.E 1984]:

$$P_{\Omega(i,j)} = T_{(i,j)}\Omega_j \tag{3.2}$$

$$p_{mec(i,j)} = \frac{\Omega_{(i,j)}^2}{\Omega_N^2} p_{mecN} \tag{3.3}$$

$$p_{stray(i,j)} = 5 \times 10^{-3} P_{\Omega(i,j)} \tag{3.4}$$

where Ω_N and p_{mecN} are rated speed and rated mechanical loss respectively.

Therefore, the cores of the efficiency map estimation are iron loss and copper loss. Iron loss and copper loss are defined by the following formula: [Lipo.T.A 2018]:

$$p_{iron(i,j)} = p_{hy(i,j)} + p_{eddy(i,j)} \tag{3.5}$$

$$p_{copper(i,j)} = p_{copper\_s(i,j)} + p_{copper\_r(i,j)} \tag{3.6}$$

$$\begin{cases} p_{hy(i,j)} = k_{hy} B^2 f_{(i,j)} \propto B^2 \Omega_{(i,j)} \\ p_{eddy(i,j)} = k_{eddy} \left(f_{(i,j)} B\right)^2 \propto \left(\Omega_{(i,j)} B\right)^2 \end{cases} \tag{3.7}$$

$$\begin{cases} p_{copper\_s(i,j)} = a I_s^2 R_s \\ p_{copper\_r(i,j)} = \dfrac{s}{1-s} T_i \Omega_{(i,j)} \end{cases} \tag{3.8}$$

where p_{hy} and p_{eddy} are hysteresis and eddy-current losses, k_{hy} and k_{eddy} are loss coefficients, f is the frequency of the stator current, B is the flux density, p_{copper_s}

and p_{copper_r} are EM stator and rotor copper losses, a is the number of phases, R_s is the stator resistance per phase, I_s is the stator current, s is the EM slip ratio.

When the EM is a PM-SM, $s = 0$, the rotor copper loss is negligible. Unfortunately, Eq. (3.7) and Eq. (3.8) still depend on EM parameters such as flux, current, resistance, etc., which must be obtained by the EM design. However, if we can establish a loss proportion function $f(T, \Omega)$ to the rated loss using Eq. (3.7) and Eq. (3.8), we can get rid of the EM parameters. So that the loss p_{loss} at any point can be deduced by the loss proportion function and the rated loss $p_{loss(N)}$.

For example, the stator copper loss $p_{copper\_s(i,j)}$ at any point can be given by:

$$p_{copper\_s(i,j)} = \left(\frac{I_{s(i,j)}}{I_{sN}}\right)^2 aI_{sN}^2 R = \left(\frac{I_{s(i,j)}}{I_{sN}}\right)^2 p_{copper\_s(N)} \tag{3.9}$$

where I_{sN} is the rated stator current, $p_{copper\_s(N)}$ is the rated stator copper loss. With appropriate calculation, $\frac{I_{s(i,j)}}{I_{sN}}$ could be expressed in a function of torque (and speed).

In the same way, the flux is a constant in the constant-torque area, thus the hysteresis loss and eddy-current loss in this area could be expressed by:

$$\begin{cases} p_{hy(i,j)} = \dfrac{\Omega_{(i,j)}}{\Omega_N} p_{hy(N)} \\ p_{eddy(i,j)} = \left(\dfrac{\Omega_{(i,j)}}{\Omega_N}\right)^2 p_{eddy(N)} \end{cases} \tag{3.10}$$

where $p_{hy(N)}$ and $p_{eddy(N)}$ are the rated hysteresis loss and eddy-current loss. In the constat-power area, the product of frequency and flux is a constant, hence Eq. (3.10) will change, more derails will be deduced in the following sections.

It can be seen that the core of the efficiency estimation in this chapter is to establish the loss proportion function. In this way, the estimation of EM efficiency map can get rid of the dependence on the EM parameters. Then the efficiency turns into a function of torque and speed: $\eta = f(T, \Omega)$. Therefore, the efficiency map could be calculated only by the basic design specifications, without pre-designing an EM. Fig. 3.1 shows the flowchart of efficiency map estimation, the basic steps could be summarized as follow. (1) Calculate the loss of the peak-efficiency point. (2) Deduce the rated loss according to the loss at the peak-efficiency point. (3) Derive the loss in different sub-regions based on the rated losses, and finally construct the efficiency map.

3.3 IM efficiency map estimation

An IM works on the principle of electromagnetic induction. The rotating stator magnetic field induces current in the rotor, which causes rotor copper loss. The

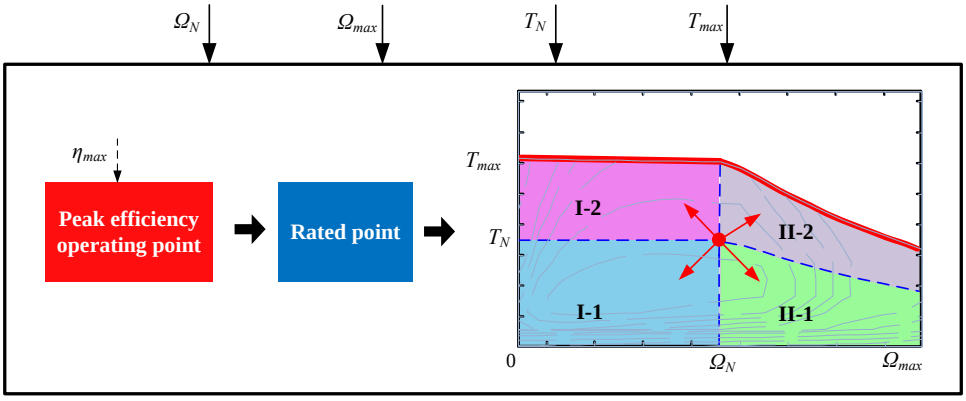

Figure. 3.1. Flowchart of efficiency map estimation

rotor copper loss is closely related to the slip ratio. According to Joule's law, the stator copper loss is proportional to the square of the stator current. Hence in order to establish a loss proportion function, it is essential to study the relationship between stator current and torque. However, with vector control, the stator current is decomposed into the excitation and torque components. The torque depends not only on the current but also on the current angle. In other words, for a specific operating point, the stator current cannot be determined simply by torque, and the copper loss proportion function cannot be directly established. Therefore, the establishment of loss proportion function for IM needs to take into account the current angle and slip ratio.

3.3.1 Current angle and slip ratio calculation

With the Rotor Flux Oriented Control (RFOC), the torque of an IM has many different expressions. To deduce the slip ratio and current angle in function of torque (and speed), the torque takes the following forms:

$$T = n_p \frac{\tau_r}{L_r} \psi_r^2 s \omega_s = n_p \frac{L_m^2}{L_r} i_{sd} i_{sq} = n_p \frac{L_m^2}{L_r} I_s^2 \sin\gamma \cos\gamma \tag{3.11}$$

with:

$$s = \frac{\omega_s - \omega_e}{\omega_s} \tag{3.12}$$

$$\psi_r = \frac{L_m}{1 + \tau_r p} i_{sd} = \frac{L_m}{1 + \tau_r p} I_s \cos\gamma \tag{3.13}$$

where n_p is the number of poles, τ_r is the rotor time constant, L_r is the rotor inductance, ψ_r is the rotor flux, ω_s is the synchronous speed, $\omega_e = n_p\Omega$ is the electrical speed of the rotor, L_m is the mutual inductance, p is the differential operator, and γ is the current angle.

3.3.1.1 Current angle and slip ratio in constant-torque region

With RFOC, the rotor flux can be regarded as a constant in the constant-torque region, hence i_{sd} is a constant referring to Eq. (3.13). The torque is proportional to the q axis current:

$$\frac{i_{sq}}{i_{sqN}} = \frac{T}{T_N} \tag{3.14}$$

Fig. 3.2 shows the vector diagram of the stator current in the constant-torque region, from which we can deduce that:

$$\begin{cases} \tan\gamma = \dfrac{i_{sdN}}{i_{sq}} \\ \tan\gamma_N = \dfrac{i_{sdN}}{i_{sqN}} \end{cases} \tag{3.15}$$

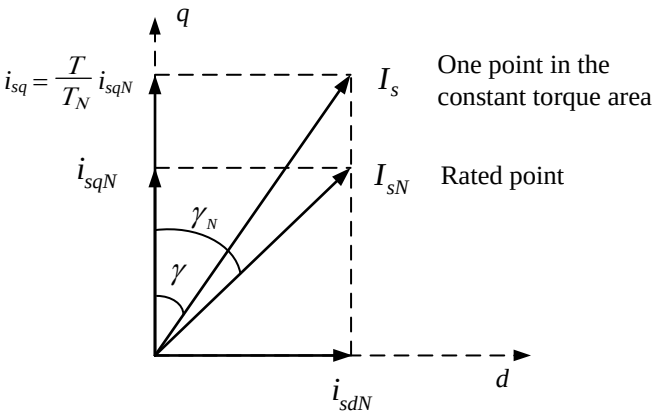

Figure. 3.2. Stator current in constant-torque region

According to Eq. (3.14) and Eq. (3.15), the current angle is derived:

$$\gamma = \arctan(\frac{i_{sdN}}{i_{sq}}) = \arctan(\frac{T_N}{T}\tan\gamma_N) \tag{3.16}$$

where γ_N is the rated current angle. There are many possibilities for γ_N through control, in this thesis, it is chosen to maximize the torque in Eq. (3.11) with the rated stator current. Solving $\frac{\partial T}{\partial \gamma_N} = 0$, we have $\gamma_N = \frac{\pi}{4}$.

For the rated point (T_N, Ω_N) and any point (T, Ω) in the constant-torque region, substituting the torque and speed into Eq. (3.11) and Eq. (3.12), we can calculate the slip rate:

$$s = \frac{T\Omega_N s_N}{T_N\Omega\,(1 - s_N) + T\Omega_N s_N} \tag{3.17}$$

where s_N is the rated slip ratio, generally $s_N = 0.01 \sim 0.03$.

Combining Eq. (3.14) and Eq. (3.16), the relationship of current at both points is given by:

$$\frac{I_s^2}{I_{sN}^2} = \frac{i_{sq}^2\left(1+\tan^2\gamma\right)}{i_{sqN}^2\left(1+\tan^2\gamma_N\right)} = \frac{T^2+T_N^2\tan^2\gamma_N}{T_N^2+T_N^2\tan^2\gamma_N} \tag{3.18}$$

3.3.1.2 Current angle and slip ratio in constant-power region

In the constant-power region, the inverter voltage has been maximized, and a higher speed must be achieved by weakening the flux. Therefore, the calculations of the current angle and the slip ratio are different from those in the constant-torque region.

The current angle and slip ratio will be deduced based on the voltage equation, which is given by:

$$\begin{cases} u_{sd} = R_s i_{sd} + p\psi_{sd} - n_p\Omega\psi_{sq} \\ u_{sq} = R_s i_{sq} + p\psi_{sq} + n_p\Omega\psi_{sd} \end{cases} \tag{3.19}$$

with:

$$\begin{cases} \psi_{sd} = L_s i_{sd} \\ \psi_{sq} = \sigma L_s i_{sq} \end{cases} \tag{3.20}$$

where $\underline{u}_{sdq}$ and $\underline{\psi}_{sdq}$ are the voltage and flux in dq frame, R_s is the resistant of the stator per phase, p is the differential operator, L_s is the stator inductance, $\sigma = 1 - \frac{L_m^2}{L_r L_s}$ is the flux leakage coefficient, generally $\sigma < 0.1$.

If neglecting the winding voltage drop, the voltage equation in steady-state could be simplified as:

$$\begin{cases} u_{sd} \approx -n_p\Omega\psi_{sq} \\ u_{sq} \approx n_p\Omega\psi_{sd} \end{cases} \tag{3.21}$$

Assume (T_1, Ω_N) and (T, Ω) are 2 operating points with the same power in the constant-power region (Fig. 3.3). Since the stator voltages are equal at both points, therefore:

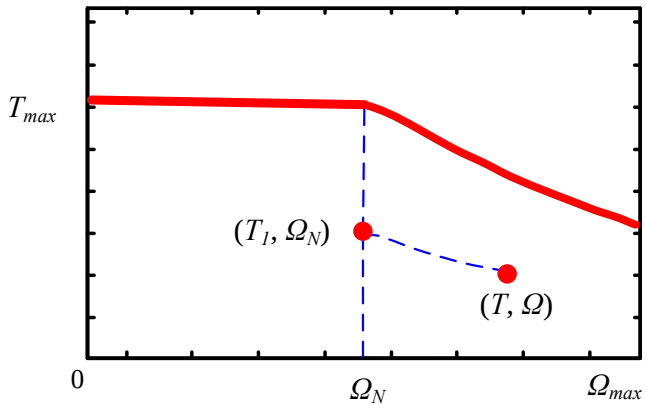

Figure. 3.3. Diagram of operating points for current angle calculation

$$n_p^2\left(\Omega^2\psi_{sd}^2+\Omega^2\psi_{sq}^2\right)=n_p^2\left(\Omega_N^2\psi_{sdN}^2+\Omega_N^2\psi_{sq1}^2\right) \tag{3.22}$$

Define a speed ratio:

$$K=\frac{\Omega}{\Omega_N} \tag{3.23}$$

Substituting Eq. (3.20) and Eq. (3.21) into Eq. (3.22), we have:

$$\Omega^2\left(L_s^2i_{sd}^2+\sigma^2L_s^2i_{sq}^2\right)=\Omega_N^2\left(L_s^2i_{sdN}^2+\sigma^2L_s^2i_{sq1}^2\right) \tag{3.24}$$

So:

$$K^2\left(\sin^2\gamma+\sigma^2\cos^2\gamma\right)I_s^2=\left(\sin^2\gamma_1+\sigma^2\cos^2\gamma_1\right)I_{s1}^2 \tag{3.25}$$

where γ_1, γ and I_{s1}, I_s are the current angles and stator currents at (T_1,Ω_N) and (T,Ω).

We can treat (T_1,Ω_N) as an operating point in the constant-torque region, where the current angle is defined by Eq. (3.16), that is:

$$\gamma_1=\arctan\left(\frac{T_N}{T_1}\tan\gamma_N\right)\approx\arctan\frac{T_N}{T_1} \tag{3.26}$$

Hence Eq. (3.25) can be rewrite as:

$$K^2\left(\sin^2\gamma+\sigma^2\cos^2\gamma\right)I_s^2=\frac{T_N^2+\sigma^2T_1^2}{T_1^2+T_N^2}I_{s1}^2 \tag{3.27}$$

If ignore the losses, so $I_s\approx I_{s1}$. By solving Eq. (3.27), the current angle in the constant-power region is:

$$\gamma=arc\cos\sqrt{\frac{K^2\left(T_N^2+T_1^2\right)-\left(T_N^2+\sigma^2T_1^2\right)}{K^2\left(1-\sigma^2\right)\left(T_N^2+T_1^2\right)}} \tag{3.28}$$

Since the points (T_1,Ω_N) and (T,Ω) have the same powers, $T_1=KT$, so Eq. (3.28) is rewritten as:

$$\gamma=arc\cos\sqrt{\frac{K^2\left(T_N^2+KT^2\right)-\left(T_N^2+\sigma^2K^2T^2\right)}{K^2\left(1-\sigma^2\right)\left(T_N^2+K^2T^2\right)}} \tag{3.29}$$

In the constant-power region, due to the flux-weakening effect, the rotor flux is no longer a constant. It turns into a function of current angle (Eq. (3.13)). Substituting the rated point (T_N,Ω_N) and any point (T,Ω) in the constant-power area into the Eq. (3.11)$\sim$ Eq. (3.13), the slip ratio in the constant-power region is obtained:

$$s=\frac{\Omega_N s_N\sin\gamma_N\cos\gamma}{\Omega_N s_N\sin\gamma_N\cos\gamma+\Omega(1-s_N)\sin\gamma\cos\gamma_N} \tag{3.30}$$

In addition, one can deduce the power factor at point (T,Ω). If the losses are ignored, the input and output powers at point (T,Ω) have the same values:

$$P=n_p\Omega\frac{L_m^2}{L_r}i_{sd}i_{sq}=\sqrt{u_{sd}^2+u_{sq}^2}I\cos\varphi \tag{3.31}$$

Combining Eq. (3.21) and Eq. (3.20), Eq. (3.31) can be reformed as:

$$(1-\sigma)\sin\gamma\cos\gamma = \sqrt{\sigma^2\cos^2\gamma + \sin^2\gamma}\cos\varphi \tag{3.32}$$

Therefore, the power factor is expressed as:

$$\varphi = \arccos\left(\frac{(1-\sigma)\sin\gamma\cos\gamma}{\sqrt{\sigma^2\cos^2\gamma + \sin^2\gamma}}\right) \tag{3.33}$$

3.3.2 Rated losses calculation

In this chapter, rated loss will be derived from the loss at the peak-efficiency point. Then the loss in different sub-regions will be deduced based on the rated loss. The above part deduces the current angle and slip ratio of an IM in different regions in a function of torque and speed, which makes it possible to derive the loss in different sub-regions. The calculation of the rated loss from the loss at the peak efficiency point is performed below.

An IM has large rotor copper losses and low efficiencies below the base speed. As the speed increases, the rotor copper losses decrease rapidly, so that the high-efficiency area of an IM is located above the base speed, near the rated torque point. To calculate the losses at the peak-efficiency point, we assume that its position is known, i.e., the peak-efficiency appears at point $(T_{\eta m}, \Omega_{\eta m})$, where:

$$\begin{cases} T_{\eta m} = \beta T_N \\ \Omega_{\eta m} = \dfrac{1}{2}(\Omega_N + \Omega_{max}) \end{cases} \tag{3.34}$$

According to hypothesis (5), an IM has the same variable and invariable losses at the peak-efficiency point, i.e., the copper loss equals the sum of iron loss and mechanical loss:

$$p_{copper\_s(m)} + p_{copper\_r(m)} \approx p_{iron(m)} + p_{mec(m)} \tag{3.35}$$

where $_{(m)}$ is the subscript for peak-efficiency point.

Substituting point $(T_{\eta m}, \Omega_{\eta m})$ into Eq. (3.2)$\sim$ Eq. (3.4), the mechanical power, mechanical loss and stray loss at the peak efficiency point are obtained. Then combining with Eq. (3.35) and Eq. (3.1), the copper loss and iron loss at the peak-efficiency point are obtained:

$$p_{copper\_tot(m)} = \frac{1}{2}\left[T_{\eta m}\Omega_{\eta m}\left(\frac{1}{\eta_{\max}} - 1\right) - p_{stray(m)}\right] \tag{3.36}$$

$$p_{iron(m)} = p_{copper(m)} - p_{mec(m)} \tag{3.37}$$

$$p_{copper\_s(m)} = p_{copper(m)} - p_{copper\_r(m)} \tag{3.38}$$

where the rotor copper loss $p_{copper\_r(m)}$ is calculated by substituting point $(T_{\eta m}, \Omega_{\eta m})$ into Eq. (3.8) and Eq. (3.30).

Rated losses are the cores of the efficiency map estimation in this thesis. Since all the losses in the 'torque-speed' plane will be calculated based on them. According to the previous assumption, the rated hysteresis and eddy-current losses are equal, namely:

$$\begin{cases} p_{iron(m)} = p_{hy(m)} + p_{eddy(m)} \\ p_{iron(N)} = p_{hy(N)} + p_{eddy(N)} \\ p_{hy(N)} = p_{eddy(N)} \end{cases} \tag{3.39}$$

Additionally, the peak-efficiency point and the rated point are both in the constant-power region, where the product of frequency and flux is approximately a constant. Hence the hysteresis and eddy-current losses of both points have the following relationship approximatively [Hall.E 2001]:

$$\begin{cases} p_{hy(m)} = \left(\dfrac{\Omega_{\eta m}}{\Omega_N}\right)^{0.6} p_{hy(N)} \\ p_{eddy(m)} = p_{eddy(N)} \end{cases} \tag{3.40}$$

By solving Eq. (3.39) and Eq. (3.40), the rated hysteresis and eddy-current losses can be derived:

$$p_{hy(N)} = p_{eddy(N)} = \frac{\Omega_N^{0.6}}{\Omega_N^{0.6} + \Omega_{\eta m}^{0.6}} p_{iron(m)} \tag{3.41}$$

Cooper loss of an IM is composed of stator copper loss and rotor copper loss. Its rated rotor copper loss can be calculated by substituting point (T_N, Ω_N) and the rated slip ratio s_N into Eq. (3.8). Nevertheless, the calculation of stator copper loss is more complex. The peak efficiency point m and the rated point N have the different current angle, meanwhile, the torque of N is higher than that of the point m. So in order to establish the loss proportion function between the rated and peak-efficiency point, the calculation of rated stator copper loss is carried out in 2 steps (Fig. 3.4): $m \rightarrow a \rightarrow N$. That is, firstly calculate the stator copper loss at the turning point a and then deduce the rated stator copper loss at N.

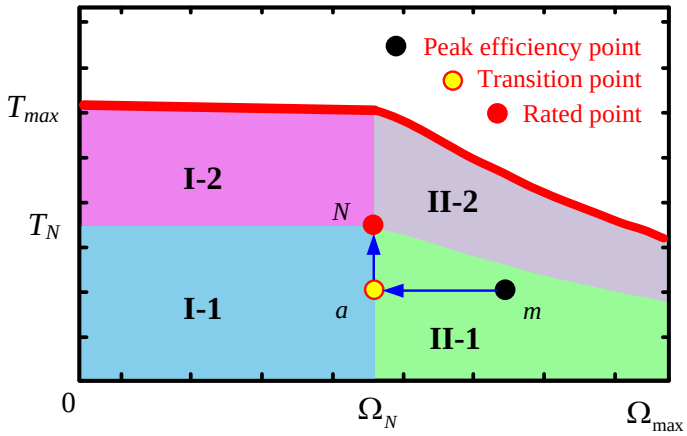

Figure. 3.4. Calculation routing of rated stator copper loss for IMs

Point m and a are both in the continuous working area. While a is located at the junction of the constant-torque and constant-power regions, and m is located in the

constant-power region. Thus, point m and a have different d axis currents. By reorganizing Eq. (3.11), we have:

$$I_s^2 = \frac{L_r}{pL_m^2}\frac{T}{\sin\gamma\cos\gamma} \tag{3.42}$$

Applying Eq. (3.42) to points m and a, the stator copper loss at a can be deduced:

$$p_{copper\_s(a)} = \frac{I_a^2}{I_m^2}p_{copper\_s(m)} = \frac{\sin\gamma_m\cos\gamma_m}{\sin\gamma_a\cos\gamma_a}p_{copper\_s(m)} \tag{3.43}$$

In the same way, N and a are all in the constant-torque region. According to Eq. (3.18), we can establish the folowing relationship:

$$p_{copper\_s(N)} = \frac{T_N^2\left(1+\tan^2\gamma_N\right)}{T_a^2\left(1+\tan^2\gamma_a\right)}p_{copper\_s(a)} \tag{3.44}$$

Therefore, with Eq. (3.43) and Eq. (3.44), the rated stator copper loss is calculated from the stator copper loss at the peak-efficiency point, as shown below:

$$p_{copper\_s(N)} = \frac{T_N^2\left(1+\tan^2\gamma_N\right)}{T_a^2\left(1+\tan^2\gamma_a\right)}\frac{\sin\gamma_m\cos\gamma_m}{\sin\gamma_a\cos\gamma_a}p_{copper\_s(m)} \tag{3.45}$$

So far, all the rated losses of the IM have been calculated.

3.3.3 Loss map calculation for IMs

According to Fig. 3.1, the 'torque-speed' plane is divided into 4 sub-regions: I-1, I-2, II-1 and II-2. The losses calculation will be carried out in each sub-region based on the rated losses.

3.3.3.1 Loss in constant-torque reagin

In the constant-torque region, the flux is a constant. Then according to Eq. (3.7), the hysteresis loss is proportional to the speed, the eddy-current loss is in proportion to the square of the speed. Thereby, the iron loss in the constant-torque region can be expressed as:

$$\begin{cases} p_{hy(i,j)} = \left(\dfrac{\Omega_{(i,j)}}{\Omega_N}\right)p_{hy(N)} \\ p_{eddy(i,j)} = \left(\dfrac{\Omega_{(i,j)}}{\Omega_N}\right)^2 p_{eddy(N)} \end{cases} \tag{3.46}$$

The stator current in d axis is a constant in the constant-torque region. In region I-1, the core is not saturated, thus the torque is proportional to the stator current in q axis. The stator copper loss in I-1 is given by:

$$p_{copper\_s(i,j)} = \frac{T_{(i,j)}^2 + T_N^2\tan^2\gamma_N}{T_N^2 + T_N^2\tan^2\gamma_N}p_{copper\_s(N)} \tag{3.47}$$

In I-2, due to the overload effects, the core saturation leads to the reduction of inductance. Hence more current is required to generate the same torque, so that the stator copper loss is increased [Peng.H 2011]. Therefore, the stator copper loss in region I-2 can be corrected as:

$$p_{copper\_s(i,j)} = \left[\frac{T_{(i,j)}^2 + T_N^2 \tan^2\gamma_N}{T_N^2 + T_N^2 \tan^2\gamma_N} + \alpha_1 \left(\frac{T_{(i,j)}}{T_N} - 1 \right)^2 \right] p_{copper\_s(N)} \tag{3.48}$$

where α_1 is the correction factor for stator copper loss in region I-2.

3.3.3.2 Loss in constant-power reagin

In the constant-power region, the flux is weakened, while the production of flux and frequency is approximately a constant. Therefore, the iron loss in the constant-power region can be expressed as:

$$\begin{cases} p_{hy(i,j)} = \left(\dfrac{\Omega_{(i,j)}}{\Omega_N} \right)^{0.6} p_{hy(N)} \\ p_{eddy(i,j)} = p_{eddy(N)} \end{cases} \tag{3.49}$$

Similarly, the stator copper losses in the regions II-1 and II-2 need to be calculated separately due to the overload effect. The stator copper loss in II-1 is:

$$p_{copper\_s(i,j)} = \frac{T_{(i,j)}}{T_N} \frac{\sin\gamma_N \cos\gamma_N}{\sin\gamma\cos\gamma} p_{copper\_s(N)} \tag{3.50}$$

The stator copper loss in II-2 is:

$$p_{copper\_s(i,j)} = \left(\frac{T_{(i,j)}}{T_N} \frac{\sin\gamma_N \cos\gamma_N}{\sin\gamma\cos\gamma} + \alpha_2 \left(\frac{T_{(i,j)}}{T_{c(i,j)}} - 1 \right)^2 \right) p_{copper\_s(N)} \tag{3.51}$$

where α_2 is the correction factor for stator loss in II-2, and $T_{c(i,j)}$ is the torque at $\Omega_{(i,j)}$ with rated power:

$$T_{c(i,j)} = \frac{T_N \Omega_N}{\Omega_{(i,j)}} \tag{3.52}$$

3.4 PM-SM efficiency map estimation

The rotor of a PM-SM is excited by PMs, hence there is no copper loss in the rotor. A PM-SM can adopt a control strategy of $i_d = 0$ in the constant-torque region to reduce losses. So that the stator copper loss is proportional to the square of the torque. Compared with the IM, only current angle is needed to be considered to establish the loss proportion function.

3.4.1 Current angle calculation

In order to derive the current angle of a PM-SM in its constant-power region, we could start from its dq model. Assuming that the 3-phase windings and currents are symmetrical, and core loss and saturation are ignored, the voltage equation of the PM-SM can be expressed as:

$$\begin{cases} u_{sd} = -n_p \Omega L_q i_{sq} + p\psi_{sd} + R_s i_{sd} \\ u_{sq} = n_p \Omega L_d i_{sd} + n_p \Omega \psi_f + p\psi_{sq} + R_s i_{sq} \end{cases} \tag{3.53}$$

with:

$$\begin{cases} u_{sd} = -U \sin \alpha \\ u_{sq} = U \cos \alpha \end{cases} \tag{3.54}$$

where $\underline{u}_{sdq}$ are the stator voltages, $\underline{i}_{sdq}$ are the stator currents in dq frame, n_p is the number of pole pairs, $\underline{L}_{dq}$ are the stator inductances, ψ_f is the flux imposed by PM, R_s is the stator resistance per phase, and α is the voltage angle.

In steady state, if the winding voltage drop is ignored, then Eq. (3.55) can be simplified as:

$$\begin{cases} u_{sd} \approx -n_p \Omega L_q i_{sq} \\ u_{sq} \approx n_p \Omega L_d i_{sd} + n_p \Omega \psi_f \end{cases} \tag{3.55}$$

Suppose point (T, Ω) is in the constant-power region. When the losses are not considered, the electromagnetic and mechanical powers are approximately equal:

$$T\Omega = U I_s \cos \varphi \tag{3.56}$$

where φ is the angle for power factor.

The torque of a PM-SM can be expressed by the following equation in dq frame:

$$T = n_p \psi_f i_{sq} + n_p \left(L_d - L_q\right) i_{sd} i_{sq} \tag{3.57}$$

Similar to IMs, defining a speed ratio K:

$$K = \frac{\Omega}{\Omega_N} \tag{3.58}$$

Combined with Eq. (3.57) and Eq. (3.58), Eq. (3.56) can be rewritten as:

$$K \Omega_N n_p \left[\psi_f i_{sq} + \left(L_d - L_q\right) i_{sd} i_{sq}\right] = U I_s \cos \varphi \tag{3.59}$$

Let (T_1, Ω_N) and (T, Ω) are the 2 operating points in the constant-power region with the same powers. Since the supply voltage is saturated thus the stator winding voltages are equal at both points. Moveover, if ignore the losses, both points have the same stator current: $I_1 \approx I$, then we have the following relationship:

$$U = U_1 = \sqrt{u_{sd1}^2 + u_{sq1}^2} \approx n_p \Omega_N \sqrt{L_q^2 i_{sq1}^2 + \left(L_q i_{sd1} + \psi_f\right)^2} \tag{3.60}$$

$$\begin{cases} i_{sd1} = -I_s \sin\gamma_1 = 0 \\ i_{sq1} = I_s \cos\gamma_1 = I \\ i_{sd} = -I_s \sin\gamma \\ i_{sq} = I_s \cos\gamma \end{cases} \tag{3.61}$$

where U_1 and $\underline{u}_{sdq1}$ are the stator voltages at point (T_1, Ω_N). γ_1 and γ are the current angle at both point.

3.4.1.1 Current angle of an I-PM-SM

For an I-PM-SM, $L_q > L_d$. Substituting Eq. (3.61) and Eq. (3.60) into Eq. (3.59), we have:

$$\cos\gamma + (\rho - 1)\,\xi \cos\gamma \sin\gamma = \frac{1}{K}\sqrt{1 + \rho^2\xi^2}\cos\varphi \tag{3.62}$$

where $\rho = \frac{L_q}{L_d}$ is the salient coefficient, $\xi = \frac{I_s}{\psi_f}$ is the flux weakening coefficient.

According to Eq. (3.54) and Eq. (3.55), the flux weakening coefficient could be deduced:

$$\xi = \frac{K_\xi^2 - \sqrt{K_\xi^4 - \left(K_\xi^2 - \rho^2\right)\left(K_\xi^2 - 1\right)}}{\left(K_\xi^2 - \rho^2\right)} \tag{3.63}$$

where $K_\xi = \frac{\Omega_{max}}{\Omega_N}$is the speed expansion ratio.

Then with Eq. (3.54), Eq. (3.55) and Eq. (3.61), the following relationship between current angle and voltage angle is obtained:

$$\tan\alpha = \frac{\rho\xi\cos\gamma}{1 - \xi\sin\gamma} \tag{3.64}$$

The current angle γ, voltage angle α and the power factor angle φ of a PM-SM have the following relationship:

$$\alpha = \gamma - \varphi \tag{3.65}$$

Combining Eq. (3.62), Eq. (3.64) and Eq. (3.65), we have:

$$\sin^2\gamma + \frac{2}{(\rho^2 - 1)\,\xi}\sin\gamma + \frac{(1 + \rho^2\xi^2)}{K^2\xi^2\,(\rho^2 - 1)} - \frac{\rho^2\xi^2 + 1}{(\rho^2 - 1)\,\xi^2} = 0 \tag{3.66}$$

In turn, the current angle and power factor angle can be solved:

$$\gamma = \arcsin\left(\frac{\sqrt{K^2 - (1 - K^2)\,(1 + \rho^2\xi^2)\,(\rho^2 - 1)} - K}{K\xi\,(\rho^2 - 1)}\right) \tag{3.67}$$

$$\varphi = \arccos\left(\frac{K\,(\cos\gamma + (\rho - 1)\,\xi\cos\gamma\sin\gamma)}{\sqrt{1 + \rho^2\xi^2}}\right) \tag{3.68}$$

3.4.1.2 Current angle of an S-PM-SM

The above equations for current angle and power factor angle are applicable to the I-PM-SM, where $\rho > 1$. For the S-PM-SM, $L_d = L_q$, $\rho = 1$. The current angle cannot be calculated by Eq. (3.67). Nevertheless, Eq. (3.62) could be rewritten as:

$$\cos\gamma = \frac{1}{K}\sqrt{1+\xi^2}\cos\varphi \tag{3.69}$$

Solving Eq. (3.62), Eq. (3.65) and (3.69), the current angle and power factor angle of a S-PM-SM are derived:

$$\gamma = \arccos\left(\frac{\sqrt{1+\xi^2}}{2K\xi}\sqrt{4-\left(\frac{\sqrt{1+\xi^2}}{K}+\frac{(1-\xi^2)K}{\sqrt{1+\xi^2}}\right)^2}\right) \tag{3.70}$$

$$\varphi = \arccos\left(\frac{1}{2\xi}\sqrt{4-\left(\frac{\sqrt{1+\xi^2}}{K}+\frac{(1-\xi^2)K}{\sqrt{1+\xi^2}}\right)^2}\right) \tag{3.71}$$

3.4.2 Rated losses calculation

Rated losses are necessary for the estimation of efficiency map in the proposed method. The losses at peak-efficiency point are prerequisite to derive the rated losses. Due to different mounting methods of the PMs, I-PM-SM and S-PM-SM have different peak-efficiency locations. Generally, the peak efficiency of an I-PM-SM appears around the rated operating point. On the contrary, a S-PM-SM has a peak efficiency around the point with rated torque and peak power [Lukic.S 2003].

3.4.2.1 Loss at the peak efficiency point

To calculate the rated losses, we assume that the peak efficiency of the PM-SM appears at point $(T_{\eta m}, \Omega_{\eta m})$, where:

$$T_{\eta m} = \begin{cases} T_N & \text{(S-PM-SM)} \\ \beta T_N & \text{(I-PM-SM)} \end{cases} \tag{3.72}$$

$$\Omega_{\eta m} = \begin{cases} \dfrac{T_{max}}{T_N}\Omega_N & \text{(S-PM-SM)} \\ \Omega_N & \text{(I-PM-SM)} \end{cases} \tag{3.73}$$

Substituting Eq. (3.72) and (3.73) into Eq. (3.36)$\sim$ (3.38), the losses at peak efficiency point are obtained:

$$p_{copper\_tot(m)} = \begin{cases} \dfrac{1}{2}\left[T_{max}\Omega_N\left(\dfrac{1}{\eta_{\max}}-1\right)-p_{stray(m)}\right] & \text{(S-PM-SM)} \\ \dfrac{1}{2}\left[\beta T_N\Omega_N\left(\dfrac{1}{\eta_{\max}}-1\right)-p_{stray(m)}\right] & \text{(I-PM-SM)} \end{cases} \tag{3.74}$$

$$p_{iron(m)} = p_{copper(m)} - p_{mec(m)} \tag{3.75}$$

$$p_{copper\_s(m)} = p_{copper\_tot(m)} \tag{3.76}$$

Similarly, Eq. (3.72) and (3.73) are substituted into Eq. (3.41) to obtain the rated iron loss:

$$p_{hy(N)} = p_{eddy(N)} = \begin{cases} \dfrac{T_N^{0.6}}{T_N^{0.6} + T_{max}^{0.6}} p_{iron(m)} & \text{(S-PM-SM)} \\ \dfrac{1}{2} p_{iron(m)} & \text{(I-PM-SM)} \end{cases} \tag{3.77}$$

3.4.2.2 Rated loss

Similar to IMs, the calculation of the rated copper loss of a PM-SM also needs to be done in several steps, as shown in Fig. 3.5, since m is overloaded with the different current angle with N. According to the assumptions, the peak efficiency point of a S-PM-SM appears in the constant-power and overloaded region (II-2). The path of rated stator copper loss calculation for a S-PM-SM is: $m \rightarrow b \rightarrow a \rightarrow N$.

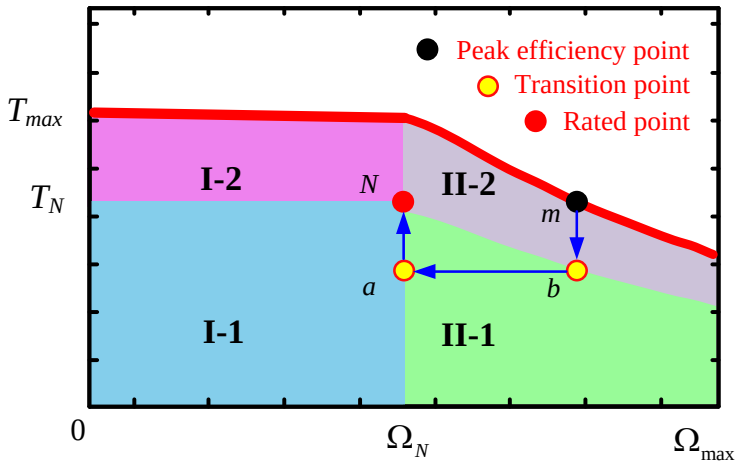

Figure. 3.5. Calculation path of rated stator copper losses for I-PM-SMs

Point m and b are both in the constant-power region. Point m is overloaded and b is at the boundary of overload and continues working region. By introducing a factor α to correct the overload effect, the stator copper losses at m and b have the following relationship:

$$\frac{p_{copper\_s(m)}}{p_{copper\_s(b)}} = \frac{i_{qm}^2 \left(1 + \tan^2 \gamma_m\right)}{i_{qb}^2 \left(1 + \tan^2 \gamma_b\right)} + \alpha \left(\frac{T_{\eta m}}{T_b} - 1\right)^2 \tag{3.78}$$

with:

$$T_b = \frac{P_N}{\Omega_{\eta m}} = \frac{T_N \Omega_N}{\Omega_{\eta m}} = \frac{T_N^2}{T_{max}} \tag{3.79}$$

where i_{qm} and i_{qb} are currents at both points, γ_m and γ_b are the current angles, T_b is the torque at b.

Since m and b have the same speeds and the same flux weakening current, thus the current in q axis of the 2 points are proportional to the torque. So we have:

$$p_{copper\_s(b)} = \left[\frac{T_{max}^2\left(1+\tan^2\gamma_m\right)}{T_N^2\left(1+\tan^2\gamma_b\right)} + \alpha\left(\frac{T_{max}}{T_N}-1\right)^2\right]^{-1} p_{copper\_s(m)} \tag{3.80}$$

In the same way, the loss relationships between point a and b can be expressed by:

$$\frac{p_{copper\_s(a)}}{p_{copper\_s(b)}} = \frac{I_{sa}^2}{I_{qb}^2\left(1+\tan^2\gamma_b\right)} = \frac{T_a^2}{T_b^2\left(1+\tan^2\gamma_b\right)} = \frac{1}{1+\tan^2\gamma_b} \tag{3.81}$$

Hence,

$$p_{copper\_s(a)} = \frac{1}{1+\tan^2\gamma_b} p_{copper\_s(b)} \tag{3.82}$$

Finally, the loss relationships of between N and a can be expressed by:

$$p_{copper\_s(N)} = \frac{T_N^2}{T_a^2} p_{copper\_s(a)} = \frac{T_{max}^2}{T_N^2} p_{copper\_s(a)} \tag{3.83}$$

Therefore, with Eq. 3.80 to Eq. 3.83, the rated stator copper loss is calculated from the stator copper loss at the peak-efficiency point, as shown below:

$$p_{copper\_s(N)} = \frac{T_{max}^2}{T_N^2}\frac{1}{1+\tan^2\gamma_b}\left[\frac{T_{max}^2\left(1+\tan^2\gamma_m\right)}{T_N^2\left(1+\tan^2\gamma_b\right)} + \alpha\left(\frac{T_{max}}{T_N}-1\right)^2\right]^{-1} p_{copper\_s(m)} \tag{3.84}$$

The I-PM-SM has the same speed for peak-efficiency and rated points, thus its rated copper loss is deduced in one step: $a \to N$, as shown in Fig. 3.6.

$$p_{copper\_s(N)} = \frac{T_N^2}{T_{\eta m}^2} p_{copper\_s(m)} = \frac{1}{\beta^2} p_{copper\_s(m)} \tag{3.85}$$

3.4.3 Loss map calculation for PM-SMs

In the same way as IM, when the rated loss is calculated, the losses in different sub-regions of a PM-SM can also be calculated.

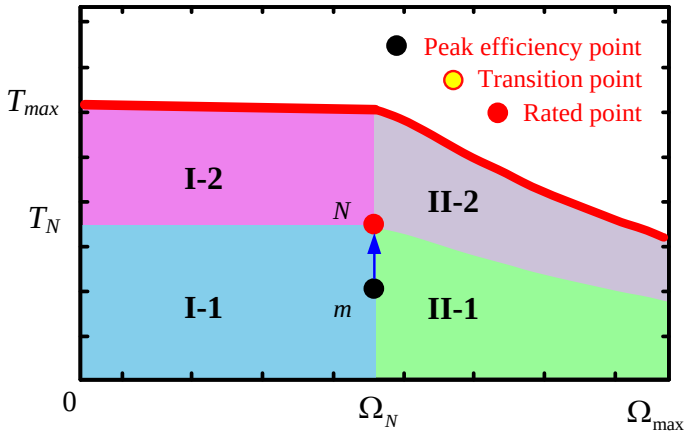

Figure. 3.6. Calculation path of rated stator copper losses for I-PM-SMs

3.4.3.1 Loss calculation in constant-torque area

The iron loss of a PM-SM in the constant-torque region is given by:

$$\begin{cases} p_{hy(i,j)} = \left(\dfrac{\Omega_{(i,j)}}{\Omega_N}\right) p_{hy(N)} \\ p_{eddy(i,j)} = \left(\dfrac{\Omega_{(i,j)}}{\Omega_N}\right)^2 p_{eddy(N)} \end{cases} \tag{3.86}$$

In I-1, the stator copper loss for a PM-SM is given by:

$$p_{copper\_s(i,j)} = \left(\frac{T_{(i,j)}}{T_N}\right)^2 p_{copper\_s(N)} \tag{3.87}$$

In I-2, the stator copper loss for a PM-SM can be modified as:

$$p_{copper\_s(i,j)} = \left[\left(\frac{T_{(i,j)}}{T_N}\right)^2 + \alpha\left(\frac{T_{(i,j)}}{T_N} - 1\right)^2\right] p_{copper\_s(N)} \tag{3.88}$$

3.4.3.2 Loss calculation in constant-torque area

The iron loss of a PM-SM in the constant-power region is given by:

$$\begin{cases} p_{hy(i,j)} = \left(\dfrac{\Omega_{(i,j)}}{\Omega_N}\right)^{0.6} p_{hy(N)} \\ p_{eddy(i,j)} = p_{eddy(N)} \end{cases} \tag{3.89}$$

In II-1, the stator copper loss for a S-PM-SM is expressed by:

$$p_{copper\_s(i,j)} = \left(\frac{T_{(i,j)}}{T_N}\right)^2 \left(1 + \tan^2\gamma\right) p_{copper\_s(N)} \tag{3.90}$$

In II-1, the stator copper loss for a I-PM-SM is calculated by:

$$p_{copper\_s(i,j)} = \left(\frac{T_{(i,j)}}{T_N}\right)^2 \frac{1}{\left(\cos\gamma + (\rho-1)\,\xi\cos\gamma\sin\gamma\right)^2} p_{copper\_s(N)} \tag{3.91}$$

In II-2, the stator copper loss for a S-PM-SM is deduced by:

$$p_{copper\_s(i,j)} = \left[\left(\frac{T_{(i,j)}}{T_N}\right)^2 \left(1+\tan^2\gamma\right) + \alpha\left(\frac{T_{(i,j)}}{T_{c(i,j)}} - 1\right)^2\right] p_{copper\_s(N)} \tag{3.92}$$

In II-2, the stator copper loss for a I-PM-SM is derived by:

$$p_{copper\_s(i,j)} = \left[\left(\frac{T_{(i,j)}}{T_N}\right)^2 \frac{1}{\left(\cos\gamma + (\rho-1)\,\xi\cos\gamma\sin\gamma\right)^2} + \alpha\left(\frac{T_{(i,j)}}{T_{c(i,j)}} - 1\right)^2\right] p_{copper\_s(N)} \tag{3.93}$$

3.5 Validation of the efficiency map estimation methods

In the above sections, the efficiency maps of IM, S-PM-SM and I-PM-SM can be deduced. This method does not require EM pre-design and does not depend on EM parameters such as inductances and resistances, only 4 basic design specifications are used. That is, the rated torque, rated speed, maximal torque and maximal speed. Meanwhile, the flux-weakening and overload effects are also considered.

3.5.1 Experimental test of EM efficiency maps

In order to validate the feasibility of the proposed method, we take 3 AC prototypes from HIT (Harbin Institute of Technology). Their efficiency maps, which are measured by experiment will be used for comparisons.The specifications of the prototypes are shown in Table. 3.1, where the peak efficiency comes from the experimental test. Fig. 3.7 shows the diagram of the experimental setup for efficiency map test, where the tested EM and the load EM are connected by sharing the same shaft. A torque and speed sensor is installed between both shafts.

Table. 3.1. Parameters of the EMs

	Rated speed Ω_N(rad/s)	Rated torque T_N(Nm)	Peak speed Ω_{max}(rad/s)	Peak torque T_{max}(Nm)	Peak efficiency η_{max}(%)
IM	120	600	450	1200	90.5
S-PM-SM	300	50	400	90	96.5
I-PM-SM	400	20	600	40	96.5

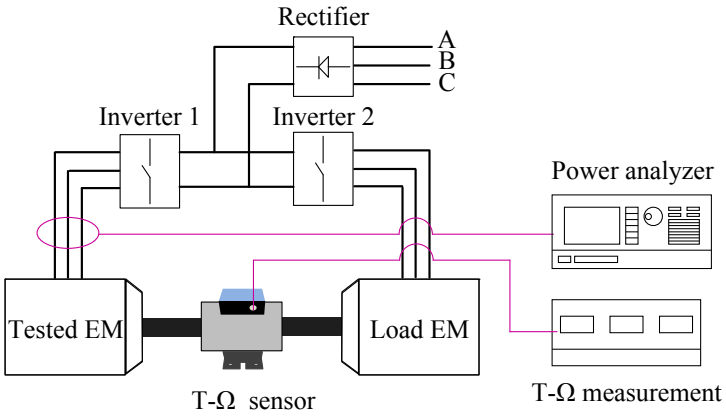

Figure. 3.7. Diagram of the experimental setup for efficiency map test

In this experiment, the tested efficiency only considers the efficiency of the EM. That is, the electrical power is calculated through the power analyzer by measuring the 3-phase AC voltages and currents. The mechanical power is calculated by the torque-speed measurement. For torque-speed sensor (JN338), the error of speed and torque measuring are $< 0.2\%$ and $< 0.5\%$. For power analyzer (TW1800), the error for power measuring is $< 0.1\%$. Meanwhile, the efficiency maps of the 3 EMs can also be calculated by the proposed method.

The specifications in Table. 3.1 defines the complete 'torque-speed' planes of the 3 EMs. It is possible to obtain their efficiency maps by the proposed method only with these specifications. The 'speed-torque' planes of the EMs are decomposed into a network with $m_s \times n_s$ nodes, where the efficiency of each node is calculated with the proposed method, then a complete efficiency map could be formed.

3.5.2 Errors of the estimated efficiency maps

Fig. 3.8∼ Fig. 3.10 illustrate the comparisons between the estimated and experimental maps. Limited by the experimental conditions, the loss maps of the prototypes cannot be measured, such as copper loss map, iron loss map, etc. To analyze the estimation errors, we define the absolute error e_{abs} and relative error e_{re}:

$$e_{abs(i,j)} = \eta_{eva(i,j)} - \eta_{exp(i,j)} \tag{3.94}$$

$$e_{re(i,j)} = \frac{\left|\eta_{exp(i,j)} - \eta_{eva(i,j)}\right|}{\eta_{exp(i,j)}} \times 100 \tag{3.95}$$

where η_{exp} and η_{eva} are experimental and calculated efficiencies respectively.

For the IM, the location of the high-efficiency area of the estimated efficiency map is basically consistent with the one of the experimental efficiency map, and the absolute error in the high-efficiency area is less than 5%. The maximum absolute error in Fig. 3.8(c) is about 20%, which is only located in the area where the speed

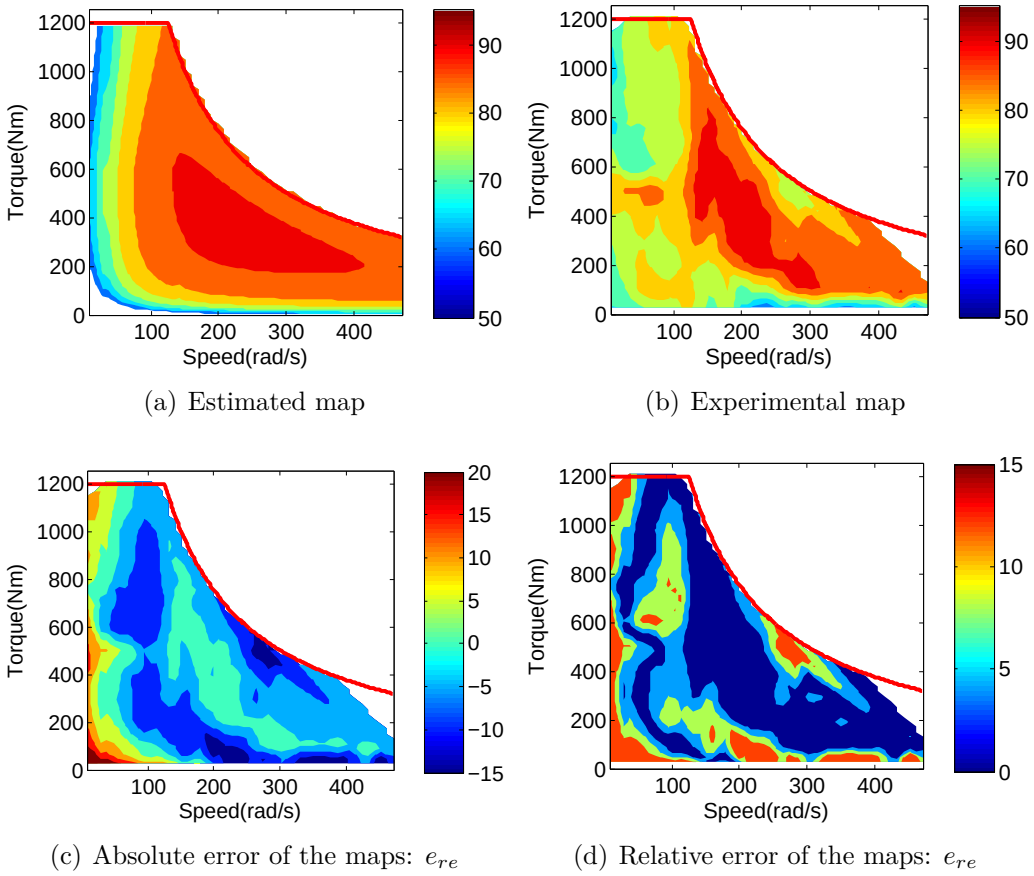

(a) Estimated map

(b) Experimental map

(c) Absolute error of the maps: e_{re}

(d) Relative error of the maps: e_{re}

Figure. 3.8. Validation of efficiency estimation method for IM

is lower than 100 rad/s, and the torque is lower than 100 Nm. When the speed increases, the iron loss is gradually increased, while the copper loss is decreased, and the absolute error is reducing. It can be seen from Fig. 3.8(d) that most of the operating points have the relative errors lower than 5%, and the operating points with larger relative errors are only scattered in the low-speed and low-torque region. Actually, copper loss dominate in an IM at low speed, so the errors in the low-speed area are mainly caused by copper losses. The error of copper loss could be derived from the calculation of current angle and slip ratio. In this thesis, the current angle and slip ratio are expressed as a function of torque and speed. However, in the real IM, the current angle and slip ratio are more complicated.

As for the S-PM-SM, the estimated efficiency map has the similar efficiency distribution trend as the experimental efficiency map, especially for the location of high-efficiency area. They are all distributed near the rated torque with peak power, which is consistent with the assumption. Similar to the IM, the maximum absolute error of the estimated map is about 20%, these points are only distributed in the area with low speed and low torque. As the speed increases, the absolute error is gradually decreasing, and the overall absolute error is less than 5%. Generally, the relative error of the S-PM-SM is less than 3%, and some areas is 5% to 10%. The area with small relative error corresponds to the high-efficiency area, which indicates

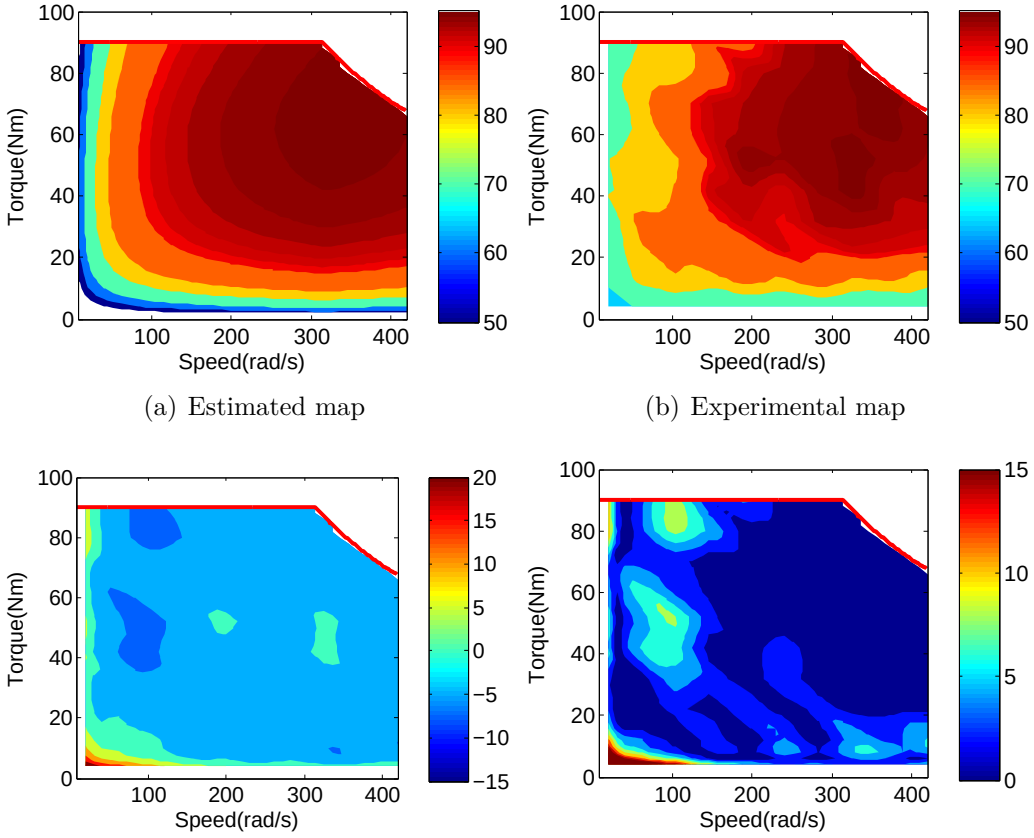

(a) Estimated map

(b) Experimental map

(c) Absolute error of the maps: e_{re}

(d) Relative error of the maps: e_{re}

Figure. 3.9. Validation of efficiency estimation method for S-PM-SM

good calculation accuracy of the proposed method in this area.

As for the I-PM-SM, the high-efficiency area of the estimated efficiency map is located near the rated operating point, which is consistent with the one of the experimental efficiency map. Regarding to the absolute error, it can be seen that the area where the absolute error is less than 2% corresponds to the high-efficiency area. It indicates that the proposed efficiency estimation method well describes the loss relationship in this area. Although the absolute error in the low-speed and low-torque area could reach up to 30%, these areas are very small. As for the relative error, the I-PM-SM has larger errors in the low-speed area or the area with high speed and high power. The maximum relative error is about 10%, but most operating points have the error less than 3%.

Table. 3.2 indicates the calculation time for the efficiency maps (processor: Intel (R) Core (TM) i7-4510U CPU@2.00 GHz 2.6 GHz). It can be seen that the proposed method is very efficient in terms of calculation time. The 3 maps are composed by the grids with 2000 to 3000 nodes, the total computation time is within 0.2 s, and the average computation time for each node is lower than 0.1 ms. The exemption of EM design and the fast calculation makes it feasible for MCM sizing. The calculation for the IM takes a longer time, because the IM also needs to calculate the rotor

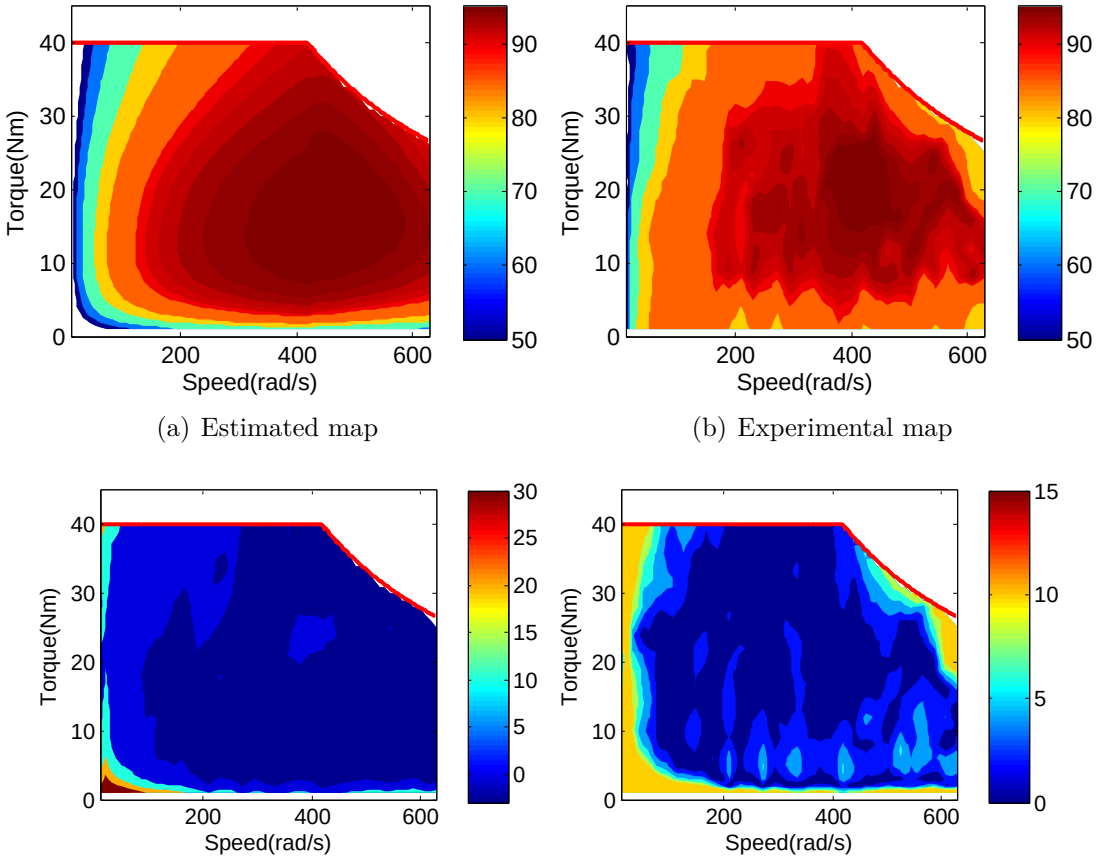

(a) Estimated map

(b) Experimental map

(c) Absolute error of the maps: e_{re}

(d) Relative error of the maps: e_{re}

Figure. 3.10. Validation of efficiency estimation method for I-PM-SM

copper loss, and the calculation of the slip rate increases the calculation time.

Table. 3.2. Calculation time of the estimation method

Parameters	IM	S-PM-SM	I-PM-SM
Number of nodes: $m_s \times n_s$	50× 60	60× 40	40 × 45
Total computation time (s)	0.19	0.024	0.020
Computation time for each node (ms)	0.063	0.010	0.013

3.5.3 Errors of vehicle energy consumption with the estimated efficiency maps

Fig. 3.8∼ Fig. 3.10 shows the accuracy of the efficiency maps from the point of view of the efficiency maps themselves. Nevertheless, unlike EMs for industry, due to the uncertainty of the driving, the traction EM of a vehicle generally works in a wide range of torque and speed. Therefore, only analysing the accuracy of the efficiency maps is not enough. It is also necessary to compare and analyze the errors of energy

consumption of the vehicle with the estimated and experimental efficiency maps under different driving cycles.

In chapter 2, the model and control of a MCM-based vehicle is established with Energetic Macroscopic Representation (EMR). It lays a foundation for the analysis of energy consumption in this chapter. Therefore, a pure EV is taken as an example to analyze the impact of different efficiency maps on vehicle energy consumption. Fig. 3.11 shows the model of a pure EV which is driven by an IM or a PM-SM. Applying the estimated and experimental efficiency maps to the EM models respectively, the energy consumptions of the vehicle with 2 maps are then obtained. The relative error e_E of energy consumption will be calculated:

$$e_E = \frac{|E_{exp} - E_{eva}|}{E_{exp}} \times 100 \tag{3.96}$$

where E_{exp} and E_{eva} are the energy consumptions with the experimental and estimated maps.

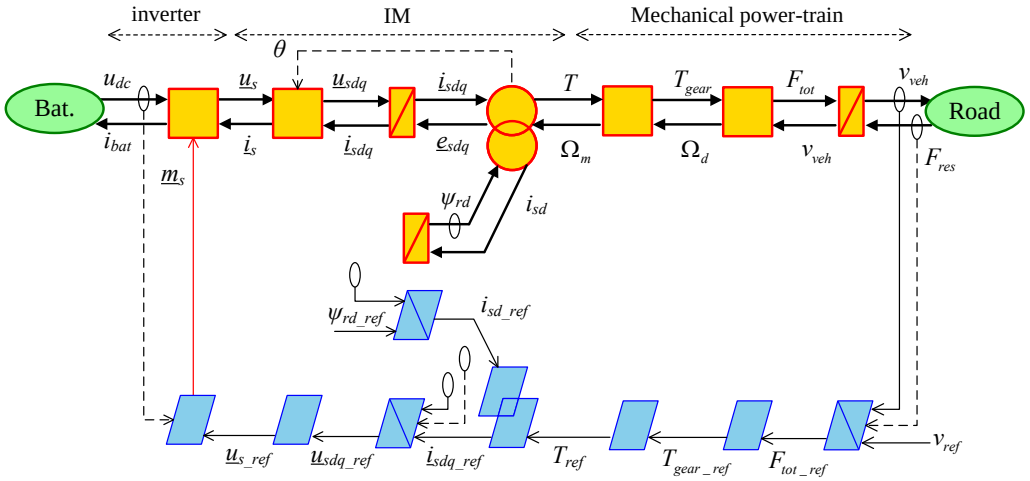

(a) EV model based on IM

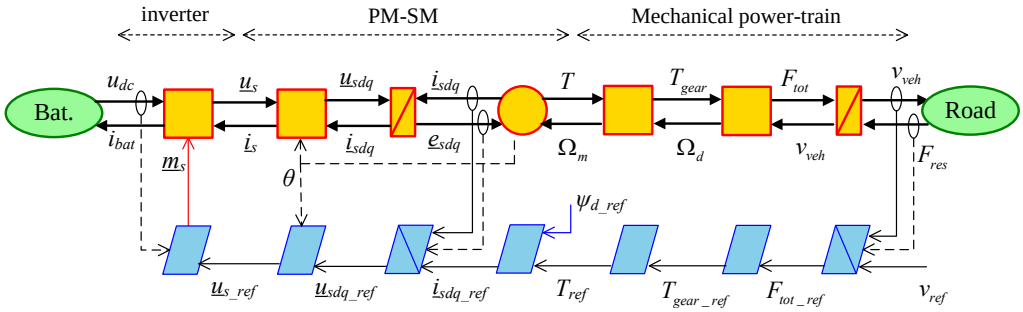

(b) EV model based on PM-SM

Figure. 3.11. EMR and control of a pure EV

Taking NEDC (New European Driving Cycle), UDDS (Urban Dynamometer Driving Schedule), HWFET (High-Way Fuel Economy Test) and J-1015 as examples, the errors of energy consumption are shown in Table. 3.3. It can be seen that in terms

of energy consumption of the vehicle, the estimated efficiency map is close to that of the experimental map, and the maximum relative error of energy consumption is 3.11%. With regard to the efficiency maps themselves, the relative error sometimes can reach 10%. Fortunately the EM works in a wide range and does not always at a certain operating point. In this way, the errors of the operating points are canceled sometimes, which leads to lower errors of energy consumption. As described before, the estimated and experimental efficiency maps have larger errors in the low-speed region, thus thee maximum error in the table appears in UDDS. Because the vehicles frequently start and stop under UDDS, and more operating points of the EM fall in the low-speed region.

Table. 3.3. Errors of energy consumptions

$e_E(\%)$	NEDC	UDDS	HFWET	J-1015
IM	2.25	2.76	1.87	2.23
S-PM-SM	1.35	2.35	1.05	1.45
I-PM-SM	1.29	3.11	1.25	2.07

Table. A.3 summarizes the characteristics of different efficiency calculation methods. It can be seen that the efficiency map estimation method proposed in this chapter does not need to design the EM in advance, only 4 basic design specifications are needed to estimate the efficiency map. The proposed method is fast with acceptable accuracy and good portability. It satisfy the requirements of MCM sizing. Therefore, the method is dedicated for MCM sizing in chapter 4.

Table. 3.4. Comparisons of different methods for efficiency map calculation

	Prerequisite	Properties	Time
Experiment	1.EM manufacturing 2.Experimental setup	1.High accuracy 2.High cost 3.Long computing time	Hours
FE method	1.EM design 2.FE model	1.Good accuracy 2.Long computation time	Hours
Linear-scale	With a map by FE or experiment	1.Fast calculation 2.Parameters independent 3.Poor accuracy 4.Poor portability	Seconds
$k_{m,n}T^m\omega^n$	With a map by FE or experiment	1.Good accuracy 2.Parameters dependent 3.Need parameter fitting 4.Poor portability	Seconds
This method	With basic specifications (T_N, T_{max}, Ω_N, Ω_{max})	1.Fast calculation 2.Good accuracy 3.Parameters independent 3.Good portability	Seconds

3.6 Conclusion

This chapter studies the efficiency map estimation method for different EMs. The model and control in chapter 2 are the means to validate the accuracy of this method.

The main works in this chapter are the following.

(1) The keys of fast efficiency map estimation are analysed.

(2) The efficiency map estimation methods of IM and PM-SM are studied.

(3) The method is verified by comparison with the experimental efficiency maps.

The main conclusion and contributions are summarized.

(1) A novel fast efficiency map estimation method is proposed, which is adaptable to IM, S-PM-SM and I-PM-SM. This method does not need EM pre-design, and does not depend on the internal parameters of the EM. Only 4 basic design parameters are needed to estimate the efficiency map.

(2) The proposed efficiency map estimation methods have acceptable accuracy. The errors of energy consumption of the vehicle with the estimated and experimental efficiency maps are less than 3.2%. The calculation speed and accuracy of the proposed efficiency map estimation method satisfies the requirements of MCM sizing.

The estimated efficiency maps are dedicated for MCM sizing in chapter 4. Actually, the efficiency map of an EM is related to its structure, masteries and so on. The method in this chapter is only suitable to estimated the efficiency map of an EM when its design specifications have not been eventually determined and the EM has not been designed. Once the specifications are defined, the EM should be designed by FEM to have more accurate results.

Moreover, the thermal behavior and cooling of the machine is not considered when estimating its efficiency map. The estimation of EM efficiency map is used for MCM sizing in chapter 4, only a static data set is needed. So the estimated efficiency is in steady state, without considering the variation versus time (or in temperature). The notion of overload is associated to the operating period and the cooling of the EM, an overloaded operating will lead to a fast temperature rise, which will further influence the efficiency. Hence the variation of efficiency due to temperature rise in the overload area could be corrected based on this map, namely, a multi-dimensional data set including temperature. In that way, the EM must be designed analytically or by FE method.

4

MCM sizing based on multi-objective optimization

This chapter deals with the MCM sizing method. Firstly, a multi-objective-based sizing method is proposed to enlarge MCM high-efficiency area, increase MCM torque density, and reduce the usage amount of Permanent Magnet (PM). Then the optimal sizing results of different MCM topologies are obtained and analysed. Finally, the impacts of different sizings on vehicle energy consumption are compared and summarised.

Contents

4.1 Introduction 77
4.2 Descriptions of the sizing problem 77
4.3 MCM sizing method 79
4.4 Results of sizing 86
4.5 Impact of different sizings on vehicle energy consumption 94
4.6 Conclusion 100

4.1 Introduction

Sizing of an Electric Vehicle (EV) is a process of determining the design specifications of some key components according to the vehicle and its dynamical requirements. These specifications would be further used for component design and manufacturing in the future. Electric drive is the power source of EVs, and its parameters directly affect the performance of the whole vehicle. A single drive system consists of only one EM, and the EM power requirement is the same as the one of the entire electric drive, i.e., having the same 'torque-speed' plane. MCM is a system with multiple Electrical Machines (EMs). Each EM is part of the MCM system. A MCM has numerous power combinations that can satisfy the 'torque-speed' characteristics of the studied electric drive. There will be more degree of freedom for MCM sizing. In order to find the optimal sizing, it is necessary to introduce a cost function to optimize the EM design specification.

In chapter 3, the efficiency estimation method for different EMs is proposed, which is an important means to form the objective function for MCM sizing. Based on this, this chapter studies a MCM sizing method, which can improve system efficiency and torque density, reduce the usage amount of PM. The sizing results of different MCM topologies are obtained, and the impacts of different sizings on vehicle energy consumption are compared.

4.2 Descriptions of the sizing problem

4.2.1 Flowchart of sizing

MCM sizing is a multi-objective-based optimization process. The selection of objective function has a significant influence on the sizing results. One of the outstanding properties of a MCM is that its high-efficiency area could be expended through corresponding strategy. However, the combination of multiple EMs inevitably increases the size and weight of the ineffective part of the system (cover and house), hence lowering the system torque density. In addition, in order to reduce the cost and the dependence on rare-earth materials, it is necessary to use less Permanent Magnets (PM). After a comprehensive analysis of MCM characteristics, the selection of the sizing objective function follows the principle of 'raise the strengths and avoid the weaknesses'. That is, improving the MCM efficiency and torque density, and reducing the cost. This could be realised by expanding system high-efficiency area, reducing the system volume and the usage amount of PM.

MCM sizing aims to determine the specifications of each EM in the MCM, such as rated torque, rated speed, peak torque, peak speed. These specifications can be used for EM design and manufacturing in the next stages. MCM sizing is mainly divided into the following steps (Fig. 4.1). (1) Calculate the initial requirements of

the MCM. It determines the MCM 'torque-speed' plane according to the vehicle parameters and its dynamical requirements. This plane defines the minimum working area that the MCM must meet. (2) Initialize the MCM topology and the specifications of each EM, namely rated torque, rated speed, peak torque, peak speed. (3) Justify whether the initialized specifications satisfy constraints, such as power constraints, torque constraints, speed constraints, and other constraints. (4) Quickly estimate the EM efficiency map, volume and the PM volume according to the EM initialized specifications. (5) Calculate the MCM optimal efficiency map, construct and optimize the objective function, then obtain the optimal sizing result.

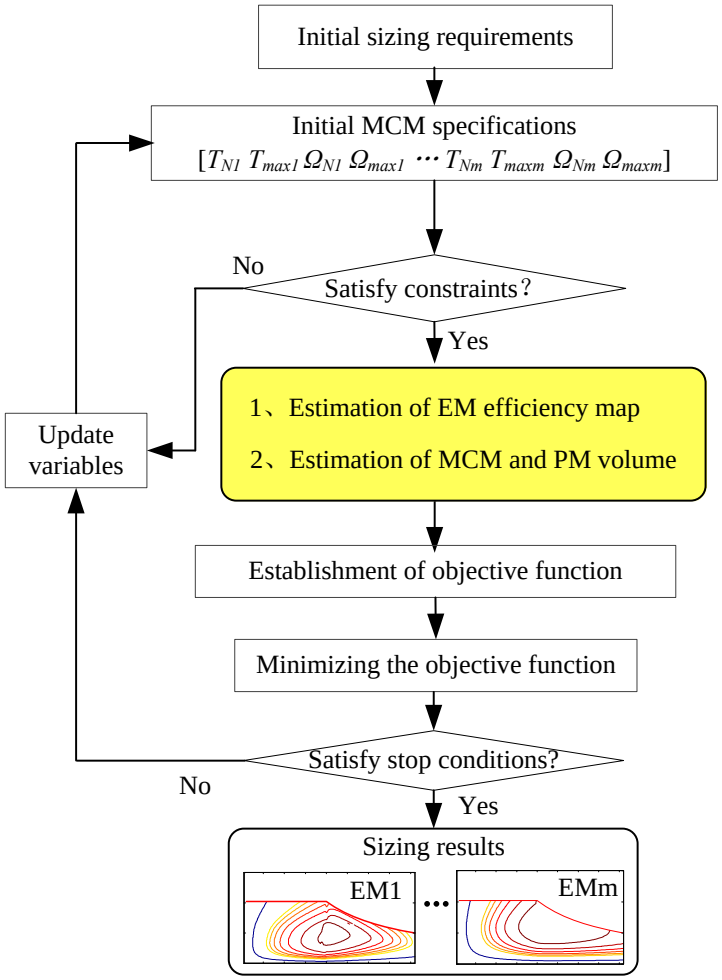

Figure. 4.1. Flowchart of sizing

4.2.2 Initial requirements of sizing

In this chapter, a pure EV (Table. 4.1) is taken as an example to study the MCM sizing. According to the sizing flowchart, the initial sizing requirements should be defined first, i.e., the demand 'torque-speed' characteristic of the traction system.

Table. 4.1. Parameters of the vehicle

Parameter	Value	Parameter	Value
Mass(kg)	1500	Final gear ratio	3.89
Front area(m^2)	1.93	Rolling friction coefficient	0.009
Wheel radius(m)	0.302	Aerodynamic drag coefficient	0.29

The parameter of the traction system of a vehicle depends on its dynamical requirements (Table. 4.2). It defines the maximal velocity, the acceleration time from 0 to 100km/h and the climbing ability, i.e., the maximal slop angle with the velocity of 20km/h. From Table. 4.1 and Table. 4.2, the initial requirements of the traction system is obtained (Table. 4.3). This process is not detailed in this thesis, but more details can be found in [Kunyuan.L 2011].

Table. 4.2. Dynamical requirements of the vehicle

Parameter	Value	Note
Maximal velocity (km/h)	130	load: 165kg
Acceleration time, 0-100km/h (s)	15	load: 165kg
Maximal climbing ability (^{o})	16.8	20km/h, load: 165kg

Table. 4.3. Initial requirements of the traction system

Rated speed $\Omega_{mcm(N)}$(rad/s)	Rated torque $T_{mcm(N)}$(Nm)	Maximal speed $\Omega_{mcm(max)}$(rad/s)	Maximal torque $T_{mcm(max)}$ (Nm)
168	160	472	270

4.3 MCM sizing method

From the perspective of system design, MCM sizing is a multi-objective optimization problem with constraints. It can be described as a process to find the perato solution, with which the MCM has a higher efficiency, higher torque density and lower cost. The general form of a multi-objective optimization problem is:

$$\begin{aligned} \min \quad & c(x) \\ s.t. \quad & h_i(x) = 0, i = 1, 2, \cdots, l \\ & g_j(x) \leq 0, j = 1, 2, \cdots, m \end{aligned}$$

where c is the cost function, $x = (x_1, x_2, \cdots, x_n)^T$ is the vector of optimization variables, h and g are the equality and inequality constraints respectively, l and m are the number of equality constraints and inequality constraints. Chapter 3 achieves

the estimation of the efficiency maps, which lays the foundation for constructing the cost function. This section will deal with the implementation of MCM sizing.

4.3.1 Objective function

As a multi-machine system, a MCM can expand its high-efficiency area with an appropriate power split strategy. However, the combination of multiple EMs leads to the increase in volume and mass in comparison with the single EM with the same power. Since PM has important impact on the cost of an EM. Thus, in order to size a MCM with higher efficiency, higher torque density and lower cost, the objective function can be defined as:

$$c\left(x\right) = \boldsymbol{w}\boldsymbol{\mu} = [w_1\ w_2\ w_3]\left[\frac{1}{\mu_1}\ \frac{1}{\mu_2}\ \mu_3\right]^T \tag{4.1}$$

among which $\boldsymbol{w}$ is the weight vector, and $w_1+w_2+w_3 = 1$, $\boldsymbol{\mu}$ is the objective function vector, and $\mu_1 \sim \mu_3$ corresponds to MCM efficiency property, torque density and the volume of PM. Due to the large difference in magnitude for $\mu_1 \sim \mu_3$, $\boldsymbol{\mu}$ is normalized in order to improve the optimization convergence and precision. In this section, Min-Max Normalization is used to re-scale the objective function.

4.3.1.1 MCM efficiency property μ_1

Efficiency property μ_1 characterizes the percentage of the area where the efficiency is greater than 85% to the total operating area. Decomposing the MCM 'torque-speed' plane evenly into a network with $N \times M$ nodes, and μ_1 is defined as:

$$\mu_1 = \frac{Q_{\eta_{mcm}\geq 0.85}}{MN} \tag{4.2}$$

where $Q_{\eta_{mcm}\geq 0.85}$ is the number of points with a system efficiency greater than 0.85.

Two basic MCM topologies are introduced in chapter 2 (Fig. 1.7). Whatever the topology, system efficiency η_{mcm} is derived by Eq. (2.3). It indicates that the system efficiency η_{mcm} is not only related to the efficiency of a single EM, but also depends on the power split. The efficiency of a single EM can be obtained by the method in chapter 3.

In order to obtain the optimal system efficiency, an optimal power split strategy is defined (Fig. 4.2). The flowchart is described as following steps. (1) Initialize an operating point $(T_{mcm\_i}, \Omega_{mcm\_j})$ for MCM. (2) Maximize the efficiency η_{mcm} by tuning the power split of the m EMs. (3) Repeating (1) and (2) to optimize the efficiencies of all the operating points in the 'torque-speed' plane of the MCM. Finally calculating μ_1 by Eq. (4.2).

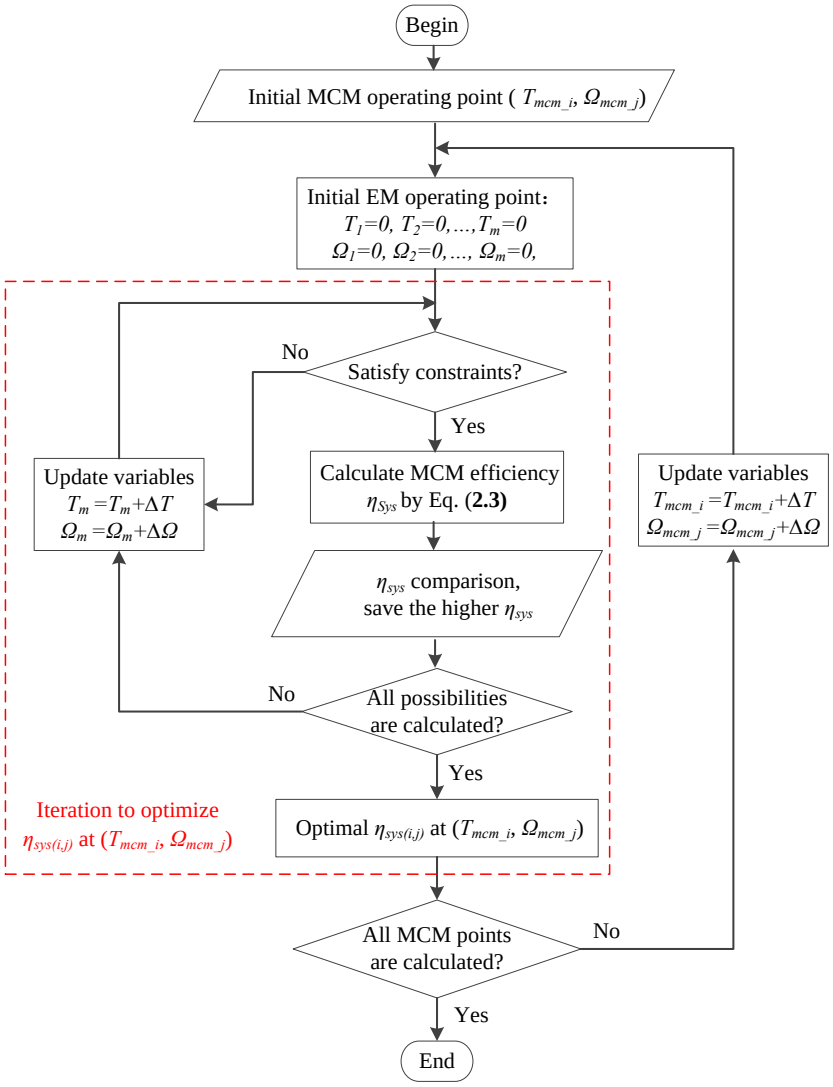

Figure. 4.2. Flowchart of the optimal power split strategy

4.3.1.2 MCM torque density μ_2

Torque density of an EM refers to the ratio of rated torque to volume [Fengfeng.S 2007]. According to the basic theory of EM, the volume of an EM is roughly determined by the torque. The relationship between torque T_N and volume is [Huang.S 1998]:

$$T_N = \frac{1}{4\left(K_\Phi + 1\right)} K_e K_i K_p \eta_N B_g A D_g^2 L_e \tag{4.3}$$

where K_Φ is the electrical load ratio of rotor to stator, K_e is the coefficient of back EMF, K_i is the current waveform factor, K_p is the electrical power waveform factor, η_N is the rated efficiency, D_g is the inner diameter of the stator, $B_g$is the amplitude of the air-gap flux density, A is the electrical load, which depends on the cooling conditions.

Eq. (4.3) is suitable for any kind of EM, but the waveform coefficients are different

regarding to different EMs (Table. 4.4). The power factor angle φ_N in Table. 4.4 for different EMs are defined by Eq. (3.33), Eq. (3.68) and Eq. (3.71) in chapter 3. $K_w \approx 0.9$ is the winding factor.

Table. 4.4. Waveform factors with sinusoidal EMF and current

	IM	S-PM-SM	I-PM-SM
K_Φ	$1.06P_N^{0.0116}n_p^{-0.062}f^{-0.054}$	0	0
K_e	$2\pi K_w$	π	π
K_i	$\sqrt{2}$	$\sqrt{2}$	$\sqrt{2}$
K_p	$0.5\cos\varphi_N$	$0.5\cos\varphi_N$	$0.5\cos\varphi_N$

[Huang.S 1998] points out that the stator teeth of an EM should be designed according to the following expression:

$$B_{ts} = \begin{cases} 2 & f \leq 20Hz \\ 5.47f^{-0.32} & 20Hz < f < 60Hz \\ 1.48 - \frac{1.48-5.47f^{-0.32}}{1.4} & f \geq 60Hz \end{cases} \tag{4.4}$$

where B_{ts} is the teeth flux density, f is the frequency.

Meanwhile, it is reveled in [Levi.E 1984] that the flux density in the air gap has the following relationship with the teeth flux density:

$$B_g = 0.5K_{fe}B_{ts}K_h \tag{4.5}$$

where $K_{fe} \approx 0.97$ is the core stacking factor, K_h is the fundamental-wave coefficient of air gap flux density. When the core is not saturated, $K_h = 1$. Otherwise, $K_h \leq \frac{\pi}{2}$. To fully utilize the core, the EM is in critical saturation at the rated point, here we take $K_h \approx 1.3$.

Generally, the air gap flux density is easy to be determined. For a PM-SM, we take $B_g \approx 1$. For an IM, we take $B_g \approx 0.78$. Therefore, the rated frequency f of the EM could be determined by the flowchart in Fig. 4.3, according to Eq. (4.3). The traction EM for electrified vehicle is developing towards high speed and high integration, and limited by the number of the poles, the rated frequency is generally higher than 20Hz.

So, the number of the poles of the EM could be deduced:

$$n_p = \frac{2\pi f}{\Omega_N} \tag{4.6}$$

So far, all the wave factors in Table 4.4 can be obtained. With Eq. (4.3), the volume of the MCM μ_2 (only the effective part) can be expressed as:

$$\mu_2 = \sum_{i=1}^{m} V_{emi} = \sum_{i=1}^{m} \left(\frac{\pi}{4} \frac{1}{\lambda_{gi}^2} D_{gi}^2 L_{ei} \right) = \sum_{i=1}^{m} \left(\frac{\pi\left(1 + K_{\Phi_i}\right)}{\lambda_{gi}^2 K_{ei} K_{ii} K_{pi} \eta_{Ni} B_{gi} A_i} T_{Ni} \right) \tag{4.7}$$

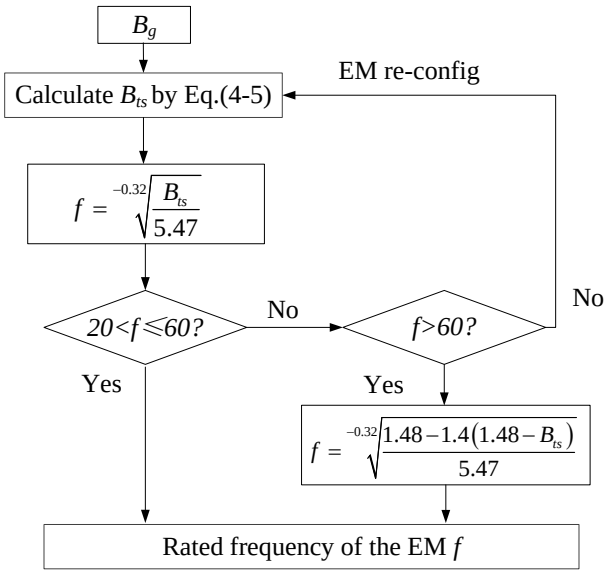

Figure. 4.3. Flowchart of rated frequency calcultion

$$\lambda_{gi} = \frac{D_{gi}}{D_{oi}} = \frac{D_{gi}}{D_{gi} + 2d_{cs} + 2d_{ss}} = \left(1 + \frac{\pi B_{gi}\alpha_{pi}}{2n_{pi}K_{fei}B_{csi}} + 2K_{si}\right)^{-1} \tag{4.8}$$

where V_{em} is the effective volume of a single EM, λ_g is the ratio of the inner diameter to the outer diameter of the stator, D_o is the stator outer diameter, $\alpha_p \approx 0.85$ is the polar arc coefficient, $B_{cs} \approx 1.5$ is the flux amplitude of stator yoke, K_s is the ratio of stator slot depth to stator inner diameter. Since all the EMs are modular designed in MCM, they have the similar diameters, thus we take $K_s \approx 0.12$. The torque density μ_2 is then expressed as:

$$\mu_2 = \frac{\sum_{i=1}^{m} T_{Ni}}{V_{mcm}} \tag{4.9}$$

where T_{Ni} is the rated torque of the i^{th} EM.

4.3.1.3 Volume of PM μ_3

PM is one of the sources of magnetomotive force of a PM-SM, and its usage amount directly reflect the EM cost. The volume of PM V_{pm} of a PM-SM can be expressed as [Beishe.W 2011]:

$$V_{pm} = k_M \pi D_g L_e \delta \approx k_M V_\delta \tag{4.10}$$

where $k_M = k_\delta \alpha_p$ is the utilization factor of PM, k_δ is the thickness coefficient PM in magnetization direction. For radial magnetization, $k_\delta \approx 4$, and for tangential magnetization, $k_\delta \approx 6.5$, δ is the length of the air-gap, and V_δ is the volume of the air-gap.

With Eq. (4.7), the PM volume of a MCM μ_3 can be expressed as:

$$\mu_3 = V_{pm\_mcm} \sum_{i=1}^{n} V_{pmi} = \sum_{i=1}^{n} \left(k_{Mi} V_{emi} \left(\lambda_{gi}^2 - \lambda_{ri}^2\right)\right) \tag{4.11}$$

with:

$$\lambda_{ri} = \frac{D_{ri}}{D_{oi}} = \frac{D_{ri}}{D_{ri} + 2\delta + 2d_{cs} + 2d_{ss}} \approx \left(1 + \frac{2\delta}{D_{ri}} + \frac{\pi B_{gi}\alpha_{pi}}{2n_{pi}K_{fei}B_{csi}} + 2K_{si}\right)^{-1} \quad (4.12)$$

where D_r is the rotor outer diameter, D_o is the stator outer diameter, n is the number of PM-SMs in MCM. The modular designed EMs in MCM have the similar diameters D_o. Considering the value difference of δ and D_o, the impact of $\frac{2\delta}{D_{ri}}$ on λ_r is small, thus we take $\frac{2\delta}{D_{ri}} \approx 0.0044$

In summary, the objective function $c(x)$ is subject to the specifications of each EM (T_N, T_{max}, Ω_N, Ω_{max}). The flowchart of objective function calculation is shown in Fig. 4.4. First, calculate the efficiency maps, rated efficiencies and rated power factors of all the EMs according to the theory in chapter 3. Then establish the objective function through optimal strategy, torque density and PM volume estimations. Indeed, the volume of the EM is considered twice implicitly in the objective function, i.e., the torque density and the volume of PM. This would potentially influence the priority of efficiency versus volume. Even though, one can tuning the weight vector based on the real demand.

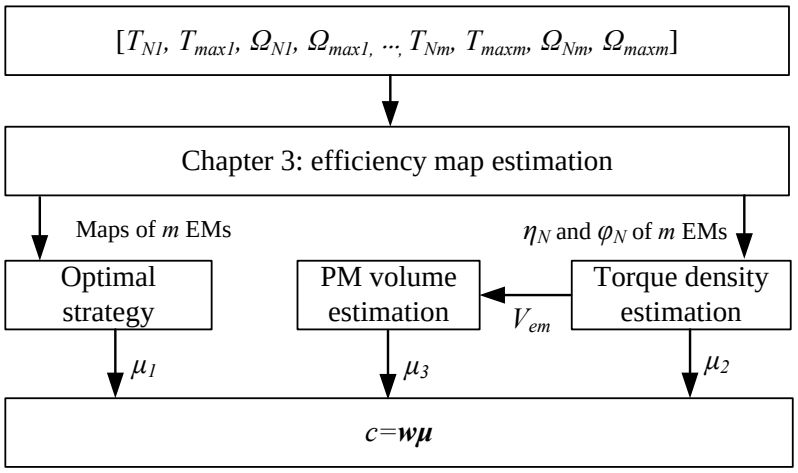

Figure. 4.4. Flowchart of cost function calculation

In the above empirical formulations of the torque density and PM volume, some coefficients some coefficients have no genericity, such K_s, which is the ratio of stator slot depth to stator inner diameter. Fortunately, thanks to the modular design of EMs in the MCM, all the EMs tends to have the same outer diameter, so does the single drive EM. To define these none 'general' coefficients, the single EM could be designed by FE method firstly. When replacing the single EM by MCM, the EMs in MCM will have the same outer diameter. Based on the parameters of the single EM, those coefficients would turn to be 'general'. Moreover, this method is only used to estimate the torque density and PM volume when the EM has not been designed. Once the specifications of the EM is fixed, torque density and PM volume should be designed by FEM.

This chapter studies the 2 MCM topologies, i.e., series and parallel MCM (Fig. 2.1). All the EMs share the same shaft in a series MCM, while the EMs in a parallel MCM are coupled by a set of gear-train. Therefore, the gear ratios will influence the system performance. Suppose the MCM has m EMs, the optimization variables x can be selected in the following way.

For a series MCM:

$$x = [T_{N1}, T_{max1}, \Omega_{N1}, \Omega_{max1}, \cdots, T_{Nm}, T_{maxm}, \Omega_{Nm}, \Omega_{maxm}] \tag{4.13}$$

For a parallel MCM:

$$x = [T_{N1}, T_{max1}, \Omega_{N1}, \Omega_{max1}, \cdots, T_{Nm}, T_{maxm}, \Omega_{Nm}, \Omega_{maxm}, k_2, \cdots, k_m] \tag{4.14}$$

where k_m is the gear ratio between the m^{th} and $(m-1)^{th}$ EM.

4.3.2 Constraints

MCM sizing is a multi-objective optimization problem. Each of its iteration needs to verify whether the initialized variable satisfies the corresponding constraints. The initial requirement of MCM sizing (section 4.2.2) defines the dynamic constraints that a MCM must satisfy, including rated speed $\Omega_{mcm(N)}$, rated torque $T_{mcm(N)}$, peak speed $\Omega_{mcm(max)}$ and peak torque $T_{max(max)}$. According to the MCM topology and the relationship of torque and speed in section 2.2, the following constraints are considered.

Overload and speed expansion constraints:

$$\begin{cases} 1 \leq \dfrac{T_{maxi}}{T_{Ni}} \leq 3 \\ 1 \leq \dfrac{\Omega_{maxi}}{\Omega_{Ni}} \leq 4 \end{cases} \tag{4.15}$$

Power constraints:

$$\begin{cases} \displaystyle\sum_{i=1}^{m} \Omega_{Ni} T_{Ni} \geq \Omega_{mcm(N)} T_{mcm(N)} \\ \displaystyle\sum_{i=1}^{m} \Omega_{Ni} T_{maxi} \geq \Omega_{mcm(N)} T_{mcm(max)} \end{cases} \tag{4.16}$$

In varies topologies, the torque and speed constraints are different. According to the topology in section 2.2, the torque and speed constraints are described the following:

$$\begin{cases} \displaystyle\sum_{i=1}^{m} T_{maxi} \geq T_{mcm(max)} & \text{(series MCM)} \\ \displaystyle\sum_{i=1}^{m} T_i \prod_{j=i+1}^{m} k_j \geq T_{mcm(max)} & \text{(parallel MCM)} \end{cases} \tag{4.17}$$

$$\begin{cases} \Omega_{maxi} \geq \Omega_{mcm(max)} & \text{(series MCM)} \\ \dfrac{\Omega_{max(i-1)}}{k_i} \geq \Omega_{mcm(max)} & \text{(parallel MCM)} \end{cases} \tag{4.18}$$

4.4 Results of sizing

In this chapter, Particle Swarm Optimization (PSO) is used to optimize the cost function. PSO is a bionics-based global optimization algorithm with simple operation and fast convergence. When an 'optimal' solution is found, PSO will still search near this 'optimal' solution with a certain probability. This makes PSO having better ability to find a global optimal solutions. It is more robust than other intelligent algorithms, such as Genetic Algorithms (GA). All the sizing algorithm of PSO in this chapter considers 50 swarms, which includes 200 particles. The type of swarm is represented by the fitness function of @fitscalingrank.

There are 3 kinds of EMs being used to form a MCM, i.e., I-PM-SM, S-PM-SM and IM. When the MCM has m EMs, various EM formalizations lead to $\frac{(m+2)!}{2m!}$ combinations. Each combination has a perato solution, one can choose one sizing with the lowest perato value as the final sizing result. Fig. 4.5 shows an example of how to choose the final sizing with $m = 2$.

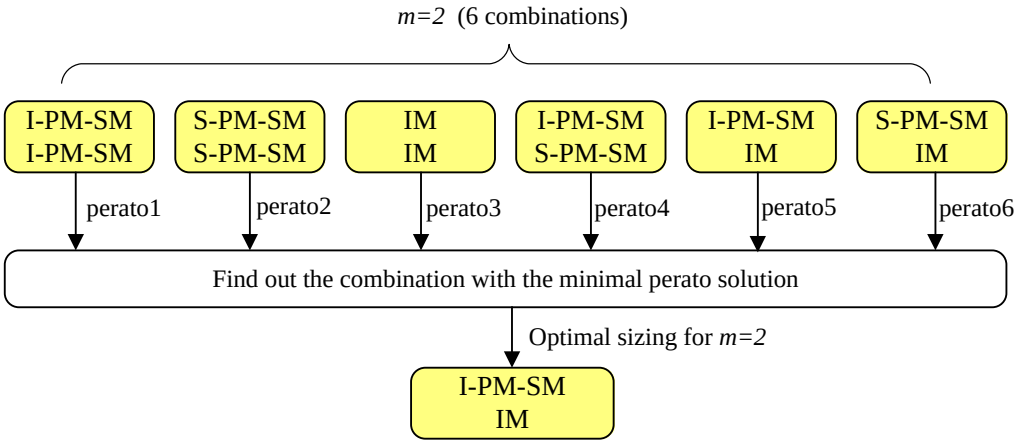

Figure. 4.5. Selection of an optimal sizing $m = 2$

4.4.1 Sizing results of series MCM

Taking $m = 1 \sim 4$ as examples, the optimal sizing results are shown in Table. 4.5. It is indicated that with the increase of m, the torque of PM-SM is decreasing while the torque of IM is increasing. The optimization of a series MCM with 2 EMs takes about 1min with Inter(R) Core (TM) i-7-4510U CPU@2.00GHz in Matlab2016a.

Table. 4.5. Optimal sizing with $m = 1 \sim 4$

	EM type	$\Omega_N(rad/s)$	$T_N(Nm)$	$\Omega_{max}(rad/s)$	$T_{max}(Nm)$
$m = 1$	I-PM-SM	168	160	472	270
$m = 2$	IM	132	74	472	130
	I-PM-SM	185	93	472	140
$m = 3$	IM	124	78	472	138
	S-PM-SM	153	42	472	75
	I-PM-SM	255	37	472	57
$m = 4$	IM	144	22	472	41
	IM	124	51	472	98
	S-PM-SM	209	31	472	47
	I-PM-SM	179	55	472	84

According to the specifications in Table. 4.5, the optimal efficiency maps for $m = 1 \sim 4$ are obtained (Fig. 4.6). It can be seen that the MCM efficiency map varies with different numbers of EMs. For example, in comparison with $m = 1$, the high-efficiency area of $m = 2$ is expanded toward low-torque reagin. Since one EM is replace by two, thus the MCM efficiency distribution benefits that of the 2 EMs. Generally, more EMs results in lower torque of each EM, which further expands the MCM high-efficiency area toward low torque. The improvement of efficiency is especially obvious in the high-speed and high-power areas. Although the efficiency of an IM (maximum efficiency 93.5%) is lower than that of a PM-SM (maximum efficiency of 96.5%), the combination of IM and PM-SM still contributes to a larger high-efficiency area.

Define a ratio to highlight the difference of the objective functions of different sizings: $e_{\mu\_i} = \frac{\mu_i - \mu_i^{PMSM}}{\mu_i^{PMSM}} \times 100\%, i = 1, 2, 3$. The ratios are show in Fig. 4.7. As the increase of m, the torque of IM increase, which leads to a higher degree of 'PM-reduction'. For example, about 44% of the PM of $m = 2$ is saved in comparison with that of the single I-PM-SM ($m = 1$). However, comparing to $m = 2$, the 'PM-reduction' for $m = 3$ and $m = 4$ is fair. Because they have close torque ratios of PM-SM to MCM. Nevertheless, the joining of IMs significantly decreases the system torque density. What is more, each EM in a MCM is structurally and functionally independent, thus the increase of m results in the increase of volume of some inactive portions, such as covers. Compared with $m = 2$, the increase of high-efficiency area and PM reduction for $m = 3$ and $m = 4$ are no longer obvious. In a word, $m = 2$ or $m = 3$ is more reasonable for the studied vehicle.

Among these sizing results, one can select according to the demands. For example, when there is a strict limit on torque density, $m = 1$ is more suitable; If the usage amount of PM is strictly restricted, $m = 3$ or $m = 4$ is more suitable.

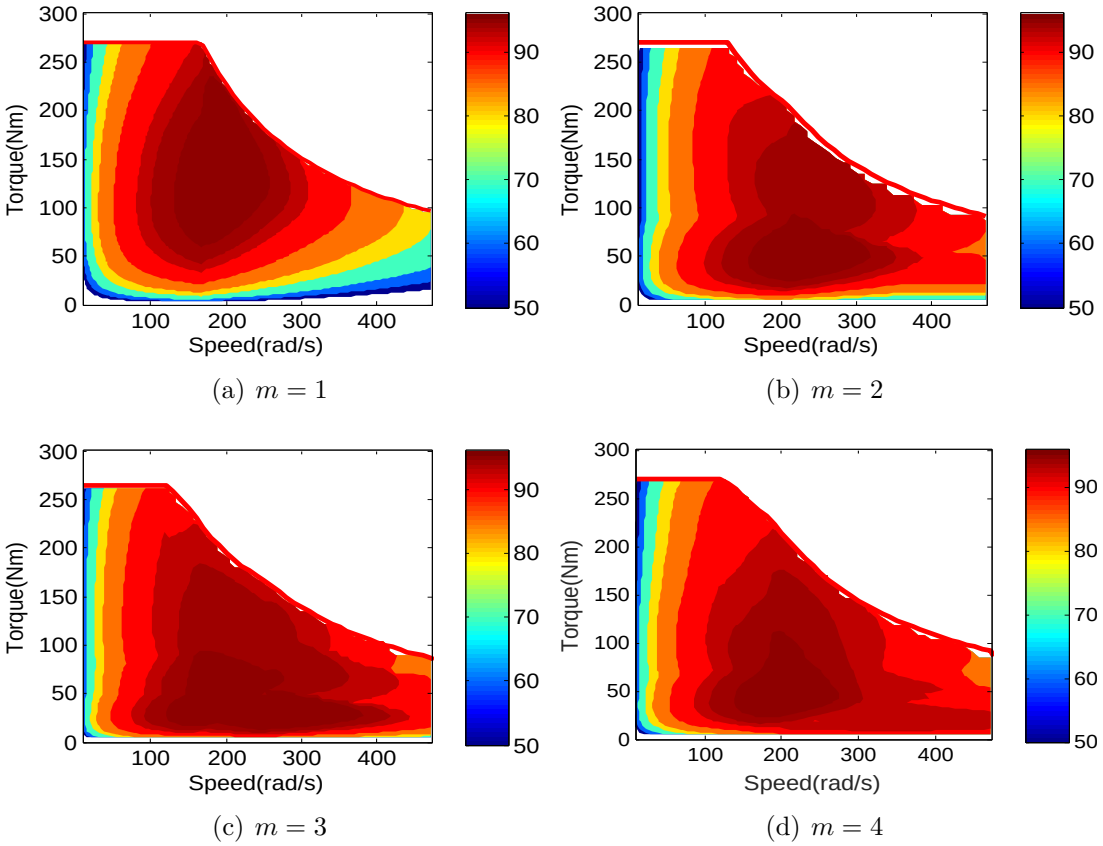

(a) $m = 1$ (b) $m = 2$

(c) $m = 3$ (d) $m = 4$

Figure. 4.6. MCM efficiency maps with $m = 1 \sim 4$

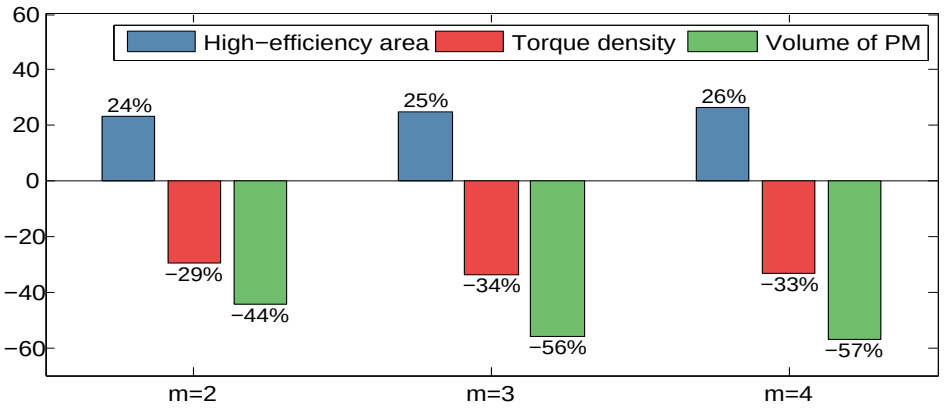

Figure. 4.7. Comparisons of different sizings than the single I-PM-SM

4.4.2 Sizing results of parallel MCM

Sizing of a parallel MCM is based on the structure in Fig. 2.1(b). Similar to the series MCM, a parallel MCM also has $\frac{(m+2)!}{2m!}$ combinations regarding to different EM and m. In this section, a parallel MCM with $m = 2$ is taken as an example to analyze the final sizing. When $m = 2$, there are 6 combinations, and each one has a perato optimal solution. Table. 4.6 is the sizing result of a parallel MCM with

$m = 2$.

Table. 4.6. Perato solutions for parallel MCM with $m = 2$

	EM type	$\Omega_N(rad/s)$	$T_N(Nm)$	$\Omega_{max}(rad/s)$	$T_{max}(Nm)$	k_1
MCM1	I-PM-SM	200	45	472	79	2.31
	I-PM-SM	559	55	1085	83	
MCM2	S-PM-SM	163	50	472	80	1.92
	S-PM-SM	307	61	906	98	
MCM3	IM	255	35	472	63	2.03
	IM	262	68	959	104	
MCM4	IM	213	62	472	95	2.13
	I-PM-SM	280	55	1000	88	
MCM5	IM	146	54	472	94	1.85
	S-PM-SM	312	59	874	95	
MCM6	I-PM-SM	170	60	472	104	1.93
	S-PM-SM	293	58	905	86	

The output shafts of both EMs are connected by a gear-train. It can be seen that among all the MCMs, the optimal gear ratio is higher than 1. That means the torque of one EM is reduced due to the gear-train, so that the volume of this EM is reduced. If it is a PM-SM, the usage amount of PM will be directly reduced. Fig. 4.8 shows the MCM efficiency maps for the 6 MCMs. It can be seen that the efficiency distribution of different MCMs are completely different. MCM1 consists of 2 I-PM-SMs with an high-efficiency area around the rated operating point. However, it is inefficient in the high-speed and high-power region, which is caused by the large flux-weakening current of the PM-SM. A S-PM-SM generally has a high-efficiency area around the point with peak power and rated torque, hence MCM2 (2 S-PM-SM) improves the system efficiency in the high-speed and high-power area. MCM3, with 2 IMs has the lowest system efficiency. MCM4 combines I-PM-SM and IM, and obtains a large efficient area. Meanwhile, the volume of PM is reduced. Compared with MCM1, the area of MCM4 where the efficiency is higher than 90% is increased, but the area with the efficiency greater than 92% is significantly reduced. MCM5 is composed of an IM and a S-PM-SM. Its high-efficiency area is in the high-torque region due to the large torque of the S-PM-SM. MCM6 is a combination of S-PM-SM and I-PM-SM, and its efficiency characteristic is similar to that of MCM2. Additionally, compared with the maps in Fig. 4.6, the maximal MCM efficiency is reduced from 96% to 94%, which is caused by the transmission losses of the gear-train.

Fig. 4.9 shows the values of the objective functions of different parallel MCMs (not including the volume of the gear-train). It can be seen that all the MCMs have the similar size of high-efficiency areas, where MCM3 has the smallest high-efficiency area. With the regards of torque density and the volume of PM, I-PM-SM is more competitive than the S-PM-SM in this case. Similar to the series MCM, the use of IM reduces the system torque density, but still ensures a large high-efficiency area and a small volume of PM. Compared with MCM4, the torque of the PM-SM

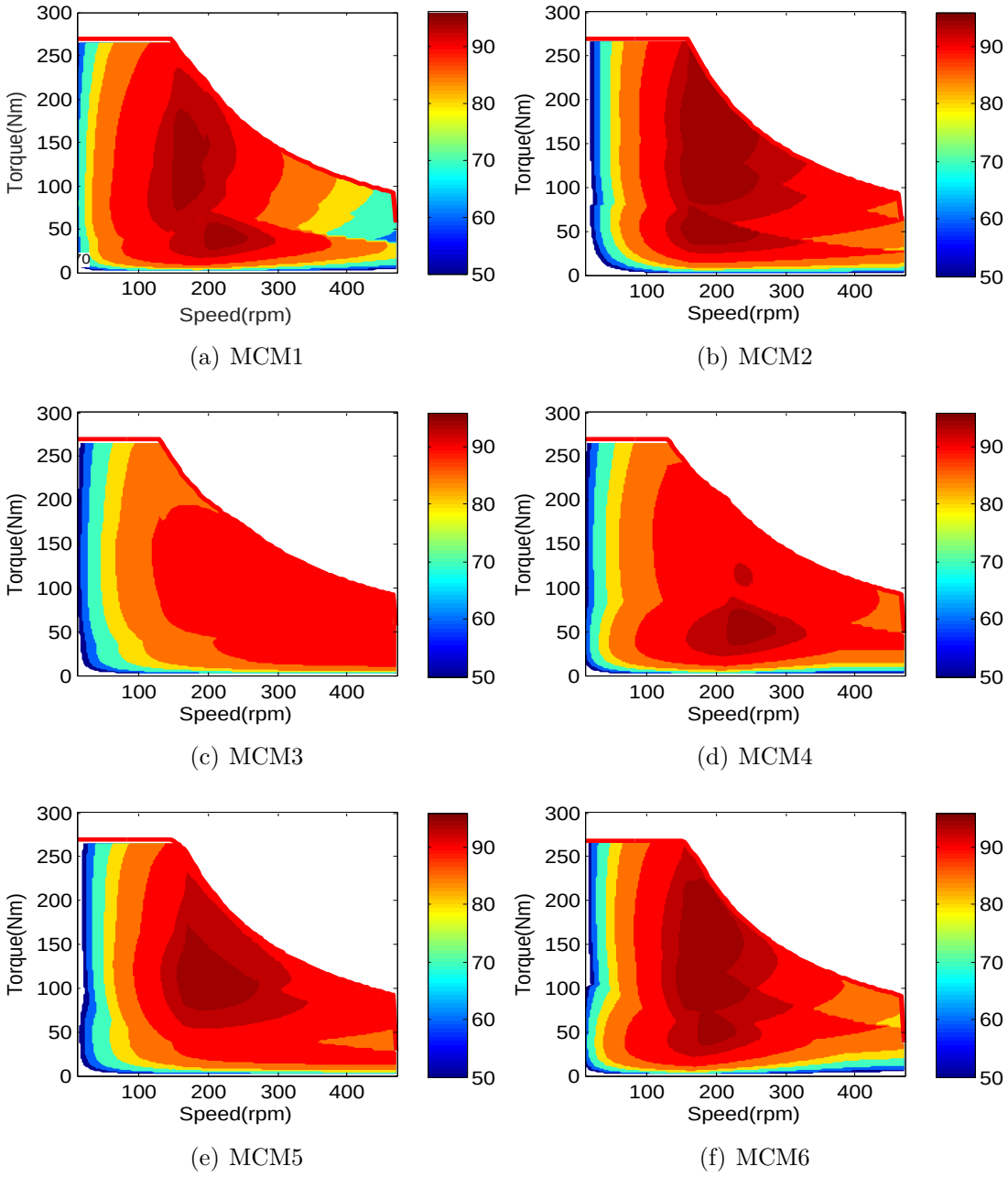

(a) MCM1 (b) MCM2

(c) MCM3 (d) MCM4

(e) MCM5 (f) MCM6

Figure. 4.8. Efficiency maps of parallel MCMs with $m = 2$

in MCM5 is larger, which leads to larger PM-SM volume and more use of PM. In addition, the use of this gear-train adds extra weight and volume to the system, which would further reduce the MCM torque density.

In the same way, one can select an appropriate sizing among these sizing results according to the demands. From the perspective of improving system efficiency and torque density, and reducing the volume of PM, MCM5 with one S-PM-SM and one IM is more suitable for the studied vehicle.

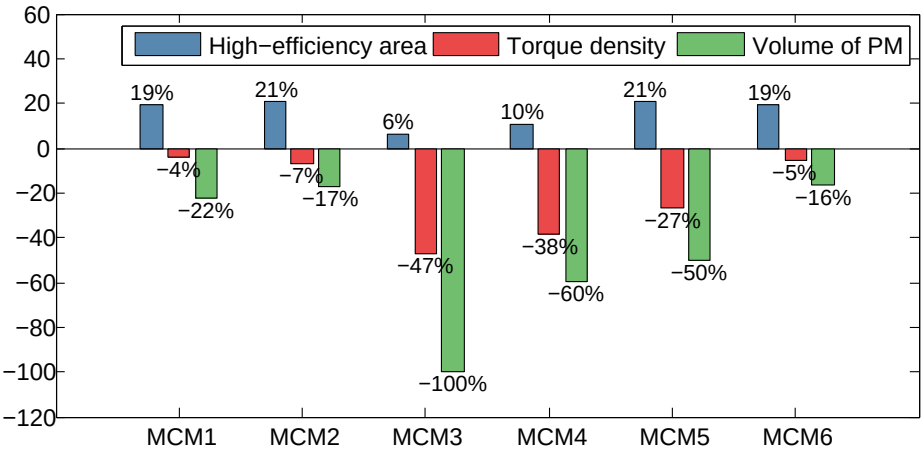

Figure. 4.9. Comparisons of different parallel MCM than the single I-PM-SM

4.4.3 Extension of MCM sizing

As stressed in subsection 2.2, the speeds of the EMs in a series or parallel MCM are coupled, and the torques are the only optimization variables. To further improve the MCM efficiency, 2 topologies based on planetary gear-train are proposed in this subsection: torque coupling and hybrid coupling (Fig. 4.10). More details about planetary gear-train could be found in Appendix A.2.

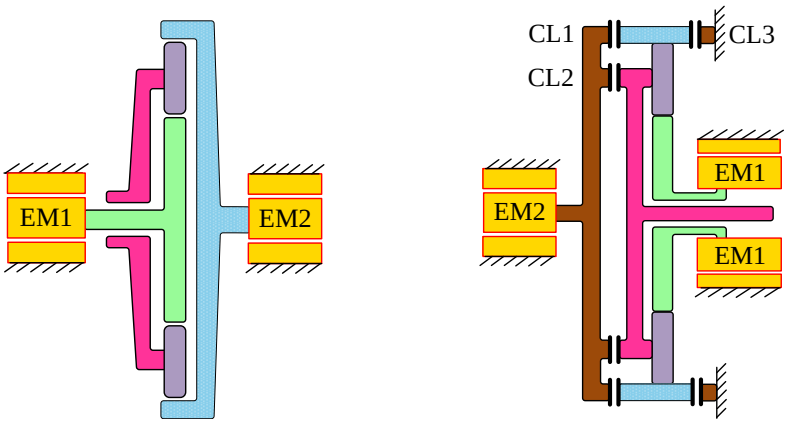

(a) Torque coupling (b) Hybrid coupling

Figure. 4.10. Planetary-gear-train-based MCMs

In the torque coupling topology, both EMs are connected to the sun gear and the ring gear respectively, and the carrier is connected to the mechanical power-train. In the hybrid coupling topology, EM1 is connected to the sun gear, the carrier is connected to the mechanical power-train. While EM2 can be connected to the carrier or the ring gear with clutches CL1, CL2 and CL3. Thus the switch between torque coupling mode and speed coupling mode is realised (Table. 4.7).

Table. 4.7. Operation modes of the clutches

Clutch	Speed coupling	Torque coupling
CL1	separated	closed
CL2	closed	separated
CL3	closed	separated

Let k_R and k_S are 2 independent gear ratios of the planetary gear-train, there is the following relationship for the torque coupling topology:

$$\begin{cases} \Omega_{mcm} = k_R\Omega_2 + k_S\Omega_1 \\ T_{mcm} = \dfrac{1}{k_S}T_1 = \dfrac{1}{k_R}T_2 \end{cases} \tag{4.19}$$

where T_1, T_2 and Ω_1 and Ω_2 are the torques and speeds of EM1 and EM2. In this way, the speeds of both EMs are decoupled. In comparison with the series or parallel MCM, the optimization of EM has been changed from torque to speed.

For the hybrid coupling topology, the torque and speed relationship satisfies Eq. (2.2) in speed coupling mode. Otherwise, the relationship is defined by the following equation in torque coupling mode:

$$\begin{cases} \Omega_{mcm} = k_S\Omega_1 = \Omega_2 \\ T_{mcm} = \dfrac{1}{k_S}T_1 + T_2 \end{cases} \tag{4.20}$$

Therefore, the hybrid coupling topology can optimize both torque and speed, and the system efficiency is expected to be further improved. Fig. 4.11 shows the optimization direction of an EM in the hybrid coupling topology, where the operating point has more possibilities for optimization.

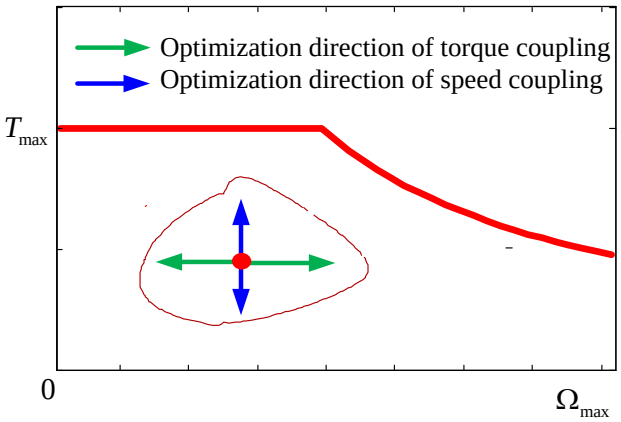

Figure. 4.11. Optimization direction of an EM in the hybrid coupling structure

With the proposed sizing method, the optimal sizing of both planetary gear-train based system are obtained (Table. 4.8). Because of the planetary gear-train, the

speed and torque ranges of both EMs are different. EM1 is connected to the sun gear, and k_S is small, so EM1 has a higher speed and a smaller torque. The optimal sizing of both topologies is an combination of IM and PM-SM. It is consistent with the efficiency characteristics of the EMs. Because IMs and PM-SMs are efficient in high-speed and low-speed areas respectively. Such a MCM can make full use of the efficient regions of both EMs.

Table. 4.8. Optimal sizing of planetary gear-train based MCM

Mode	EM type	Ω_N (rad/s)	T_N (Nm)	Ω_{max} (rad/s)	T_{max} (Nm)	k_S	k_R
Torque coupling	IM (EM1)	454	31	1050	47	0.1748	0.8252
	I-PM-SM (EM2)	97	116	340	223		
Hybrid coupling	IM (EM1)	510	32	947	48	0.4298	0.5702
	I-PM-SM (EM2)	116	104	185	158		

According to Table. 4.8, the optimal efficiency map of the MCMs can be calculated. In Fig. 4.12(a), the areas in deep-red ($\eta_{mcm} \geq 93\%$) correspond to the high efficiency area of the I-PM-SM and the IM respectively, which accords with the rule of speed optimization. Additionally, the contours for the hybrid coupling topology is rather tortuous, since the system is frequently switched between the torque coupling mode and the speed coupling mode. During sizing, the dynamic of the clutches are not considered. Actually, the dynamical response of the clutch takes a certain time, hence the efficiency map in Fig. 4.12(b) needs to be corrected according to the dynamical properties of the clutches.

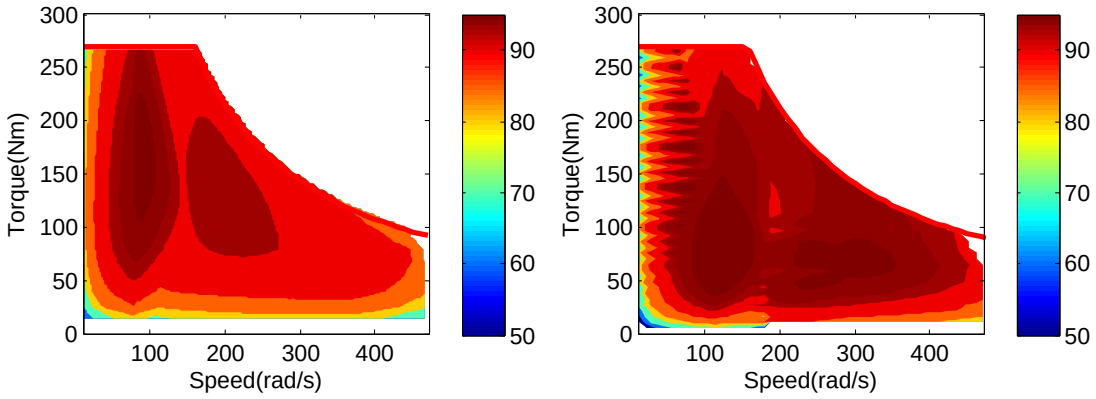

(a) Torque coupling (b) Hybrid coupling

Figure. 4.12. Efficiency maps of MCMs with planetary gear-train

Table. 4.9 shows the ratio of high-efficiency area to the total operating area of different MCM topologies. It can be seen that although the planetary gear has a loss of about 2%∼3%, the high-efficiency area of the planetary gear-train based MCM is still larger than those of the series and parallel MCM. In general, the planetary

gear-train based MCMs have better efficiency characteristics, but the presence of the clutches and planetary gear-train leads to more complex structure and control.

Table. 4.9. Comparisons of high-efficiency areas of different MCM topologies

Parameter	Series MCM	Parallel MCM	Torque coupling	Hybrid coupling
Ratio μ_1 (%)	84	82	89	92

4.5 Impact of different sizings on vehicle energy consumption

In the previous sections, the MCM sizing method was studied and different sizing results were obtained. Generally, the traction system usually works in a wide speed and torque range, it is difficult to justify the efficiency properties of different sizings only by their efficiency maps. Therefore, trip analysis is necessary to compare the interest of different MCM systems.

Dynamic Programming (DP) is widely used to determine the optimal solution of a system [Salmasi.F.R 2007]. The determination of this optimum is necessarily based on the knowledge of the future. This makes DP unusable in real time. However, it allows to obtain a theoretical optimum, and its result can be used for system comparisons. In order to use DP to determine an optimized power split strategy, a "backward" model is required [Mayet.C 2014a]. The "backward" model of the MCM-based vehicle can be deduced from its EMR, as shown in Fig. 4.13, where the EMs are modeled with static models by imposing the efficiency maps [Li.K 2018]. DP divides the problem into many locally sub-problems and search for the local optimum in a backward way. By tuning the control inputs, an overall optimization of the system could be realised based on the principle of optimality of Bellman [Bellman.R 1966]. More details about the implementation of the strategy could be found in Appendix A.3.

4.5.1 MCM for pure EV

Choosing UDDS (Urban Dynamometer Driving Schedule), UDDSHDV (Urban Dynamometer Driving Schedule for Heavy Duty Vehicles), WLTC (Worldwide harmonized Light vehicles Test Cycles) and HWFET (High-Way Fuel Economy Test) as the test cycles, the energy reductions of a pure EV (see parameters in Table. 2.2) are compared with different sizings. Here, we define an energy reduction rate e_{red} and an average energy reduction rate e_{ave}:

$$e_{red} = \frac{E_s - E_{mcm}}{E_s} \tag{4.21}$$

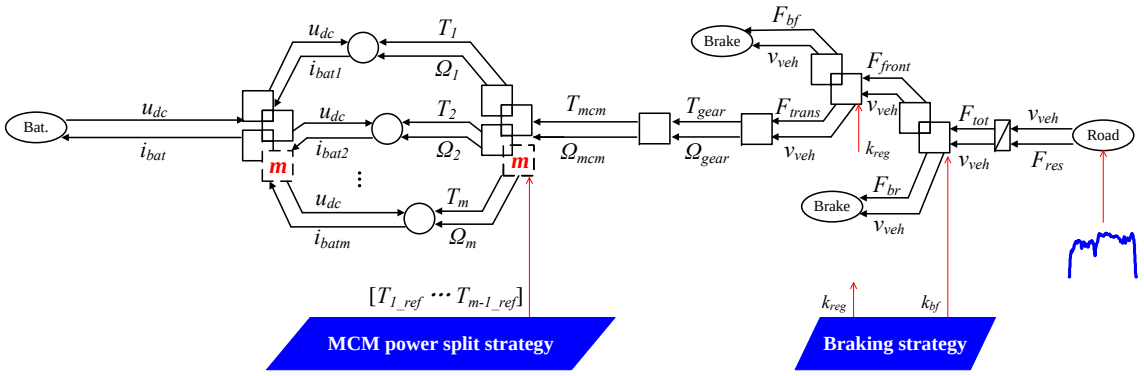

(a) MCM-based EV

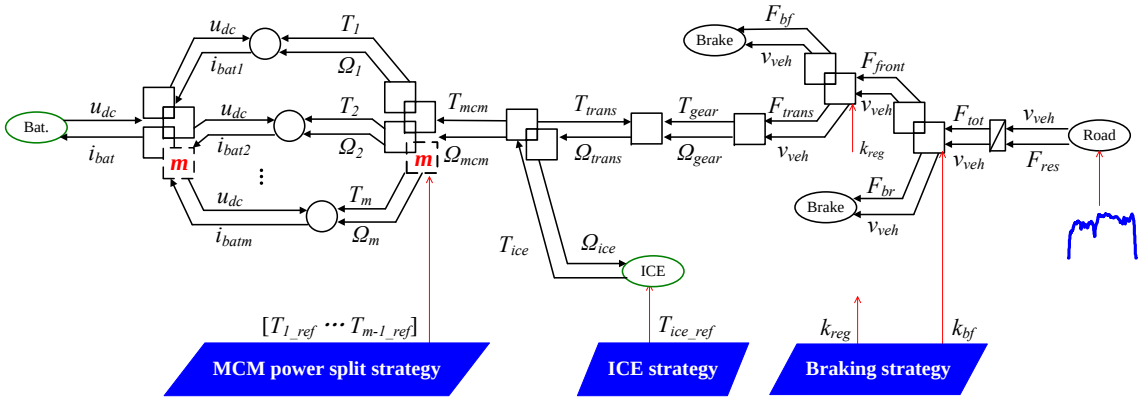

(b) MCM-based parallel HEV

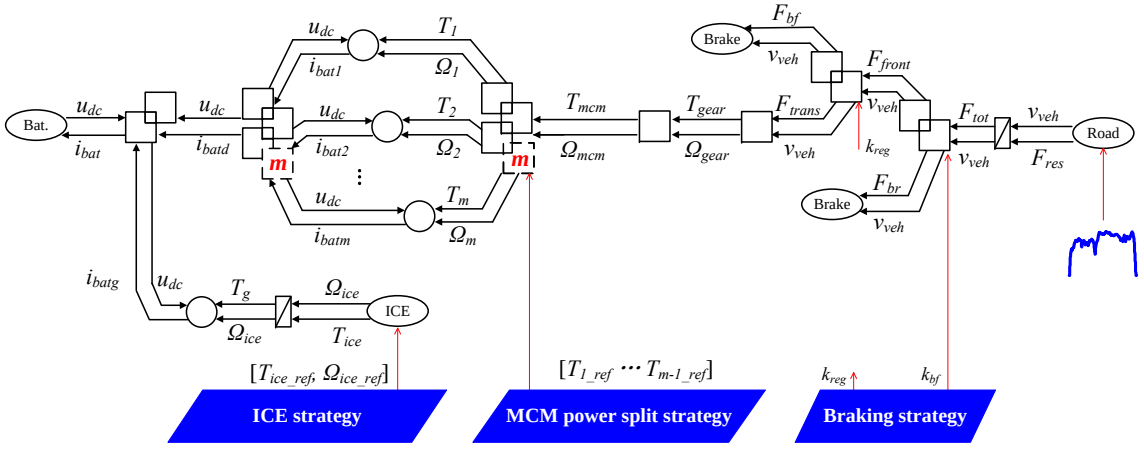

(c) MCM-based vehicle

Figure. 4.13. Backward model of the MCM-based vehicle based on EMR

$$e_{eva} = \frac{e_{red}}{m} \tag{4.22}$$

where E_{mcm} and E_s are the energy consumptions of the MCM-based EV and single drive EV. Energy reduction rate indicates the energy-saving potential of the MCM system than a single drive system. While average energy reduction rate represents the contribution of each EM to reduce the energy consumption.

Table. 4.10 and Table. 4.11 shows the energy reduction rates for the series MCM, where $m = 1$ means single-drive based system, its parameters are defined in Table.4.3. Parameters of the MCMs are shown in Table. 4.5.

Table. 4.10. Energy reduction (%) of different series MCMs

Number of EMs	UDDS	UDDSHDV	WLTC	HWFET
m=1	-	-	-	-
m=2	10.41	5.34	11.24	17.97
m=3	12.08	6.52	13.23	20.89
m=4	13.55	7.72	15.87	21.21

Table. 4.11. Average energy reduction (%) of different series MCMs

Number of EMs	UDDS	UDDSHDV	WLTC	HWFET
m=1	-	-	-	-
m=2	5.21	2.67	5.62	8.99
m=3	4.02	2.17	4.41	6.96
m=4	3.39	1.93	3.97	5.30

One can derive that a MCM-based EV has obvious energy-reduction ability than the classical single drive EV ($e_{red} > 0$). The more EMs there are, the more energy will be reduced. Moreover, e_{eva} is decreasing when m increases. For example, e_{eva} for $m = 2 \sim 4$ under UDDS are 5.205%, 4.02% and 3.39% respectively. Since an EM has already had a relatively large high-efficiency operation area, the benefit of adding one more EM tends to saturate.

Table. 4.12 shows the comparisons of different parallel MCMs with $m = 2$ than a single drive systems. The energy-reduction ability is lower than that of the series MCM. This is caused by the mechanical losses in the coupling gear-train. Regarding to the assemble-ability, the coupling gear-train makes the parallel MCM more unwieldy. Despite this, the parallel MCM could be of interest in the applications where there are strict limitations in axial length.

Table. 4.12. Energy reduction (%) of different parallel MCMs (m=2)

	UDDS	UDDSHDV	WLTC	HWFET
MCM1	9.82	5.14	10.71	17.14
MCM2	9.71	5.33	10.32	17.45
MCM3	2.18	4.21	10.21	16.21
MCM4	9.83	5.26	10.23	16.22
MCM5	9.12	5.02	10.31	17.23
MCM6	9.68	5.14	10.42	17.21

Thus we can conclude that comparing to the parallel topology, the series MCM is more competitive to reduce the energy consumption, and a MCM with 2 EMs has

the largest average energy reduction rate. Considering the system efficiency, torque density, cost, structural and control complexity, the sizing of a series MCM with $m = 2$ is more suitable for this application.

4.5.2 MCM for HEV

In this subsection, a truck (see parameters in Table. 4.13) will be used to analyse the interest of MCM in HEV. The parameters of the original traction systems are indicated in Table. 4.14.

Table. 4.13. Parameters of the HEV

Item	Value	Item	Value
Total mass (kg)	7258	Final gear ratio	8.4
Front area (m^2)	6.9	Wheel radius (m)	0.397

From the above comparisons, a series MCM with 2 EMs could be of competitiveness in terms of energy reduction and cost. Therefore, we will use two-EM MCM to replace its original EM. In Table. 4.14, the single EM will be replaced by the MCM. MCM is optimally sized by the method in this chapter in order to have wider high-efficiency area, higher torque density and lower cost (Table. 4.15). Meanwhile, the MCM has the same power as the original EM.

Table. 4.14. Parameters of the traction system of the HEV

		$T_N(Nm)$	$T_{max}(Nm)$	$\Omega_{max}(rad/s)$	$P_{max}(kW)$
Parallel HEV	ICE	-	1660	177	205
	EM	380	550	245	58
Series HEV	ICE	-	568	177	70
	EM	1270	1750	245	263
	GM	70	114	881	70

Table. 4.15. Parameters of the MCM system

		$T_N(Nm)$	$T_{max}(Nm)$	$\Omega_{max}(rad/s)$	$P_{max}(kW)$
Parallel HEV	EM1	212	265	220	26
	EM2	171	285	220	32
series HEV	EM1	563	935	245	187
	EM2	627	815	245	76

Then apply the optimal power split strategy to different HEVs and calculate the fuel reduction rate than the original HEVs, as shown in Table. 4.16. It can be seen that the MCM-based parallel HEV have close fuel consumption than the original HEV,

Table. 4.16. Fuel reduction (%) of MCM-based HEV than classical HEV

	UDDS	UDDSHDV	WLTC	HWFET
Parallel HEV	0.05	0.15	0.01	0.18
Series HEV	6.65	5.23	4.31	5.26

almost no fuel is saved. Nevertheless, the MCM-based series HEV possesses a fuel reduction rate from 4.31% to 6.65%.

The figures in Table. 4.16 could be explained from the perspective of power flow. According to power conservation principle, we have the following relationship for a parallel HEV and a series HEV:

$$P_{veh} = \begin{cases} \left(P_{fuel}\eta_{ice} + P_{bat}\eta_{trac}\right)\eta_{mech} & \text{(parallel HEV)} \\ \left(P_{fuel}\eta_{ice}\eta_{ge} + P_{bat}\right)\eta_{trac}\eta_{mech} & \text{(series HEV)} \end{cases} \tag{4.23}$$

where P_{veh}, P_{bat} and P_{fuel} are the powers of the vehicle, the battery and the fuel, η_{trac}, η_{ice}, η_{mech}, η_{ge} are the efficiencies of the traction machine, the ICE, the mechanical power-train and the generator.

The fuel power P_{fuel} can be derived:

$$P_{fuel} = \begin{cases} \dfrac{1}{\eta_{ice}\eta_{mech}}P_{veh} - \dfrac{\eta_{trac}}{\eta_{ice}}P_{bat}dt & \text{(parallel HEV)} \\ \dfrac{1}{\eta_{ice}\eta_{ge}\eta_{trac}\eta_{mech}}P_{veh} - \dfrac{1}{\eta_{ice}\eta_{ge}}P_{bat} & \text{(series HEV)} \end{cases} \tag{4.24}$$

Then the fuel consumption E_{fule} is calculated by:

$$E_{fuel} = \begin{cases} \dfrac{1}{\eta_{ice}\eta_{mech}}\displaystyle\int P_{veh}dt - \dfrac{\eta_{trac}}{\eta_{ice}}\int P_{bat}dt & \text{(parallel HEV)} \\ \dfrac{1}{\eta_{ice}\eta_{ge}\eta_{trac}\eta_{mech}}\displaystyle\int P_{veh}dt - \dfrac{1}{\eta_{ice}\eta_{ge}}\int P_{bat}dt & \text{(series HEV)} \end{cases} \tag{4.25}$$

For a specific cycle, the vehicle kinetic energy $\int P_{veh}dt = E_{veh}$ is a constant. For the battery, its SoC is a state variable in the DP algorithm, and it has the same value in the beginning and in the end, thus $\int P_{bat}dt = 0$.

Therefore,

$$E_{fuel} = \begin{cases} \dfrac{E_{veh}}{\eta_{ice}\eta_{mech}} & \text{(parallel HEV)} \\ \dfrac{E_{veh}}{\eta_{ice}\eta_{ge}\eta_{trac}\eta_{mech}} & \text{(series HEV)} \end{cases} \tag{4.26}$$

We can find that for a parallel HEV, the improvement of traction efficiency η_{trac} does not help to reduce the fuel consumption. For a series HEV, the fuel consumption is in inverse proportion to the traction efficiency, and a increase of traction efficiency directly contributes to the fuel reduction. In the same way, we can infer that for a

parallel-series HEV, the impact of traction efficiency on fuel consumption is between that of the parallel and series HEV. Hence the figures in Table. 4.16 complies with the theoretical analysis.

Regarding to the operating points of the ICE for both parallel HEVs, they spread in a wide region (Fig. 4.14(a)), since the ICE is coupled with the wheel. Moreover, most of the operating points of both ICEs are closely located, despite several small shifts. As a consequence, both ICEs have the similar efficiency distributions statistics (Fig. 4.14(b)), which results in the similar fuel consumptions.

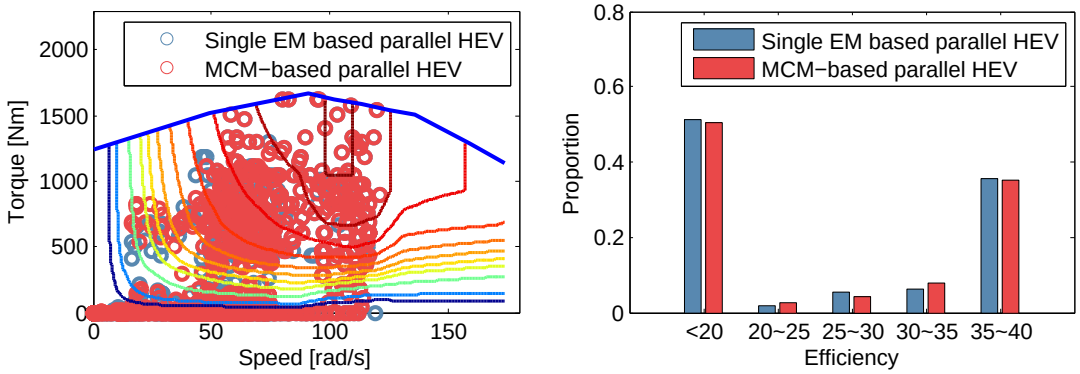

(a) Operating points of the ICE (b) Efficiency distribution of the ICE

Figure. 4.14. Comparisons of the ICE of the parallel HEV under UDDS

When it comes to the series HEV, the mechanical decoupling between the ICE and the wheel makes the operating points of the ICE better optimized (Fig.4.15(a)). Most of the points are in the high-efficiency area. From the statistics of the ICE operating points, we can refer that the ICE of the MCM-based series HEV works more frequently in the area where the efficiency is higher than 30%. This benefit leads to a considerable fuel reduction rate.

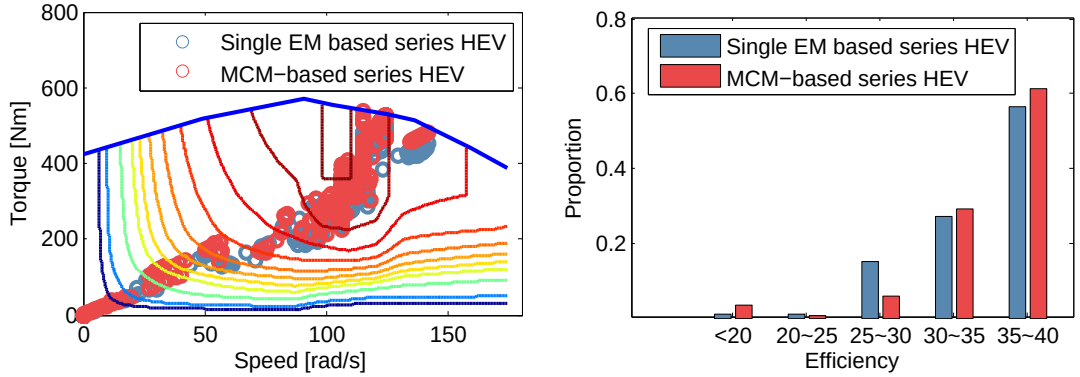

(a) Operating points of the ICE (b) Efficiency distribution of the ICE

Figure. 4.15. Comparisons of the ICE of the series HEV under UDDS

4.6 Conclusion

This chapter deals with the method of MCM sizing, which aims to optimize the system efficiency, torque density and the usage amount of PM. The model and control in chapter 2 and the efficiency map estimation method in chapter 3 are the inputs of this work.

The main works are the following.

(1) A multi-objective-based MCM sizing method is proposed, and different sizing results are analysed.

(2) The impacts of different sizings on vehicle energy consumption are compared and summarised

The main conclusion and contributions are summarized.

(1) The proposed MCM sizing method based on multi-objective optimization can expand MCM high-efficiency area, increase system torque density and reduce the usage amount of PM. It enables to optimize the comprehensive characteristics of a MCM.

(2) The study shows that the combination of IM and I-PM-SM can not only reduce the usage amount of PM by about 44%, but also ensure the system a large high-efficiency area.

(3) The proposed hybrid coupling MCM system changes the 'speed' coupling of the series and parallel MCM. It can not only optimize the EM torque, but also can optimize the EM speed, thus it has better system efficiency.

(4) A MCM system has considerable energy-reduction ability for pure EVs and series HEVs. The series MCM is more competitive in terms of efficiency and complexity. A MCM with 2 EMs has the highest average energy reduction rate, and the highest ratio of energy reduction to investment.

The work in this chapter is suitable to determine the design specifications of a MCM. It narrows down the range where the optimal specifications could be located. Once defined, they could be used for EMs designed by FEM.

5

Power split strategy of a MCM system

In this chapter, two real-time MCM power split strategies are developed, using Adaptive Network based Interface System (ANFIS) and model predictive control. All the strategies are compared by simulation in terms of Electrical Machine (EM) operating characters and vehicle energy consumption. Then the strategies are validated in real time by reduced-scale Hardware-In-the-Loop (HIL) simulation.

Contents

5.1 Introduction 102
5.2 MCM design based on the sizing results 102
5.3 Description of MCM power split 103
5.4 Design of MCM power split strategies 105
5.5 MCM power split strategy validation 114
5.6 Conclusion 122

5.1 Introduction

MCM is a multi-machine system, regarding to a certain power demand, the possible power split solution of a MCM is numerous. Nevertheless, there would be one solution that can maximize the system efficiency. Hence how to efficiently manage the powers of each Electrical Machine (EM) in the MCM in order to have better global efficiency is one of the key technology of MCM. Some research proves that when the power split is achieved with the goal of maximizing the global efficiency, the EMs have bad operating character. The EMs start and stop frequently, noise and vibrations are observed in the experiment. If the power split is designed to improve the EM operating characters, the system efficiency decrease obviously. Therefore, how to develop an efficient and reliable power split strategy for a MCM is still challenging.

This chapter aims at developing a more advanced power strategy for a MCM. Firstly, the selected MCM is designed by Finite Element Method (FEM) based on the sizing result in chapter 4, in order to have more accurate characters. Then the Adaptive Network based Fuzzy Interface System (ANFIS) based strategy and predictive-based power split strategies are developed. Finally a Hardware-in-the-Loop simulation platform is established to validate the strategies in real-time.

5.2 MCM design based on the sizing results

It has been proved in chapter 4 that a MCM with 2 EMs has the highest average energy saving rate, i.e., each EM has the highest contribution to reduce the energy consumption. A hybrid MCM consisting of a I-PM-SM (Interior Permanent Magnet Synchronous Machine) and an IM (Induction Machine) is not only efficient, but also use fewer Permanent Magnet (PM), which leads to a lower cost. Therefore, this hybrid MCM will be selected for the study of MCM power split strategy in this chapter, considering its efficiency, cost and complexity. Chapter 4 defines the design specifications of each EM, which could be used for EM design by FEM. The FE models and the parameters of the EMs are show in Fig. 5.1 and Table. 5.1.

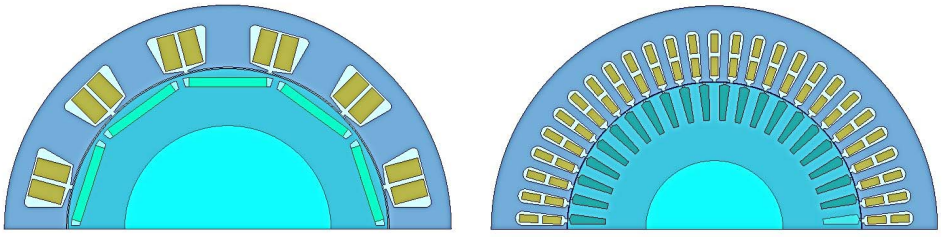

(a) I-PM-SM (b) IM

Figure. 5.1. Simulation model of the EM by FEM

Table. 5.1. Basic parameters of the EM by FEM

Item	Parameters	I-PM-SM	IM
Design specifications	Rated torque T_N (Nm)	93	74
	Maximal torque T_{max} (Nm)	140	130
	Rated speed Ω_N (rad/s)	185	132
	Maximal speed Ω_{max} (rad/s)	472	472
Basic parameters	Number of slot Z	12	54
	Number of poles $2n_p$	10	6
	Stator outer diameter D_o (mm)	260	260
	Stator inner diameterD_g (mm)	186	172
	Rotor outer diameter D_r (mm)	184.2	171.1
	Length of the EM L_e (mm)	93	100

Then the efficiency map of both EMs could be simulated by FEM, which are shown in Fig. 5.2. Both efficiency maps will be used to calculate the MCM efficiency when developing the power split strategy.

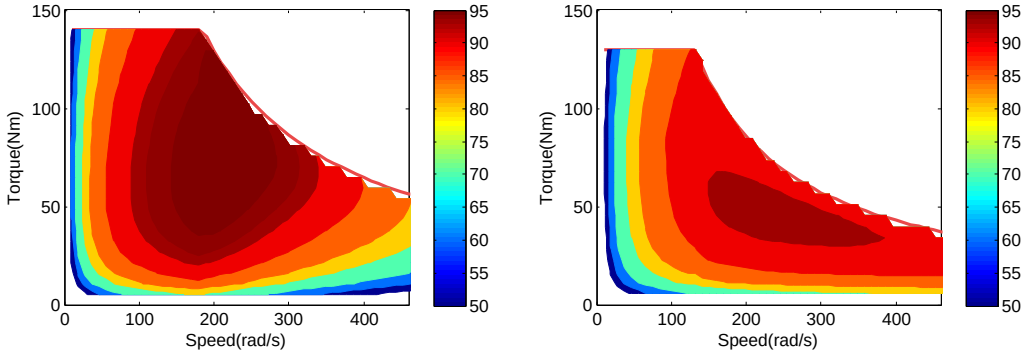

(a) I-PM-SM (b) IM

Figure. 5.2. Efficiency maps of the EMs by FE

5.3 Description of MCM power split

Since a MCM is more interesting in pure EVs and series HEVs, this chapter selects an EV for study. So, EMR of the MCM-based vehicle can be simplified, as shown in Fig. 5.3. The model is described by Energetic Macroscopic Representation (EMR), which highlights the important couplings. The control structure based on inversion rules clearly points out the key elements for energy management, i.e., T_{1_ref}, k_{reg} and k_{bf}. T_{1_ref} defines the MCM power split strategy between both EMs, k_{reg} and k_{bf} are used for braking. k_{bf} determines the front and rear braking force distribution. While k_{reg} defines the proportion of the regenerative force in the front during braking. The value of k_{reg} and k_{bf} will be given by the Dynamical Programming (DP) based strategy in chapter 4.

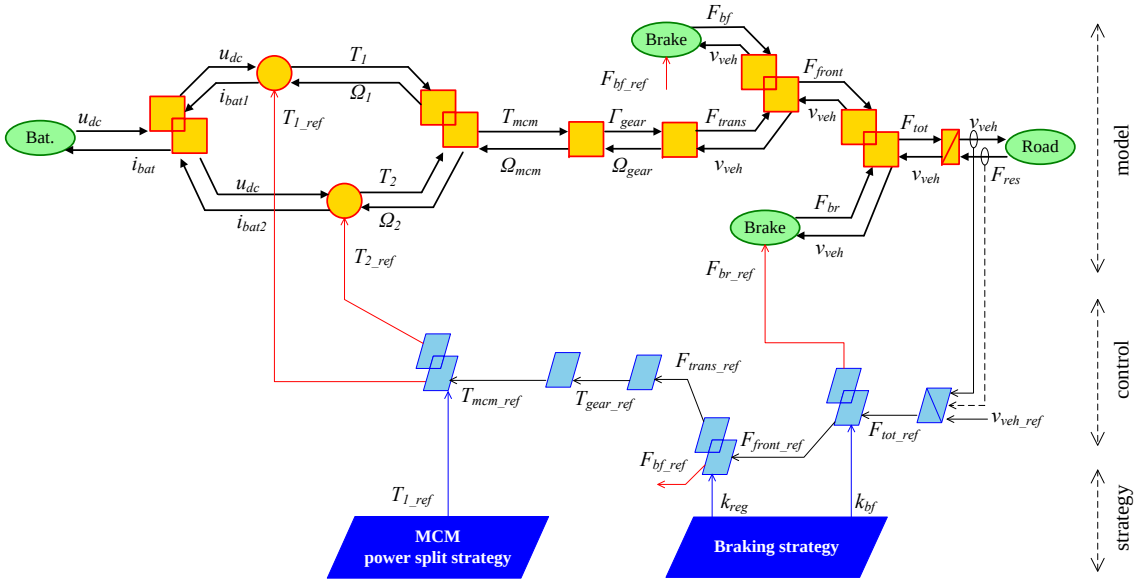

Figure. 5.3. EMR of the hybrid-MCM-based EV

The power split of MCM is based on the efficiency maps of the EMs. The inputs of the strategy are torque reference T_{mcm_ref} and speed measurement Ω_{mcm_mea} of MCM, its output is the torque reference T_{1_ref} of EM1, as shown in Fig. 5.4. The torque reference T_{2_ref} of EM2 is then given by Eq.(5.1).

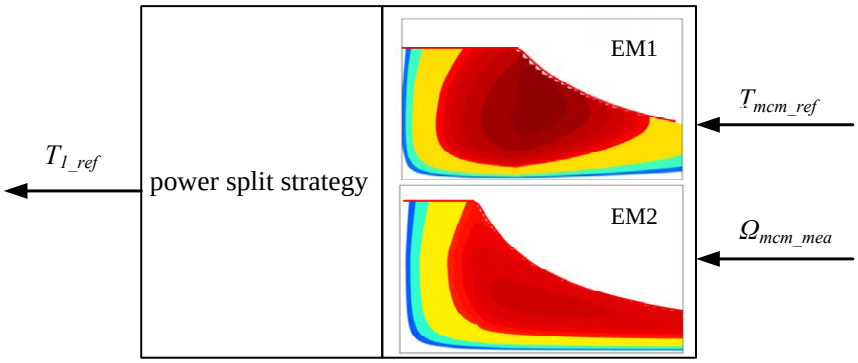

Figure. 5.4. Philosophy of MCM power split

$$T_{2\_ref} = T_{mcm\_ref} - T_{1\_ref} \tag{5.1}$$

Power split of a MCM is a non-linear energy management problem, which is realized by managing T_{1_ref} in Fig. 5.3. The optimal-efficiency strategy which was studied in [Han.S 2015] only optimizes the system efficiency, regardless of the EM operating character. It makes the EMs switch frequently between different operating points, which generates noise and vibration. Hence it is necessary to develop more advanced strategies. More details about the optimal-efficiency strategy could be found in Appendix A.4.

5.4 Design of MCM power split strategies

5.4.1 ANFIS-based strategy

Fuzzy logical control is now widely used for the control of a specific system which has corresponding nonlinear properties. However, it relies heavily on the experience and knowledge of the expert. Artificial Neural Network (ANN) has powerful self-learning ability, which can be used to adjust neural network parameters. ANFIS combines the fuzzy system with ANN, hence has the ability of fuzzy reasoning and parameters self-learning [Jang.J.S 1993].

ANFIS can automatically generate a set of fuzzy rules and membership functions based on a set of data, rather than based on experience or intuition. This requires a lot of training data to estimate the mapping relationship from the inputs to the outputs, through the self-learning process and its parallel distribution structure. For this two-EM MCM, its power split is a optimization process with 2 inputs (Ω_{mcm_mea} and T_{mcm_ref}) and 1 output (T_{1_ref}). Its network is illustrated in Fig. 5.5, where there are 5 layers.

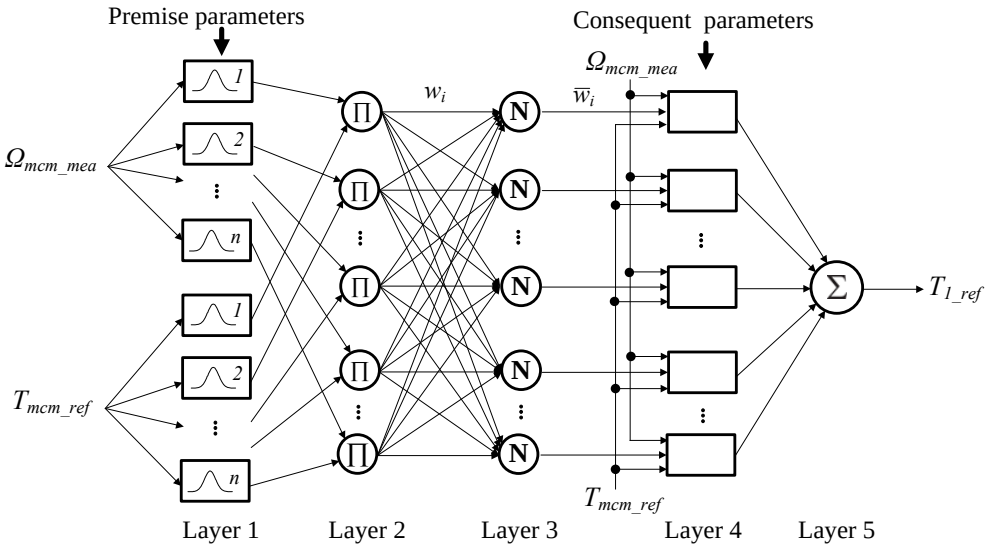

Figure. 5.5. Structure of an ANFIS with two inputs

Layer 1 In this layer, there are n membership functions for each input. The input of each node is fuzzyfied by the means of node function below:

$$O_i^{(1)} = \hbar_i\left(\Omega_{mcm\_mea}\right) = a_i exp\left(-\frac{\left(\Omega_{mcm\_mea} - b_i\right)^2}{2c_i^2}\right) \tag{5.2}$$

where $\hbar$ is the membership function, $\{a_i, b_i, c_i\}$ is the premise parameter set.

Layer 2 The credibility w_i of a rule is calculated by producing all the inputs of a

node:

$$O_i^{(2)} = w_i = \hbar_i\left(\Omega_{mcm\_mea}\right) \times \hbar_i\left(T_{mcm\_ref}\right) \tag{5.3}$$

Layer 3 The output of the i^{th} node is the normalised credibility $\overline{w_i}$ which is given by:

$$O_i^{(3)} = \overline{w_i} = \frac{w_i}{\sum_{i=1}^{n^2} w_i} \tag{5.4}$$

Layer 4 Every node in this layer is an adaptive node with a node function given by:

$$O_i^{(4)} = \overline{w_i} f_i = \overline{w_i}\left(p_i \Omega_{mcm\_mea} + q_i T_{mcm\_ref} + r_i\right) \tag{5.5}$$

where $\{p_i, q_i, r_i\}$ is the consequent parameter set.

Layer 5 The single node in this layer generates the final output of the ANFIS in the form of summing all the inputs:

$$T_{1\_ref} = O_i^{(5)} = \sum_{i=1}^{n^2} \overline{w_i} f_i \tag{5.6}$$

Through the above equations, it can be seen that the ANFIS generates the membership functions and fuzzy rules in the layer 2 and layer 4 with the premise and consequent parameters.

This adaptive network is a multi-layer forward-feed network. To realise better performances, the parameters in layer 1 and layer 4 need to be well trained. The gradient learning method can be used for parametric learning, but it is slow and easy to fall into the local minimum. In this thesis, we used a hybrid learning algorithm parametric learning. The network training depends on the expert experience library, which is replaced by an optimal-efficiency torque distribution data (Fig. 5.6) which is obtained from the optimal-efficiency strategy. In Fig. 5.6, the table data are the optimal torque of EM1.

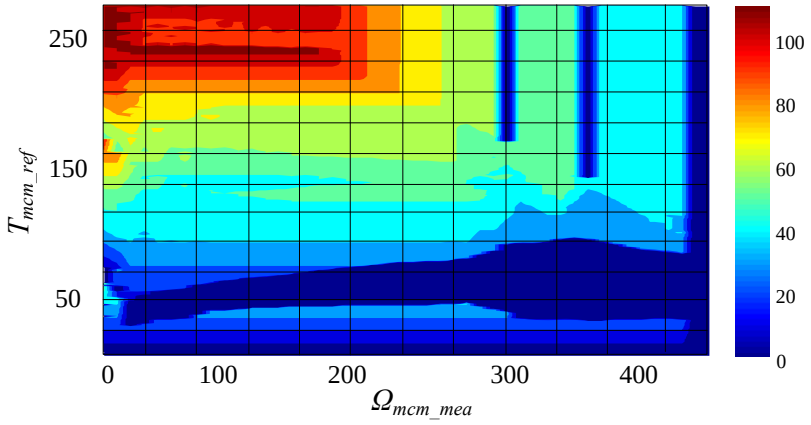

Figure. 5.6. Training data (the optimal torque of EM1)

The studied ANFIS in this thesis has 2 inputs and 1 output. By generating a 30×50 grid in Fig. 5.6 with a speed step of 9 rad/s and a torque step of 9 Nm.

70% of the grid points are selected randomly to train the network and others are used for testing. Matlab toolbox provides 11 kinds of membership functions for an ANFIS: trimf, trapmf, gbellmf, gaussmf, gauss2mf, pimf, dsigmf, sigmaf, zmf, smf and psigmf. In this thesis, power demand of a MCM is stochastic, thus the symmetrical membership function is preferred in order to avoid over learning and to have better abilities of generalization. Among all the symmetrical membership functions, gaussmf is selected since it has better performance over the test data set. In a fuzzy control system, the number of membership functions N_i and the fuzzy rules N_r has the relationship of $N_r = \sum N_i$. Thus the number of membership functions will directly related to the number of fuzzy rules, which would further influence the output performance. In this thesis, in comparison with the optimal efficiency strategy in a trip analysis, more fuzzy rules leas to poor EM operating characters (more stop/start times), while less rules results in more energy consumption. Finally, 100 rules with 10 membership functions for demand torque and speed are selected by experience.

After the network training, the learned membership functions of both inputs and the fuzzy rule surface are obtained, as shown in Fig. 5.7 and Fig. 5.8.

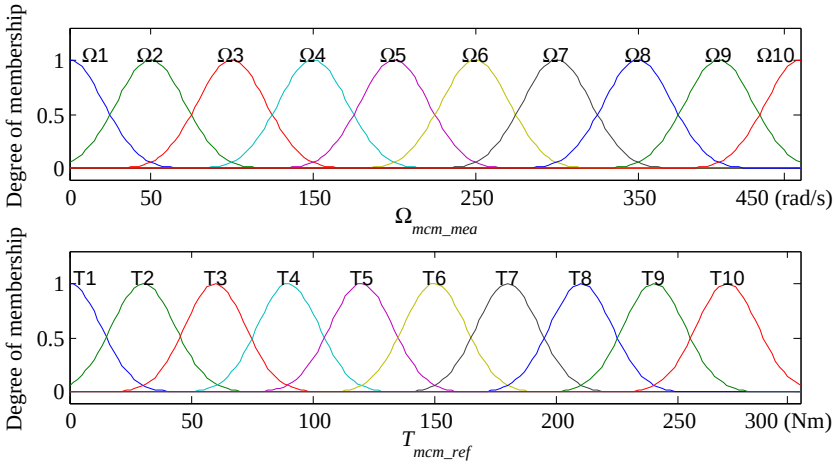

Figure. 5.7. Membership functions of both inputs

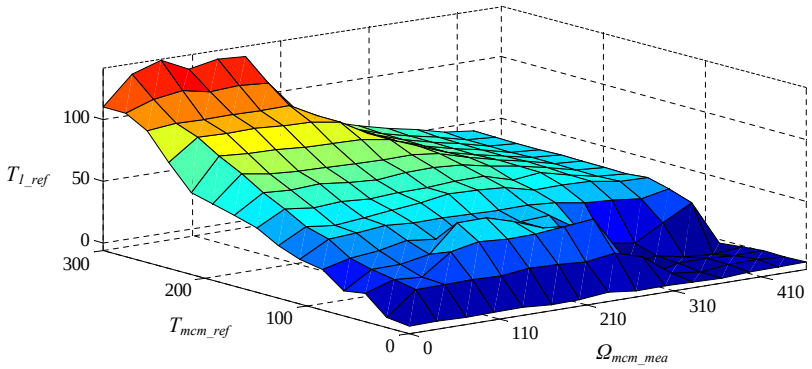

Figure. 5.8. Surface view of the fuzzy rules

5.4.2 Predictive-based strategy

The ANFIS-based strategy above focuses only on the current power demand. However, the power demand of MCM is stochastic. To optimize the EM operating character, the current power split needs to be adjusted in conjunction with the historical and future power demands. Model Predictive Control (MPC) is one kinds of online strategy, which is mainly used in HEV to improve its fuel economy. By MPC, one can better manage the present energy or power sources according the predicted information. Actually, predictive-based strategy could also be applied to a MCM-based EV, which could be helping to improve the operating characters of each EM in MCM. Once the velocity is predicted in a predictable horizon, the power demand and the optimal power split of the MCM could be predicted. Combined with the historical power split, the current EM power can be further optimized.

Regarding to the time-varying property of transportation information, predicting the vehicle velocity becomes more demanding. In this thesis, a velocity prediction method based on wavelet transformation and neural network is proposed. The input signal (velocity in the past) is firstly decomposed by wavelet transformation, and we acquires the approximation ('A_i') and details ('D_i') of the signal (i represents the decomposition level). Then the approximation and detail signals will pass through the well trained neural network, which outputs the predicted approximation and detail signals. Finally an entire predicted signal can be obtained by reconstruction. Fig. 5.9 indicates a velocity predictor with a 3-level wavelet transformation.

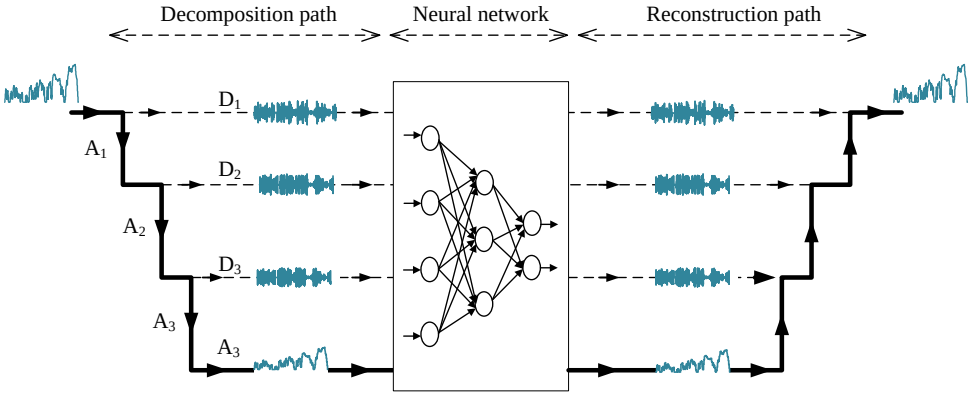

Figure. 5.9. Velocity predictor with 3-level wavelet transformation

The velocity is predicted by analyzing the velocities in the past, which takes the form of:

$$\left[v_{veh}^{(t+1)} \quad v_{veh}^{(t+2)} \cdots \; v_{veh}^{(t+L_{pre})}\right] = wavelet\_net\left(v_{veh}^{(t-L_{pre})} \cdots v_{veh}^{(t-2)} \quad v_{veh}^{(t-1)}\right) \tag{5.7}$$

where v_{veh} is the velocity, $wavelet\_net$ is the well trained network including wavelet transformation, L_{pre} is the prediction length. In this problem, the purpose of the strategy is to improve the operating characters of the EMs, hence L_{pre} cannot be too long. Each EM in MCM updates its torque after a control period of the Vehicle

Control Unit (VCU). In that case, L_{pre} is set to $30T_{veh}$. $T_{veh} = 100ms$ is the control time for the VCU. In this thesis, a 3-second time is the prediction length, during this time, 30 command signals from the VCU could be updated with the control time of 100ms. The strategy could modified and the operating point of the EM will update in each control period. Meanwhile, an EM has a very fast response, so the control time of 100ms is enough to avoid the start-stops of the EM.

Considering the stochastic process of the driving cycle, a wavelet mother function with more ripples are preferred when performing the transformation. Meanwhile, the wavelet mother is expected to have better symmetry, compact support and higher vanishing moments. The properties of different wavelet mother functions could be found in Appendix A.5. Thereby, a Daubechies wavelet with 9 filters is applied owing to its satisfactory fitting capacity in this thesis.

With the help of wavelet transformation, one can acquire more details of the input signal, which is expected to improve the prediction accuracy. Normally, the more level there is, the more details could be acquired. Fig. 5.10 shows a simple example with respect to a level 1 wavelet decomposition of UDDS. The data of A_1 expresses the rough tendency of the velocity, while the data of D_1 successfully reflect the subtle changes.

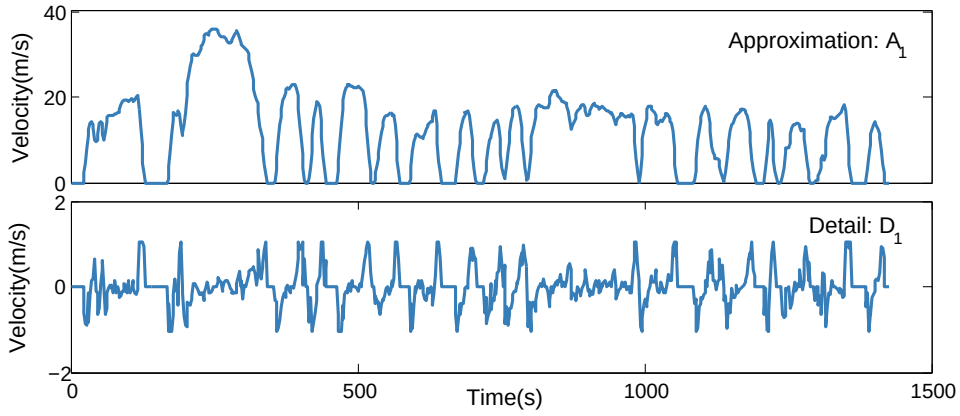

Figure. 5.10. UDDS decomposition with level 1

To train the network, 7 cycles are selected. Namely, UDDS, UDDSHDV, HWFET, WLTC, NEDC, J-1015 and US06. Table. 5.2 illustrates the comparisons of velocity predictions results. It can be seen that level 1 wavelet transformation helps to reduce the prediction error. However, the error increases for level 2 and level 3, since there are more cycle details, and the networks are overfitted. The calculation time covers the wavelet decomposition, network prediction and wavelet reconstruction. They are all within 20ms, which makes it possible for real-time implementation. Overall, the velocity predictor with level 1 wavelet transformation is preferred in this study. Fig. 5.11 shows the results of velocity prediction. The velocity is well predicted during strong acceleration/deceleration, since where the velocity is nearly linear changing. While the prediction error increases with fluctuant acceleration or deceleration.

Table. 5.2. Comparisons of velocity predictions results

	Average root-mean-square error (m/s)	Calculation time (ms)
* Level 0	1.92	≈13.3
Level 1	1.67	≈14.5
Level 2	1.79	≈15.7
Level 3	1.81	≈18.9

*Level 0 means no wavelet transformation

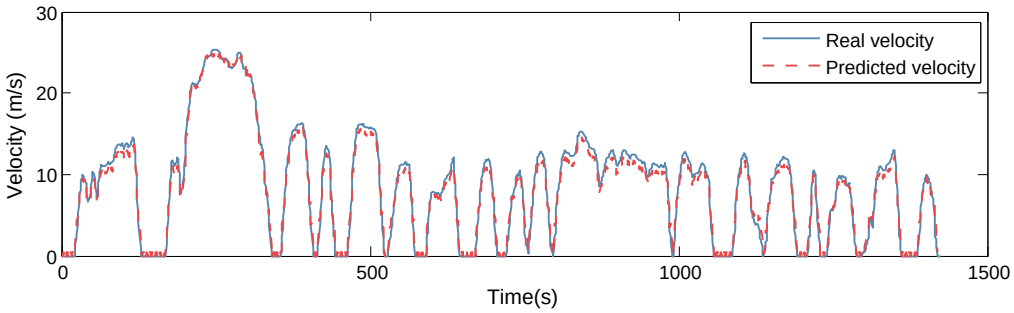

Figure. 5.11. Prediction results for UDDS with level 1 wavelet transformation

Once the velocity is predictable, the MCM power split strategy could be better improved. Fig. 5.12 shows the philosophy of the predictive-based strategy. At each vehicular control time, the velocity of the vehicle in the future 3s ($30T_{veh}$) will be predicted using the velocities in the past 3s. The demand power thus could be calculated backward. This calculation can complete within 2 ms since only simple mathematic relationships are used. Then the theoretically optimal torques in the predictable horizon could be acquired by looking-up tables, which is obtained off-line.

In that case, we obtained 30 optimal torque references in the predictable horizon, then with the 30 actual torques in the past, we can make a nonlinear regression using a quadratic function T_θ:

$$T_\theta(t) = \theta_2 t^2 + \theta_1 t + \theta_0 \tag{5.8}$$

where t is the time, θ_i are the coefficients that need to be updated in each control period.

The cost function J of this nonlinear regression is defined in order to estimate the regression error:

$$J(\theta_2, \theta_1, \theta_0) = \frac{1}{2L_{pre}+1} \sum_{i=t-L_{pre}}^{t+L_{pre}} \left(T_1^{(i)} - T_\theta\left(t^{(i)}\right)\right)^2 \tag{5.9}$$

where T_1 is the historical and predicted torque observation of EM1.

Finally the optimized torque reference T_{1_ref} of EM1 is obtained with nonlinear interpolation by using the optimized θ_i^* :

$$T_{1\_ref}^{(t)} = T_{\theta^*}(t) = \theta_2^* t^2 + \theta_1^* t + \theta_0^* \tag{5.10}$$

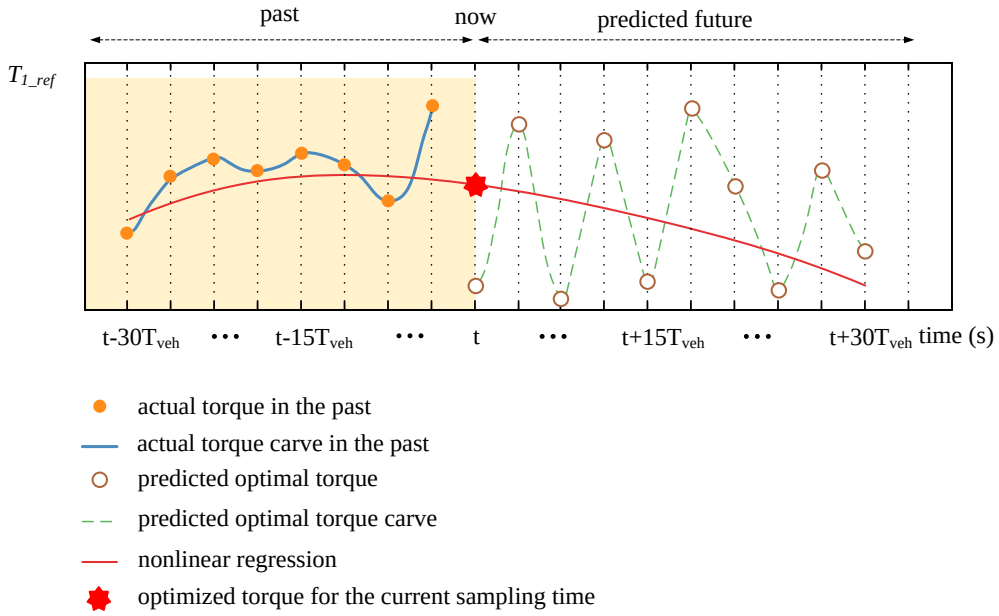

Figure. 5.12. Predictive-based power split strategy

5.4.3 Comparisons of MCM power split strategies

In the above subsections, two kinds of MCM power split strategies are developed. In this subsection, these strategies will be compared in terms of machine operating characters and vehicle energy consumption.

Taking UDDS as an example, Fig. 5.13 to Fig. 5.14 indicates the torque carves of both EMs in MCM with the strategies in [Han.S 2015] and in this thesis. It can be seen that the I-PM-SM is more frequently used and the IM is mainly used for traction. Sometimes, the IM helps to provide regenerative braking force.

With the optimal-efficiency strategy, both EMs have bad operating characters, since the strategy only concentrates on the instant efficiency. It is reflected in the phenomena of frequent stop and start (e.g. around 200s), as well as torque oscillation. This may result in noise and vibrations. This occurs especially when the demand power changes sharply. The deterministic rule-based strategy improves the EM operating character to a certain extent, but the tendency of torque variations of both EMs have changed obviously than that with the optimal-efficiency strategy. This will reduce the system efficiency and increase the energy consumption. With the strategies proposed in this thesis, the torque variations are improved with ANFIS-based strategy, since the strategy defines a smooth rule-surface according to the membership functions. The EMs stop and start more rarely, but still with some torque oscillation (i.e. around 600s and 1000s). The torques are better smoothed with the predictive-based strategy, since it does not only focus on the system efficiency, but also takes care the historical and predicted torques. Thanks to the nonlinear regression, the strategy could make the torque get close to the optimum, and the interpolation avoids the torque oscillation.

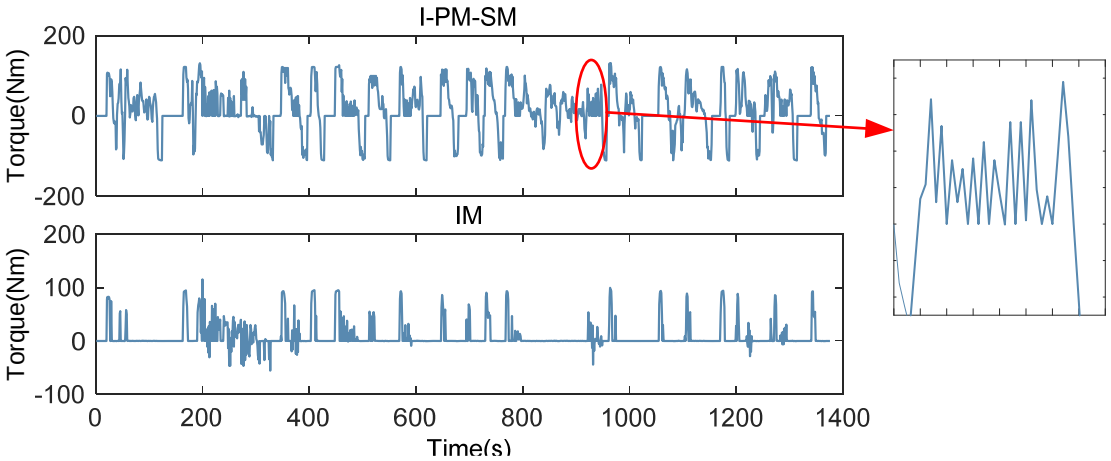

(a) Optimal-efficiency strategy

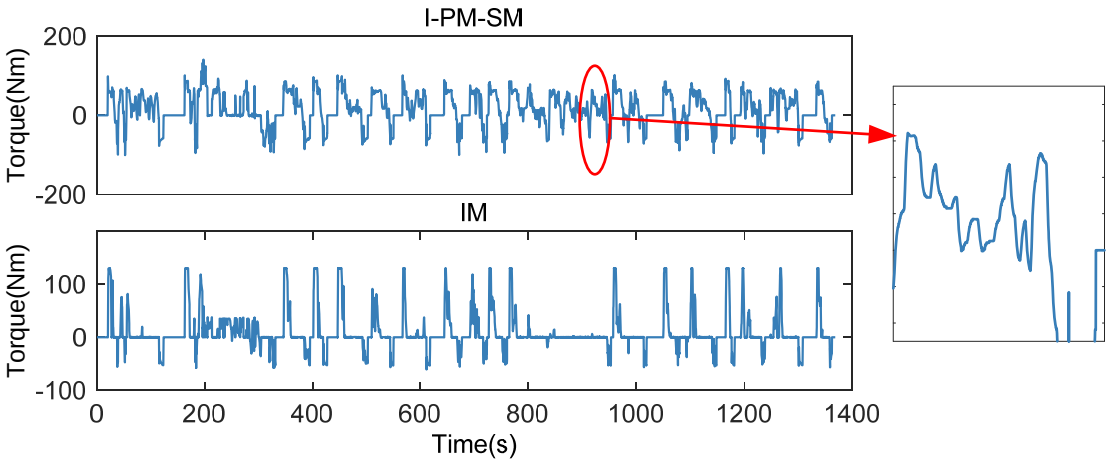

(b) Rule-based strategy

Figure. 5.13. Torque carves with the power split strategies in [Han.S 2015]

Table. 5.3 indicates the statistics of EM operating characters. The predictive-based strategy has the least stop and start times, which are about half of those the optimal strategy. While the deterministic rule-based strategy and the ANFIS-based strategy lead to the similar EM operating characters.

Table. 5.3. Start/Stop times of different strategies

	Strategies	I-PM-SM	IM
In [Han.S 2015]	Optimal-efficiency strategy	219	132
	Rule-based strategy	136	104
This thesis	ANFIS-based strategy	145	92
	Predictive-based strategy	103	69

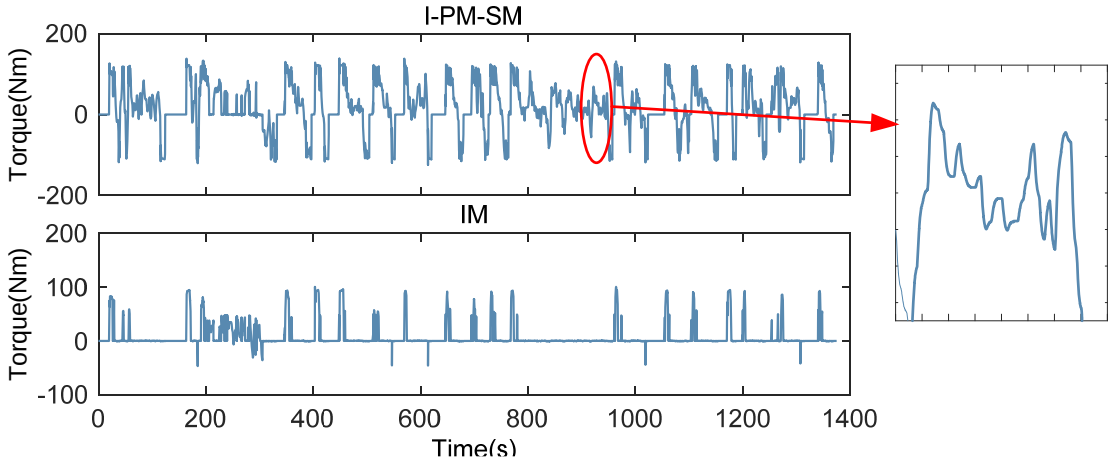

(a) ANFIS-based strategy

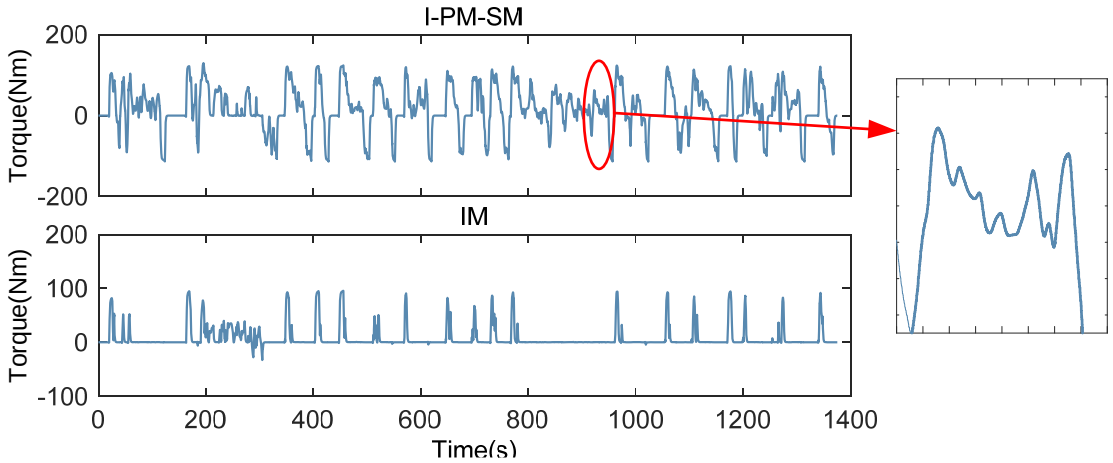

(b) Predictive-based strategy

Figure. 5.14. Torque carves with the power split strategies in this thesis

Table .5.4 shows the energy consumptions of the MCM-based EV with different power split strategies. It can be seen the least energy is consumed with the optimal-efficiency strategy, since it can ensure the optimal system efficiency for any power demand. The predictive-based strategy optimizes the EM power using nonlinear regression, the actual torque of the EMs are closer to the optimal torques. Although the efficiency is sacrificed to some extent, the energy consumption is still low. In contrast, the ANFIS-based strategy results in more energy consumption, because the limited number of membership functions weaken its ability to approximate the optima. It can be inferred that increasing the number of membership functions in the ANFIS could improve the system efficiency, but too many membership functions would overfit the fuzzy surface, which is not conducive to optimize the EM operating character. The deterministic rule-based power split strategy has the most energy

consumption, which is mainly caused by the rule switching between different regions. It tries to smooth the torque characters by a set of rules, nevertheless, these rules have limited ability to maximize the system efficiency.

Table. 5.4. Energy consumptions of different strategies

	Strategy	UDDS	UDDSHDV	WLTC	HWFET
In [Han.S 2015]	Optimal-efficiency strategy	6.24	4.75	14.35	1.37
	Rule-based strategy	6.44	4.91	14.75	1.41
The thesis	ANFIS-bases strategy	6.37	4.83	14.66	1.39
	Predictive-based strategy	6.30	4.81	14.53	1.38

5.5 MCM power split strategy validation

In in section, Hardware-In-the-Loop (HIL) simulation will be used to validate the MCM power split strategy in real time. This experiment is carried out with the platform in Harbin Institute of Technology (China). HIL simulation is a technique that being used in the development and test of a complex real-time systems [Bouscayrol.A 2009]. Generally, full-scale HIL simulations are used because the objective is to test the real device to be inserted in the complete system. Nevertheless, the MCM prototypes that could be used for HIL does not match the powers of the demanded MCM (see parameters in Table. 5.5). In this case, reduced-scale HIL simulations are used as intermediary steps [Allegre.A 2010].

Table. 5.5. Parameters of MCM system

Parameters	Demanded MCM		MCM prototypes	
	EM1	EM2	EM1	EM2
Rated power P_N (kW)	9.8	17.2	4	8
Rated speed Ω_N (rad/s)	132	185	200	400
Rated torque T_N (Nm)	74	93	20	20
Maximal speed Ω_{max} (rad/s)	472	472	400	600
Maximal torque T_{max} (Nm)	130	140	40	40

5.5.1 Methodology of the reduce-scale HIL

The following methodology is used to progressively build this reduced-scale HIL simulator. Firstly, the full-scale traction system is simulated, including the energy sources, electric drive, mechanical power train, and their controls, as shown in Fig. 5.15. The models and controls are corresponding to the model and control in Fig. 5.3. In this structure, all the systems are in full-scale, and it can provide some initial validation and analysis of the system.

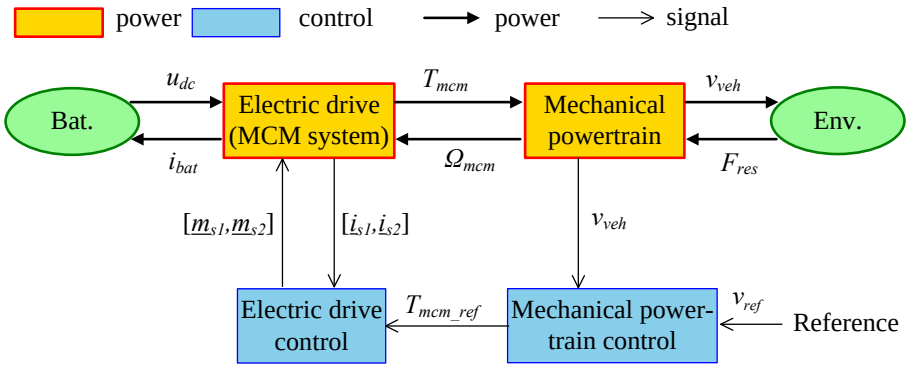

Figure. 5.15. Principle of the full-scale system

In the second step, the full-power MCM system and control in the simulation will be replaced by the reduced-power MCM system and control. The simulated full-scale power EV mechanical transmission and environment are not changed. Power adaptations (rectangle with 2 oblique bars) are required to adapt the reduced and full scale parts [Allegre.A 2010]. In this way, the power adaptation can be studied in simulation before a real-time implementation (Fig. 5.16).

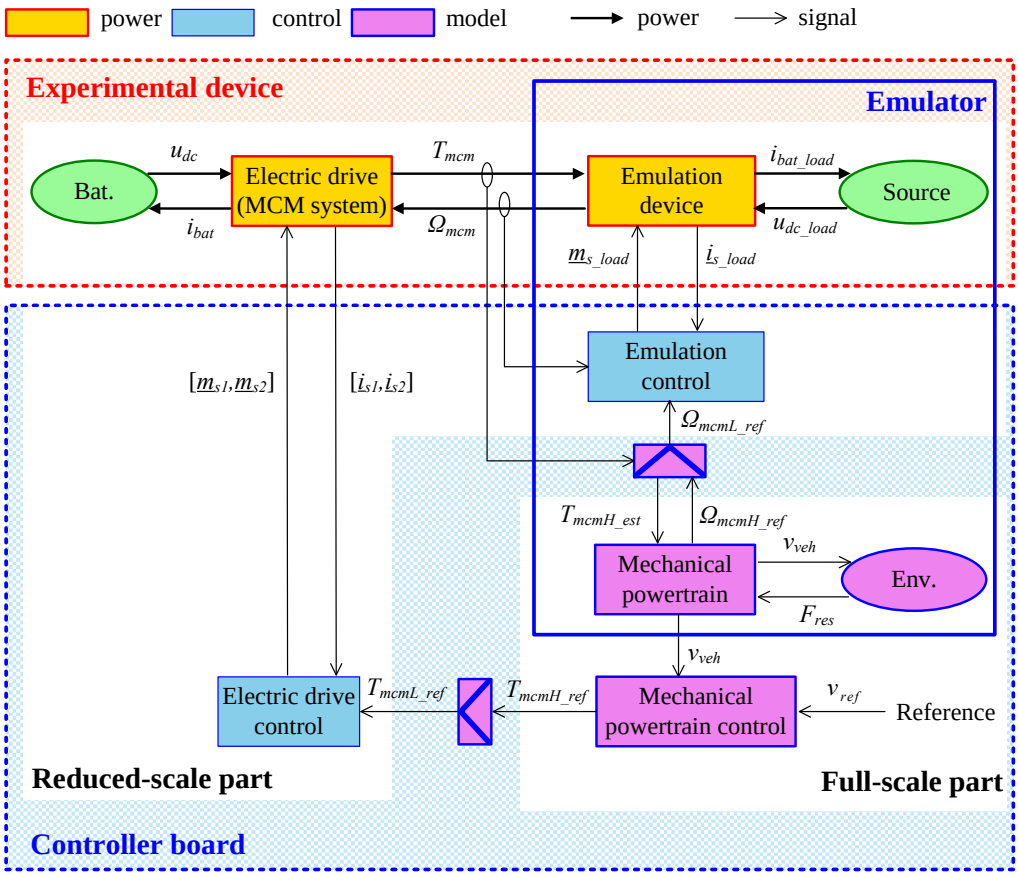

Figure. 5.16. Integration of the interface subsystem (emulation drive)

Torque coefficients k_T is defined between the demanded torque T_{mcmH} of the high-

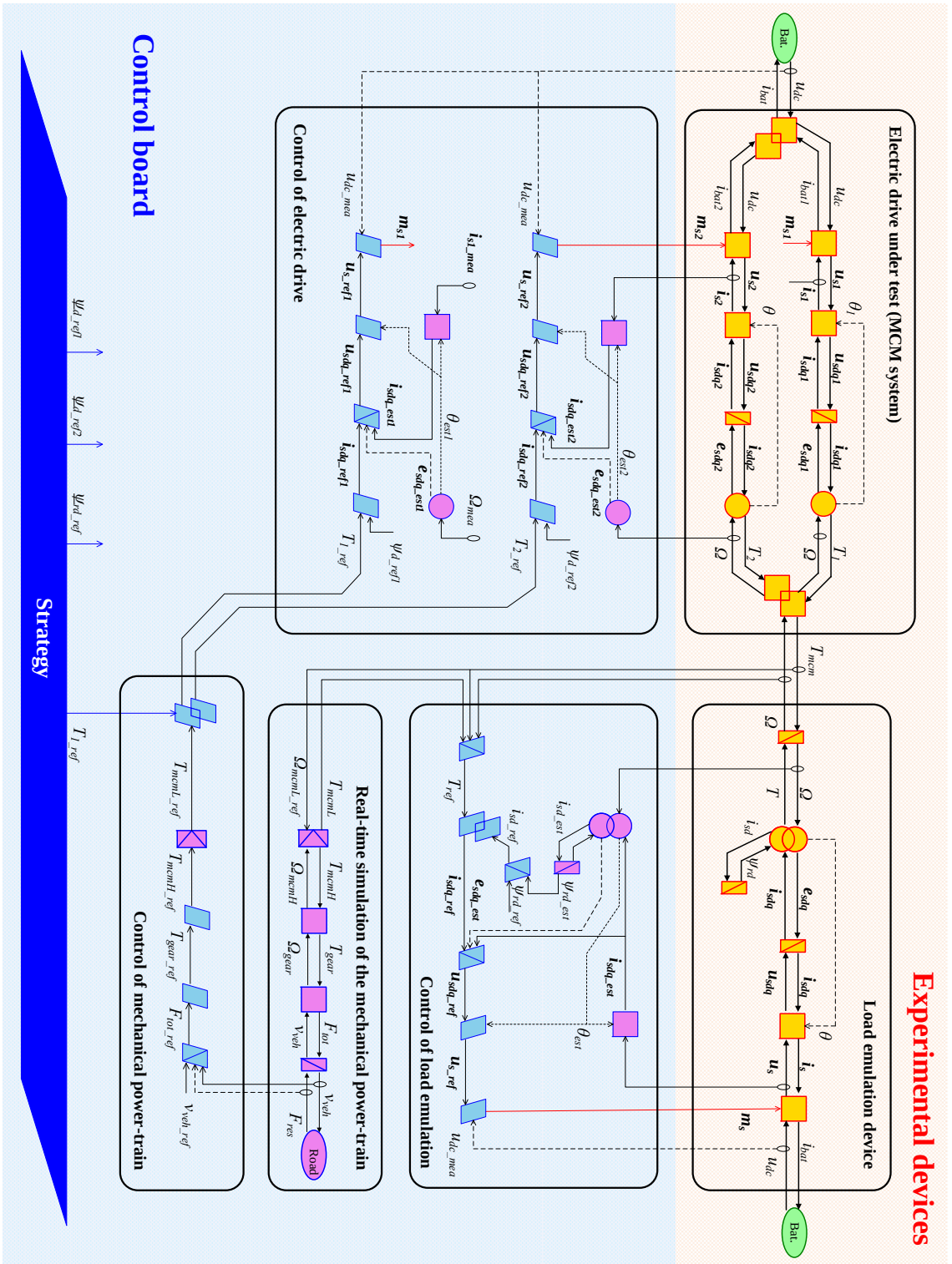

Figure. 5.17. Simulation structure of the reduced-scale HIL

power subsystems and the torques T_{mcmL} of the low-power subsystems. In the same way, speed coefficients k_Ω is defined by the speed of high-power subsystems Ω_{mcmH} and low-power subsystem Ω_{mcmL} :

$$\begin{cases} T_{mcmH} = k_T T_{mcmL} \\ \Omega_{mcmH} = k_\Omega \Omega_{mcmL} \end{cases} \tag{5.11}$$

Both adaptation coefficients must be carefully chosen in order to respect the non-linear curve of the maximal torque versus rotation speed [Allegre.A 2010]. The control of the mechanical power-train delivers the torque reference T_{mcmH_ref} for the high-power mechanical system. The control of the reduced-scale drive requires a torque reference T_{mcmL_ref} being associated with the low-power part. Thus, relationship of Eq. (5.11) is inverted:

$$T_{mcmL\_ref} = T_{mcmH\_ref} \frac{1}{k_T} \tag{5.12}$$

Finally, a load emulation drive must be connected to the reduced-scale drive in order to impose the same behavior as the mechanical power-train. The load emulation EM shares the same shaft as the MCM system, which leads to the common speed Ω from the load torque T and MCM torque T_{mcm} :

$$J \frac{d\Omega}{dt} = T_{mcm} - T \tag{5.13}$$

where J is the total initial of the experimental setup.

5.5.2 Real-time implementation

EMR and control of the studied system and of the experimental set-up are merged in Fig. 5.17. However, the model of the reduced-scale part (electric drive, emulation device, etc.) are replaced by their real components. The hardware parts are then inserted in the simulation loop. A dSPACE 1005 controller board is used to control the experimental set-up, and to simulate the full-scale mechanical system.

For the experimental setup, the traction system (MCM system) is composed of 2 EMs (see Table. 5.5) supplied independently by 2 converters. Both converters share the same DC bus with the voltage of 380 V. The shafts of both traction EMs are connected end-by-end. The output shaft of the MCM system is coupled to an load EM which is supplied by a four-quadrant converter and another DC bus with the voltage of 380 V. The power adaption coefficients are set to $k_T = 2$ and $k_\Omega = 1.1$. The power scale of both traction machines in MCM system is 2.2. Experimental setup is shown in Fig. 5.18.

The simulation program has been developed in Matlab–Simulink, using EMR. The control blocks are directly compiled to dSPACE using Real-Time Interface (RTI) and Real-Time Workshop (RTW) interface.

Figure. 5.18. Experimental platform of the reduced-scale HIL

5.5.3 Experimental results

Selecting a simple driving cycle (NEDC) to test the experiment setup and MCM power split strategy. The developed 2 MCM power split strategies are integrated into the dSPACE controller board, and the optimal-efficiency strategy is used for comparison.Some experimental results are obtained.

Both prototypes in MCM can work individually, but with the optimal-efficiency strategy, there is some torque oscillations (Fig. 5.19). That means the torque of an EM jumps to another value with a high slop ratio, then it changes after holding a very short duration. This is caused by the nonlinear properties of efficiency distribution. Torque oscillation is frequently observed for EM2 (for example, around 680 s, 770 s and 820 s). Actually, when the torque oscillation occurs, obvious mechanical noise and vibration are observed. For the distribution of operating points (Fig. 5.20), EM1 has more operations points located in the low speed area (speed lower than 200 rad/s), since it has a lower base speed, which complies with the efficiency distribution properties. In the high speed area (speed higher than 200 rad/s), EM2 works more, and EM1 works for torque assistance when there is a large demand torque, since EM2 is more efficiency than EM1 in high speed area.

For the ANFIS-based strategy, it ensures the similar torque revelation tendencies as the optimal-efficiency strategy (Fig. 5.21). Fortunately, the torque oscillation is reduced, and the noise and vibration are also reduced to some extent. Nevertheless, the limited number of fuzzy rules leads to some considerable shifts than the optimal operating points. For example, with the optimal-efficiency strategy, only EM2 works around 30s, but with the ANFIS strategy, both EMs work. This can also be observed around 110s, 200s, 305s, etc. It would result in the increase of energy consumption. The operating points of both EMs are more concentrated in some small groups than the optimal-efficiency strategy (Fig. 5.24). Since the ANFIS fuzzyfied the demand torque and speed by corresponding membership functions, so that the power

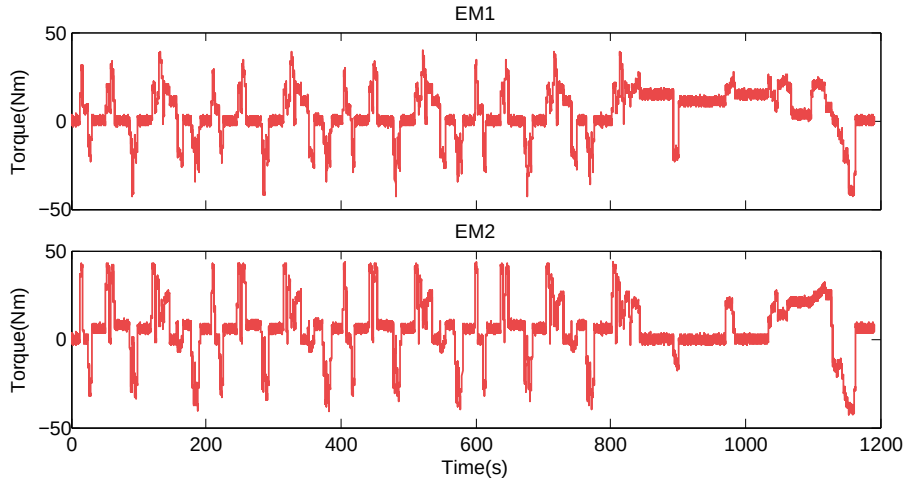

Figure. 5.19. Torque estimations with optimal-efficiency strategy

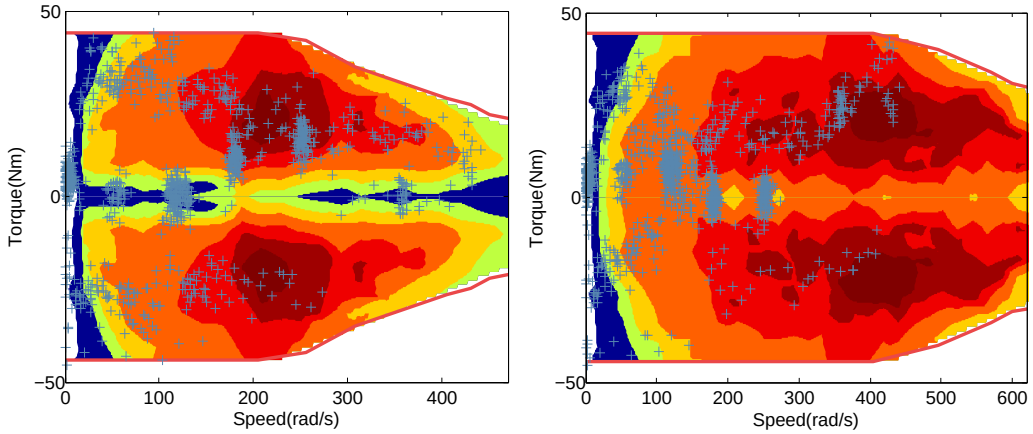

(a) EM1 (b) EM2

Figure. 5.20. Operating points with optimal-efficiency strategy

demands with small difference may result in the same fuzzy output.

For the predictive-based strategy, the torques of both EMs are much better smoothed than the 2 strategies above, especially for EM1 (Fig. 5.23). Even there is still slight oscillation for EM2, the variational range is much smaller. As a result, mechanical noise and vibrations are reduced obviously during the experiment. It proves that the proposed predictive-based strategy can better improve the operating characters of the MCM. As for the operating points distribution, there also exist some small concentrated groups, but they are not concentrated as that of with the ANFIS strategy, as shown in Fig. 5.24. Since the predictive-based strategy optimizes the present torque according to the predicted optimal torques and the actual torques in the past, thus the torque variation by predictive-based strategy is more close to that of with the optimal-efficiency strategy. This results complies with the simulation.

Except from the characteristics of the MCM, power of the DC bus could be observed

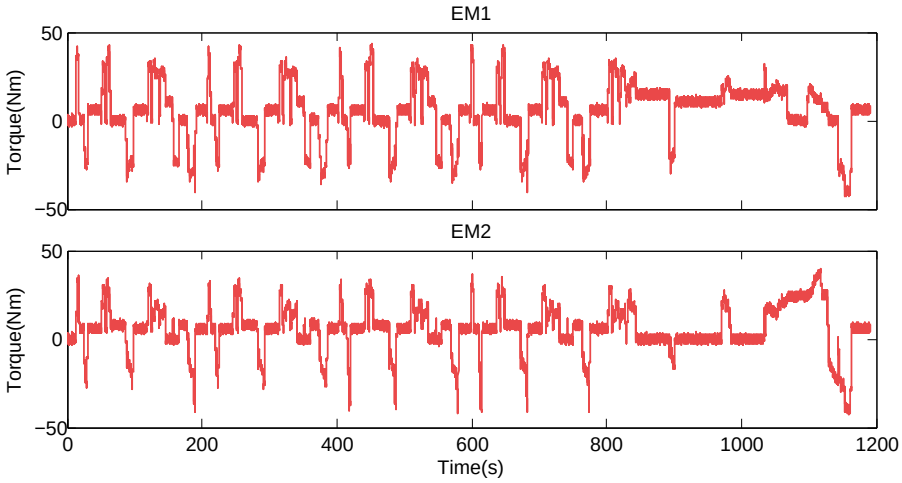

Figure. 5.21. Torque estimations with ANFIS-based strategy

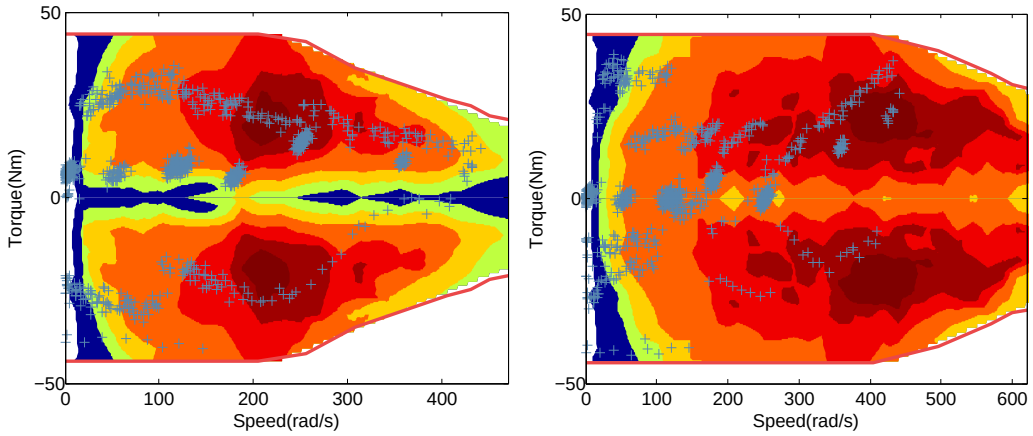

(a) EM1 (b) EM2

Figure. 5.22. Operating points with ANFIS-based strategy

in order to analysis the energy consumptions with different strategies. The DC bus comes from a 3-phase rectifier, which is connected to the grid through a transformer. The filter capacitor is so large that the DC bus is treated a constant. The current in the DC bus is measured then the power of DC bus is observed (Fig. 5.25). In that way, the efficiencies of the MCM inverters are also taken into account implicitly. It is indicated that with the 3 strategies, the DC bus has the similar tendencies. It complies with the powers of the vehicle, which is related to the driving cycle. Nevertheless, there exists small differences. The optimal-efficiency strategy has the highest system efficiency so that it requires the least power from the DC bus (in traction mode). Similarly, the DC bus with ANFIS-based strategy has a highest power, and it is in the middle with the predictive-based strategy.

Then the energy consumptions are calculated by integrating the powers with time. Fig. 5.26 shows the energy consumption of the MCM. It is indicated that the optimal-efficiency strategy has the lowest energy consumption, then followed by

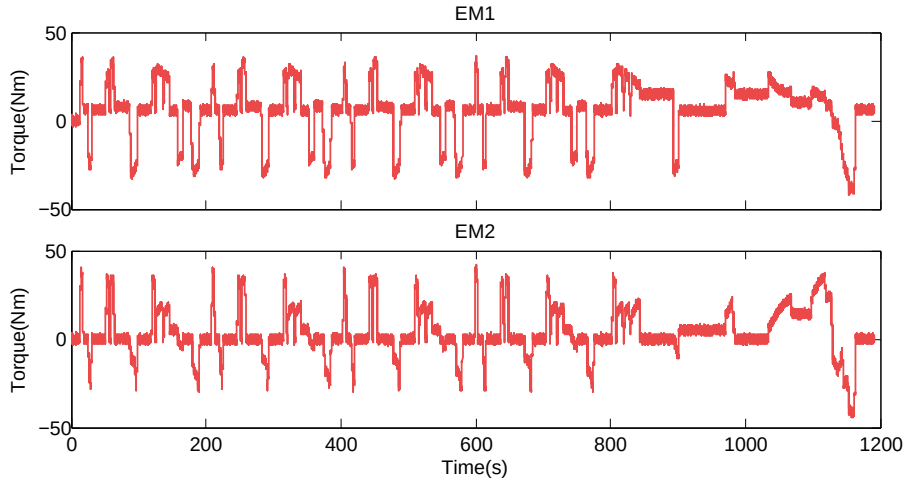

Figure. 5.23. Torque estimations with predictive-based strategy

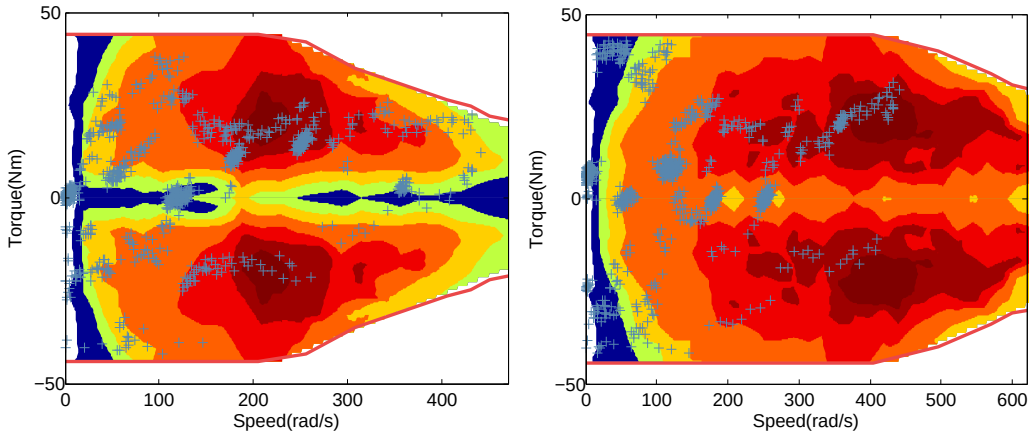

(a) EM1 (b) EM2

Figure. 5.24. Operating points with predictive-based strategy

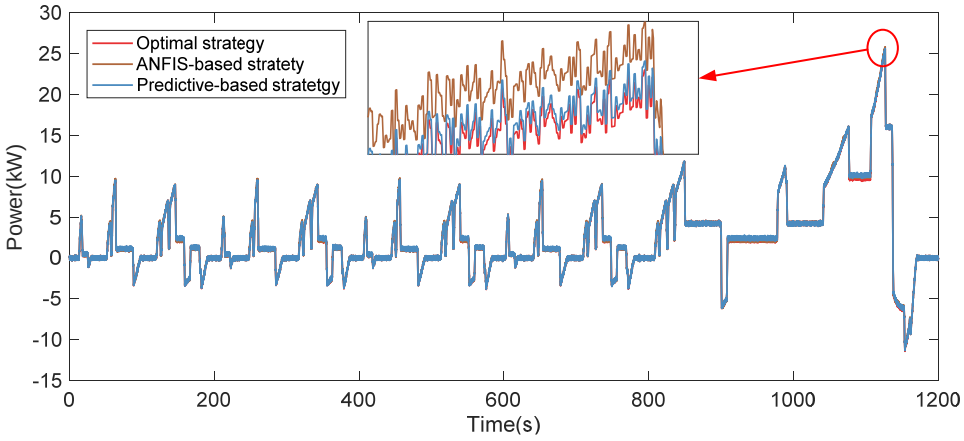

Figure. 5.25. Power of the DC bus

the predictive-based strategy (increased by 1.4%). The ANFIS-based strategy leads to the most energy consumption (increased by 2.45%). This real-time validation proves that the optimal-efficiency strategy can have the lowest energy consumption, but the EMs have bad operating characters. The predictive-based strategy improved the EMs operating character by sacrificing the efficiency, but the increase of energy consumption is acceptable. Additionally, the experimental energy consumptions are higher than those by simulation. This is mainly caused by the mechanical losses. Since there are 3 EMs being connected by sharing the same shaft, the concentricity is difficult to be guaranteed, which leads to more energy consumptions.

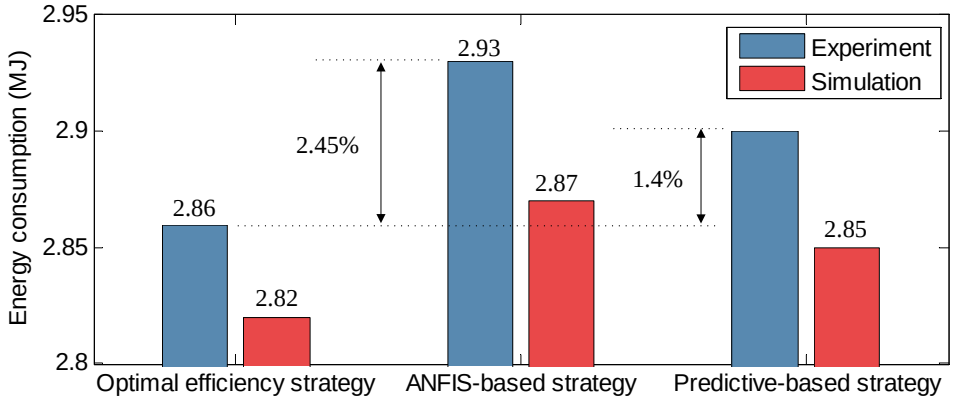

Figure. 5.26. Comparison of energy consumption

5.6 Conclusion

This chapter aims at developing different power split strategies for a MCM system.

The main works of this chapter are the following.

(1) The MCM is designed by FEM according to the sizing result in chapter 4.

(2) The problem of MCM power split is described, and a hybrid series MCM is selected for developing the power split strategy.

(3) An ANFIS-based strategy and a predictive-based strategy are developed, they are compared in simulation and experiment.

The main conclusion and contribution are summarized.

(1) The proposed velocity prediction model based on wavelet transform and neural network effectively improves the accuracy of velocity prediction. The predictive-based strategy combines the historical and prediction data, the operating character of the EMs in the MCM system are improved.

(2) The real-time validation proves that the optimal-efficiency strategy can have the lowest energy consumption, but the EMs have bad operating characters,

and the setup has obvious noise and vibrations. The ANFIS-based strategy reduces the noise and vibrations to some extent. Nevertheless, the consumed energy is increased by 2.45%. The predictive-based strategy improved the EMs operating character, the noise and vibrations are reduced significantly. The energy consumption is increased only by 1.4%. Hence the predictive-based strategy is appropriate for MCM.

Conclusion

Modular Connected Machines (MCM) system is a kind of multi-machine system where several machines are integrated into a module. It has wider high-efficiency area, better fault tolerance ability and numerous operation modes. It has potentiality in the fields of electrified vehicles. Meanwhile, this multi-machine system also leads to some complex problems, such as sizing and power split of a MCM. The objective of this PhD subject is to develop different kinds of MCM systems for electrified vehicles. The main contribution and conclusions of this thesis are summarised the following:

Chapter 1 deals with the context and objective of this PhD subject. First, summarising the development of traction EM, then highlighting the state-of-art of the traction systems. Next, the key challenges of multi-machine system are compared, and some methods that related to the study of MCM are summarised. Finally the objective of this PhD subject is introduced. In conclusion, multi-machine systems are developed more and more for electrified vehicles. They offers more degree of freedom in sizing, control and energy management that can increase the global efficiency. MCM is thus a category of multi-machine system.

Chapter 2 focuses on the modelling and control of a MCM-based vehicle, which is organised by Energetic Macroscopic Representation (EMR). Then the control of the MCM-based vehicle is deduced step-by-step according to inversion rules. The complete model and control of a MCM-based vehicle that considers all the component losses lay a foundation for the work of the following chapters. It has been proved that the use of EMR provides a clear way of organization of a complex system. It highlights the interactions between each subsystem and emphasises the important couplings that distribute energy. It makes possible to systematically deduce the control scheme of the system according to inversion rules.

Chapter 3 studies the fast efficiency map estimation method for IM and PM-SM. It is the means to establish the objective function of MCM sizing when the

EM design specifications have not been eventually defined and the EMs have not been designed. The proposed method is validated by comparison with experimental efficiency maps. The proposed method does not need EM pre-design and only 4 basic parameters are required (rated speed, rated torque, maximal speed and maximal torque). Neither FE nor experimental data (inductance and resistance) is used. It has been proved that the proposed method can evaluate an efficiency map within 0.2 s. Meanwhile, the errors of energy consumption of the vehicle with the estimated and experimental efficiency maps are less than 3.2%. Therefore, the speed and accuracy of the proposed efficiency map estimation method satisfies the requirements of MCM sizing methods. This method is only suitable in MCM sizing to determine the EM design specifications, once the specifications are finally defined, the EMs have to be designed by finite element method for more accurate characters.

Chapter 4 deals with the sizing method of different MCM systems. A MCM sizing method based on multi-objective optimization is proposed. Then different MCM sizing results are analysed and compared for different vehicles. It has been proved that with the proposed MCM sizing method, the MCM high-efficiency area is expended, the torque density is increased and the usage amount of PM is reduced. It enables to optimize the comprehensive characteristics of a MCM. A hybrid MCM with one IM and one IPM-SM has the best comprehensive properties. It has larger high-efficiency area, and almost 44% of the PM is saved in comparison with the PMSM-based MCM system, which makes this hybrid MCM system a valuable alternative. The proposed hybrid coupling MCM system based on planetary gear-train changes the 'speed' coupling of the series and parallel MCM. It can not only optimize the EM torque, but also can optimize the EM speed, thus it has better system efficiency. Moreover, the study shows that MCM system is of interest for pure EVs and series HEVs in terms of energy reduction. The series MCM is more competitive in terms of efficiency and complexity. A MCM with 2 EMs has the highest average energy reduction rate, and the highest ratio of energy reduction to investment.

Chapter 5 deals with the power split strategy of the MCM system. Firstly, the selected MCM is designed by finite element method based on the sizing result, in order to obtain more accurate efficiency maps. Then an ANFIS-based strategy and a predictive-based strategy are developed and compared. Filially, different strategies are validated in real time. The study shows that the proposed velocity prediction model can improves the accuracy of velocity prediction. The predictive-based strategy combines the historical and prediction data, the operating characters of the EMs in the MCM system are improved. The real-time validation proves that the optimal-efficiency strategy leads to the lowest energy consumption, and obvious noise and vibrations of the setup. With the ANFIS-based strategy, the noise and vibrations of the setup are reduces to some extent. Nevertheless, the energy consumption is increased by 2.45%. With the predictive-based strategy, the noise and vibrations are reduced significantly. And the energy consumption is increased only by 1.4%. In conclusion, the predictive-based strategy is appropriate for MCM power split regarding the efficiency and EMs operating characters.

Perspectives:

The following work could be of interest in the future work:

1. As a multi-machine system, the coordinate work of all the EMs are important to have a good system performance. It has been shown that noise and vibration may occur in some cases. In this thesis, only the system level solution are studied. Hence it could be of interest to study the noise and vibration in component level.

2. In MCM, all the EMs are independent and each of them is supplied by their own inverter. The power split strategies of a MCM with the aim of improving system efficiency and EM operating characters have been studied in chapter 5. Nevertheless, it only considers the normal operation, the fault tolerance during failure case is still remained to be studied.

3. Before integrating a MCM in a real vehicle, it is necessary to test the system and control by Hardware-In-the-Loop (HIL) simulation. In chapter 5, a reduced-scale HIL is used due to the limitation of the facilities. Thus it could be of interest to design and manufacture the full-scale prototypes and conduct the full-scale HIL.

A

Appendix

Contents

A.1 Energetic Macroscopic Representation 128
A.2 Planetary gear-train 130
A.3 Optimal strategy of a MCM-based vehicle 131
A.4 Optimal-efficiency strategy of a MCM system 134
A.5 Properties of different wavelet mother functions 135

A.1 Energetic Macroscopic Representation

EMR has 4 kinds of elements (Table. A.1). Source element (green ovals) is the terminal of the system, it is used to generate or receive energy. Regarding to the specific action/reaction relationships, a complex subsystem can be treated as an equivalent source element. For example, a battery and an ICE could be regarded as voltage source and torque source respectively. Conversion element (orange various) ensures the energy conversion without energy accumulation. Square and circle pictograms corresponding to the mono and multi-domain conversions. Accumulation element (orange rectangular pictograms with an oblique bar) converts energy with energy storage. Hence there will be some delay from input to output. Then coupling element (overlapped orange various) can be used to split or merge different power flows, and it is the key elements for energy management. Similar to conversion elements, the overlapped square and circle corresponding to the mono and multi domain couplings. All these elements are connected through exchange vectors according to the principle of action and reaction.

Table. A.1. Basic EMR elements

Source	Conversion	Accumulation	Coupling
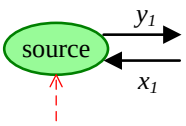	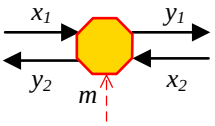	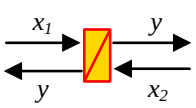	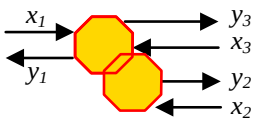

Generally, a certain system has unique EMR formalization and unique Maximal Control Scheme (MCS), which is composed of the maximum of control operations and measurements [Bouscayrol.A 2012].

Conversion elements can be inverted directly:

$$y(t) = kx(t) \quad \longrightarrow \quad x_{ref}(t) = \frac{y_{ref}(t)}{k} \tag{A.1}$$

On the contrary, accumulation elements are inverted using controllers $C(t)$ due to the integration relationship. Direct inversion will result in derivation, which is not allowable in a real system. $C(t)$ could de be PI, IP, PID or other advanced controllers.

$$y(t) = \int x(t)dt + y(0) \quad \longrightarrow \quad x_{ref}(t) = C(t)\left[y_{ref}(t) - y_{mea}(t)\right] \tag{A.2}$$

Moreover, inversion of coupling elements requires criterion inputs, which allocate the energy distribution criterion within the system:

$$y(t) = x_1(t) + x_2(t) \quad \longrightarrow \quad \begin{cases} x_{1\_ref}(t) = y_{ref}(t)\, k_t(t) \\ x_{2\_ref}(t) = \left[1 - k_t(t)\right] y_{ref}(t) \end{cases} \tag{A.3}$$

Fig. A.1 shows some examples of inversion-based control. Based the above inversion rules, the model of a system can be inverted. Suppose all the variables are measurable, one can deduce a MCS systematically. In practice, some simplifications can be made based on the requirements and compromises, since some variables are not measurable as expected. Therefore, some estimations are required. In order to obtain the required estimator, parts of the EMR can be copied directly.

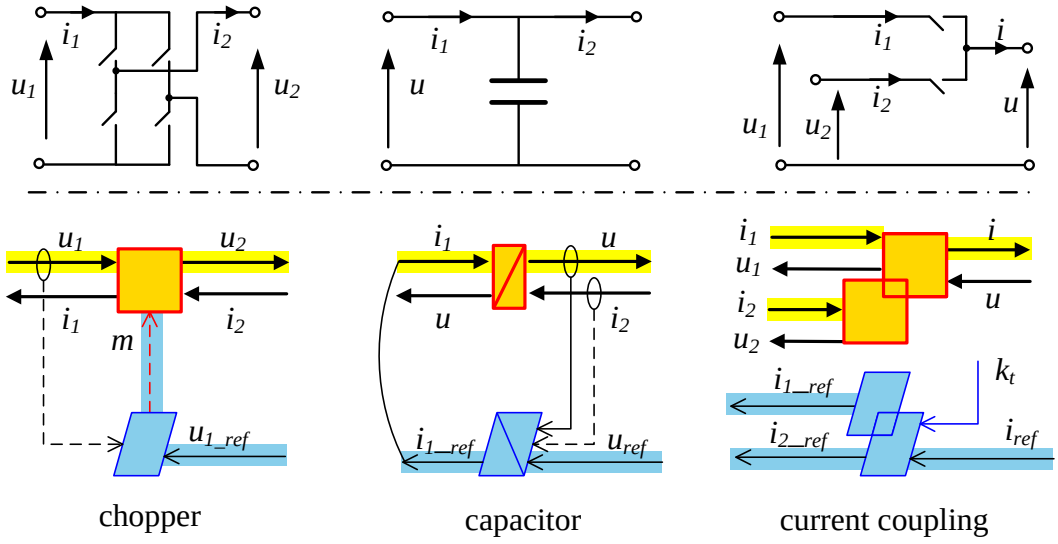

Figure. A.1. Examples of inversion-based control

A.2 Planetary gear-train

The structure of a planetary gear-train is show in Fig. A.2. Generally, there are 3 shafts, but with only 2 independent state variables in a planetary gear-train. The relationship between the torques and speeds could be described by:

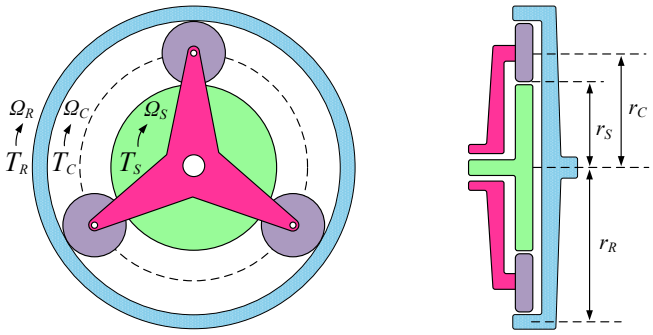

Figure. A.2. Structure of the planetary gear-train

$$\begin{cases} \Omega_C = k_R \Omega_R + k_S \Omega_S \\ \Gamma_R = k_R T_C \\ T_S = k_S T_C \end{cases} \tag{A.4}$$

with

$$\begin{cases} k_R = \dfrac{r_R}{2r_C} \\ k_S = \dfrac{r_S}{2r_C} \end{cases} \tag{A.5}$$

where T_R, T_C, T_S and Ω_R, Ω_C, Ω_S are the torques and speeds of the ring gear, carrier and the sun gear, r_R, r_C and r_S are the radius.

A.3 Optimal strategy of a MCM-based vehicle

The cost function of the optimal power split strategy of a MCM-based vehicle is to minimize the energy consumption (fuel consumption for HEV and electrical energy consumption for pure EV). Thus the cost function J is defined as:

$$J = \sum_{k=0}^{N} g^{(k)} \left(x^{(k)}, u^{(k)} \right) \tag{A.6}$$

$$g^{(k)} \left(x^{(k)}, u^{(k)} \right) = (\tau_1 \vee \tau_2) \, \dot{f}_{ice}^{(k)} + (1 - \tau_1)(1 - \tau_2) \, u_{dc}^{(k)} i_{bat}^{(k)} \tag{A.7}$$

where g is the cost function for each sub-problems, N is the number of sub-problems, the superscript (k) represents the k^{th} sub-problems, x is the state variable and u is the control variable, τ_1 and τ_2 is the selecting coefficients for different vehicles, their definition could be found in Table. A.2, $\vee$ is the logical operator of 'or', $\dot{f}_{ice}$ is the fuel consumption of the ICE.

Table. A.2. Selecting coefficients in terms of different vehicles

	τ_1	τ_2
Pure EV	0	0
Series HEV	0	1
Parallel HEV	1	0

The fuel consumption $\dot{f}_{ice}$ (gram per second) is calculated from the operating points of torque T_{ice_ref} and speed Ω_{ice} using a fuel map as the following:

$$\dot{f}_{ice}^{(k)} = \dot{f}_{ice}^{(k)} \left(T_{ice}^{(k)}, \Omega_{ice}^{(k)} \right) \tag{A.8}$$

with

$$\begin{cases} T_{ice}^{(k)} = (\tau_1 \vee \tau_2) \, T_{ice\_ref}^{(k)} \\ \Omega_{ice}^{(k)} = \tau_1 \Omega_{trans}^{(k)} + \tau_2 \Omega_{ice\_ref}^{(k)} \end{cases} \tag{A.9}$$

Similarly, the battery current i_{bat} is the sum of electric drive current i_{batd} and generation drive current i_{batg}. Of course, the generation drive current i_{batg} only exists for a series HEV:

$$i_{bat}^{(k)} = \tau_2 i_{batg}^{(k)} + i_{batd}^{(k)} = \tau_2 \frac{T_g^{(k)} \Omega_g^{(k)}}{u_{dc}^{(k)} \eta_{ge}^{(k)} \eta_{invge}^{(k)}} + \sum_{i=1}^{m} \frac{T_i^{(k)} \Omega_i^{(k)}}{u_{dc}^{(k)} \eta_{emi}^{(k)} \eta_{invi}^{(k)}} \tag{A.10}$$

with

$$\begin{cases} T_g^{(k)} = \tau_2 T_{ice}^{(k)} \\ \Omega_g^{(k)} = \tau_2 \Omega_{ice}^{(k)} \end{cases} \tag{A.11}$$

where m is the number of EMs in MCM.

In this optimization problem, we can choose State-of-Charge (SoC) of the battery as a state variable $x = SoC$, then:

$$x^{(k+1)} = x^{(k)} - \frac{i_{bat}^{(k)} \eta_{bat}^{(k)}}{3600 C_{bat}} \tag{A.12}$$

where C_{bat} is the battery capacity, η_{bat} is the battery charging or discharging efficiency:

$$\eta_{bat} = \begin{cases} 1 & i_{bat} \geq 0 \\ 0.9 & i_{bat} < 0 \end{cases} \tag{A.13}$$

The battery is considered as a voltage source in series with a resistance, its output voltage u_{dc} is derived by the following relationship:

$$u_{dc}^{(k)} = u_{oc}^{(k)} \left(x^{(k)} \right) - R_{bat} \left(x^{(k)} \right) i_{bat}^{(k)} \tag{A.14}$$

where u_{oc} and R_{bat} are the open circuit voltage and battery resistance, which are in a function of SoC.

The control inputs varia in a function of vehicle type. By utilizing the selecting coefficients, the control variables could be expressed in the following way:

$$\begin{aligned} u^{(k)} = & (1-\tau_1)(1-\tau_2) \begin{bmatrix} T_{1\_ref}^{(k)} & \cdots & T_{(m-1)\_ref}^{(k)} & k_{bf}^{(k)} & k_{reg}^{(k)} \end{bmatrix} \\ & + \tau_1 \begin{bmatrix} T_{1\_ref}^{(k)} & \cdots & T_{(m-1)\_ref}^{(k)} & T_{ice\_ref}^{(k)} & k_{bf}^{(k)} & k_{reg}^{(k)} \end{bmatrix} \\ & + \tau_2 \begin{bmatrix} T_{1\_ref}^{(k)} & \cdots & T_{(m-1)\_ref}^{(k)} & T_{ice\_ref}^{(k)} & \Omega_{g\_ref}^{(k)} & k_{bf}^{(k)} & k_{reg}^{(k)} \end{bmatrix} \end{aligned} \tag{A.15}$$

Once defined the cost function J, state variable x and the control variable u, the optimization should also respect some physical constraints.

(1) MCM constraints

Whatever the configuration of MCM, the system torque and power cannot be lower than the demand. Regarding to different MCM structures, the MCM constraints are given by:

$$\begin{cases} |T_{mcm\_ref}| \leq \tau_{se} \sum_{i=1}^{m} |T_{i\_max}| + (1-\tau_{se}) \sum_{i=1}^{m} T_{i\_max} \prod_{j=i+1}^{m} k_j \\ |P_{mcm\_ref}| \leq \sum_{i=1}^{m} |P_{emi\_ref}| \end{cases} \tag{A.16}$$

with:

$$T_{i\_max} = -T_{i\_min} = \begin{cases} T_{emi\_max} & (\Omega \leq \Omega_{iN}) \\ \dfrac{T_{emi\_max} \Omega_{iN}}{\Omega} & (\Omega_{iN} < \Omega \leq \Omega_{imax}) \end{cases} \tag{A.17}$$

where τ_{se} is the selecting coefficient.

What is more, the torque and speed of each EM in MCM should work in their feasible range:

$$\begin{cases} 0 \leq \Omega_i \leq \Omega_{imax} \\ T_{i\_min} \leq T_i \leq T_{i\_max} \end{cases} \tag{A.18}$$

(2) Battery constraints

The power of the battery varies in a function of SoC, hence the battery power P_{bat} should be limited in its feasible range:

$$P_{bat\_min} \leq P_{bat} \leq P_{bat\_max} \tag{A.19}$$

where P_{bat_min} and P_{bat_max} are the minimal and maximal power of the battery.

The maximal output power P_{bat_max} depends on the output voltage:

$$P_{bat\_max} = u_{dc} \frac{u_{oc}(x) - u'_{dc}}{R_{bat}(x)} \tag{A.20}$$

with:

$$u'_{dc} = max\left(\frac{u_{oc}(x)}{2}, u_{bat\_min}, u_{em\_min}\right) \tag{A.21}$$

where u_{bat_min} and u_{em_min} are the minimal voltage of the battery and the EM.

Suppose the battery is charged with maximal current when $SoC < 0.7$ and with constant voltage when $SoC \geq 0.7$, thus the minimal battery power is defined by:

$$P_{bat\_min} = \begin{cases} \left[u_{oc}(x) - I_{char\_max} R_{bat}(x)\right] I_{char\_max} & (if\ x \leq 0.7) \\ u_{dc\_char} \dfrac{u_{oc}(x) - u_{dc\_char}}{R_{bat}(x)} & (if\ x > 0.7) \end{cases} \tag{A.22}$$

where I_{char_max} is the maximal charge current and u_{dc_char} is the charging voltage.

Finally, SoC should be limited in its feasible range, and its final state should have the same value as the initial state for HEV:

$$\begin{cases} x_{min} \leq x \leq x_{max} \\ (\tau_1 \vee \tau_2)\left[x(0) - x(N)\right] = 0 \end{cases} \tag{A.23}$$

A.4 Optimal-efficiency strategy of a MCM system

For any power demand of the MCM, there exists countless power split possibilities, and it is necessary to find the optima. Fig. A.3 is a flowchart which indicates the process of maximizing the system efficiency.

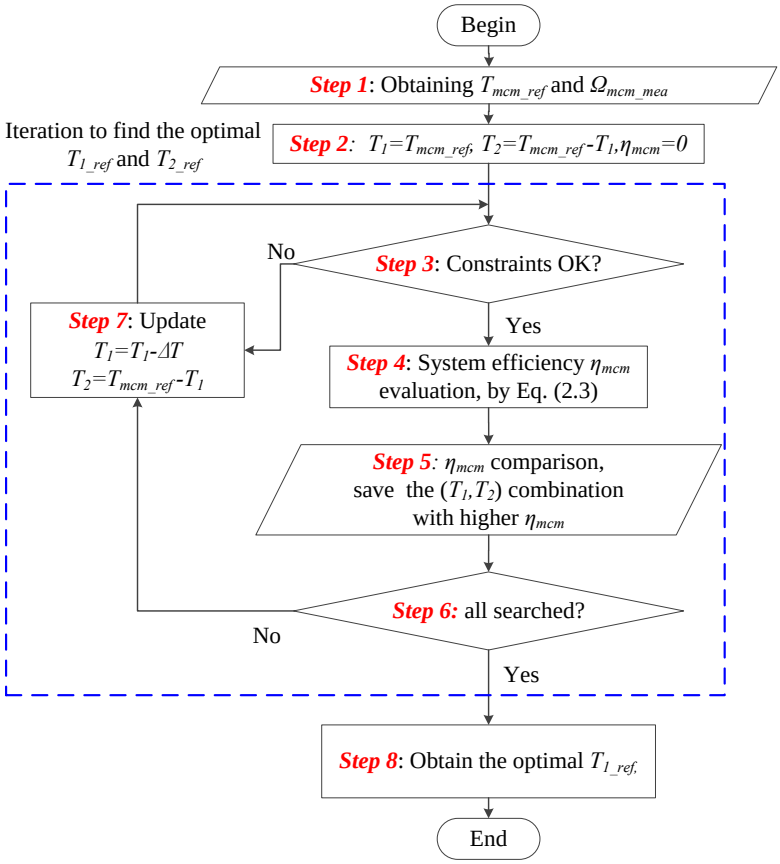

Figure. A.3. Flowchart of the optimal efficiency strategy

The implementation of the algorithm is composed of different steps. Step 1: at any time, the demand torque T_{mcm_ref} and actual speed Ω_{mcm_mea} can be obtained. Step 2: the initial torque values of EM1 and EM2 are set to $T_1 = T_{mcm\_ref}$ and $T_2 = T_{mcm\_ref} - T_1$, and the initial system efficiency η_{mcm} is set to 0. Step 3: checking if the current torque distribution satisfies the constraints. Step 4: obtaining the efficiencies of EM1 and EM2 by looked-up tables, then calculating the system efficiency η_{mcm} by Eq. (2.3). Step 5: comparing the system efficiency obtained in step 4 with the saved system efficiency, saving the higher system efficiency and T_1, T_2. Step 6: checking if all possibilities are searched. Step 7: updating the torque of EM1 and EM2 with $T_1 = T_1 - \Delta T$, $T_2 = T_{mcm\_ref} - T_1$. Step 8: when all the possibilities are searched, output the optimal torque reference of EM1 T_{1_ref}. If the torque step ΔT is smaller enough, the output T_{1_ref} is equivalent to be optimal.

A.5 Properties of different wavelet mother functions

Table. A.3. Comparisons of different methods for efficiency map calculation

Wavelet mother	Harr	Daubechies	Biorthogonal	Morlet	Meyer
Expression	haar	db N	bior	morl	meyr
Orthogonality	Yes	Yes	No	No	Yes
Compacted support	Yes	Yes	Yes	No	No
Symmetry	Yes	$\approx$ Yes	No	Yes	Yes
Vanishing moment	1	$2N$-1	$2N_i$+1	[-4 4]	[-8 8]

B

Publications

Journal articles

(1) K. Li, A. Bouscayrol, S. Han and S. Cui, "Comparisons of Electric Vehicles Using Modular Cascade Machines System and Classical Single Drive Electric Machine," in *IEEE Transactions on Vehicular Technology*, vol. 67, no. 1, pp. 354-361, Jan. 2018.

(2) K. Li, S. Han, S. Cui and A. Bouscayrol, "Sizing of Modular Cascade Machines System for Electric Vehicles," in *IEEE Transactions on Vehicular Technology*, vol. 68, no. 2, pp. 1278-1287, Feb. 2019.

(3) K. Li, A. Bouscayrol, S. Cui. "A Hybrid Modular Cascade Machines System for Electric Vehicles using Induction Machine and Permanent Magnet Synchronous Machine," in *IEEE Transactions on Vehicular Technology*, **(under review)**.

Conference proceedings

(1) K. Li, A. Bouscayrol and S. Cui, "Heat Description of a Modular Cascade Machines System Using Energetic Macroscopic Representation," 2018 *IEEE Vehicle Power and Propulsion Conference (VPPC)*, Chicago, IL, 2018, pp. 1-6.

(2) K. Li, S. Cui, A. Bouscayrol and M. Hecquet, "Analytical Derivation of Efficiency Map of an Induction Machine for Electric Vehicle Applications," 2018

IEEE Vehicle Power and Propulsion Conference (VPPC), Chicago, IL, 2018, pp. 1-6.

(3) K. Li, S. Cui, A. Bouscayrol, Z. Zhang and S. Han, "Reduced-Scale Hardware-In-the-Loop Simulation of an Electric Vehicle Using Modular Cascade Machines," 2017 *IEEE Vehicle Power and Propulsion Conference (VPPC)*, Belfort, 2017, pp. 1-5.

(4) K. Li, S. Cui, S. Han and Z. Zhang, "Torque Distribution Strategy based on Adaptive Network based Fuzzy Interface System for an Electrical Vehicle using Modular Cascade Machines," 2017 *IEEE Transportation Electrification Conference and Expo, Asia-Pacific (ITEC Asia-Pacific)*, Harbin, 2017, pp. 1-6.

(5) K. Li, A. Bouscayrol, S. Cui and S. Han, "Energetic Macroscopic Representation and Inversion-Based Control of an Electrical Vehicle Using Modular Cascade Machines," 2016 *IEEE Vehicle Power and Propulsion Conference (VPPC)*, Hangzhou, 2016, pp. 1-6.

List of Figures

1.1 Efficiency distributions of different EMs 7
1.2 Modular switching reluctance machine 8
1.3 Integral modular EM 9
1.4 Mono-machine system 10
1.5 Multi-machine systems for EVs 11
1.6 Other distributed multi-machine systems for EVs 11
1.7 Categories of MCM system 12
1.8 Comparisons of THS and Voltec 13
1.9 Honda hybrid system 14
1.10 Topology of CHS 14
1.11 Topology of JJE dual-machine system 15
1.12 Example of the above graphical description tools 19
1.13 Research plan of the thesis 22

2.1 Basic topologies of a MCM 25
2.2 Principles of EMR 27

2.3 Topology of the inverter model considering losses 29
2.4 EMR of an IM drive 32
2.5 EMR of an PM-SM drive 33
2.6 Methodology of inversion-based control 34
2.7 EMR and control scheme of an IM drive 36
2.8 EMR and control scheme of a PM-SM drive 36
2.9 Structure of control validation 37
2.10 Experimental platform 37
2.11 Experimental results of IM control validation 38
2.12 Experimental results of SM control validation 38
2.13 The configuration of the studied vehicle 40
2.14 EMR of the MCM drive 41
2.15 EMR and control scheme of the MCM-based EV 43
2.16 Configuration of MCM-based HEV 43
2.17 EMR and control scheme of the MCM-based parallel HEV 44
2.18 EMR and control scheme of the MCM-based series HEV 45
2.19 Tuning path of the MCM-based EV 48
2.20 Control path of the MCM-based EV 48

3.1 Flowchart of efficiency map estimation 54
3.2 Stator current in constant-torque region 55
3.3 Diagram of operating points for current angle calculation 56
3.4 Calculation routing of rated stator copper loss for IMs 59
3.5 Calculation path of rated stator copper losses for I-PM-SMs 65
3.6 Calculation path of rated stator copper losses for I-PM-SMs 67
3.7 Diagram of the experimental setup for efficiency map test 69

3.8 Validation of efficiency estimation method for IM 70
3.9 Validation of efficiency estimation method for S-PM-SM 71
3.10 Validation of efficiency estimation method for I-PM-SM 72
3.11 EMR and control of a pure EV 73

4.1 Flowchart of sizing 78
4.2 Flowchart of the optimal power split strategy 81
4.3 Flowchart of rated frequency calcultion 83
4.4 Flowchart of cost function calculation 84
4.5 Selection of an optimal sizing $m = 2$ 86
4.6 MCM efficiency maps with $m = 1 \sim 4$ 88
4.7 Comparisons of different sizings than the single I-PM-SM 88
4.8 Efficiency maps of parallel MCMs with $m = 2$ 90
4.9 Comparisons of different parallel MCM than the single I-PM-SM . . . 91
4.10 Planetary-gear-train-based MCMs 91
4.11 Optimization direction of an EM in the hybrid coupling structure . . 92
4.12 Efficiency maps of MCMs with planetary gear-train 93
4.13 Backward model of the MCM-based vehicle based on EMR 95
4.14 Comparisons of the ICE of the parallel HEV under UDDS 99
4.15 Comparisons of the ICE of the series HEV under UDDS 99

5.1 Simulation model of the EM by FEM 102
5.2 Efficiency maps of the EMs by FE 103
5.3 EMR of the hybrid-MCM-based EV 104
5.4 Philosophy of MCM power split 104
5.5 Structure of an ANFIS with two inputs 105
5.6 Training data (the optimal torque of EM1) 106

5.7 Membership functions of both inputs . . . 107
5.8 Surface view of the fuzzy rules . . . 107
5.9 Velocity predictor with 3-level wavelet transformation . . . 108
5.10 UDDS decomposition with level 1 . . . 109
5.11 Prediction results for UDDS with level 1 wavelet transformation . . . 110
5.12 Predictive-based power split strategy . . . 111
5.13 Torque carves with the power split strategies in [Han.S 2015] . . . 112
5.14 Torque carves with the power split strategies in this thesis . . . 113
5.15 Principle of the full-scale system . . . 115
5.16 Integration of the interface subsystem (emulation drive) . . . 115
5.17 Simulation structure of the reduced-scale HIL . . . 116
5.18 Experimental platform of the reduced-scale HIL . . . 118
5.19 Torque estimations with optimal-efficiency strategy . . . 119
5.20 Operating points with optimal-efficiency strategy . . . 119
5.21 Torque estimations with ANFIS-based strategy . . . 120
5.22 Operating points with ANFIS-based strategy . . . 120
5.23 Torque estimations with predictive-based strategy . . . 121
5.24 Operating points with predictive-based strategy . . . 121
5.25 Power of the DC bus . . . 121
5.26 Comparison of energy consumption . . . 122

A.1 Examples of inversion-based control . . . 129
A.2 Structure of the planetary gear-train . . . 130
A.3 Flowchart of the optimal efficiency strategy . . . 134

List of Tables

1.1 Evaluations of different EMs for electrified vehicles 7

2.1 Parameters of the experimental prototypes 37

3.1 Parameters of the EMs 68

3.2 Calculation time of the estimation method 72

3.3 Errors of energy consumptions 74

3.4 Comparisons of different methods for efficiency map calculation . . . 74

4.1 Parameters of the vehicle 79

4.2 Dynamical requirements of the vehicle 79

4.3 Initial requirements of the traction system 79

4.4 Waveform factors with sinusoidal EMF and current 82

4.5 Optimal sizing with $m = 1 \sim 4$ 87

4.6 Perato solutions for parallel MCM with $m = 2$ 89

4.7 Operation modes of the clutches 92

4.8 Optimal sizing of planetary gear-train based MCM 93

4.9 Comparisons of high-efficiency areas of different MCM topologies . . . 94
4.10 Energy reduction (%) of different series MCMs 96
4.11 Average energy reduction (%) of different series MCMs 96
4.12 Energy reduction (%) of different parallel MCMs (m=2) 96
4.13 Parameters of the HEV 97
4.14 Parameters of the traction system of the HEV 97
4.15 Parameters of the MCM system 97
4.16 Fuel reduction (%) of MCM-based HEV than classical HEV 98

5.1 Basic parameters of the EM by FEM 103
5.2 Comparisons of velocity predictions results 110
5.3 Start/Stop times of different strategies 112
5.4 Energy consumptions of different strategies 114
5.5 Parameters of MCM system 114

A.1 Basic EMR elements 128
A.2 Selecting coefficients in terms of different vehicles 131
A.3 Comparisons of different methods for efficiency map calculation . . . 135

Bibliography

Ahn, J.-W., Park, S.-J., and Lee, D.-H. (2004). Hybrid excitation of srm for reduction of vibration and acoustic noise. *IEEE Transactions on Industrial Electronics*, 51(2):374–380. (Cited on page 6)

Allegre, A., Bouscayrol, A., Verhille, J., Delarue, P., Chattot, E., and El-Fassi, S. (2010). Reduced-scale-power hardware-in-the-loop simulation of an innovative subway. *IEEE Transactions on Industrial Electronics*, 57(4):1175–1185. (Cited on pages 114, 115, 117)

Allègre, A.-L., Bouscayrol, A., and Trigui, R. (2013). Flexible real-time control of a hybrid energy storage system for electric vehicles. *IET Electrical Systems in Transportation*, 3(3):79–85. (Cited on page 2)

Beishe, W., Zhidi, Q., Huiyong, W., and Jianxu, D. (2011). Analysis of permanent magnet size of rare earth permanent magnet motor. *Dongfang Electrical Machine*, 39(04):10–12. (Cited on page 83)

Bellman, R. (1966). Dynamic programming. *Science*, 153(3731):34–37. (Cited on page 94)

Boulon, L. (2009). *Modélisation multiphysique des éléments de stockage et de conversion d'énergie pour les véhicules électriques hybrides. Approches systémique pour la gestion d'énergie*. Thesis, Université de Franche-Compté, France. (Cited on page 23)

Boulon, L., Bouscayrol, A., Hissel, D., Pape, O., and Pera, M.-C. (2013). Inversion-based control of a highly redundant military hev. *IEEE Transactions on Vehicular Technology*, 62(2):500–510. (Cited on page 2)

Bouscayrol, A., Davat, B., De Fornel, B., François, B., Hautier, J., Meibody-Tabar, F., and Pietrzak-David, M. (2000). Multi-converter multi-machine systems: application for electromechanical drives. *The European Physical Journal Applied Physics*, 10(2):131–147. (Cited on pages 1, 2)

Bouscayrol, A., Dauphin-Tanguy, G., Geitner, G.-H., Guillaud, X., Pennamen, A., and Hautier, J. (2005). Different energetic descriptions for electromechanical systems. In *Power Electronics and Applications, 2005 European Conference on*, pages 10 pp.–P. 10. IEEE. (Cited on page 19)

Bouscayrol, A., Guillaud, X., Delarue, P., and Lemaire-Semail, B. (2009). Energetic macroscopic representation and inversion-based control illustrated on a wind-energy-conversion system using hardware-in-the-loop simulation. *IEEE transactions on Industrial Electronics*, 56(12):4826–4835. (Cited on page 114)

Bouscayrol, A., Hautier, J.-P., and Lemaire-Semail, B. (2012). Graphic formalisms for the control of multi-physical energetic systems: Cog and emr. *Systemic design methodologies for electrical energy systems: analysis, synthesis and management*, pages 89–124. (Cited on pages 2, 18, 27, 128)

Bruyère, A. (2009). *Modélisation et commande d un alterno-demarreur heptaphase application automobile micro-hybride*. Thesis, Université de Lille l, France. (Cited on page 23)

Cengelci, E., Enjeti, P., and Gray, W. (1999). A new modular motor-modular inverter (mm-mi) concept for medium voltage adjustable speed drive systems. In *Industry Applications Conference, 1999. Thirty-Fourth IAS Annual Meeting. Conference Record of the 1999 IEEE*, volume 3, pages 1972–1979. IEEE. (Cited on page 7)

Chan, C. C., Bouscayrol, A., and Chen, K. (2010). Electric, hybrid, and fuel-cell vehicles: Architectures and modeling. *IEEE transactions on vehicular technology*, 59(2):589–598. (Cited on page 9)

Chan, C. C. (2013). The rise & fall of electric vehicles in 1828–1930: Lessons learned [scanning our past]. *Proceedings of the IEEE*, 101(1):206–212. (Cited on pages 1, 6, 9)

Chau, K. and Wong, Y. (2002). Overview of power management in hybrid electric vehicles. *Energy conversion and management*, 43(15):1953–1968. (Cited on page 17)

Chau, K., Chan, C. C., and Liu, C. (2008). Overview of permanent-magnet brushless drives for electric and hybrid electric vehicles. *IEEE Transactions on industrial electronics*, 55(6):2246–2257. (Cited on pages 1, 6, 6)

Chau, K. and Li, W. (2014). Overview of electric machines for electric and hybrid vehicles. *International Journal of Vehicle Design: journal of vehicle engineering, automotive technology and components*. (Cited on page 6, 6, 6)

Chau, K. (2016). Overview of electric vehicle machines-from tesla to tesla, and beyond. In *2016 International Conference of Asian Union of Magnetics Societies (ICAUMS)*, pages 1–6. IEEE. (Cited on page 6, 6)

Chedot, L., Friedrich, G., Biedinger, J., and Macret, P. (2007). Integrated starter generator: The need for an optimal design and control approach. application to a permanent magnet machine. *IEEE Transactions on Industry Applications*, 43(2):551–559. (Cited on page 20)

Chen, Y. (2010). *Common Energetic Macroscopic Representation and Unified Control Structure for Different Hybrid Electric Vehicles*. Thesis, Université de Lille l, France. (Cited on pages 19, 23)

Cheng, Y., Trigui, R., Espanet, C., Bouscayrol, A., and Cui, S. (2011). Specifications and design of a pm electric variable transmission for toyota prius ii. *IEEE Transactions on Vehicular Technology*, 60(9):4106–4114. (Cited on page 22)

Chu, W., Zhu, Z., Zhang, J., Liu, X., Stone, D., and Foster, M. (2015). Investigation on operational envelops and efficiency maps of electrically excited machines for electrical vehicle applications. *IEEE Transactions on Magnetics*, 51(4):1–10. (Cited on page 6)

Cui, S., Han, S., and Chan, C. (2014). Overview of multi-machine drive systems for electric and hybrid electric vehicles. In *Transportation Electrification Asia-Pacific (ITEC Asia-Pacific), 2014 IEEE Conference and Expo*, pages 1–6. IEEE. (Cited on pages 2, 9, 11)

Cui, S., Wang, S., Wu, S., Yurievich, O. S., and Milyaev, I. M. (2017). Design and analysis of a modular pulsed alternator power system for driving 32-mj muzzle energy railgun. *IEEE Transactions on Plasma Science*, 45(7):1128–1133. (Cited on page 22)

Cui, S., Wang, Z., Han, S., Zhu, C., and Chan, C. (2018). Analysis and design of multiphase receiver with reduction of output fluctuation for ev dynamic wireless charging system. *IEEE Transactions on Power Electronics*. (Cited on page 22)

Delarue, P., Bouscayrol, A., and Semail, E. (2003). Generic control method of multileg voltage-source-converters for fast practical implementation. *IEEE Transactions on power electronics*, 18(2):517–526. (Cited on page 28)

Diallo, D., Benbouzid, M. E. H., and Masrur, M. A. (2013). Special section on condition monitoring and fault accommodation in electric and hybrid propulsion systems. *IEEE Transactions on Vehicular Technology*, 62(3):962–964. (Cited on page 1)

Dizqah, A. M., Lenzo, B., Sorniotti, A., Gruber, P., Fallah, S., and De Smet, J. (2016). A fast and parametric torque distribution strategy for four-wheel-drive energy-efficient electric vehicles. *IEEE Transactions on Industrial Electronics*, 63(7):4367–4376. (Cited on page 1)

dos Santos Moraes, T. J., Trabelsi, M., Nguyen, N. K., Semail, E., Meinguet, F., and Guerin, M. (2017). Inverter open circuit faults diagnosis in series-connected six-phases permanent magnet drive. In *2017 IEEE 11th International Symposium on Diagnostics for Electrical Machines, Power Electronics and Drives (SDEMPED)*, pages 188–194. IEEE. (Cited on page 1)

Du, B., Wu, S., Han, S., and Cui, S. (2016a). Application of linear active disturbance rejection controller for sensorless control of internal permanent-magnet synchronous motor. *IEEE Transactions on Industrial Electronics*, 63(5):3019–3027. (Cited on page 22)

Du, B., Wu, S., Han, S., and Cui, S. (2016b). Interturn fault diagnosis strategy for interior permanent-magnet synchronous motor of electric vehicles based on digital signal processor. *IEEE Transactions on Industrial Electronics*, 63(3):1694–1706. (Cited on page 22)

Ehsani, M., Gao, Y., and Miller, J. M. (2007). Hybrid electric vehicles: Architecture and motor drives. *Proceedings of the IEEE*, 95(4):719–728. (Cited on page 1)

Ehsani, M., Gao, Y., Longo, S., and Ebrahimi, K. (2018). *Modern electric, hybrid electric, and fuel cell vehicles*. CRC press. (Cited on page 1)

Emadi, A., Lee, Y. J., and Rajashekara, K. (2008). Power electronics and motor drives in electric, hybrid electric, and plug-in hybrid electric vehicles. *IEEE Transactions on Industrial Electronics*, 55(6):2237–2245. (Cited on page 1)

Fengfeng, S. and Arui, Q. (2007). Analysis of power and torque density for the induction motor. *Explosion Proof Electric Machine*, 42(1):1–3. (Cited on page 81)

Fish, S. and Savoie, T. B. (2001a). Simulation-based optimal sizing of hybrid electric vehicle components for specific combat missions. *IEEE Transactions on Magnetics*, 37(1):485–488. (Cited on page 16)

Fish, S. and Savoie, T. B. (2001b). Simulation-based optimal sizing of hybrid electric vehicle components for specific combat missions. *IEEE Transactions on Magnetics*, 37(1):485–488. (Cited on page 16, 16)

Gao, Y. and Ehsani, M. (2006). Parametric design of the traction motor and energy storage for series hybrid off-road and military vehicles. *IEEE Transactions on Power electronics*, 21(3):749–755. (Cited on page 16)

Ghayebloo, A. and Radan, A. (2016). Superiority of dual-mechanical-port-machine-based structure for series–parallel hybrid electric vehicle applications. *IEEE Transactions on Vehicular Technology*, 65(2):589–602. (Cited on page 1)

Graovac, D. and Purschel, M. (2009). Igbt power losses calculation using the datasheet parameters. *Infineon application note*, 1(1). (Cited on page 28)

Grebe, U. D. and Nitz, L. T. (2011). Voltec–the propulsion system for chevrolet volt and opel ampera. *ATZautotechnology*, 11(2):28–35. (Cited on page 13)

Hall, E., Ramamurthy, S., and Balda, J. (2001). Optimum speed ratio of induction motor drives for electrical vehicle propulsion. In *Applied Power Electronics Conference and Exposition, 2001. APEC 2001. Sixteenth Annual IEEE*, volume 1, pages 371–377. IEEE. (Cited on pages 16, 59)

Han, S. and Cui, S. (2013). A new modular cascade machine system. *Diangong Jishu Xuebao(Transactions of China Electrotechnical Society)*, 28(2):155–162. (Cited on pages 2, 9, 11)

Han, S. (2015). *Research on Modular Cascade Machines System for Electric vehicles*. PhD thesis, Harbin Institute of Technology. (Cited on pages 2, 2, 2, 9, 11, 12, 16, 18, 104, 111, 112, 112, 114, 141)

Hautier, J.-P. and Barre, P.-J. (2004). The causal ordering graph a tool for system modelling and control law synthesis. *Studies in informatics and control*, 13(4):265–284. (Cited on page 18)

Hedlund, S. and Rantzer, A. (2002). Convex dynamic programming for hybrid systems. *IEEE Transactions on Automatic Control*, 47(9):1536–1540. (Cited on page 17)

Heins, G., Ionel, D. M., Patterson, D., Stretz, S., and Thiele, M. (2016). Combined experimental and numerical method for loss separation in permanent-magnet brushless machines. *IEEE Transactions on Industry Applications*, 52(2):1405–1412. (Cited on pages 19, 20)

Higuchi, N., Sunaga, Y., Tanaka, M., and Shimada, H. (2013). Development of a new two-motor plug-in hybrid system. *SAE International Journal of Alternative Powertrains*, 2(1):135–145. (Cited on page 13)

Hoeijmakers, M. J. and Ferreira, J. A. (2006). The electric variable transmission. *IEEE transactions on industry applications*, 42(4):1092–1100. (Cited on page 1)

Honda, T. (2015). Development of handling performance control for sport hybrid sh-awd. Technical report, SAE Technical Paper. (Cited on page 14)

Horrein, L. (2015). *Gestion d'énergie décomposée d'un véhicule hybride intégrant les aspects thermiques via la représentation énergétique macroscopique*. Thesis, Université de Lille l, France. (Cited on page 23)

Hua, W., Cheng, M., Zhu, Z., and Howe, D. (2008). Analysis and optimization of back emf waveform of a flux-switching permanent magnet motor. *IEEE Transactions on Energy Conversion*, 23(3):727–733. (Cited on page 8)

Huang, S., Luo, J., Leonardi, F., and Lipo, T. A. (1998). A general approach to sizing and power density equations for comparison of electrical machines. *IEEE Transactions on Industry Applications*, 34(1):92–97. (Cited on pages 81, 82)

Ide, H., Sunaga, Y., and Higuchi, N. (2014). Development of sport hybrid i-mmd control system for 2014 model year accord. *Introduction of new technologies*. (Cited on page 13)

Jack, A. G., Mecrow, B. C., and Haylock, J. A. (1996). A comparative study of permanent magnet and switched reluctance motors for high-performance fault-tolerant applications. *IEEE transactions on industry applications*, 32(4):889–895. (Cited on page 8)

Jang, J.-S. (1993). Anfis: adaptive-network-based fuzzy inference system. *IEEE transactions on systems, man, and cybernetics*, 23(3):665–685. (Cited on page 105)

Johannesson, L., Asbogard, M., and Egardt, B. (2007). Assessing the potential of predictive control for hybrid vehicle powertrains using stochastic dynamic programming. *IEEE Transactions on Intelligent Transportation Systems*, 8(1):71–83. (Cited on page 17)

Karnopp, D., Margolis, D. L., and Rosenberg, R. C. (1990). *System Dynamics: A Unified Approach, 2nd*, volume 514. New York: Wiley. xiv. (Cited on page 18)

Kostic Perovic, D. (2012). Making the impossible, possible–overcoming the design challenges of in wheel motors. *World Electric Vehicle Journal*, 5(2):514–519. (Cited on page 11)

Kunyuan, L., Liang, C., Wei, W., and Cong, G. (2011). Parameter matching design and optimization of electric vehicle based on body characteristic of permanent magnetic synchronous motor. In *Measuring Technology and Mechatronics Automation (ICMTMA)*, pages 831–835. IEEE. (Cited on page 79)

Labak, A. and Kar, N. C. (2012). Outer rotor switched reluctance motor design for in-wheel drive of electric bus applications. In *2012 XXth International Conference on Electrical Machines*, pages 418–423. IEEE. (Cited on page 11)

Le, T. G. (2007). A hybrid drive for a heavy vehicle. French PATENT FR0704612A, Nexter Systems. (Cited on page 14)

Lee, C., Krishnan, R., and Lobo, N. (2009). Novel two-phase switched reluctance machine using common-pole e-core structure: concept, analysis, and experimental verification. *IEEE transactions on industry applications*, 45(2):703–711. (Cited on page 8)

Lee, H., Cha, S. W., Kim, N., Jeong, J., Vijayagopal, R., and Rousseau, A. (2017a). Development of vehicle component sizing process using optimization algorithm. In *2017 IEEE Vehicle Power and Propulsion Conference (VPPC)*, pages 1–5. IEEE. (Cited on page 16)

Lee, H., Cha, S. W., Kim, N., Jeong, J., Vijayagopal, R., and Rousseau, A. (2017b). Development of vehicle component sizing process using optimization algorithm. In *2017 IEEE Vehicle Power and Propulsion Conference (VPPC)*, pages 1–5. (Cited on page 16)

Lequesne, B. (2015). Automotive electrification: The nonhybrid story. *IEEE Transactions on Transportation Electrification*, 1(1):40–53. (Cited on page 1)

Letrouvé, T. (2013). *Structuration de la commande de la simulation au prototype d'un véhicule hybride double parallèle au travers de la Représentation Energétique Macroscopique*. Thesis, Université de Lille l, France. (Cited on pages 19, 23)

Levi, E. (1984). *Polyphase motors: a direct approach to their design*. Wiley New York, NY. (Cited on pages 19, 52, 82)

Lhomme, W. (2007). *Gestion d'énergie de véhicules électriques hybrides basée sur la REM*. Thesis, Université de Lille l, France. (Cited on pages 19, 23)

Lhomme, W., Bouscayrol, A., Syed, S. A., Roy, S., Gailly, F., and Pape, O. (2017). Energy savings of a hybrid truck using a ravigneaux gear train. *IEEE Transactions on Vehicular Technology*, 66(10):8682–8692. (Cited on page 14)

Li, G. and Zhu, Z. (2016). Demagnetization of modular surface mounted permanent magnet machines. In *Electrical Machines (ICEM), 2016 XXII International Conference on*, pages 702–708. IEEE. (Cited on page 8)

Li, J., Song, X., and Cho, Y. (2008). Comparison of 12/8 and 6/4 switched reluctance motor: Noise and vibration aspects. *IEEE transactions on magnetics*, 44(11):4131–4134. (Cited on page 6)

Li, K., Bouscayrol, A., Cui, S., and Han, S. (2016). Energetic macroscopic representation and inversion-based control of an electrical vehicle using modular cascade machines. In *2016 IEEE Vehicle Power and Propulsion Conference (VPPC)*, pages 1–6. (Cited on pages 2, 9, 11)

Li, K., Bouscayrol, A., Han, S., and Cui, S. (2018). Comparisons of electric vehicles using modular cascade machines system and classical single drive electric machine. *IEEE Transactions on Vehicular Technology*, 67(1):354–361. (Cited on page 94)

Li, S., Yang, J., Zhang, T., Ma, Z., and Yu, H. (2012a). Double planetary row four-axis hybrid power transmission device. U.S. Patent US8382624B2, Corun Chs Technology Co Ltd. (Cited on page 14)

Li, S., Yang, J., Zhang, T., Yu, W., Ma, Z., and Yu, H. (2012b). Power system of hybrid electric vehicle. EUROPEAN PATENT EP2472144A1, Corun Chs Technology Co Ltd. (Cited on page 14)

Li, S., Yang, J., Zhang, T., Yu, W., Ma, Z., and Yu, H. (2013). Powertrain for hybrid electrical vehicle. U.S. Patent US8382624B2, Corun Chs Technology Co Ltd. (Cited on page 14)

Lipo, T. A. (2018). Calculation of induction machine losses. *Introduction to AC Machine Design, First Edition*, pages 193–250. (Cited on page 52)

Liu, B., Li, L., Wang, X., and Cheng, S. (2018). Hybrid electric vehicle downshifting strategy based on stochastic dynamic programming during regenerative braking process. *IEEE Transactions on Vehicular Technology*, 67(6):4716–4727. (Cited on page 17)

Lukic, S. and Emado, A. (2003). Modeling of electric machines for automotive applications using efficiency maps. In *Electrical Insulation Conference and Electrical Manufacturing & Coil Winding Technology Conference, 2003. Proceedings*, pages 543–550. IEEE. (Cited on pages 6, 64)

Lyons, D., StraubelErik, J. B., and Garriga, S. (2013). Rotor design for an electric motor. U.S. Patent 20130069476A1. (Cited on page 6)

Mahmoudi, A., Soong, W. L., Pellegrino, G., and Armando, E. (2015). Efficiency maps of electrical machines. In *Energy Conversion Congress and Exposition (ECCE), 2015 IEEE*, pages 2791–2799. IEEE. (Cited on pages 6, 20)

Mahmoudi, A., Soong, W. L., Pellegrino, G., and Armando, E. (2017). Loss function modeling of efficiency maps of electrical machines. *IEEE Transactions on Industry Applications*, 53(5):4221–4231. (Cited on pages 6, 20)

Mao, S.-H. and Tsai, M.-C. (2005). A novel switched reluctance motor with c-core stators. *IEEE Transactions on Magnetics*, 41(12):4413–4420. (Cited on page 8)

Martinez, J. S., Hissel, D., Pera, M.-C., and Amiet, M. (2011). Practical control structure and energy management of a testbed hybrid electric vehicle. *IEEE Transactions on Vehicular Technology*, 60(9):4139–4152. (Cited on page 1)

Matthe, R. and Eberle, U. (2014). The voltec system—energy storage and electric propulsion. In *Lithium-Ion Batteries*, pages 151–176. Elsevier. (Cited on page 13)

Mayet, C., Horrein, L., Bouscayrol, A., Delarue, P., Verhille, J. N., Chattot, E., and Lemaire-Semail, B. (2014a). Comparison of different models and simulation approaches for the energetic study of a subway. *IEEE Transactions on Vehicular Technology*, 63(2):556–565. (Cited on page 94)

Mayet, C., Pouget, J., Bouscayrol, A., and Lhomme, W. (2014b). Influence of an energy storage system on the energy consumption of a diesel-electric locomotive. *IEEE transactions on Vehicular Technology*, 63(3):1032–1040. (Cited on page 17)

Mineeshma, G., Chacko, R. V., Amal, S., Sreedevi, M., and Vishnu, V. (2016). Component sizing of electric vehicle/hybrid electric vehicle subsystems using backward modelling approach. In *2016 IEEE International Conference on Power Electronics, Drives and Energy Systems (PEDES)*, pages 1–5. IEEE. (Cited on page 16)

Mock, P. (2017). European vehicle market statistics. *Pocketbook: Lugano, Germany*. (Cited on page 10)

Muta, K., Yamazaki, M., and Tokieda, J. (2004). Development of new-generation hybrid system ths ii-drastic improvement of power performance and fuel economy. Technical report, SAE Technical Paper. (Cited on page 13)

Nguyen, N. K., Meinguet, F., Semail, E., and Kestelyn, X. (2015). Fault-tolerant operation of an open-end winding five-phase pmsm drive with short-circuit inverter fault. *IEEE Transactions on Industrial Electronics*, 63(1):595–605. (Cited on page 1)

Ono, K. (2014). Electric drive system for sport hybrid sh-awd. Technical report, SAE Technical Paper. (Cited on page 14)

Patel, V. I., Wang, J., Nugraha, D. T., Vuletić, R., and Tousen, J. (2016). Enhanced availability of drivetrain through novel multiphase permanent-magnet machine drive. *IEEE Transactions on Industrial Electronics*, 63(1):469–480. (Cited on page 1)

Peng, H., Lei, H., Changyun, M., and Wencheng, G. (2011). Maximum torque-to-current control of ipmsm considering saturation effect. *Power Electronics*, 30:41–43. (Cited on page 61)

Pourabdollah, M., Egardt, B., Murgovski, N., and Grauers, A. (2018). Convex optimization methods for powertrain sizing of electrified vehicles by using different levels of modeling details. *IEEE Transactions on Vehicular Technology*, 67(3):1881–1893. (Cited on page 17)

Raisemche, A., Boukhnifer, M., Larouci, C., and Diallo, D. (2014). Two active fault-tolerant control schemes of induction-motor drive in ev or hev. *IEEE Transactions on Vehicular Technology*, 63(1):19–29. (Cited on page 1)

Ramakrishnan, K., Stipetic, S., Gobbi, M., and Mastinu, G. (2018). Optimal sizing of traction motors using scalable electric machine model. *IEEE Transactions on Transportation Electrification*, 4(1):314–321. (Cited on page 16)

Ramamurthy, S. S. and Balda, J. C. (2001). Sizing a switched reluctance motor for electric vehicles. *IEEE Transactions on Industry Applications*, 37(5):1256–1264. (Cited on page 16)

Routex, J. Y., Gay-Desharnais, S., and Ehsani, M. (2002). Study of hybrid electric vehicle drive train dynamics using gyrator-based equivalent circuit modeling. Report 0148-7191, SAE Technical Paper. (Cited on page 18)

Salmasi, F. R. (2007). Control strategies for hybrid electric vehicles: Evolution, classification, comparison, and future trends. *IEEE Transactions on vehicular technology*, 56(5):2393–2404. (Cited on pages 17, 94)

Samanta, C., Padhy, S. K., Panigrahi, S. P., and Panigrahi, B. K. (2013). Hybrid swarm intelligence methods for energy management in hybrid electric vehicles. *IET Electrical Systems in Transportation*, 3(1):22–29. (Cited on page 17)

Samanta, C., Panigrahi, S. P., and Panigrahi, B. K. (2014). Genetic-based bacteria foraging to optimise energy management of hybrid electric vehicles. *IET Electrical Systems in Transportation*, 4(3):53–61. (Cited on page 17)

Sayed, S. (2012). *Energetic Macroscopic Representation and Multi-Level Energy Management for Heavy-Duty Hybrid Electric Vehicles using Double Planetary geartrain*. Thesis, Université de Lille l, France. (Cited on pages 19, 23)

Schönfeld, R. and Geitner, G. (2004). Power flow and information flow in motion control system. In *Proc. EPE-PEMC*. (Cited on page 18)

Sharifan, S., Ebrahimi, S., Oraee, A., and Oraee, H. (2015). Performance comparison between brushless pm and induction motors for hybrid electric vehicle applications. In *2015 Intl Aegean Conference on Electrical Machines & Power Electronics (ACEMP), 2015 Intl Conference on Optimization of Electrical & Electronic Equipment (OPTIM) & 2015 Intl Symposium on Advanced Electromechanical Motion Systems (ELECTROMOTION)*, pages 719–724. IEEE. (Cited on page 6)

Silvas, E., Hofman, T., Murgovski, N., Etman, L. P., and Steinbuch, M. (2017). Review of optimization strategies for system-level design in hybrid electric vehicles. *IEEE Transactions on Vehicular Technology*, 66(1):57–70. (Cited on page 17)

Stanislav, F., Jan, B., and Jiri, L. (2013). Analytical derivation of induction machine efficiency map. In *Power Engineering, Energy and Electrical Drives (POWERENG), 2013 Fourth International Conference on*, pages 1206–1210. IEEE. (Cited on page 20)

Su, J., Gao, R., and Husain, I. (2018). Model predictive control based field-weakening strategy for traction ev used induction motor. *IEEE Transactions on Industry Applications*, 54(3):2295–2305. (Cited on page 6)

Taras, P., Li, G., and Zhu, Z. (2015). Comparative study of alternative modular switched flux permanent magnet machines. In *Industrial Technology (ICIT), 2015 IEEE International Conference on*, pages 658–663. IEEE. (Cited on page 8)

Vagg, C., Akehurst, S., Brace, C. J., and Ash, L. (2016). Stochastic dynamic programming in the real-world control of hybrid electric vehicles. *IEEE Transactions on Control Systems Technology*, 24(3):853–866. (Cited on page 17)

Vandana, R. and Fernandes, B. (2010). Optimal sizing of motor—battery system for in wheel electric vehicles. In *IECON 2010-36th Annual Conference on IEEE Industrial Electronics Society*, pages 2510–2515. IEEE. (Cited on page 16)

Wan, Y., Wu, S., and Cui, S. (2016). Choice of pole spacer materials for a high-speed pmsm based on the temperature rise and thermal stress. *IEEE Transactions on Applied Superconductivity*, 26(7):1–5. (Cited on page 22)

Wang, Z., Qu, C., Zhang, L., Xue, X., and Wu, J. (2018). Optimal component sizing of a four-wheel independently-actuated electric vehicle with a real-time torque distribution strategy. *IEEE Access*. (Cited on page 16)

Werner, Q., Pierfederici, S., Takorabet, N., and Neidig, N. (2017). Increasing modularity and accuracy of voltage source inverter loss model for automotive virtual testing. In *2017 19th European Conference on Power Electronics and Applications (EPE'17 ECCE Europe)*, pages 1–6. IEEE. (Cited on page 28)

Williamson, S. S., Emadi, A., and Rajashekara, K. (2007). Comprehensive efficiency modeling of electric traction motor drives for hybrid electric vehicle propulsion applications. *IEEE Transactions on Vehicular Technology*, 56(4):1561–1572. (Cited on page 20)

Wipke, K. B., Cuddy, M. R., and Burch, S. D. (1999). Advisor 2.1: A user-friendly advanced powertrain simulation using a combined backward/forward approach. *IEEE transactions on vehicular technology*, 48(6):1751–1761. (Cited on page 19)

Wirasingha, S. G. and Emadi, A. (2011). Classification and review of control strategies for plug-in hybrid electric vehicles. *IEEE Transactions on vehicular technology*, 60(1):111–122. (Cited on page 17)

Wu, J., Cui, N.-X., Zhang, C.-H., and Pei, W.-H. (2010). Pso algorithm-based optimization of plug-in hybrid electric vehicle energy management strategy. In *2010 8th World Congress on Intelligent Control and Automation*, pages 3997–4002. IEEE. (Cited on page 17)

Wu, S., Cheng, D., and Cui, S. (2013). Optimization design and research of a hybrid excitation compulsator. *IEEE Transactions on Plasma Science*, 41(5):1280–1284. (Cited on page 22)

Wu, X. (2013). *Research on Powertrain Parameters Design of Pure Electric Car*. Thesis, Jilin University, China. (Cited on page 16)

Xu, Q. (1998). Hybrid power system of toyota. *World Auto*. (Cited on page 13)

Xu, Q., Sun, J., Ye, X., Wang, Z., Liu, X., and Wang, H. (2017). Optimized parameters sizing between evt and ths used for hybrid electric vehicles. In *Transportation Electrification Asia-Pacific (ITEC Asia-Pacific), 2017 IEEE Conference and Exp*, pages 1–5. IEEE. (Cited on page 16)

Yang, H., Lim, Y.-C., and Kim, H.-C. (2013). Acoustic noise/vibration reduction of a single-phase srm using skewed stator and rotor. *IEEE Transactions on Industrial Electronics*, 60(10):4292–4300. (Cited on page 6)

Yu, H., Yu, W., Zhang, T., Li, S., Yang, J., and Ma, Z. (2011). Hybrid electric vehicle power system braking control device. WORLD PATENT WO2011022939A1, Corun Chs Technology Co Ltd. (Cited on page 14)

Yu, P., Ye, X., Wang, T., and Wang, X. (2015). Electromagnetism tooth embedded clutch and dual-motor hybrid power system. Chinese PATENT CN204109779U, JingJin Electric Co Ltd. (Cited on page 15)

Zhang, L., Fan, Y., Lorenz, R. D., Cui, R., Li, C., and Cheng, M. (2017). Design and analysis of a new five-phase brushless hybrid-excitation fault-tolerant motor for electric vehicles. *IEEE Transactions on Industry Applications*, 53(4):3428–3437. (Cited on page 1)

Zhang, X. (2013). Sensorless induction motor drive using indirect vector controller and sliding-mode observer for electric vehicles. *IEEE Transactions on Vehicular Technology*, 62(7):3010–3018. (Cited on page 6)

Zhu, Z. and Howe, D. (2007). Electrical machines and drives for electric, hybrid, and fuel cell vehicles. *Proceedings of the IEEE*, 95(4):746–765. (Cited on pages 1, 6)

Zhu, Z. and Chan, C. (2008). Electrical machine topologies and technologies for electric, hybrid, and fuel cell vehicles. In *2008 IEEE Vehicle Power and Propulsion Conference*, pages 1–6. IEEE. (Cited on page 1)

Zou, Y., Kong, Z., Liu, T., and Liu, D. (2017). A real-time markov chain driver model for tracked vehicles and its validation: Its adaptability via stochastic dynamic programming. *IEEE Transactions on Vehicular Technology*, 66(5):3571–3582. (Cited on page 17)